UCGE Reports
Number 20264
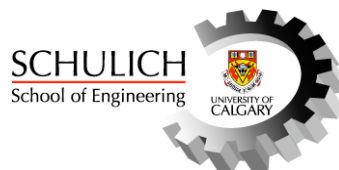
Department of Geomatics Engineering

New Enhanced Sensitivity Detection Techniques for GPS L1 C/A and Modernized Signal Acquisition
(URL: http://www.geomatics.ucalgary.ca/research/publications/GradTheses.html)

by

Surendran Konavattam Shanmugam

January 2008

SCHULICH
School of Engineering

UNIVERSITY OF CALGARY

UNIVERSITY OF CALGARY

New Enhanced Sensitivity Detection Techniques for GPS L1 C/A and Modernized

Signal Acquisition

by

Surendran K. Shanmugam

A DISSERTATION

SUBMITTED TO THE FACULTY OF GRADUATE STUDIES

IN PARTIAL FULFILLMENT OF THE REQUIREMENTS FOR THE

DEGREE OF DOCTOR OF PHILOSOPHY

DEPARTMENT OF GEOMATICS ENGINEERING

CALGARY, ALBERTA

January, 2008

Abstract

Throughout history, there has been a constant effort to master the art of navigation for its importance in trade and commerce. Even today, this pursuit of better navigation is still active for its continual impact in various fields. In the last decade, the navigation field witnessed drastic changes with the advent of global navigation satellite system (GNSS) in the form of the global positioning system (GPS). This decade is currently witnessing the expansion of its scope far beyond its traditional focus. On the other hand, these expansions has brought upon new challenges to the current GPS system that were never encountered before. Hence, the legacy GPS system is expected to overcome some stern impediments inherent to these new applications for its continual dominance. For instance, massive signal attenuation, radio frequency interference (RFI) and multipath readily represents, *the axis of evil*, in the view point of GPS operations as applied to these new applications. More specifically, massive signal attenuation and RFI conditions poses a grave difficulty in terms of traditional GPS operations. Subsequently, one has to resort to enhanced sensitivity GPS receivers for successful GPS operations under these adverse signal conditions. A number of detection algorithms have been utilized to permit successful GPS operations under degraded signal environments.

In this dissertation, an earnest effort is made to establish these detection algorithms in a cohesive fashion. Fundamental theoretical considerations based on the generalized likelihood ratio test (GLRT), as applied to GPS signal detection, are discussed. An unified approach is adopted to establish various post-correlation detection schemes as the best approximations of the GLRT. For assumed deterministic signals the GLRT further reduces to a matched filter. This implies that the navigation data, code phase and carrier parameters are known at the receiver. Besides, it unifies the well-known post-correlation non-coherent detection (PCND) and the newly proposed

post-correlation differential detection (PCDD) in terms of GLRT. Finally, new variants of these detection algorithms is proposed both at pre and post-correlation levels. Two asymptotic versions of GLRT, namely the multi-correlation differential detection (MCDD) (pre-correlation level) and the generalized post-correlation differential detection (GPCDD)(post-correlation level) are proposed. It is shown that the asymptotic version of the GLRT is equivalent to an estimator correlator (EC). The use of a novel *pre-filtering* operation for pre-correlation noise suppression is also introduced in the context of pre-correlation differential scheme.

The benefits of the proposed detectors are further established for interference detection/suppression and modernized GPS signal acquisition. The MCDD based novel continuous wave interference detection, estimation, and suppression scheme is introduced. The application of MCDD is also introduced as an efficient detector for GPS L5 NH code acquisition in the presence of residual frequency errors. Similarly, the use of GPCDD for GPS L2C acquisition is corroborated in terms of CM and CL code detection. The proposed detectors as well as the traditional ones were implemented in MATLAB$^{\text{TM}}$ environment for subsequent performance analysis. The major findings of the presented research were duly validated using hardware simulated and/or live GPS signals in addition to theoretical and numerical analysis.

Acknowledgments

It is with pleasure that I acknowledge my heartfelt thanks and gratitude to my doctoral supervisors, Professor Gérard Lachapelle and Professor John Nielsen for their encouragement, direction, and patience throughout my research. The valuable suggestions of Dr. Cillian O' Driscoll, Dr. Mark Psiaki and Dr. Abraham Fapojuwo that helped to improve this work are truly appreciated. Special thanks to Dr. Mark Psiaki for his MATLAB based GPS L1 software simulator, which enabled me to further verify various aspects of the results. Dr. Driscoll is further acknowledged for his thoughtful suggestions and great discussions over the past six months.

I owe special thanks to Robert Watson, Cécile Mongredien, Changlin Ma, Mark Petovello, Kannan Muthuraman, Cyrille Gernot, the TOPS project members and many others in the PLAN research group for their support during the course of my research. I am thankful to Nyunook Kim and Florence Macchi for their assistance during the GPS data collection. I also wish to thank my fellow graduate students and faculty and staff members of the Department of Geomatics Engineering for providing a pleasurable and conducive environment during my studies.

iCORE, the University of Calgary Silver Anniversary Graduate Fellowship, the Graduate Faculty Council Scholarship, the Institute of Navigation (ION) National Graduate Scholarship, the KIS-94 Graduate Scholarship, ION Student Chapter Award, are acknowledged for their financial support. The Swiss Institute of Navigation (ION-CH), and the U.S.-based Institute of Navigation are also acknowledged for their student sponsorship, which enabled me to present research papers at their respective conferences.

I am grateful to my undergraduate professors Dr. S. Srikanth and Dr. K. Murali from Anna University, Chennai, who taught me the basic knowledge and skills and

encouraged me to pursue higher studies.

I owe very special thanks to my aunt meenakshi, my brother, Sasi, my sister-in-law Aruna and to a special someone named Saranya. Most importantly, I am greatly thankful to my family and friends for their immense support. Without their encouragements and understanding, I would not have come this far.

In loving memory of my mother, Rajalakshmi

"The Wind Beneath My Wings"

and to my father, Shanmugam

"The Good Shepherd"

Table of Contents

List of Tables

List of Figures

Notations

Abbreviations and Acronyms

2-D	...	Two Dimensional
AWGN	...	Additive White Gaussian Noise
A/D	...	Analog-to-Digital (i.e. Converter)
AM	...	Amplitude Modulation
ARNS	...	Aeronautical Radio Navigation Service
ASIC	...	Application Specific Integrated Chip
AGPS	...	Assisted Global Positioning System
AGC	...	Automatic Gain Control
BOC	...	Binary Offset Carrier
BPSK	...	Binary Phase Shift Keying
C/N$_0$	...	Carrier-to-Noise Density Ratio (dB-Hz)
CDF	...	Cumulative Distribution Function
CDMA	...	Code Division Multiple Access
CL	...	Civil Long
CM	...	Civil Moderate
C/A	...	Coarse or Clear Acquisition Code (i.e.PRN code)
CMF	...	Coherent Matched Filter
COTS	...	Commercial Off The Shelf
CWI	...	Continuous Wave Interference
DAQ	...	Data Acquisition Card
DC	...	Deflection Coefficient
DLL	...	Delay Locked Loop
DS-SS	...	Direct Sequence-Spread Spectrum
DBZP	...	Double Buffered Zero Padded
E911	...	Enhanced 911 (U.S.)
FFT	...	Fast Fourier Transform
FCC	...	Federal Communication Commissions
FPGA	...	Field Programmable Gated Array
FIFO	...	First In First Out
FEC	...	Forward Error Control (i.e Channel coding)
FLL	...	Frequency Locked Loop
FM	...	Frequency Modulation
GIOVE	...	Galileo,In-Orbit Validation Element
GLRT	...	Generalized Likelihood Ratio Test
GPCDD	...	Generalized Post-Correlation Differential Detector
GHz	...	Giga-Hertz (10^9 Hz)
GNSS	...	GLObal NAvigation Satellite System
GLONASS	...	Global Navigation Satellite System
GPS	...	Global Positioning System
HS GPS	...	High Sensitivity Global Positioning System
I/Q	...	Inphase/Quadrature

ICD	. . .	Interface Control Document
IF	. . .	Intermediate Frequency
ITU	. . .	International Telecommunication Union
kHz	. . .	kilo-Hertz (10^3 Hz)
LFSR	. . .	Linear Feedback Shift Register
LOS	. . .	Line-of-Sight
LNA	. . .	Low Noise Amplifier
MF	. . .	Matched Filter
MAP	. . .	Maximum *a posteriori*
MLE	. . .	Maximum Likelihood Estimate or Estimation
MHz	. . .	Mega-Hertz (10^6 Hz)
MMSE	. . .	Minimum Mean Squared Error
MCDD	. . .	Multi-Correlation Differential Detector
NBI	. . .	Narrow Band Interference
NH	. . .	Neuman Hofman
NF	. . .	Noise Figure
NLOS	. . .	Non Line-of-Sight
NCO	. . .	Numerically Controlled Oscillator
OCXO	. . .	Ovenized Crystal Oscillator
PC	. . .	Personal Computer
PDA	. . .	Personal Digital Assistant
PLL	. . .	Phase Locked Loop
PVT	. . .	Position, Velocity and Time
PCDD	. . .	Post-Correlation Differential Detector
PCND	. . .	Post-Correlation Noncoherent Detector
PSNR	. . .	Post-correlation SNR(dB)
PSD	. . .	Power Spectral Density
PDD	. . .	Post-correlation Differential Detector
PF	. . .	Pre-Filtering
PF/MCDD	. . .	Pre-Filtering/Multi-Correlation Differential Detector
PDF	. . .	Probability Distribution Function
PRN	. . .	Pseudo-Random Noise (i.e. sequence)
RF	. . .	Radio Frequency
RFI	. . .	Radio Frequency Interference
RHCP	. . .	Right Hand Circularly Polarized
RMS or rms	. . .	Root Mean Square
SAM	. . .	Shift-And-Multiply (i.e. PRN code property)
SS	. . .	Spread Spectrum
SAW	. . .	Surface Acoustic Wave (i.e Filter)
SNR	. . .	Signal-to-Noise Ratio(dB)
TCXO	. . .	Temprature Controlled Crystal Oscillator
TTFF	. . .	Time To First Fix (i.e Position fix)
UWB	. . .	Ultra WideBand system

Symbols

ϕ	...	Phase value
ω	...	Frequency in radians
f	...	Frequency in Hertz
ϖ	...	Frequency drift in rad/sec^2
ω_{L1}	...	GPS L1 frequency in radians
f_{L1}	...	GPS L1 frequency in Hertz (i.e. 1575.42 MHz)
ΔF	...	Residual frequency offset in Hertz
ϕ_0	...	Residual phase offset in radians
τ	...	Residual code offset in seconds
ΔF_{err}	...	Residual frequency error in Hertz
τ_{err}	...	Residual code phase error Hertz
T_c	...	C/A code chip duration (i.e. $T_c = \approx 977.5$ ns)
N_c	...	C/A code length in chips (i.e. $N_c = 1023$)
T_p	...	P(Y) code chip duration (i.e. $T_p = 0.1T_c$)
T_r	...	Code repetition duration (i.e. $T_r = N_c T_c$)
T_b	...	Bit duration (i.e. $T_b = 20T_r$ or 20 ms)
T_{cm}, T_{cl}	...	CM/CL code chip duration (i.e. $T_{cm} = T_{cl} = 2T_c$)
N_{cm}, N_{cl}	...	CM/CL code length in chips (i.e. $N_{cl} = 75N_{cm}$, $N_{cm} = 10N_c$)
T_{I5}, T_{Q5}	...	I5/Q5 code chip duration (i.e. $T_{I5} = T_{Q5} = 0.1T_c$)
N_{I5}, N_{Q5}	...	I5/Q5 code length in chips (i.e. $N_{I5} = N_{Q5} = 10N_c$)
T_m	...	Differential Delay ($T_m = mT_c$ or $T_m = mT_r$)
k	...	Chip sample index (i.e. kT_c)
n	...	Code sample index (i.e. nT_r)
$x(k)$	...	Received composite GPS signal samples
$d(k)$	...	Navigation data samples
$c(k)$	...	PRN or C/A code samples
$\phi(k)$	...	Instantaneous carrier phase
$w(k)$	...	AWGN samples
$y(n)$	...	Sampled matched filter output
$R(\bullet)$	...	Correlation or time ambiguity function
$\psi(n)$	...	Frequency ambiguity function
$sinc(n)$	...	sinc-function
$T(\mathbf{x})$	...	Detector Statistics
θ	...	Parameter vector (i.e. $\theta = [m, \tau, \phi_0, \Delta F]$)
$\Psi(\hat{\theta})$	...	Decision Statistics
j	...	Imaginary number (i.e. $\sqrt{-1}$)
$\lfloor a \rfloor$	...	Greatest value less than a
$|a|$	...	Absolute value of a
$\langle \mathbf{a}, \mathbf{b} \rangle$	...	Periodic correlation between vectors $\mathbf{a}$ and $\mathbf{b}$
r	...	Shift register length
T_{eq}	...	Equivalent Noise Temperature
N_0	...	Noise Spectral Density
^0K	...	Kelvin (i.e. Temperature Scale)
κ	...	Boltzmen Constant (i.e. $\kappa = $ -228.6 dBW/^0K-Hz)

T_0	...	Channel coherence time
f_0	...	Channel coherence bandwidth
f_d	...	Doppler spread
S_4	...	Std. Dev. of power variation due to ionospheric scintillation
P_d	...	Probability of correct detection
P_{fa}	...	Probability of false alarm
H_0	...	Null hypothesis (wrong cell)
H_1	...	Alternate hypothesis (correct cell)

Chapter 1

Introduction

Civilian Global Positioning System (GPS) operations have evolved from positioning to the current multitude of applications including timing, vehicular navigation, telecommunications, earth sciences, and most importantly safety critical applications such as civil aviation and enhanced–911 (E911) emergency call location (Mathieu et al. [2005]; Enge and Misra [1999]). Unfortunately, users of these new applications are often located in environments that cause major signal obstructions, which result in severe signal attenuation (Klukas et al. [2004]). For instance, GPS operation in degraded signal environments requires reception of GPS signals attenuated by 20 dB or more from nominal unobstructed (open-sky) levels (Kaplan and Hegarty [2006]). Additionally, detection of GPS signals in rapid fashion (Wolfert et al. [1998]) or under severe dynamics (Haag de and Kelly [2004]) is also required for certain GPS applications. Most commercial receivers fail to operate when the carrier-to-noise density ratio (C/N_0) falls below 35 dB-Hz (Diggelen van [2002]; Chansarkar and Garin [2000]). Significant additional signal processing gain is required to extract the GPS signal from the background noise in degraded signal environments. Consequently, one has to resort to enhanced GPS operation through. Several high sensitivity techniques have been proposed for enhanced GPS detection under degraded signal environments. This dissertation attempts to *investigate* and *unify* contemporary detection schemes and to *develop novel* detection schemes for enhanced sensitivity GPS signal acquisition.

1.1 Background

In degraded signal environment, any one or combination of the following scenarios can hinder the reception of the transmitted GNSS signal:

- Massive signal attenuation

- Strong radio frequency interferences

- Self-interference due to stronger GNSS signals from other satellite vehicles (SV)

- Multipath fading and Non Line of Sight (NLoS) propagation

Significant additional signal processing gain is required to extract the weak GNSS signal from the background noise in degraded signal environments. The GNSS community has based their efforts on: (1) High sensitivity receiver technology and (2) GNSS modernization to deal with the aforementioned challenges. While high sensitivity receiver technology has progressed remarkably, the GNSS modernization has started to take shape with the launch of modernized GPS IIR–M and Galileo GIOVE satellites.

Enhanced Sensitivity GPS

The miniaturization of GPS and substantial improvements in power management has paved the way for the integration of GPS chips into small hand held devices such as personal data assistants (PDA) and cellular mobile phones. The personal navigation services offered by these devices necessitate the reception of GPS signals both in outdoors and indoors. The indoor situations may widely vary from few floors of wooden construction or high-rise buildings comprising of steel reinforcements to concrete basements. Depending on the environment, the received GPS signal can undergo attenuations in excess of 20 dB from nominal conditions (MacGougan et al. [2002]). Accordingly, substantial signal processing gain is required to compensate for this massive

signal attenuation to allow for successful GPS signal detection (or acquisition). Conventional GPS receiver operations fall short under these conditions due to its inability for extended signal observation (coherently or noncoherently) alongside limited hardware resources.

High sensitivity GPS receivers, on the other hand, utilize large banks of correlators and digital signal processing for enhanced signal detection under adverse conditions. The use of parallel correlation techniques significantly reduces acquisition time resulting in faster times to first fix (TTFF) under nominal signal power levels. Under weak signal conditions, the extra signal processing power is efficiently utilized to integrate coherently or noncoherently to a point, where signal tracking could be established. The rapid advancement in packaged integrated chip technology and efficient power management schemes provides the major thrust behind HS GPS approach. For instance, Figure 1.1 shows the evolution in terms of total number of packaged correlators utilized by GPS receivers over the years. More remarkably, the current HS GPS receivers are capable
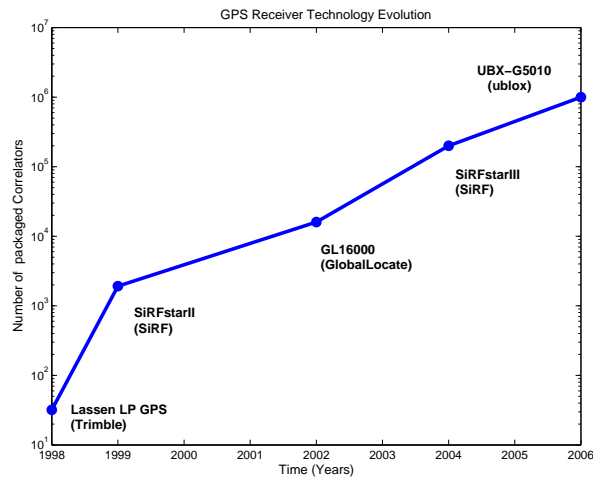
Figure 1.1: GPS Receiver Technology – Evolution

of acquiring GPS signals even under 30 dB attenuation levels (Burgi et al. [2006]). It should be emphasized here that the HS GPS technology will have a continual impact even amidst GNSS modernization. On the other hand, the introduction of modernized

GNSS signals will potentially push the limits of the current high sensitivity receiver technology.

GNSS Modernization

The legacy GPS has performed extremely well beyond expectations in the past but faced serious challenges as it was being adopted by the new civilian applications. Several initiatives were launched since early 90's to serve and capitalize the rapidly growing civilian market primarily in U.S and partly in Europe. Consequently, these efforts led to the birth of second-generation GNSS systems. The GNSS modernization process began with the onset of four major global initiatives:

- Revamping of legacy Russian Global Navigation Satellite System (GLONASS)

- GPS Modernization (Phase II and III)

- Development of European Union's (EU) Galileo system

- Development of Chinese Compass (Beidou) GNSS system

The existing GLONASS system is currently being revamped to ensure the Russian presence in space based navigation. Accordingly, a major directive is set to restore the GLONASS performance on par with the competing GPS and Galileo systems by 2010 (Revnivykh [2006]). While the GLONASS system is currently operating off the normal mode with 10 operating satellites, major initiatives to increase the number of satellites to 18 and finally to 24 by the end of 2007 and 2009, respectively, has already started. While these efforts evidently will improve the availability of GNSS signals, the lack of signal modernization in GLONASS limits its scope compared to its counterparts.

GPS II and Galileo system are of critical interest as they bring forth innovation at various levels of their respective navigation system. Interestingly, the Galileo system already played a significant role in expediting the removal of selective availability from

the GPS system (Ashjaee [2006]). It was also a major catalyst behind the GPS modernization project and revamping of the GLONASS system. The Galileo project is well positioned to benefit from the three decades of GPS and GLONASS experience. Each Galileo satellite will transmit 10 different navigation signals that collectively offer open service, safety-of-life, commercial service, and public regulated services. The Galileo L1F signal is of particular interest as it was intended for mass civilian applications and is characterized by key innovations in terms of modulations in comparison to legacy and phase II GPS signals. The Galileo system will transmit these navigation signals in the GPS spectrum to ensure interoperability with GPS. Finally, China's Compass GNSS system is expected to broadcast signals in four frequency bands (E2, E1, E6, and E5b). Grelier et al. [2007] reported that the Compass signals being transmitted at E2, E6 and E5b bands utilized quadrature phase shift keying (QPSK) or hybrid phase shift keying (HPSK) with two-tiered PRN code structure similar to the GPS L5 and Galileo signals.

Among the aforementioned initiatives, the GPS II modernization project is of utmost importance to the GNSS community owing to its immediate availability. The GPS modernization began with the augmentation of new civilian and military signals to the legacy GPS system. For military applications, the existing P(Y) signals on the L1 and L2 frequencies are augmented with a spectrally separated new Military code (M). For civilian applications, a new civilian signal at L2 frequency is added. To satisfy the needs of aviation, a third civil frequency (L5) will be centred at 1176.45 MHz in the aeronautical radio navigation services (ARNS) band. The standardization procedure for third civilian signal at L1 frequency is already being initiated.

Modernized signal structure is a major outcome of GNSS modernization that will provide the foremost benefit to the civilian GNSS community. The modernized signals include key innovations such as data less channel, improved navigation data message format and new modulations schemes. Currently, three Block IIR-M (SV 7, 12, and

31) satellites are successfully transmitting both L1 C/A and L2C signals from space. Similarly, a single GIOVE A satellite is broadcasting the Galileo navigation signals at L1 and E5 frequencies (ESA [2007]). Further plans include the launch of second GIOVE satellite (i.e. GIOVE A2) during the second half of 2008, which would be followed by two more satellite launches. The Galileo system is expected to be operational by 2011-2012 with launch of remaining 26 satellites. After its launch on April 13 2007, the first medium earth orbit (MEO) satellite of the Compass system, the Beidou 2B, is successfully transmitting the Compass GNSS signals at E2 (1561.1 MHz), E6 (1268.52 MHz) and E5b (1207.14 MHz) (Grelier et al. [2007]). The Compass system is expected to be fully functional by the end of 2010 with the launch of remaining 29 satellites.

1.2 Relevant Research

The GPS system was developed to operate in outdoor environments with clear line-of-sight (LOS) between satellites and the receiver. The minimum received signal power level for a L1 GPS signal under open-sky conditions is -160 dBW (Kaplan and Hegarty [2006]). Depending on the propagation characteristics and radio frequency (RF) front end, this could typically translate to a Carrier-to-Noise density (C/N_0) ratio between 40 dB-Hz and 50 dB-Hz. However, operation in degraded signal environment requires reception of GPS signals attenuated by 20 dB or more from their outdoor counterparts (van Diggelen and Abraham [2001]). With a nominal C/N_0 ratio of 42 dB-Hz, this would result in a C/N_0 of 22 dB-Hz or less under these degraded environments. Multipath phenomenons such as reflection, diffraction, and shadowing introduces both short and long term fluctuations in received signal power level (MacGougan [2003]). Finally, the proliferation of short-range RF devices such as ultra wideband systems (UWB), RF identification tags constitutes a major source of RFI. Consequently, significant amount of signal processing gain is required to extract the GPS signal from the background

noise under these degraded signal conditions (Watson [2005]).

The most difficult aspect of a GPS receiver operation is the synchronization process that involves the *initial detection* and *subsequent tracking* of the weak GPS signals. Under nominal signal conditions, the initial synchronization process incurs minimum burden as the GPS signal could be acquired with a few milliseconds of signal observation (or correlation). In degraded environments, due to the compromises in antenna, RF bandwidth, and implementation complexity, the desired target could be in the range of 18 dB-Hz to 24 dB-Hz. For example, Moreau et al. [1999] pointed that most commercial receivers fail to acquire the GPS signals for C/N_0 levels below 35 dB-Hz. Increasing the sensitivity by 20 dB or more requires integration time of hundred times or more from the nominal one millisecond integration time (Tsui [2000]). Unlike traditional GPS receivers, a HS GPS receiver relies on extended integration time to significantly enhance the acquisition sensitivity (Chansarkar and Garin [2000]). Several detection algorithms have been reported in the literature to address the problem of high sensitivity acquisition under weak GPS signal conditions. These detection schemes can be broadly categorized under *coherent*, *noncoherent*, *differential* detection or combinations of the three.

The most beneficial approach is to employ coherent detection due to its optimality under Gaussian noise conditions. Unfortunately, the maximum coherent integration time in a GPS receiver can be limited by a variety of factors. For instance, the presence of navigation data modulation typically limits the coherent integration time to less than 20 ms. Akos et al. [2000] reported that the coherent integration time couldn't be extended beyond 10 ms (half of bit duration) without *a priori* information on navigation data transition. However, it is still possible to accomplish high sensitivity in the presence of external aiding. While this concept has been widely utilized in assisted GPS (AGPS) receivers, the earliest reference for AGPS operation can be found in a patent granted

to Taylor and Sennott [1984]. However, AGPS requires a separate communication link connected to a backbone network for obtaining assistance information. Besides, the reliability of the external link also raises an issue in terms of network delay and communication link performance under harsh signal conditions.

Extreme HS GPS techniques utilizing coherent integration time even up to several seconds have been reported in the literature (Watson et al. [2005]). However, Watson et al. [2005] approach was limited to post-mission mode and critically relied on accurate modelling of second order satellite/receiver dynamic effects. More recently, Mitelman et al. [2006] demonstrated a real time receiver with extreme HS GPS capabilities, which tracked signals at whopping -176 dBm power levels (corresponds to a C/N_0 of -2 dB-Hz) under controlled environment. The developed setup utilized a well-positioned outdoor reference receiver aiding the indoor HS GPS receiver. Mitelman et al. [2006] further noted that none of the existing HS -GPS receivers was able to track a single satellite reliably despite over twenty minutes of searching even for -156 dBm power levels. The use of very long coherent integration not only limits TTFF but also the position update rate.

Longer coherent integration times beyond 20 ms without any assistance can be realized using advanced acquisition techniques. For instance, Psiaki [2001] proposed an alternate half-bit acquisition method that was able to detect signals with 18 dB-Hz C/N_0 levels. The algorithm decomposed the entire data block into alternate 10 ms chunks and performed coherent detection on the individual chunks with the assumption that at least one set would be minimally affected by data bit transitions. In the meanwhile, the coherent detection outputs of the individual chunks were further accumulated noncoherently. Ziedan and Garrison [2004] proposed a weak signal acquisition based on navigation data bit prediction. Nevertheless, the reliability and the computational complexity of these approaches is still an issue. Moreover, other factors limit the

coherent integration time aside from just the navigation data transition (Chansarkar and Garin [2000]). Longer coherent integration times increase the number of frequency bins to be searched, which in-turn increases the search space (in the frequency domain) to a significant extent. More importantly, the stability of the reference oscillator in a GPS receiver also limits the maximal coherent integration time. Finally, the coherence time of the propagation medium (or channel) and time varying Doppler limits the maximal coherent integration time due to the satellite/receiver dynamics.

Unlike the coherent approaches, the noncoherent approach relies on short coherent integration followed by a large number of noncoherent summations. By invoking noncoherent detection, the phase variations introduced by navigation data as well as residual carrier can be nearly eliminated. Noncoherent approach although optimal in the presence of unknown phase (or phase variations) results in a signal-to-noise ratio (SNR) loss, which is often termed *squaring loss*. The squaring loss is significant especially at lower C/N_0 levels. Consequently, the noncoherent approach requires a larger number of noncoherent summations to overcome the adverse SNR loss. Recent studies include the post-correlation differential detection (PCDD) technique, wherein the detection output is obtained as a product of the current coherent detection output to its delayed output. Subsequently, the SNR loss in PCDD is decreased in comparison to post-correlation noncoherent detection (PCND), as the detection output involves the product of two independent noise terms. The post-correlation differential approach was originally proposed by Zarrabizadeh and Sousa [1997] for CDMA acquisition and was later applied to GPS signals by Park et al. [2002]. The acquisition sensitivity improvements of the differential detection was validated in theory by Schmid and Neubauer [2004] and using live GPS data by Shanmugam et al. [2005].

The performance gain of differential detection over standard noncoherent detection vanishes rapidly in the presence of frequency drifts (Schmid and Neubauer [2005]).

For longer coherent integration periods, the performance degradation in the differential approach is substantial due to the residual effects from navigation data transition (Shanmugam et al. [2007a]). In the post-correlation differential approach, the phase variation introduced by the residual carrier is translated into a complex phase rotation after the differential detection. Elders-Boll and Dettmar [2004] utilized this basic principle to develop a fine Doppler estimation technique. Schmid and Neubauer [2005] also adopted the same approach for an adaptive phase correction loop, which yielded performance gain for larger variations in residual frequency errors and drift. However, the fine Doppler estimation reported in Elders-Boll and Dettmar [2004] as well as Schmid and Neubauer [2005] requires longer observation to overcome the inherent SNR loss incurred during the differential detection.

Finally, safety critical applications such as E911 require rapid position solution determination to speed up rescue operations. Furthermore, an application where a GPS receiver experiences high dynamics also requires rapid acquisition or reacquisition. Thus, the contemporary GPS receivers are expected to provide faster time-to-first fix or position fix (TTFF). A typical GPS receiver can start in any one of the three modes: hot, warm or cold start depending on the *a priori* information with cold starts resulting in the longest TTFF. Furthermore, there are factors aside from start mode that affect TTFF. For instance, favourable locations with a high number of satellites in view can aid in TTFF reduction. More generally, the TTFF of a GPS receiver depends on the extent of *a priori* information and/or hardware resources at its disposal. For example, Van Nee and Coenen [1991] proposed the use of fast Fourier transforms (FFT) techniques for correlation implementation to aid rapid acquisition. The FFT based approach exploited the time/frequency duality and periodicity of GPS C/A code signal to its advantage. On the other hand, GPS receivers can greatly reduce the frequency search space with Doppler aiding in assistance mode (van Diggelen and Abraham

[2001]). Finally, a GPS receiver can also utilize massive parallel correlator structures to exhaust all time/frequency combinations for all visible PRN's instantaneously (Burgi et al. [2006]). The TTFF critically depends on the mean acquisition time performance of an acquisition scheme (Hopkins [1977]). The mean acquisition time is directly related to the number of time/frequency search bins (or cells), the average dwell time per cell and finally the probability of detection (P_D) for a given probability of false alarm (P_{FA}) and the C/N$_0$ level. For a constant dwell time, the acquisition scheme (or a detection technique) that maximizes the P_D for a given P_{FA} over a wide range of C/N$_0$ values would yield the lowest mean acquisition time.

Alternatively, the mean acquisition time can be reduced by decomposing the two-dimensional search in time and frequency into a linear search in time or frequency. For instance, by performing a differential detection at the chip or sample level, one can nearly eliminate the effect of both data and residual carrier to allow for frequency independent code phase acquisition. Lin and Tsui [2000] proposed this differential approach (at the sample level) in the form of a *delay-and-multiply* technique for software receiver based GPS acquisition. However, the application of differential detection on the sample level will incur correlation performance degradation due to the partial correlation of the underlying PRN code. It is interesting to note that the authors were unaware of the earlier work by Coenen and Van Nee [1992] and Chung [1995] on chip level differential detection. For instance, Coenen and Van Nee [1992] proposed a pre-correlation differential scheme in the early 90's for GPS and GLONASS signals and Chung [1995] for CDMA in mid 90's. Moreover, their approaches correctly utilized the *delay-and-multiply* (DAM) property of the Gold codes to ensure similar correlation characteristics. Coenen and Van Nee [1992] further proposed the use of multiple differential branches to suppress the noise enhancement but pointed the limitation in the presence of residual carrier. However, the authors made an incorrect assumption concerning the effect of DAM on

the PRN code utilized in GPS L1 modulation, which led to less successful implementation. Hence, the pre-correlation differential detection (PDD) albeit yielding the fastest acquisition time was essentially plagued by significant noise enhancement (i.e. Coenen and Van Nee [1992]; Lin and Tsui [2000]). Alternatively, code independent frequency estimation is also desirable as the number of search bins in time (i.e. code phases) is significantly higher than that of frequency search bins. Unfortunately, there were no published works - at least in the area of GPS acquisition - at the time of this writing.

The widespread proliferation of GPS technology in the commercial sector often involves safety critical applications (Carroll [2003]). On the other hand, many commercial receivers are equipped with minimal or basic levels of protection to external RFI (Parkinson [1996]). Acquisition of GPS signals is more difficult in the presence of strong CW or narrow band interference as the receiver has no *a priori* knowledge of either signal or interference parameters (Deshpande and Cannon [2004]). Hence, interference *detection* and *mitigation* are central for protecting the GPS receiver against external RFI (Ward [1995]). Finally, the presence of external RFI can critically limit the use of aforementioned detectors for GPS signal acquisition (Kaplan and Hegarty [2006]). For example, the coherent detection is no longer optimal due to the non-Gaussian noise distribution arising from interference (Kay [1993a]). Interestingly, differential detection brings forth new perspectives to the problem of GPS signal acquisition under RFI. Hence, it would be desirable to investigate the effect of interference on the newly proposed differential detection schemes as applied to GPS signal acquisition.

The GPS modernization efforts, which includes the GPS L2C and L5 signal brings forth new opportunities as well as challenges. For instance, the adoption of advanced signal structure offers tremendous opportunities due to the presence of pilot signal. However, the time-multiplexed data/pilot structure in the L2C signal and the presence of NH code in the L5 signal necessitates modified acquisition strategies. More

importantly, the detection schemes developed for legacy GPS signal acquisition should be cautiously adapted to address the problem of modernized GPS signal acquisition. For instance, Cho et al. [2004] extended the differential detection approach for L2 CM code acquisition. However, the acquisition scheme sacrificed correlation properties as it involved partial correlation. On the other hand, Psiaki [2004] and Yang [2005] innovatively extended the FFT based block acquisition to address the problem of CM and CL code acquisition. The acquisition schemes reported in Psiaki [2004] and Yang [2005] primarily focused on segmented correlation and zero-padding to overcome memory buffer limitations and that of navigation data modulation. On the other end, Moghaddam et al. [2006] reported the use of hyper-code correlation that exploited the asymptotic orthogonality of CM and CL codes for rapid acquisition of L2C signals. It is also desirable to develop alternative solutions to address the CM and CL code acquisition besides the aforementioned algorithms.

The new GPS L5 signal owing to its large bandwidth and innovative signal structure offers better resistance to background noise, multipath and external interference. For instance, longer coherent integration is readily accomplished through joint detection of PRN as well as short Neuman-Hofman (NH) code (Hegarty et al. [2003]). More recently, Macabiau et al. [2003] reported the vulnerability of the short NH code acquisition in the presence of residual frequency errors. Interestingly, Zheng and Lachapelle [2004] utilized the DAM approach to suppress the effects of NH code, data and that of residual carrier at the expense of significant noise enhancement. Hence, it is desirable to develop modified acquisition strategies to overcome some of the limitations faced by the NH code acquisition. It should be emphasized here that the NH codes were originally reported by Neuman and Hofman [1971] more than three decades ago and were not obtained through exhaustive search. Accordingly, it is important to identify relevant performance measures for optimal short synchronization code design and also to obtain new binary

codes for use in future GNSS systems.

At a more fundamental level, the GPS signal acquisition can be viewed as the *initial detection* of the PRN code signal and subsequent *coarse estimation* of its parameters. Therefore, one can readily establish many previously proposed acquisition schemes by applying detection/estimation theory and also to develop new acquisition strategies. Based on the aforementioned assessments, this dissertation derives its motivation from the following (but not limited to) reasons:

- A *detection/estimation* theoretical approach can provide a better understanding of various detection schemes, which are already being utilized for GPS signal acquisition

- While there has been a great deal of research directed toward various detection approaches for GPS signal acquisition, there exists still a question of *unified theory* to relate these different detection approaches

- The utilization of differential detection provides new perspective for the problem of GPS signal acquisition under RFI. Further analysis on the effect of RFI on differential detection can offer new prospects to the interference detection and suppression

- The arrival of modernized GNSS signals put forth new challenges for developing novel acquisition schemes to wholly utilize the innovative signal structures

1.3 Research Objectives

Having reviewed the various detection strategies for GPS signal acquisition, this dissertation expands upon the work described in the previous section by attempting to *investigate*, and *unify* existing detectors utilized by traditional acquisition schemes using

detection/estimation theory. Most importantly, it endeavours to *develop novel* detection algorithms that not only offer enhanced sensitivity but also sufficient resilience to dynamics.

Given these primary objectives, several issues and aspects should be addressed during the course of the research. The task of reaching these objectives has been categorized into the following research goals:

1. Analyze fundamental detection techniques utilized by traditional GPS signal acquisitions schemes in terms of signal effects. To identify the merits, limitations and scope of these existing schemes for enhanced sensitivity GPS detection

2. Utilize the detection/estimation approach to understand the GPS acquisition process. Develop a unified approach to encompass various detection algorithms utilized GPS signal acquisition.

3. Identify key characteristics of PRN code that could be utilized for developing novel algorithms for enhanced acquisition of GPS signals.

4. Explore and develop novel detection algorithms that enable efficient GPS signal acquisition under adverse signal conditions such as weak signal, high dynamics, and interference environments

5. To assess and quantify the benefits of modernized GPS signals. Develop innovative detection techniques that can take advantage of their innovative signal structure

6. Develop a software receiver framework to implement the developed algorithms for further validation and performance evaluation using hardware simulated and live GPS signals

1.4   Dissertation Outline

The dissertation consists of seven chapters and are related to each other in the fashion illustrated by Figure 1.2. To provide a broad perspective of this research, the remainder of this dissertation is structured in the following way.
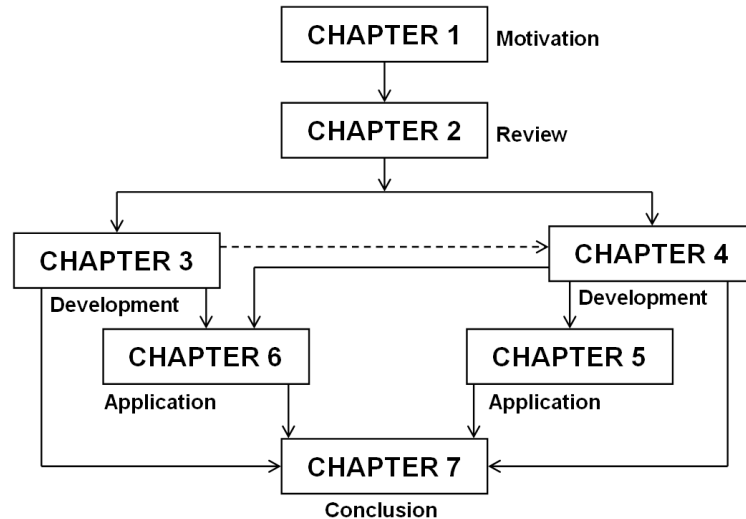
Figure 1.2: Thesis Flow Diagram

Chapter 1 presented the motivation and the central objectives of the research described in this dissertation. The relevant background of the research and its importance was also described to bring the current research topic into the right perspective.

Chapter 2 carries out a systematic analysis of GPS receiver processing. The legacy GPS L1 signal structure and its corresponding correlation and spectral characteristics are elucidated. The periodic property and more importantly the DAM property of C/A code is established in theory. Major limiting factors pertaining to signal propagation as well as inherent system limitations are identified. The developed software-based receiver signal processing approach utilized during the course of this research is detailed in the context of GPS digital receiver signal processing. A brief review of HS GPS detection and its limitations is presented in the context of thesis motivation.

Chapter 3 forms the foundation of the research presented in this dissertation. After introducing the signal and noise models, the problem of GPS signal acquisition is addressed using a *detection/estimation* theoretical approach. Fundamental theoretical considerations based on the generalized likelihood ratio test (GLRT), as applied to GPS signal detection, are discussed. For assumed deterministic signals the GLRT further reduces to a matched filter. This implies that the navigation data code phase and carrier parameters are known. For a received GPS signal with unknown signal parameters, the *energy detector* is derived as the optimal detector. The popular detectors utilized in GPS signal acquisition were then established as the best approximations of GLRT. It is shown that the asymptotic version of the GLRT is equivalent to an estimator correlator (EC) and is further developed in the form of *novel generalized post-correlation differential detector*. Theoretical detection performance as well as the acquisition/frequency sensitivity performance analysis is also presented.

Chapter 4 further develops the research presented in Chapter 3. A novel pre-correlation noise suppression mechanism using the PRN code periodicity is developed. The implications of *pre-filtering* technique on traditional detectors is described. An asymptotic form of the pre-correlation differential detector structure was developed in the form of *novel multi-correlation differential detector*. The various implementation aspects of pre-filtering/multi-correlation differential detection (PF/MCDD) is also described. The correlation suppression as well as the detection performance of the multi-correlation differential detection is theoretically derived. The chapter winds up with acquisition/frequency sensitivity analysis of the PF/MCDD in comparison to the detectors introduced during the previous chapter.

Chapter 5 further shapes the research by analyzing the effect of RFI on the estimator-correlator in the context of multi-correlation differential detection. The detection output

for standard and also for the MCDD structure is characterized in the presence of interference. Subsequently, a novel CWI detection, estimation, and suppression based on the multi-correlation differential detection is presented. The advantages of using multi-correlation differential detection in conjunction with auxiliary interference mitigation schemes is outlined. Finally, the detection performance of both standard and proposed MCDD is evaluated under CW and narrowband interference scenarios.

Chapter 6 further extends the detectors developed in Chapters 3 and 4 to address the problem of modernized GPS signal acquisition. The systematic description of the modernized GPS L2C and L5 signal structure is followed by a critical review of various detection algorithms utilized by modernized GPS signal acquisition. The chapter then focuses on key aspects of modernized signal acquisition, where developed research is of critical appeal and correspondingly extends the proposed detectors for GPS L2C and GPS L5 NH code acquisition. In addition, it draws out relevant performance measures for optimal synchronization code design. Interestingly, it also proves the existence of better synchronization codes in addition to the standardized NH codes. Finally, acquisition sensitivity performance of the proposed detectors is analyzed and also compared with existing solutions.

Chapter 7 identifies the key innovations, results and findings realized in this dissertation. Accordingly, it draws attentions to the major contributions of the proposed research in the area of enhanced sensitivity GPS signal processing and generally in the areas of detection/estimation theory. Finally, it recognizes the limitations of the presented work and makes functional recommendations.

Chapter 2

GPS – Theory, Limitations and Challenges

This chapter briefly reviews the evolution of GPS and outlines the challenges faced by the legacy GPS system. Beginning with a description of the legacy GPS L1 signal structure, the chapter delves into related correlation and spectral properties. The effect of mutual interference arising from other satellites in terms of cross-correlation suppression performance is analyzed. The basic receiver operation chain alongside the software receiver implementation is introduced. Major limitations in GPS receiver operations under various signal degradations are described. Theory and limitations of high sensitivity detection are discussed. The chapter concludes with a short discussion on the critical challenges faced by detection algorithms utilized by traditional GPS signal acquisition.

2.1 Historical Evolution

The initial seeds for GPS were sown in the early 70's through various initiatives taken by U.S. Air Force and Navy. Parkinson [1996] details the predecessors of the modern GPS system including *Transit* system, *Timation* and *621B* program. The Transit system not only proved the reliability of space borne ranging systems, it also validated satellite prediction algorithms. The Timation satellites successfully corroborated precise time transfer through very precise onboard clocks. The 621B system was the first navigation system that demonstrated the satellite-ranging concept using PRN modulation. The project also included innovations such as slow data communication link and use of high eccentric satellite orbits. In 1973, the joint program office (JPO) was formed that laid the foundation for NAVSTAR, the Global Positioning System. The

navigation technique for GPS utilized a passive (one-way) ranging concept whereby the user equipment received ranging signals from four or more satellites and compared the received phase with the user's reference oscillator.

The legacy GPS system essentially includes synchronized broadcast of a primary ranging signal at 1575.42 MHz (L1) and a secondary signal at 1227.6 MHz (L2). The primary ranging signal in turn composed of an inphase civilian *clear or coarse acquisition* (C/A) code signal at a chipping rate of 1.023 MHz. The quadrature phase consists of a long Precise (P) code broadcasted at a chipping rate of 10.23 MHz at both L1 and L2 frequencies. Applications that use C/A code signal alone often referred to as *standard positioning services* (SPS). On the other hand, the use of P code signal provides *precise positioning service* (PPS).

Two key decisions paved the way for continual dominance of GPS in positioning and navigation field. The first decision led to the removal of selective availability (SA), which prohibited metre level accuracies for civilian operations by incorporating voluntary degradations in the broadcast ephemeris (Clinton [2000]). The second decision led to the GPS modernization with the augmentation of new civilian signals at L2 and L5 frequencies (Gore. [1999]).

2.2   Legacy GPS Signal Characteristics

The design of ranging signals is of critical significance due to the various trade-offs involved in the GPS system. For instance, the international telecommunication union (ITU) has set maximum flux density limit to -154 dBW/m^2 for a satellite communication link in the 1.525 to 2.5 GHz band. Moreover, this flux density limit is applied for any 4 kHz band and is primarily intended to protect the terrestrial microwave communication links. There exists an additional constraint from radio astronomy that typically operates in the bands 1370–1400 MHz and 1606.8–1722.2 MHz. In addition, the GPS ranging

signal should also possess the following characteristics (Spilker [1996]):

- Tolerance to intra-system (from other GPS satellites) and inter-system (from other GNSS) interference arising from other ranging signals that potentially share the same frequency spectrum

- Tolerance to reasonable levels of unintentional or intentional interference, jamming or spoofing intended to degrade GPS performance from other communication systems

- Tolerance to reasonable levels of multipath interference originating from natural or man made sources

- Maintain minimum levels of interference at all times to coexisting communication systems

To meet the aforementioned requirements, GPS system relied on *spread spectrum signalling*, wherein the transmitter signal energy is uniformly spread over a much wider bandwidth. More importantly, the direct sequence (DS) version of spread spectrum signalling was utilized as it allows for a precise timing recovery and permits RF carrier recovery. The basic signal structure and the corresponding properties are detailed in the subsequent sections.

2.2.1 Signal Structure

The GPS satellite broadcasts two ranging signals at L1 (1575.4 MHz) and L2 (1227.6 MHz) frequencies. The ranging signal at L1 is considered exclusively here as it is intended for civilian operations besides serving military purposes. The two frequencies are readily obtained by integer multiplication of a fundamental frequency (of master clock), F_0, which is 10.23 MHz. For example, the L1 and L2 frequencies are obtained

by multiplying the fundamental frequency with integers 154 and 120, respectively. Furthermore, the clock rates for carrier, PRN code and navigation data are coherently related. The transmitted GPS signal at both L1 and L2 is band limited to 20.46 MHz for spurious transmission prevention. The transmit power levels were set to guarantee a minimum received power level of –160 dBW for a user equipment employing a 0 dBic antenna. Note that the –160 dBW received power level is only for the civilian C/A code signal. The received power levels for military P(Y) signal is around –163 dBW and –166 dBW at L1 and L2 frequencies. The GPS signals are right hand circularly polarized (RHCP) and characterized by axial ratio or ellipticity [1] of no worse than 1.2 dB for L1 and 3.2 dB for L2 within an angle of $\pm 14.3^0$ from boresight. Figure 2.1 shows the simplified block diagram of GPS signal generation at the satellite.
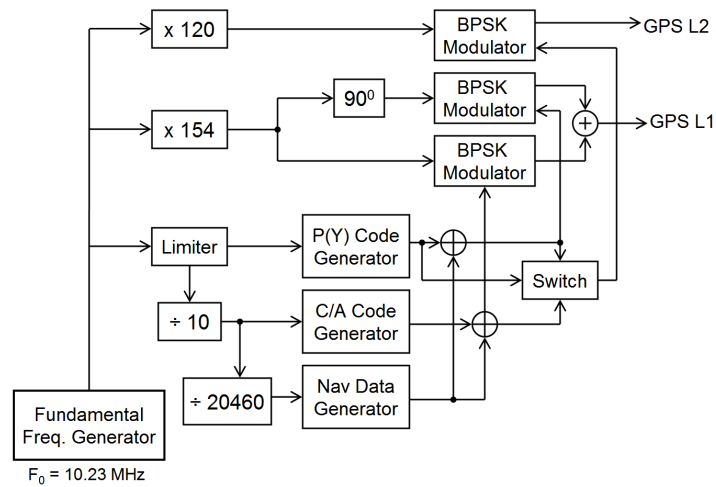
Figure 2.1: Legacy GPS Signal Generation

The GPS L1 signal consists of an in-phase and a quadrature carrier (or component) that carries the civilian and military signals. The civilian C/A and military P(Y) code signals are modulated on to these carriers with a phase offset of less than $\pm$ 0.1 rad

---

[1]Ellipticity is the ratio between the maximum and minimum in antenna power as the antenna is rotated through all angles. For instance, an antenna with 0 dB ellipticity is said to be circularly polarized.

from nominal 90^0. The signal transmitted by the jth satellite is given by,

$$S_{L_{1j}}(t) = \sqrt{\frac{C}{2}}d_j(t)c_j(t)cos\left(2\pi f_{L1}t + \theta\right) + \sqrt{\frac{P}{2}}d_j(t)p_j(t)sin\left(2\pi f_{L1}t + \theta\right) \qquad (2.1)$$

where f_{L1} is the L1 frequency and θ represents the random phase offset. C and P represent the transmitted signal power levels of C/A and P(Y) code signals. $c_j(t)$, $p_j(t)$ and $d_j(t)$ denotes the PRN or C/A code, P(Y) code and navigation data respectively. That is,

$$c_j(t) = \sum_{k=-\infty}^{k=\infty} c_j(k)g_{T_c}\left(t - kT_c\right) \qquad (2.2)$$

$$p_j(t) = \sum_{k=-\infty}^{k=\infty} p_j(k)g_{T_p}\left(t - kT_p\right) \qquad (2.3)$$

and

$$d_j(t) = \sum_{k=-\infty}^{k=\infty} d_j(k)g_{T_b}\left(t - kT_b\right) \qquad (2.4)$$

where $c_j(k)$, $p_j(k)$ and $d_j(k)$ are binary phase shift keying (BPSK) symbols (i.e. ± 1). $g(\bullet)$ is the pulse shaping function which is usually assumed to be a normalized rectangular function. That is,

$$g_T\left(t\right) = \begin{cases} 1 & 0 \le t \le T, \ T \in \{T_b, T_c, T_p\} \\ 0 & elsewhere \end{cases} \qquad (2.5)$$

The chip durations T_p, T_c and bit duration T_b are related in the following fashion. The P(Y) chip duration is inverse of the fundamental clock frequency (i.e. $T_p = 1/\mathrm{F_0}$). The chip duration of P(Y) code is one-tenth of C/A code chip duration (i.e. $T_c = 10T_p$). The C/A code $c_j(k)$ is a periodic code of length, $N_c = 1023$, in chips. Accordingly, the C/A code signal $c_j(t)$ repeats every 1 ms (i.e. $T_r = N_cT_c$). The C/A code repetition period is one-twentieth of the navigation data bit duration (i.e. $T_b = 20T_r = 20N_cT_c$).

The choice of individual signal parameters such as chipping rate and data rate essentially reflects the conditions imposed during the signal design. For instance, the low navigation data rate provides substantial processing gain that enables the robust

decoding of navigation data. The short C/A code enables faster acquisition due to relatively shorter code period. On the other hand, the P(Y) code has a very long period (i.e. $N_p T_p \approx 38$ weeks, but short cycled to 1 week) to allow for maximal encryption.

2.2.2 Correlation and Spectral Characteristics

The essence of a GPS receiver signal processing is captured by the correlation detection process and thus it is vital to study the correlation properties of underlying PRN codes. The spectral characteristics are directly related to correlation property of the code itself and will be a subject of study as well. This section will primarily focus on the C/A code generation and its related properties. However, the readers can refer to Spilker [1996] and ICD-GPS-200 [1997] for a more detailed treatment on GPS L1 C/A and P(Y) code signals.

As mentioned earlier, the C/A code is a relatively short code with a period of $2^{10} - 1 = 1023$ chips that repeats every 1 ms, when generated at a 1.023 MHz rate. The main intent behind the selection of a short code period is to permit rapid acquisition, (as there are only 1023 code phases to be searched). The choice of C/A code period critically reflects the trade-offs between auto and cross-correlation properties. While auto-correlation measures the self-similarity over time, the cross-correlation measures the similarity of the signal under interest with other signals. The choice of PRN code is essentially a multi-objective optimization involving both auto and cross-correlation properties. For instance, binary codes that possess minimum out-of-phase auto-correlation and cross-correlation values among each other are desired for PRN code design. However, not all the codes can guarantee optimal auto and cross-correlation properties. For example, maximal length sequences (or m-sequences) possess optimal two-valued auto-correlation function but are characterized by poor cross-correlation properties. Hence, the C/A codes are selected from a family of Gold codes, which in-

turn are formed by multiplication in binary field, $c(k) \in \{+1, -1\}$, of preferred pairs of m-sequence of similar period. The Gold sequence can be readily expressed as,

$$c(k) = G1(k)G2(k - i), \ i = 0, \ldots, 2^r - 1. \tag{2.6}$$

where $G1(\bullet)$ and $G2(\bullet)$ are the preferred m-sequences, and r is the shift register length (i.e. $N_c = 2^r - 1$). The total number of Gold sequences generated is actually $2^r + 1$, which includes the $2^r - 1$ unique shifts and the two m-sequences itself (obtained by setting the corresponding shift register's to zeros). However, only 37 codes were selected for GPS PRN code assignment that demonstrated optimal cross-correlation properties (ICD-GPS-200 [1997]). The recursive equations for the two preferred m-sequences are given by (Spilker [1996]),

$$G1(i) = G1(i - 10)G1(i - 3)$$
$$G2(i) = G2(i - 10)G1(i - 9)G2(i - 8)G1(i - 6)G2(i - 3)G1(i - 2) \tag{2.7}$$

The particular initial condition (initial states of the shift registers) for generating the 37 unique PRN codes can be found in ICD-GPS-200 [1997]. The Gold sequences are obtained utilizing the "shift-and-add" property of linear feedback shift register (LFSR) sequences (Gold [1967]). This property will be dealt with in great detail in subsequent chapters due to its crucial role in the development of acquisition schemes. The auto and cross-correlation function for the selected PRN codes can readily expressed as follows (Misra and Enge [2001]):

$$\langle \mathbf{c}_j, \mathbf{c}_j \rangle \in \left\{ 1, \frac{-1}{N_c}, \frac{-\beta(r)}{N_c}, \frac{\beta(r) - 2}{N_c} \right\}$$
$$\langle \mathbf{c}_i, \mathbf{c}_j \rangle \in \left\{ \frac{-1}{N_c}, \frac{-\beta(r)}{N_c}, \frac{\beta(r) - 2}{N_c} \right\} \tag{2.8}$$
$$\beta(r) = 1 + 2^{\lfloor (r+2)/2 \rfloor}$$

where $\langle \bullet \rangle$ is the correlation operation and $\lfloor a \rfloor$ denotes the greatest integer less than a. The correlation operation can be readily expressed as,

$$R(k - i) = \frac{1}{N_c} \sum_{k=0}^{N_c - 1} c(k)c(k - i), \ i = 0, \ldots, N_c - 1. \tag{2.9}$$

Figure 2.2 shows the auto-correlation plot for PRN1 C/A code along side its zoomed version. The auto-correlation function is correlated within chip duration and is traditionally approximated by a triangular function as follows:

$$R\left(k - \frac{t}{T_c}\right) = \begin{cases} 1 - \left|\frac{t}{T_c}\right| & 0 \leq t \leq T_c \\ 0 & elsewhere \end{cases} \tag{2.10}$$

However, the front-end bandwidth will readily effect the shape of $R(\bullet)$ with narrower bandwidth leading to smoothened triangle function due to front-end correlation.
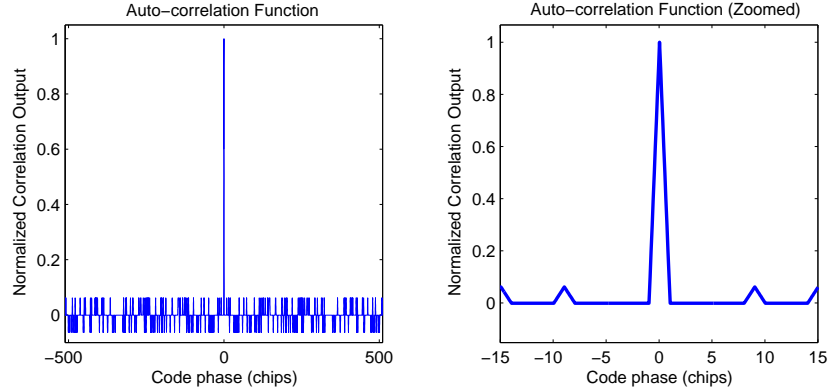
Figure 2.2: GPS C/A Code Auto-Correlation (Left) and Zoomed-in view about $\pm$ 15 chips (Right)

Since the power spectral density (PSD) and the auto-correlation of a wide-sense stationary signal form a Fourier pair[2], the amplitude spectrum can be readily obtained by applying a Fourier transform on the auto-correlation function and taking its magnitude. The auto-correlation of C/A code is periodic triangular function with the period being $T_r = N_c T_c$. Accordingly, the resulting spectrum takes a squared sine-cardinal form. Furthermore, the spectrum exhibits periodic spectral lines with the fundamental period being the inverse of its code repetition period[3]. Finally, the presence of out-of-phase correlation would result in the deviation of the line spectrum from the ideal

---

[2] $S(f) = \int_{-\infty}^{\infty} R(\tau) e^{j2\pi f\tau} d\tau$, $S(f)$ and $R(\tau)$ being the power spectrum and auto-correlation function.
[3] $\sum_{n=-\infty}^{\infty} \delta(t - nT_r) = \frac{1}{T_r} \sum_{k=-\infty}^{\infty} \delta\left(f - \frac{k}{T_r}\right)$

sine-cardinal form. Figure 2.3 shows the spectrum of both C/A code and P(Y) code for the 20 MHz bandwidth.
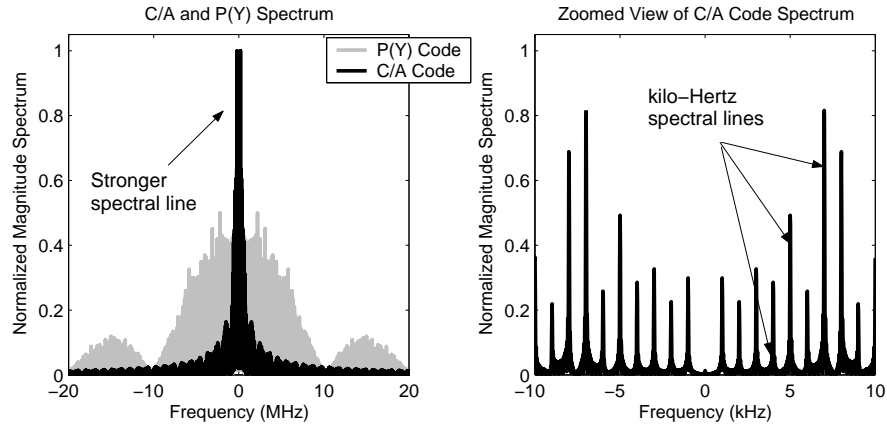
Figure 2.3: GPS L1 Signal Spectrum (Left) and Zoomed view of C/A Code Spectrum (Right)

The spectral plots readily follows the sine-cardinal form with occasional deviation due to the presence of stronger spectral lines. The 20 MHz filtering leaves the C/A code spectrum unfiltered up to the 10th order side-lobe but filters out the secondary lobes of the P(Y) code. Moreover, the zoomed view of the C/A code spectrum reveals the periodic spectral lines with varying magnitudes. The individual spectral lines are also characterized by finite bandwidth (i.e. T_b^{-1} Hz) arising from the navigation data modulation. A typical GPS receiver relies on cross-correlation suppression to demodulate the desired PRN code amidst interfering signals from other satellites. Unfortunately, the correlation suppression performance tends to degrade in the presence of multiple PRN's with varying magnitudes and Doppler's.

2.2.3 PRN Code Properties

In the previous section, the correlation and spectral characteristics were briefly described. However, the following PRN code properties are of critical importance and has been extensively utilized during the course of the developed research.

Periodic Property

The underlying PRN code is generated at 1.023 MHz and has a code length of $N_c = 1023$ in chips. Accordingly, the code is periodic every $N_c T_c = 1\ ms$. That is,

$$c(k) = c(k + lN_c),\ l = 0, 1, 2, \ldots \tag{2.11}$$

The direct implication of this aforementioned property is that the resulting signal is characterized by discrete periodic spectrum with the spectral line separation being $T_r = (N_c T_c)^{-1}$ or 1 kHz. Although, the C/A code periodicity often considered as undesirable in the view point of interference, it can be used advantageously during GPS signal acquisition. In the subsequent chapters, this periodic property is extensively utilized for the development of new detection algorithms.

Delay-and-Multiply Property

The DAM property in its original form holds good for m-sequences and is used in the generation of Gold sequences (Sarwate and Pursley [1980]). The DAM property can be stated as follows: Multiplication of a m-sequence with its delayed version (integer chips) yields the same m-sequence with a different phase shift (or time shift). That is,

$$u(k)u(k - m) = u(k - l),\ u(k) \in \{+1, -1\},\ 1 \leq m \leq N_c - 1. \tag{2.12}$$

Interestingly, the GPS C/A code (or Gold code) is generated by utilizing the DAM property of the preferred m-sequences. The PRN code, $c(k)$ is generated by,

$$c(k) = G1(k)G2(k - m) \tag{2.13}$$

The delay m is accomplished by tapping off at appropriated tap outputs in the secondary shift register as expressed in (2.7).

Theorem: The DAM property for the C/A code, or more generally, for Gold code can be stated as follows. The multiplication of a Gold code with its chip (or integer

chip) delayed version yields a different Gold code from the set of $N_c + 1$ Gold codes. That is,

$$c_m(k) = c(k)c(k - m), \ m = 1, 2, \ldots, \ m \neq N_c \tag{2.14}$$

where $c_m(k)$ is the new Gold code obtained by multiplying the original Gold code, $c(k)$, with its m-chip delayed version. Besides, the delay m is not bounded by $N_c - 1$ as the underlying code is periodic.

Proof: To prove this, we have to express the product of Gold sequence in (2.14) using the original m-sequence as given in (2.12),

$$c_m(k) = \Big(G1(k - \alpha)G2(k - \beta) \Big) \Big(G1(k - \alpha - m)G2(k - \beta - m) \Big) \tag{2.15}$$

Since $\alpha \neq \beta$ and $m \neq N_c$, we have $(\alpha - m) \neq (\beta - m)$. Note that it is possible to bring delay m into the individual m-sequences $G1(k)$ and $G2(k)$ as $c(k - m)$ is still the same C/A code but shifted by m. The above multiplication operation is both commutative and associative in the binary field $\{-1, 1\}$. Invoking the commutative[4] and the associative property[5] of binary multiplication, we can rearrange the above equation as,

$$c_m(k) = \Big(G1(k - \alpha)G1(k - \alpha - m) \Big) \Big(G2(k - \beta)G2(k - \beta - m) \Big) \tag{2.16}$$

Utilizing the DAM property of m-sequences as expressed in (2.12), we have,

$$c_m(k) = G1(k - \alpha_1)G2(k - \beta_2), \tag{2.17}$$

where α_1 and β_1 are different time shifts. From (2.17) with (2.14), we can readily infer that $c_m(k)$ will also be a Gold sequence if not C/A code. To further validate, the auto-correlation of the modified C/A code and its cross-correlation with the original C/A code is shown in Figure 2.4. The PRN1 C/A code was utilized and the modified code $c_1(k)$

---

[4]x and y are said to commutative under a binary operation, $\oplus$, if: $x \oplus y = y \oplus x$
[5]x, y, and z are said to associative under a binary operation, $\oplus$, if: $x \oplus (y \oplus z) = (x \oplus y) \oplus z$
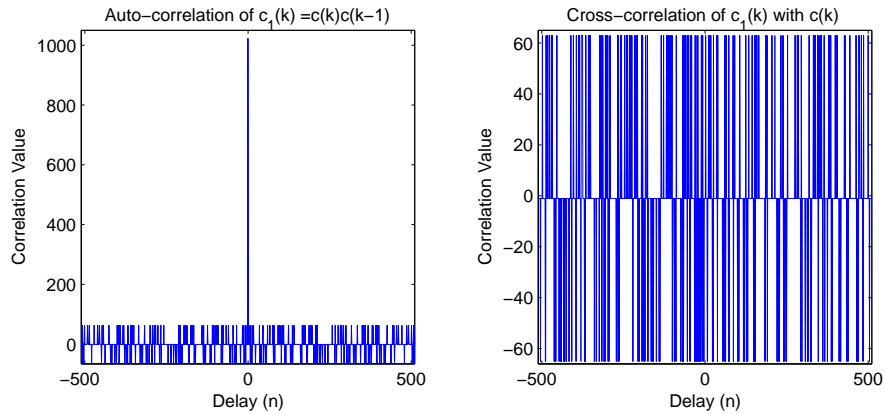
Figure 2.4: DAM Property of GPS PRN 1 C/A Code. (Left) Auto-correlation and (Right) Cross-correlation

was obtained using a one-chip DAM operation. The correlation plots readily confirm the earlier proof that the product of Gold sequence with its delayed version yields another Gold sequence. The periodic and the DAM property are extensively utilized in the subsequent chapters during the development of novel detection algorithms.

2.3 GPS Digital Receiver Signal Processing

This section describes the basic architecture of a digital GPS receiver in terms of initial sequence of operations. However, more emphasis is given to the baseband signal processing using software receiver due to its significance in the developed research. The readers are referred to Kaplan and Hegarty [2006] and van Dierendonck [1996] for a detailed treatment on GPS receiver signal processing. Figure 2.5 shows the block diagram of a generic GPS receiver.

2.3.1 Antenna and Preamplifier

The receiver antenna is right hand circularly polarized to match the incoming signal and also to reject the reflections that are either linearly polarized (LP) or left hand circularly polarized (LHCP). The effect of double reflection will still exist but remain weaker
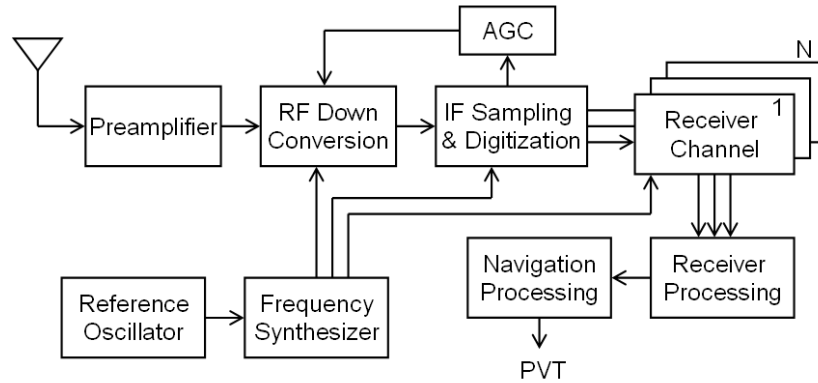
Figure 2.5: Digital GPS receiver block diagram

compared to the direct LOS signals. The antenna pattern is essentially hemispherical with sharp reductions at low elevation angels (i.e. 5^0) to reject the ground reflections. The antennas also provide an out-of-band rejection as well as spatial filtering. The antenna phase centre calibration and variation plays a crucial role in GPS application requiring millimetre level accuracies. GPS antennas can range from low-cost microstrip patch to phased arrays and include special structures such as choke-rings. The antenna radiation pattern of the GPS L1 antenna utilized during the research and its related characteristics can be found in Novatel [2006]. The 3 dB passband bandwidth extends from -15 to 30 MHz with respect to L1 frequency. The out-of-band rejection is around 30 dBc for the between -15 to -30 and 30 to 50 MHz. The antenna gain at zenith is 5 dBic with a 13 dB gain roll-off factor from zenith to horizon. The multipath rejection in terms of LHCP rejection is around 16 dB at the zenith.

The RF signal captured through the antenna is supplied to the preamplifier, which also sets the noise figure (i.e. C/N_0) of the receiver. The main objective of preamplfier is to boost the signal while maintaining minimum levels of noise enhancements. Many GPS antennas are designed so as to include the preamplifier itself to minimize subsequent cable losses. Under these situations, the supply voltage is passed through the preamplifier to power the upstream active antenna and any cascaded preamplifiers.

The gain provided by the preamplifier typically ranges between 25 to 40 dB with noise figures less than 2 dB levels. A pre-selection filter is often included to reject unwanted image frequencies prior to down conversion. Thus, the overall noise figure could be as much as 4 dB due to additional losses from pre-selection filtering, burnout protection and other associated operations. The Novatel GPS antenna utilized for data collection also including a preamplifier that had a low noise amplification (LNA) gain of 27 dB and less than 2 dB noise figure.

2.3.2   RF Downconversion and Digitization

The RF signal is conditioned through filtering, amplification, downconversion prior to being subjected to digitization. Given the low power nature of GPS signals, stronger out-of-band interference from terrestrial systems are rejected using surface acoustic wave (SAW) filters with sharp cut-off frequencies. Amplification is straightforward for single-bit receivers but involves control signals from AGC for multi-bit receivers. The downconversion can be performed directly using a single stage or through multiple stages (typically two stages) prior to sampling and digitization. Multistage downconversion typically translates the received RF signal close to baseband (≤ 5 MHz) and allows for sufficient image suppression through intermediate filtering. Direct downconversion is attractive as it eliminates the need for intermediate stages but translates the received RF signal farther away from baseband (≥ 30 MHz) (Misra and Enge [2001]).

The final signal bandwidth and quantization level are selected based on the type of the receivers. For example, low-end commercial receivers limit themselves with narrow 2 MHz bandwidth and single-bit quantization. On the other hand, high-end receivers utilize the entire 20 MHz bandwidth with quantization ranging from 1.5 to 3 bits. Note that the bandwidth also critically affects the shape of correlation output aside from signal power loss. Similarly, the use of single-bit quantization ideally results (assuming

infinite bandwidth) in a 1.96 dB power degradation. However, the gain from multi-bit quantization over single-bit can be achieved only when the AGC positions the received signal precisely to the dynamic range of A/D converter.

2.3.3 Baseband Signal Processing

The two foremost parameters to be extracted from the received GPS signal is the *code phase* and *carrier phase*. While code phase measurements are utilized for determining pseudoranges, carrier phase measurements are required for navigation data demodulation and often for precise range measurement. Both the acquisition and tracking processes are essentially accomplished in baseband signal processing. The process of baseband conversion is carried out by analog mixing or by IF sampling. Modern GPS receivers typically utilize the IF sampling (or passband sampling), wherein the process of sampling and digitization are carried out in the final IF stage itself (van Dierendonck [1996]). Pre-correlation (or anti-aliasing) filtering is often utilized to prevent frequency aliasing arising from sampling process. However, this filtering also introduces correlation losses as the side lobes of the C/A code spectrum are filtered out. At this point, the signal is split into multiple channels for simultaneous tracking of multiple satellites. Baseband signal processing primarily consists of pre-correlation sampling, code and Doppler removal, post-correlation filtering and finally navigation processing.

The first processing block is the Doppler removal unit, which essentially performs the phase rotation (or derotation) on the received I/Q samples. This process is used by the carrier tracking loops to track either the phase or the frequency of the received samples. The carrier tracking loops controls the numerically controlled oscillator (NCO) to generate the inphase and quadrature outputs for Doppler removal. The Doppler removal is followed by code removal, wherein the I/Q samples are mixed with three versions (early, late, and prompt) of the local PRN code to form the corresponding

correlation values. The PRN code tracking is maintained through delay locked loop (DLL) where the error signal is obtained by differencing the early and late correlation functions. The pre-detection integration interval can be extended from 1 ms to up to 20 ms after navigation data bit synchronization. The code and carrier phase discriminator outputs are formed in the microprocessor using the code and carrier phase measurements and subsequently fed back to the code and carrier NCO to maintain the loop. The pseudoranges and velocity measurements are then obtained from the code and carrier phase estimates, which are then collectively processed to obtain the navigation solution. The readers are further referred to Kaplan and Hegarty [2006] and van Dierendonck [1996] for a detailed description of baseband signal processing.

2.4   Software Receiver Implementation

Traditionally, receiver functions such as code and Doppler removal and correlation are implemented in application specific integrated circuits (ASIC), wherein the mega-hertz I/Q samples are processed to output kilo-hertz pre-detection or discriminator outputs. These measurements in-turn are supplied to the receiver and navigation processing to obtain the position, velocity, and time (PVT) solutions. However, this approach lacks the much desired flexibility to accommodate new signal structures and algorithms as reported in Ledvina et al. [2003]. More importantly, the proposed research necessitates raw I/Q data collection for assessing the developed acquisition algorithms. Figure 2.6 illustrates the test methodology alongside prototype software receiver developed during the course of research.

The developed framework allowed GPS data collection in two different modes. The controlled mode includes a Spirent GSS 7700 signal generator unit capable of outputting L1, L2C, and L5 signals. The output of the signal generator is supplied to an external LNA with a gain of 30 dB prior to feeding it to the front-end. The test setup also allows
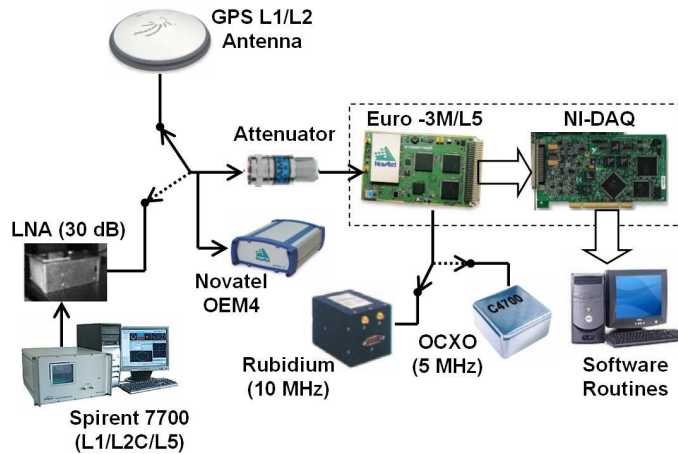
Figure 2.6: Developed Test Methodology

for live GPS data collection through Novatel's GPS –701 antenna (Novatel [2006]), which has a built-in LNA. The output of the signal generator or the antenna is supplied to the Novatel front-end. The design utilized the Euro-3M card for L1/L2C and Euro-L5 for L5 signal processing. In Euro-3M, the IF signal were centred around 70.42 MHz with 3 bit quantization. The individual I and Q samples were sampled at 40 MHz resulting in a combined sampling rate of 20 MHz. It is furthermore capable of outputting both L1 and L2C samples simultaneously at 70.42 and 70.1 MHz intermediate frequencies with two bit quantization. In the case of Euro-L5, the ensuing IF signal were centred around 69.95 MHz, which was subsequently sampled at 28 MHz (combined). The IF data from the Novatel front-end were buffered using a commercial DAQ card and finally stored in PC memory. The reference oscillator can be selected either between an internal temperature controlled crystal oscillator (TCXO), an external Rubidium reference (10 MHz) or an external Ovenized crystal oscillator (OCXO) with a fundamental frequency of 5 MHz. Weak signal scenarios were emulated either by setting low transmit power levels in the signal generator or by using variable attenuators. Finally, a Novatel OEM4 receiver was used for signal quality monitoring during the real data collection Novatel [2005].

For GPS L1 C/A acquisition, the GPS data was resampled from the original 20 MHz rate down to 2.046 MHz to emulate a typical mass manufactured GPS chip. The integer sampling [6] is adopted to allow for easy implementation of certain detectors that will be introduced in subsequent chapters. On the other hand, the original sampling rates were retained for the GPS L2C and L5 signals. The resampling process employed the MATLAB routine *resample* that utilized an anti-aliasing filter, wherein the filter delay is also compensated. To validate the developed software implementation in terms of data collection and subsequent processing, acquisition of a known PRN 10 was carried out in one of the data sets. The code acquisition was performed on the original data with 20 MHz sampling rate. Furthermore, the acquisition results for two different sampling rates namely 2.046 MHz and 4.75 MHz were also obtained. The coherent integration time was set to 1 ms with 2 noncoherent accumulations. The detection performance was measured using the post-correlation SNR (PSNR), which is defined as follows:

$$PSNR = 10\log_{10}\left[\frac{(R(\hat{\tau}=\tau) - E\left[R(\hat{\tau}\neq\tau)\right])^2}{var\left[R(\hat{\tau}\neq\tau)\right]}\right] \qquad (2.18)$$

The different sampling rates resulted in the same PSNR value of around 26 dB, which is in accordance with the 52 dB-Hz C/N_0 level. Figure 2.7 shows the normalized correlation plot for the different sampling frequencies. The zoomed view of the plot readily shows the problem of integer sampling rate in terms of peak distortion. Akos and Pini [2006] rightly noted this issue of integer sampling rate in the view point of nonlinear distortion in the DLL discriminators. However, the carrier Doppler modifies the chip rate and thus the number of samples per chip, which can minimize the effect on the correlation function. On the other hand, the correlation peak corresponding to 4.75 MHz almost aligns with the 20 MHz thus showing that the resampling process does not incur any distortions in the original signal. While the limitation of choosing integer chip sampling rates is acknowledged, its effect on detection performance of the acqui-

---

[6]Integer sampling involves an integer ratio of sample rate to chip rate. i.e. $T_c/T_s = 1, 2, 3, ..$

sition schemes can readily be marginalized. It should also be noted that the detector structures are not limited by the sampling frequency constraints.
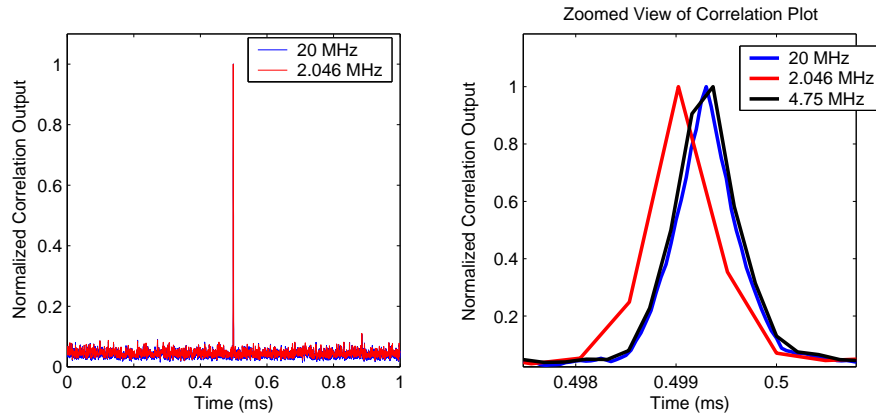
Figure 2.7: Correlation Output of PRN 10 (C/N_0 = 51 dB-Hz, Δ F = 2.01 kHz, T $_{COH}$ = 1 ms, N =2)

The prototype receiver comprises of library of software routines developed primarily in the MATLAB^{TM} environment. The software routines are also clustered to form a stand-alone executable function. The receiver functions as IF carrier removal and associated operations in acquisition stages are implemented in software. Currently, the developed software routines allow for acquisition of L1, L2C and L5 signals using a variety of acquisition schemes. Furthermore, dedicated routines that perform specialized processing such as interference suppression are incorporated in the developed software receiver. Finally, it has the necessary flexibility to accommodate new acquisition algorithms. Extensive usage of matrix computations has been utilized to optimize the efficiency of data processing (Hartfiel [2000]). For instance, the acquisition techniques were implemented using block FFT techniques. The data processing time is further minimized by providing critical information such as PRN, Doppler and sometimes code phase information. It should be emphasized here that the developed software implementation is mainly intended to implement different acquisition schemes and to assess their detection performance under various signal conditions. Further enhancements and

augmentations in terms of code/carrier tracking implementations are currently being conducted.

2.5 GPS Limitations – Signal Degradation Effects

Having described the basic receiver GPS operations and the corresponding software receiver implementations, we now review the major impediments encountered during GPS operation under degraded signal conditions.

2.5.1 Path Loss

The GPS satellite typically dedicates approximately 14 dBW of power for the C/A code signal on L1. Assuming that the C/A signal is emanating uniformly in all directions, then the PSD at a radial distance of R metres would be $1/4\pi R^2$ times the original radiated power. This reduction of power is often called *path loss* or*spreading loss*, which simply accounts for the spreading of the radiated energy over the surface area of a hypothetical sphere with the satellite at its centre. The altitude or the distance from the GPS receiver positioned at sea level to the satellite at zenith is approximately 20,193 km. Moreover, this mean distance is also a function of satellite elevation angle at the GPS receiver. For instance, the distance could be as much as 25,237 km for a satellite elevation angle of 5^0, which accounts for a additional 2 dB loss. The received power is directly proportional to the power density of the incident field times the antenna's effective area. For instance, the effective area for a isotropic antenna (whose gain is 1) is essentially $\lambda^2/4\pi^2$, where λ is the wavelength of received signal. However, the GPS receiver antennas typically provides +4 dBIC at zenith to -4 dBIC for elevation angles lower than 5^0. Therefore, the received power can be expressed in terms of antenna gain as follows (Enge and Misra [1999]):

$$P_R = \frac{P_T G_T G_R \lambda^2}{L_A \left(4\pi R\right)^2} \tag{2.19}$$

where P_T, P_R are the respective transmit and received powers, G_T and G_R are the respective gains of transmitter and receiver antennas. L_A is the loss associated for the signal propagation through atmosphere. The received C/A code signal power can be readily obtained by substituting the appropriate values in (2.19). For instance, the received C/A code signal power can take -156 dBW for a satellite positioned at zenith with a +4 dBIC gain receiver antenna. Nevertheless, the received signal is also affected from other signal degradation at various stages, which are described briefly in the following subsections.

2.5.2 Thermal Noise

The thermal noise mainly pertains to the noise generated in the receiver and is directly related to the receiver noise figure (NF) and equivalent noise temperature (T_{eq}). The noise spectral density is given by,

$$N_0 = \kappa T_{eq}$$
$$T_{eq} = T_A/L + (L-1)T_0/L + T_R \ ^0K, \ T_R = T_0(NF-1)$$

(2.20)

where T_R, T_0, and T_A are the receiver noise, ambient, and antenna noise temperature. L is the associated losses pertaining to connecting cables and filters. κ is the Boltzman's constant (i.e. κ = -228.6 dBW/^0K-Hz). Assuming typical values[7], the equivalent noise density takes a value of -205.2 dBW/Hz. Note that the peak signal (or carrier) power spectral density is readily obtained from PT_c^{-1}. For instance, the C/A power spectral density for the received power of -160 dBW is -220.1 dBW/Hz. Accordingly, the C/A code spectrum even at its spectral peak is 14.9 dB below the noise power density. Similarly, the C/N$_0$ can be obtained from received signal power and noise spectral density from P/N_0 or -160 - 205.2 = 45.2 dB-Hz. Note that this is the effective ratio of carrier signal power to noise power over a bandwidth of 1 Hz. Consequently, one can also obtain the signal-to- noise ratio (SNR) from the C/N$_0$ from $SNR = C/N_0 BW^{-1}$.

---

[7]F = 0.259, T_R = 75.1 ^{0}K, L = 1.1, T_A = 130 ^{0}K

For example, the received SNR for a 2.046 MHz front-end bandwidth is around -18 dB. Therefore, the signal is buried under noise prior to any kind of signal conditioning.

2.5.3   Interference

Radio frequency interference (RFI) is one of the foremost concerns in safety critical applications that utilize GPS (Carroll [2003]). GNSS receivers rely on external RF signals and thus are vulnerable to other unwanted RF interference signals. RF interference (RFI) sources either intentional or unintentional in the vicinity of the victim receiver can potentially mask the weak GPS signals (Kaplan and Hegarty [2006]). RFI is normally categorized under wideband or narrowband, depending on the bandwidth of the interfering signal to the received GPS signal bandwidth. Wideband interference can take a Gaussian pulse form as in the case of ultra wideband systems or frequency/phase modulated as in the case of harmonics from television transmitters. There is a certain level of interference among the signals of similar type transmitted from other satellites that are sharing the same spectrum. For instance, intra-system interference (or self interference) refers to the mutual interference experienced between signals within a system such as GPS and Galileo. On the other hand, inter-system interference often refers to the interference experienced between signals of similar type but are emitted from different systems (i.e. between GPS and Galileo signals).

Narrowband interference could originate from frequency/phase modulated signals such as from AM or FM stations. Furthermore, continuous wave (CW) transmissions such as unmodulated carrier signals from other transmitters represent an extreme form of narrowband interference. Wideband interference increases the background noise floor to an extent where the receiver fails to acquire or track the GPS signals. On the other hand, narrowband and CW interference can mix with the C/A code spectral lines and leak through the correlators. Most commercial receivers are equipped with no or

minimum levels of protection against in-band RFI (Spilker and Natali [1996]). A more detailed treatment of RFI and corresponding detection and mitigation techniques can be found in Chapter 5 of this dissertation.

2.5.4 Radio Propagation

Radio propagation under various conditions results in power variations at the receiver end. There are three chief mechanisms that impact radio signal propagation: *reflection*, *diffraction* and *scattering*. Reflection arises when a propagating electromagnetic wave impinges on a smooth surface with very large dimensions compared to the signal wavelength. Diffraction occurs when the radio path is blocked by a large dense body with dimensions much larger than the signal wavelength. Diffraction results in secondary wave generation and is often termed shadowing as the diffracted field will still be able to reach the receiver but with significant attenuation. Scattering results from the impingement of radio waves on a large rough surface or any surface with the dimension similar or less than signal wavelength. Typical signal obstructions include lamp posts, street posts and foliage. The effects of these radio propagation mechanisms can either be large scale (such as shadowing) or small scale (such as fading). Besides, irregularities in the propagation medium (i.e. ionosphere) can also introduce variations in signal power levels. The effects of various radio propagation mechanisms and related performance measures can be found in Sklar [1997].

Large Scale Shadowing

Shadowing effects arise from excess (even massive) attenuation of the LOS GPS signal. The large scale fading or shadowing represents the average signal power attenuation or excess path loss due to the motion in large areas. This phenomenon is effected primarily by prominent terrain contours such as hills, forest canopies, downtown areas and even indoors. The received GPS signal can experience various levels of attenua-

tion depending on the propagation medium. Klukas et al. [2004] reported that typical building infrastructures such as cinder blocks could attenuate GPS signals by 23 dB or more. Figure 2.8 shows the fading experienced indoors with respect to nominal outdoor conditions (Lachapelle et al. [2003]). Under extreme conditions, the LOS is severely attenuated to an extent that the receiver is only able to track the multipaths.
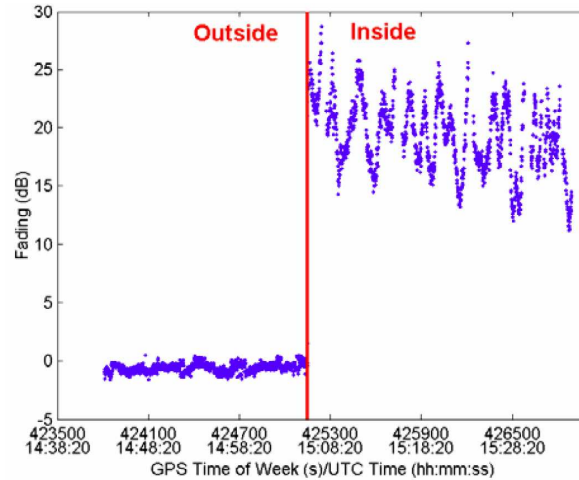
Figure 2.8: Shadowing Effects in Indoor Environments (ref: Lachapelle et al. [2003])

Small Scale Multipath Fading

Small scale fading refers to dramatic variations in signal amplitude and phase arising from small changes (wavelength variations) in the spatial separation between the transmitter/receiver pair. Small scale fading takes a *Rician* distribution in the presence of a dominant LOS signal and a *Rayleigh* distribution in the absence of LOS signal. Small scale fading manifests itself into signal dispersion and time-variant propagation characteristics. The time spreading mechanism is often characterized by multipath delay spread in the time domain and using coherence bandwidth in the frequency domain. Similarly, the time-variant mechanism is characterized using channel coherent time in time domain and by Doppler spread in frequency domain.

The coherence bandwidth (f_0), is of particular importance as it represents the range of frequencies over which the propagation medium passes all spectral components with

approximately equal gain and linear phase. The channel coherence bandwidth is inversely related to the maximum delay spread. The following expressions relate the RMS delay spread (σ_τ) and Doppler spread (f_d) with the channel coherence time (T_0) and bandwidth (Sklar [1997]):

$$f_0 \approx \frac{1}{2\pi\sigma_\tau}$$
$$T_0 \approx \frac{1}{f_d} \tag{2.21}$$

Furthermore, the radio propagation is also characterized as frequency non-selective (or flat) fading if the maximum delay spread is less than the basic pulse duration.

Ionospheric Scintillation

Ionospheric scintillation represents the rapid fluctuation in the received signal power arising from the irregularities in the the ionospheric layer. Scintillation occurs mainly due to the irregularities in electron density, which are more predominant in equatorial regions. Scintillation is also affected by the 11-year solar cycle. The power fluctuation, δP, is generally modelled using the Nakagami-m pdf as (Skone et al. [2005]):

$$p(\delta P) = \frac{m^m \delta P^{m-1}}{\Gamma(m)} e^{-m\delta P}, \geq 0 \tag{2.22}$$

$p(\delta P)$ has a unity mean value and standard deviation of $\sqrt{1/m}$. The standard deviation of the power variation is often denoted by the S_4 index. Ionospheric scintillation impacts the GPS operation in two different ways. Firstly, deeper amplitude fade could result in the loss of code and carrier phase lock. Secondly, the phase variations introduce a level of dynamics that is difficult to be tracked by the phase locked loop.

2.6   High Sensitivity Detection

The federal communications commission's (FCC) mandate that all cell phones must be able to locate automatically with GPS accuracy set the tone for the tremendous growth in GPS industry. For instance, the total sales from the top four GPS manufacturers

accounted for two million units (Abraham and van Diggelen [2001]). Successful adoption of GPS into cell phones requires that the technology meet new demands, including indoor operation, near-instantaneous TTFF, and low power consumption. Moreover, the impact of augmenting the GPS chip should be minimal in terms of manufacturing cost (i.e. less than \$10). More importantly, the GPS receiver is now expected to successfully operate under indoor conditions that result in massive signal attenuations. The ability to extract the GPS signal from the background noise is readily obtained from the product of the transmitted signal bandwidth and coherent integration time. That is,

$$G = \frac{T}{T_c} \tag{2.23}$$

where T is the coherent observation period and G is the processing gain. The integration time increases exponentially with the decrease in the C/N_0 levels. Figure 2.9 shows the required coherent integration time to achieve a post-correlation SNR of around 15 dB as a function of C/N_0 for a receiver with a front-end bandwidth of 2.046 MHz. For instance, the coherent observation should exceed 1 s to acquire a 15 dB-Hz GPS signal. Accordingly, the processing power should be increased by several hundred times under these extreme conditions.
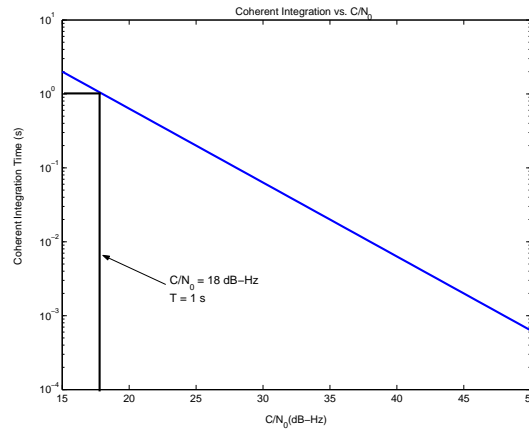
Figure 2.9: Effect of C/N_0 on Coherent Integration Time (T)

Unfortunately, the integration time is critically effected by two fundamental lim-

itations – navigation data modulation and frequency deviation. The navigation data introduces a random phase shift (0 or π) every 20 ms in the transmitted signal. Accordingly, the navigation data modulation manifests itself as 50 Hz dispersion in frequency domain. Thus, the coherent integration time cannot exceed 20 ms without any *a priori* information. However, the integration time is much lower than 20 ms as the data bit boundary is unknown.

The second limitation arises from the frequency mismatch between the transmitter and receiver clock. The effect of a constant uncompensated Doppler offset for a coherent detection performance is a power attenuation following the well-known sinc-squared characteristic, whereby the total received power is given according to Figure 2.10 with a fractional frequency offset of F Hz, where $1/T$ is the first-null frequency and T is the coherent integration period. The second order effect namely the frequency drift smears the sinc-function as shown in Figure 2.10 over a range of frequencies. Finally, the frequency offset and drift effects also manifests in code dispersion. The next section briefly introduces two prominent high sensitivity GPS (HS GPS) techniques adopted by the industry.
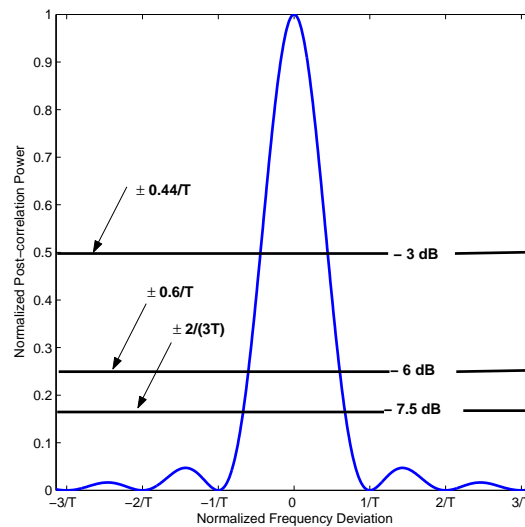
Figure 2.10: Effect of Frequency Deviation on Post-correlation SNR

2.6.1 HS GPS Overview

HS GPS techniques allows for extended integration time and thereby accomplishes substantial processing gain. The high sensitivity operation is realized either in assisted or stand-alone mode. Assisted GPS (AGPS) receivers rely on external aiding in the form of ephemeris or almanac aiding. Assisted GPS techniques include time, frequency, location and Doppler aiding and typically involve a wireless network infrastructure to communicate with the GPS device in the field. AGPS utilizes the time and frequency information to confine the frequency search space and to wipe-off the navigation data. Consequently, the AGPS provides the fastest TTFF and with sufficient hardware resources can enable weak signal acquisition and tracking.

On the other hand, a stand-alone HS GPS (often referred to as HS GPS) receiver operates in the autonomous mode but utilizes massive hardware resources and advanced algorithms to enable rapid or weak signal acquisition. The presence of several hundred thousand correlators enable the search of code phase and carrier Doppler in parallel. While the use of extensive hardware resources does increase the silicon size, it can allow for efficient parallel acquisition strategies O' Driscoll [2007]. Under weak signal conditions, the required processing gain is achieved through a combination of coherent and noncoherent detection. The use of noncoherent detection eliminates the need for navigation data estimation or prediction and allows for less stringent frequency estimation.

2.6.2 Limiting Factors of HS GPS

While AGPS and HS GPS provide substantial improvements, they can still be limited by further challenges imposed by the propagation environment and by the receiver. For instance, the stand-alone HS GPS techniques are critically limited by the presence of unknown navigation data. On the other hand, the AGPS solution alleviates this issue by supplying the receiver with aiding information. Nevertheless, the stability of the ref-

erence oscillator in the receiver readily limits gain that could be achieved with AGPS. Furthermore, AGPS techniques can also be limited in terms of the network coverage. While both AGPS and HS GPS provide minimum levels or no protection against additional degradations due to multipath, scintillation and other associated phenomena. Therefore, there is still a need for innovative acquisition schemes to overcome at least some of the aforementioned challenges.

2.7 Discussion

The characteristics of legacy GPS signals was analyzed using correlation and spectral properties. The receiver operation chain was briefly introduced with respect to a generic GPS receiver. The software receiver implementation developed during the course of this research was briefly described. The limitations of standard GPS receiver operations as a result of various signal degradations was briefly introduced. A brief overview of AGPS and stand-alone HS GPS techniques and their inherent limitations were exemplified. Two key properties namely the periodic and the shift-and-add property of the underlying C/A code was established in theory.

The development of novel acquisition schemes critically relies on the comprehensive understanding of the existing solutions using fundamental theory. Accordingly, in the next chapter, we take a detection/estimation theoretical approach to breakdown the detection algorithms utilized by the traditional GPS acquisition schemes for high sensitivity signal detection.

Chapter 3

Enhanced GPS C/A Code Signal Detection – Theory, Analysis and Innovations

This chapter primarily focuses on enhanced detection of the GPS C/A code signal. After introducing the discrete signal and noise representation, the GPS signal acquisition is developed as a *detection/estimation* problem. More emphasis is placed on the detection aspect of GPS signal acquisition in accordance to the thesis objective. In this chapter, an unified approach is adopted to establish various pre and post correlation detection schemes as the best approximations of the generalized likelihood ratio test (GLRT). The optimal detector is derived as the one that maximizes the likelihood ratio based on the *Neyman-Pearson criterion*. The different detectors are developed based on the extent of *a priori* information of the signal model. For assumed deterministic signals, the NP detector is shown to be equivalent to a *matched filter*. Moreover, it is shown here that the asymptotic version of GLRT is equivalent to an *estimator-correlator*. Finally, the well-known post-correlation noncoherent and the newly proposed differential detection are established in terms of GLRT and EC formulations.

The remainder of this chapter deals with the development of an efficient detector: the *generalized post-correlation differential detector*. The proposed detector readily assumes the post-correlation noncoherent/differential detector as its specialized forms. The analysis of residual signal effects for both the traditional detectors and the proposed detector is performed. Theoretical detection performance analysis in terms of probability of false alarm and correct detection is carried out. The various system level concepts developed in this chapter are initially validated using hardware simulated GPS data. Finally, the acquisition performance in terms of noise/frequency sensitivity of the

various detectors is also carried out.

3.1 Signal and Noise Models

A rudimentary GPS signal model is adopted in this dissertation to allow for the simplified analysis of developed detectors. The developed theoretical model does not include the effects of front-end, intermediate stages and sampling/quantization. Accordingly, it is assumed that the received RF signal is down-converted and sampled without any distortion yielding the following complex baseband signal,

$$x(t) = \sum_{m=0}^{M-1} \sqrt{C_m} d_m(t' - \tau_m) c_m(t' - \tau_m) e^{j\phi_m(t')} + w(t), \tag{3.1}$$

The instantaneous transmitted power, C_m, of the mth satellite. The BPSK modulated data symbols and the PRN (or C/A) code are denoted by $d_m(t)$ and $c_m(t)$, respectively. The PRN code, $c_m(t)$, is a periodic code that is generated at 1.023 MHz rate and has a length of $N_c = 1023$ in chips. The navigation data $d_m(t)$ consists of equiprobable symbols and is generated at the rate of 50 Hz. The ratio of the PRN code chip rate to the navigation data rate is often termed processing gain (i.e. $PG = T_b/T_c$, where T_b and T_c are data and PRN code chip duration) of the GPS system. The variable t' is an arbitrary function of t, whose second order approximation is given by,

$$t' = t + \eta_m t + \frac{1}{2}\xi_m t^2 \tag{3.2}$$

where η_m is the Doppler shift (or the time dilation coefficient) and ξ_m is the Doppler shift rate arising from relative motion of satellite and the receiver (Axelrad and Brown [1996]). τ_m comprises of integer code period (λ) and chip delay (iT_c), $\tau = \lambda T_r + iT_c$. The integer ambiguity, λ, of the C/A code period is considered a nuisance parameter and is readily ignored. On the other hand, the chip delay component is modelled as an integer (i.e. i= 0, 1, 2,..., N_c-1). The time dilation promptly manifests into the

code and data Doppler in the received signal, which is ignored alongside code and data Doppler shift rates to allow for mathematical tractability. While this assumption holds for moderate integration times, it is severely limiting for longer integration times and has to be accounted for[1]. Finally, the instantaneous carrier phase $\phi_m(t)$ is modelled as:

$$\phi_m(t) = \phi_0 + \omega_m t + \frac{1}{2}\varpi_m t^2 \tag{3.3}$$

where ϕ_0 is the initial carrier phase value. The initial carrier Doppler is denoted by ω_m and is related to ω_{L1} as $\omega_m = \eta_m \omega_{L1}$. The carrier Doppler shift rate is denoted by ϖ_m and is related to ω_{L1} as $\varpi_m = \xi_m \omega_{L1}$. The second order effect represented by $\ddot{\phi}_m(t)$ is ignored for the most part of this dissertation except during the frequency drift analysis. The propagation medium (i.e. multipath) is assumed to be relatively time invariant during the entire acquisition period. Since the analysis is primarily concerned with the demodulation of the GPS C/A code signal pertaining to a satellite of interest, we can ignore the variable m in (3.1). For $M >> 1$, the interference from other visible satellites is approximated as a Gaussian process using a central limit theorem argument. The carrier power is assumed to be time-invariant during the signal demodulation and thus its time dependence is also ignored. For convenience, the received signal is assumed to be sampled at integer multiples of the basic chip duration (i.e. $T_s = T_c/N_s$, where S is the sampling factor $N_s = 1, 2, ...$) resulting in the following discrete signal,

$$x(k) = \sqrt{C}d(k - \tau)c(k - \tau)e^{j\phi(k)} + w(k), \ \phi(k) = 2\pi\Delta F k + \phi_0. \tag{3.4}$$

The thermal noise is assumed to be an additive white Gaussian noise (AWGN) process. The AWGN assumption is still a good approximation even as the front-end filtering introduces finite correlation in the received samples. The noise process $w(k)$ essentially

---

[1]Acquisition schemes implemented for performance analysis accounted for both carrier and code Dopplers

consists of real and imaginary components with equal variance. That is,

$$w(k) = w'(k)e^{j\phi(k)}$$

$$w(k) = w_I(k) + jw_Q(k)$$

(3.5)

The noise processes $w_I(k)$ and $w_Q(k)$ are assumed to be zero mean independent white Gaussian noise with variance $\sigma_I^2 = \sigma_Q^2 = 0.5N_0T_c^{-1}$, where $N_0 = \kappa T_{eq}$ as expressed in (2.20). Accordingly, $w(k)$ is zero mean and complex Gaussian with the variance $\sigma_w^2 = \sigma_I^2 + \sigma_Q^2 = N_0 B_{IF}$, where B_{IF} is the IF bandwidth.

3.2   Detection/Estimation Problem in Signal Acquisition

The fundamental objective of GPS receiver processing involves the demodulation of the individual satellite signals from the received composite signal and subsequent extraction of measurements such as pseudoranges and Doppler to allow for a navigation solution. The initial acquisition and subsequent tracking essentially guarantees the continuous extraction of the above mentioned parameters. Acquisition is generally regarded as the initial or coarse synchronization, and tracking is often called continuous or fine synchronization. The acquisition process later initiates the fine synchronization or tracking process by supplying the following parameters from the received signal:

- SV PRN Code (m)

- Code phase offset (τ)

- Carrier frequency offset (ΔF)

- Residual phase offset (ϕ_0)

- Navigation Data $(d(k))$

Let $\theta = [m, \tau, \phi_0, \Delta F, d(k)]$ be the actual parameter vector pertaining to the SV signal of interest. The receiver utilizes $N = TT_s^{-1}$ samples of the received signal $x(k)$ to obtain an

estimate $\hat{\theta}$, where T is the total observation period. The parameter estimation process can be accomplished using any one of the following estimators.

- Minimum mean squared error (MMSE)

- Maximum a posteriori (MAP)

- Maximum likelihood (ML)

Let θ be the actual parameter vector pertaining to the mth transmitter. The receiver utilizes the N observations of the received signal $\mathbf{x} = [x(0), x(1), \ldots, x(N-1)]^T$ and forms the minimum mean squared error (MMSE) estimate $\hat{\theta}$. The MMSE estimator minimizes the mean squared error between the estimated and the actual parameter. That is,

$$\hat{\theta} = E\left[\theta \mid \mathbf{x}\right] \tag{3.6}$$

On the other hand, the MAP estimator attempts to maximize the posterior probability that the estimate is correct, given that the vector $\mathbf{x}$ is received. Accordingly, the MAP estimator chooses a $\hat{\theta}$ that maximizes the posterior PDF. That is

$$\hat{\theta} = \arg\ \max_\theta p\left(\theta \mid \mathbf{x}\right) \tag{3.7}$$

The above maximization is equivalent to the minimization of Bayes risk. By maximizing $p(\theta|\mathbf{x})$, we observe that,

$$p(\theta|\mathbf{x}) = \frac{p(\mathbf{x}|\theta)p(\theta)}{p(\mathbf{x})} \tag{3.8}$$

A limitation with MMSE and the MAP estimator is their inherent dependence on the availability of $p(\theta)$ or $p(\mathbf{x})$. Hence, $p(\mathbf{x})$ has to be computed when applied to GPS acquisition problem. Alternatively, the maximum likelihood estimator (MLE) can be adopted. The MLE for the vector parameter θ is defined to be the value that maximizes the likelihood function $p(\mathbf{x}; \theta)$ over θ. If the likelihood function is differentiable, then

the MLE solution is obtained from,

$$\frac{\partial \ln p(\mathbf{x}; \theta)}{\partial \theta} = 0 \tag{3.9}$$

In GPS signal acquisition, it is not necessary to estimate all of the unknown parameters as some are considered nuisance (i.e. signal power, phase offset). Accordingly, the estimators can be designed to be invariant to those nuisance parameters. Secondly, it is sufficient to obtain a coarse estimate of θ . Hence, it is more appropriate to maximize the probability that the estimation error is within some predefined bound. Note that the SV PRN, code phase and frequency offset is usually constrained within a certain range (i.e. $m \in [1, 37]$, $\tau \in [0, 1]$ ms, and $\Delta F \in \pm$ 10 kHz). The ML parameter estimation is typically performed as a multi-dimensional search process. The multi-dimensional parameter space is generally discretized into smaller cells leading to an approximation in the maximum likelihood parameter estimation. The approximation is readily allowed as an accurate estimate of parameters is not required during the acquisition process. Often, the parameter space is decomposed into a two-dimensional space of code phase and residual frequency offset by marginalizing the effect of other parameters such as the residual phase offset and the navigation data modulation. For example, Figure 3.1 depicts the discretized two-dimensional search space in code phase and residual frequency offset.

Interestingly, the discretization of parameter space effectively translates the GPS signal acquisition from an estimation problem to a detection problem. During acquisition, the detector carries out a likelihood test to determine the presence of the signal using the supplied parameter estimate. The detection process is repeated for other cells in order to span the entire parameter space. Accordingly, the generalized likelihood ratio can therefore be given as,

$$L(\mathbf{x}) = \frac{p\left(\mathbf{x}; \hat{\theta} \approx \theta\right)}{p\left(\mathbf{x}; \hat{\theta} \neq \theta\right)} > \gamma \tag{3.10}$$
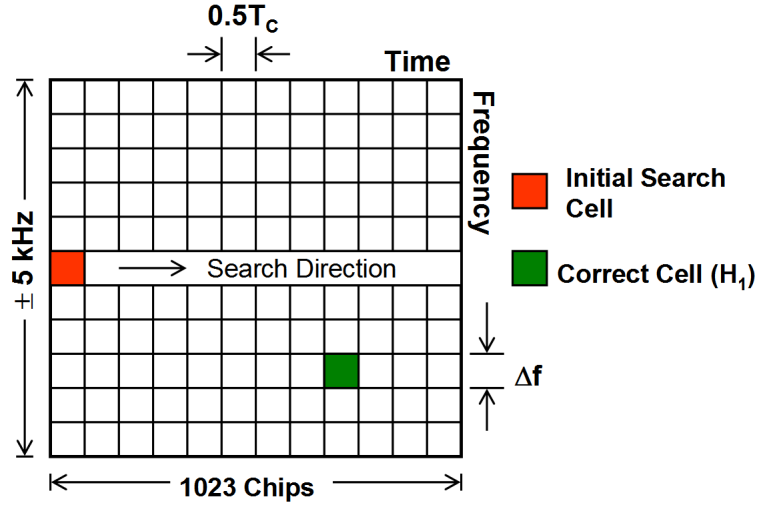
Figure 3.1: Discretized Two-dimensional Search Space in Code Phase and Residual Frequency Offset

Thus, the acquisition process is generally considered as a joint detection/estimation problem. Firstly, the likelihood ratio is calculated for all possible parameter estimates (cells) in the parameter space. Subsequently, the estimate $\hat{\theta}$ that maximizes the likelihood ratio is chosen as the ML estimate. Secondly, the corresponding $L(\mathbf{x})$ is compared against a predefined threshold γ and a decision is made based on the result. While the GPS signal acquisition is a multi-hypothesis problem, it can also viewed as a binary hypothesis. For instance, the presence of particular PRN code signal (m) is essentially a binary hypothesis problem. However, as shown in Figure 3.1, the estimation of its parameters is essentially a GLRT. Therefore, we have

$$
\begin{aligned}
H_0 &: x(k) = s_{\hat{\theta} \neq \theta}(k) + w(k) \quad k = 0, 1, \ldots, N-1. \\
H_1 &: x(k) = s_{\hat{\theta} \approx \theta}(k) + w(k) \quad k = 0, 1, \ldots, N-1.
\end{aligned}
\tag{3.11}
$$

where $s(k)$ is the transmitted GPS signal and $w(k)$ is the AWGN process with variance σ_w^2. N is the number of samples pertaining to the total observation period T (i.e. $N = TT_s^{-1}$). Accordingly, the detection approach simply follows the theory of hypothesis testing where the PDF of individual hypotheses are known or can be approximated. The performance of any detector can readily be characterized by two probability measures:

the probability that the detector falsely decides on signal presence; and the probability that detector correctly decides on signal presence. Let H_0 and H_1 be the hypotheses for signal absence and signal presence, respectively. Accordingly, the probability that a detector decides on H_1 when H_0 is correct is often called as the probability of *false alarm* (P_{FA}). Similarly, the probability of that detector choosing H_1 when H_1 is correct is known as the probability of *correct detection* (P_D). It is not possible to optimize both the probabilities and typical approach attempts to maximize P_D for a fixed upper-limit on P_{FA}. The primary approaches for hypothesis testing are the classical approach based on the *Neyman-Pearson* lemma and the Bayesian approach based on the minimization of *Bayes risk* Kay [1993a].

The optimal detector using Neyman-Pearson theorem approach, is the one that maximizes P_D for a given $P_{FA} = \alpha$, which decides H_1 if,

$$L(\mathbf{x}) = \frac{p(\mathbf{x}; H_1)}{p(\mathbf{x}; H_0)} > \gamma \tag{3.12}$$

where the threshold γ can be determined from

$$P_{FA} = \int_{\{\mathbf{x}: L(\mathbf{x}) > \gamma\}} p(\mathbf{x}; H_0) d\mathbf{x} = \alpha \tag{3.13}$$

The proof for the Neyman-Pearson theorem can be found in Kay [1993a]. Note that the function $L(\mathbf{x})$ is known as the the *likelihood ratio* as it indicates for each value of $\mathbf{x}$, the likelihood of H_1 versus the likelihood of H_0. The test as expressed in (3.12) is often called the likelihood ratio test (LRT).

Alternatively, the Bayesian approach attempts to minimize the Bayes risk by achieving minimum probability of error. The probability of error can be determined by taking the probability of false detection and the probability of missed detection as,

$$P_e = P(H_1|H_0)P(H_0) + P(H_0|H_1)P(H_1) \tag{3.14}$$

The Bayesian detector compares the *conditional likelihood* ratio to the threshold, wherein the threshold is determined based on prior probabilities. Thus, the optimal detector

essentially achieves minimum P_e by deciding H_1 if,

$$\frac{p(\mathbf{x}|H_1)}{p(\mathbf{x}|H_0)} > \frac{P(H_0)}{P(H_1)} = \gamma' \tag{3.15}$$

A number of detectors exists that are optimal in the NP sense and are obtained based on the different modelling of the signal and noise. Table 3.1 summarizes the different NP detectors based on the different modelling of θ and $w(k)$.

Signal	Noise Characteristics	
Characteristics	AWGN	Coloured
θ completely known or deterministic	Coherent Matched Filter Filter	Generalized Matched Filter
θ unknown and jointly Gaussian	Estimator Correlator (uses MMSE estimate)	Estimator Correlator
θ unknown unknown PDF	GLRT (uses ML estimate) (uses ML estimate)	GLRT

Table 3.1: Detection Problem – Hierarchy

In Section 3.3 of this chapter, the optimal detector structure for a known deterministic signal under AWGN is derived. The NP detector for a known θ in AWGN is the matched filter detector and is summarized in (3.22). Assuming the noise id AWGN, and θ is unknown but can be modelled as Gaussian, then the NP detector is considered an estimator-correlator (Refer to Appendix A). The incoherent matched filter implementation summarized in (3.62) is essentially an estimator-correlator and was obtained as a result of modelling the phase offset ϕ_0 as a uniform distribution. The estimator-correlator requires a pre-whitener in order to use it for correlated signals. Alternatively, the generalized likelihood ratio test (GLRT) detectors can be applied for an unknown signal and in the absence of apriori information of the PDF of θ. The derivation of the GLRT detector is given in Section 3.4 and is summarized in (3.60). The GLRT, in contrast to an estimator-correlator, utilizes the MLE rather than the MMSE estimate as the unknown PDF of θ. The GLRT receiver typically utilizes the MLE estimate as

summarized in (3.60) and is rewritten here as,

$$\hat{s}(k) = s(k) + w(k) \qquad (3.16)$$

Hence, the estimation process is critically influenced by the noise variance. Accordingly, the post-correlation implementations including the post-correlation noncoherent, differential and the generalized post-correlation differential schemes utilize the energy detector in conjunction with the initial coherent matched filter. The differential detector structures utilize an adhoc estimate rather than MLE to ensure that the noise variables are uncorrelated. Subsequently, the squaring type loss in the differential schemes is reduced in comparison to the noncoherent detection. However, they also incur a certain amount of power loss due to signal decorrelation.

In summary, the GPS signal acquisition can be more aptly viewed as a joint detection/estimation process. For instance, the parameter estimation is typically carried out as a *multi-dimensional* search process. The multi-dimensional parameter space is generally discretized into smaller cells leading to an approximation in the maximum likelihood parameter estimation. The approximation is readily allowed as an accurate estimate of parameters is not required during the acquisition process. Often, the parameter space is decomposed into a two-dimensional space of code phase and residual frequency offset by marginalizing the effect of other parameters such as residual phase offset and that of navigation data modulation. During the search process, the detector is supplied with an estimate of the parameters pertaining to a particular cell. The detector then carries out a likelihood test based on the Neyman-Pearson lemma to determine the presence of the signal using the supplied parameter estimate. The detection process is repeated for other cells with different parameter estimates until the correct cell, (H_1), is detected or the entire search space is spanned.

Since the focus of this thesis is squarely placed on the detection aspect of the GPS signal acquisition, the estimation part is not considered in its entirety. The readers are

referred to O' Driscoll [2007] for a more detailed treatment of the acquisition search process in the context of GPS signal acquisition. Nevertheless, it is worth mentioning here that, the mean acquisition time is influenced by the performance of the detector and also by the search strategy.

3.3   Optimal Detection – Known Signal Parameters

The derivations for optimal detection structures developed in the subsequent sections essentially follow the approach reported in Kay [1993a]. However, the detector analysis presented here is carried out in the context of GPS signal acquisition.

3.3.1   The Matched Filter Detector

The structure of an optimal detector is developed by considering the detection of the known PRN signal under AWGN. As mentioned above, it is assumed that detector is positioned at the correct cell or the H_1 cell to allow for a binary hypothesis testing. Accordingly, the derivation of decision statistics and the corresponding detecting performance analysis is carried out with the perfect estimate of the parameter vector (i.e. $\hat{\theta} = \theta$). In the presence of a perfect estimate of the transmitted parameter vector (θ), the detection problem in GPS signal acquisition reduces to a binary hypothesis testing. Thus, the detection problem can be expressed as below:

$$H_0 : x(k) = w(k), \ k = 0, 1, \ldots, N.$$
$$H_1 : x(k) = s(k) + w(k), \ k = 0, 1, \ldots, N. \tag{3.17}$$

where $s(k) = d(k - \tau)c(k - \tau)e^{j\phi(k)}$ and N_s is the number of samples received over the observation period T (i.e. $N = TT_s^{-1}$). $w(k)$ is the complex AWGN with variance σ_w^2. The Neyman-Pearson criterion discussed in Section 3.2, is utilized here and throughout the thesis to derive the optimal decision statistic. Since $x(k)$ is the composite signal (superposition of GPS signal from a number of satellites), we can approximate the PDF

of $x(k)$ using a Gaussian distribution. Therefore, the PDF of $x(k)$ for signal presence and its absence is given respectively by,

$$
\begin{aligned}
p\left(\mathbf{x}; H_0\right) &= \frac{1}{\left(2\pi\sigma_w^2\right)^{\frac{N_s}{2}}} e^{\left[-\frac{1}{2\sigma_w^2}\sum_{k=0}^{N_s-1}|x(k)|^2\right]} \\
p\left(\mathbf{x}; H_1\right) &= \frac{1}{\left(2\pi\sigma_w^2\right)^{\frac{N_s}{2}}} e^{\left[-\frac{1}{2\sigma_w^2}\sum_{k=0}^{N_s-1}|x(k)-s(k)|^2\right]}
\end{aligned}
\tag{3.18}
$$

Taking the likelihood ratio as given by (3.12), we get

$$
L(\mathbf{x}) = \frac{\frac{1}{\left(2\pi\sigma_w^2\right)^{\frac{N_s}{2}}} e^{\left[-\frac{1}{2\sigma_w^2}\sum_{k=0}^{N_s-1}|x(k)-s(k)|^2\right]}}{\frac{1}{\left(2\pi\sigma_w^2\right)^{\frac{N_s}{2}}} e^{\left[-\frac{1}{2\sigma_w^2}\sum_{k=0}^{N_s-1}|x(k)|^2\right]}} > \gamma'
\tag{3.19}
$$

The log likelihood ratio is then obtained by taking the logarithm of $L(\mathbf{x})$. It is emphasized here that the logarithm operation does effect the inequality as it is a monotonically increasing transformation. Therefore, we have

$$
l(\mathbf{x}) = \ln L(\mathbf{x}) = -\frac{1}{2\sigma_w^2}\left[\sum_{k=0}^{N_s-1}|x(k)-s(k)|^2 - \sum_{k=0}^{N_s-1}|x(k)|^2\right] > \ln \gamma'
\tag{3.20}
$$

The signal presence is declared, if

$$
\frac{1}{\sigma_w^2}\sum_{k=0}^{N-1}x(k)s^*(k) - \frac{1}{2\sigma_w^2}\sum_{k=0}^{N-1}|s(k)|^2 > \ln \gamma'
\tag{3.21}
$$

Since $s(k)$ is assumed to be completely deterministic (known carrier, code and data), it can be incorporated to the threshold. Upon further simplification, we have,

$$
T(\mathbf{x}) = \sum_{k=0}^{N-1}x(k)s^*(k) > \gamma
\tag{3.22}
$$

where, the threshold γ is given by,

$$
\gamma = \sigma_w^2\ln \gamma' + \frac{1}{2}\sum_{k=0}^{N-1}|s(k)|^2
\tag{3.23}
$$

The decision statistic expressed in (3.22) alongside the threshold γ constitutes the optimal detector based on the Neyman-Pearson theorem that maximizes the P_D for a given $P_{FA} = \alpha$. The optimal detector of (3.22) is often referred as *replica-correlator* as the received signal is correlated with a locally generated replica of itself.

One can also view the decision statistic in (3.22) as a filtering of the received signal with a finite impulse response (FIR) filter with impulse response $h(k)$. That is,

$$y(k) = \sum_{n=0}^{N-1} h(k-n)x(n), k \geq 0 \tag{3.24}$$

Letting the impulse response be the flipped version of the original signal (or PRN code), we have,

$$h(k) = s(N-1-k), k = 0, 1, \ldots, N-1. \tag{3.25}$$

Substituting the above equation in (3.24) and sampling the output at $k = N - 1$, we have

$$y(N-1) = \sum_{n=0}^{N-1} s(n)x(n) \tag{3.26}$$

The above expression is the same as the original test statistic expressed in (3.22) with the summation variable k being replaced by n. The FIR implementation of the NP detector is often called the *matched filter* since the impulse response of the FIR filter is matched to the signal. To further investigate the structure of optimal detector, we expand the decision statistics in (3.22) as,

$$T(\mathbf{x}) = \sum_{r=0}^{N_r-1} \sum_{k=0}^{N_r-1} x(k - rN_sN_c - \tau)\hat{d}(k - \hat{\tau})c(k)e^{-j\hat{\phi}(k)} \tag{3.27}$$

where $N = N_r N_c N_s$ is the sampled version of the received signal, and N_r is the number of code periods (i.e. $N_r = TT_r^{-1}$). In the above equation, we see that the data removal process is also accomplished through matched filtering. The structure of the developed detector is shown in Figure 3.2. An initial inspection of Figure 3.2 would readily reveal the use of the same matched filter structure as expressed in (3.22) for the demodulation of both PRN code and the navigation data. The received samples after carrier removal are initially supplied to the PRN code matched filter and are accumulated over its code period. The accumulated output is subsequently sampled every code period (i.e. $T_r = N_cT_c$) and is correlated with the estimate of data. The navigation data is also

sampled at $t = tT_r$ to yield $d(r)$. The correlation output is once again coherently accumulated over an arbitrary duration (i.e. $T = N_r T_r$) to form the final decision statistic. The decision statistic is then compared against a predefined threshold γ to decide between the signal presence (H_1) or its absence (H_0).
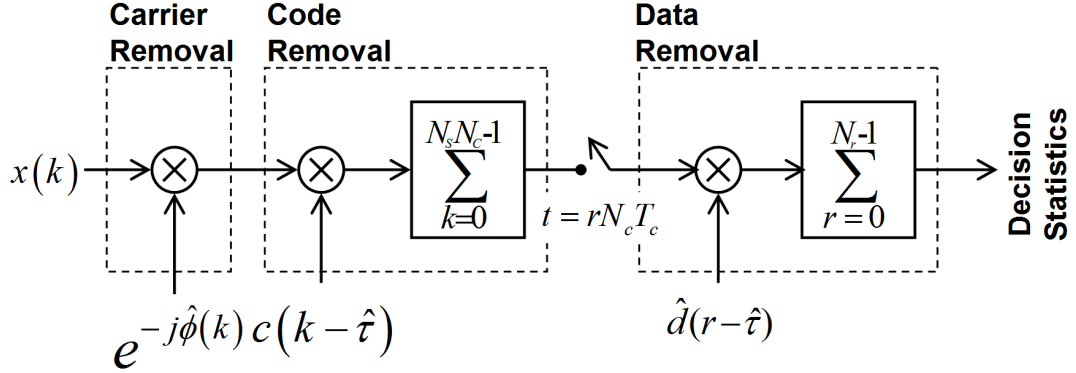
Figure 3.2: Maximum Likelihood Detection of GPS Signals

The matched filter implementation of the optimal detector readily allows for frequency domain interpretation. The output $y(k)$, is readily obtained by applying the inverse Fourier transform on the product of the Fourier transforms of $h(k)$ and $x(k)$. That is,

$$y(k) = \int_{-\frac{F_s}{2}}^{\frac{F_s}{2}} H(f)X(f)e^{j2\pi fkT_s}df \tag{3.28}$$

where $H(f)$, $X(f)$ are the discrete Fourier transforms and the integration limits are normalized to the sampling frequency. Utilizing the time-shift theorem[2], we can express $H(f)$ in terms of $S(f)$ as,

$$H(f) = S^*(f)e^{-j2\pi f(N_s - 1)} \tag{3.29}$$

where $*$ is the complex conjugate operation. On substitution in (3.28) and sampling the output at, $k = N_s - 1$, produces

$$y(N_s - 1) = \int_{-\frac{F_s}{2}}^{\frac{F_s}{2}} S^*(f)X(f)df \tag{3.30}$$

---

[2] $\mathscr{F}\{x(k+\tau)\} = X(f)e^{j2\pi f\tau}$, $\mathscr{F}$ denotes the discrete Fourier transform

Thus, the frequency domain implementation of a matched filter essentially weights the bands where there is more signal power.

3.3.2 Residual Signal Effects

In the previous section, the detection performance analysis was based on the assumption that the detector was supplied with the perfect estimate of the transmitted parameter vector, $\theta = [\tau, \phi(k), d(k)]$. However, in reality, the detector is only supplied with an estimate $\hat{\theta}$. Moreover, the extent of *a priori* knowledge of θ critically depends on the type of receiver technology. In stand-alone HS GPS technology, the receivers have very limited *a priori* information such as visible PRNs. Hence, a GPS receiver typically attempts to estimate some of the parameters while suppressing the influence of other parameters during acquisition. On the other hand, in AGPS technology, the GPS receiver is supplied with navigation data along with good timing estimate and Doppler estimate (Bryant [2005]). Nevertheless, the GPS receivers, regardless of the receiver technology, are still required to estimate the code phase and residual frequency offset. Generally, the code phase and the residual frequency offset estimates are obtained by traversing through a discretized two-dimensional space as shown in Figure 3.1. Depending on the search step (or resolution), the search process incurs an error in the code and carrier offset estimates (i.e. $\theta_{err} = |\theta - \hat{\theta}|$). Thus, it is necessary to analyze the effect of these residual errors on the performance of matched filter detector.

To investigate the effect of these residual errors (or residual signals), it would be highly desirable to characterize the signal at the output of the matched filter. The matched filter detector output for a particular code and carrier offset $\hat{\theta} = [\hat{\tau}, \hat{\phi}(k), \hat{d}(k)]$ is given by,

$$\Psi_{MF}(\hat{\theta}) = \frac{1}{N_r} \sum_{r=0}^{N_r-1} \left[\frac{\sqrt{C}}{\sqrt{2}N_s N_c} \sum_{k=rN_s N_c}^{(r+1)N_s N_c - 1} \left(d_{\tau_{err}}(k)c_{\tau_{err}}(k)e^{j\phi_{err}k} + w(k)c(k-\hat{\tau})e^{-j\hat{\phi}(k)} \right) \right]$$

$$(3.31)$$

where $c_{\tau_{err}}(k) = c(k-\tau)c(k-\hat{\tau})$, $d_{\tau_{err}}(k) = d(k-\tau)\hat{d}(k-\hat{\tau})$, and $\phi_{err}(k) = \phi(k) - \hat{\phi}(k)$.

The inner summation in (3.31) is conveniently rewritten as,

$$y(r) = \sqrt{\frac{C}{2}} \frac{1}{N_s N_c} \sum_{k=rN_sN_c}^{(r+1)N_sN_c-1} \left(d_{\tau_{err}}(k)c_{\tau_{err}}(k)e^{j\phi_{err}k} + w(k)c(k-\hat{\tau})e^{j\hat{\phi}(k)} \right) \tag{3.32}$$

The output $y(r)$, is the code matched filter output that is sampled every $t = rN_cT_c$ seconds and is given by,

$$y(r) \approx \sqrt{\frac{C}{2}} d_{\tau_{err}}(r) R(\tau_{err})\psi_{\Delta F_{err}}(r) + w(r) \tag{3.33}$$

where $d_{\tau_{err}}(r)$ is the integrated output of $d_{\tau_{err}}(k)$ over one code period and is given by,

$$d_{\tau_{err}}(r) = \sum_{k=rN_sN_c}^{(r+1)N_sN_c-1} d(k-\tau)\hat{d}(k-\hat{\tau}) \tag{3.34}$$

Similarly, $R_{\tau_{err}}$ is the auto-correlation function (that is often called the time ambiguity function) of the C/A code. The auto-correlation function can be expressed as,

$$R_{\tau_{err}}(r) = \sum_{k=0}^{N_sN_c-1} c(k-\tau)c(k-\hat{\tau}) \tag{3.35}$$

$\psi_{\Delta F_{err}}(r)$ is the frequency ambiguity function and is expressed as,

$$\psi_{\Delta F_{err}}(r) = \frac{1}{N_s N_c} \sum_{k=rN_sN_c}^{(r+1)N_sN_c-1} e^{j\left(\phi(kT_s)-\hat{\phi}(kT_s)\right)} \tag{3.36}$$

In the above equation, the sample index k is replaced by kT_s to reflect the fact that the phase input to the accumulator is being sampled at $t = kT_s$. Utilizing the summation identity[3], we have,

$$\sum_{k=rN_sN_c}^{(r+1)N_sN_c-1} e^{j\phi_0} \left(e^{j(2\pi\Delta F_{err}T_s)} \right)^k = e^{j(2\pi\Delta F_{err}rN_cN_sT_s+\phi_0)} \left[\frac{1 - e^{j2\pi\Delta F_{err}N_sN_sT_s}}{1 - e^{j2\pi\Delta F_{err}T_s}} \right] \tag{3.37}$$

Utilizing the trigonometric identity[4] and upon further simplification, we can express the second term on the right hand side of (3.37) as,

$$\left[\frac{1 - e^{j2\pi\Delta F_{err}N_cN_sT_s}}{1 - e^{j2\pi\Delta F_{err}T_s}} \right] \approx e^{j\pi\Delta F_{err}T_s(N_sN_c-1)} \frac{sin(\pi\Delta F_{err}N_cN_sT_s)}{\pi\Delta F_{err}T_s} \tag{3.38}$$

---

[3] $\sum_{k=r}^{N_r-1} e^k = (e^r - e^{N_r})/(1-e)$
[4] $sin(\theta) = \frac{e^{j\theta} - e^{-j\theta}}{2j}$

Substituting (3.37) and (3.38) in (3.36) produces

$$\psi_{\Delta F_{err}}(r) = \frac{1}{N_s N_c} \frac{sin(\pi \Delta F_{err} N_c N_s T_s)}{\pi \Delta F_{err} T_s} e^{j\left(2\pi \Delta F_{err}\left[rN_s N_c + \frac{N_s N_c - 1}{2}\right]T_s + \phi_0\right)} \tag{3.39}$$

The frequency ambiguity function can be compactly expressed utilizing the sinc-function[5] as,

$$\psi_{\Delta F_{err}}(r) = sinc(\pi \Delta F_{err} N_c N_s T_s) e^{j\left(2\pi \Delta F_{err}\left[rN_s N_c + \frac{N_s N_c - 1}{2}\right]T_s + \phi_0\right)} \tag{3.40}$$

Finally, the noise term $w(n)$ is given by,

$$w(r) = \frac{1}{N_s N_c} \sum_{k=rN_s N_c}^{(r+1)N_s N_c} w(k)c(k - \hat{\tau})e^{j\left(2\pi \Delta \hat{F} k T_s + \phi_0\right)} \tag{3.41}$$

The final detection output is obtained by coherently accumulating $y(n)$ and is given by,

$$\Psi_{MF}(\hat{\theta}) \approx \sqrt{\frac{C}{2}} \frac{1}{N_r} \sum_{r=0}^{N_r - 1} d_{\tau_{err}}(r) R_{\tau_{err}}(r) \psi_{\Delta F_{err}}(r) + w(r) \tag{3.42}$$

From the above equation, one can readily relate the influence of navigation data, code and carrier on the matched filter output. Accordingly, any residual errors in these components readily manifests into an SNR loss as the locally generated components are no longer matched with the received signal. The following sections briefly analyze the resultant of these signal effects on the matched filter output.

Navigation Data Modulation

Ignoring the effects of residual carrier and that of background noise, the matched filter output is,

$$\Psi_{MF}(\hat{\theta}) = \frac{1}{N_r} \sum_{r=0}^{N_r - 1} \sum_{k=rN_c N_c}^{(r+1)N_r - 1} d(k - \tau)\hat{d}(k - \hat{\tau}) \tag{3.43}$$

For AGPS receivers, the navigation data is known *a priori* (i.e. $\hat{d}(k) = d(k)$) at the receiver end. However, the latency in the communication link introduces an error in the order of few micro-seconds to several hundred micro-seconds Syrjarinne [2001]. Correspondingly, the SNR loss due to this timing error can be readily ignored. On

---

[5]$sinc(x) = sin(x)/x$

the other hand, for stand-alone GPS receivers, the navigation data is unknown and the corresponding matched filter output can be obtained by substituting $\hat{d}(k) = 1$ in (3.43). The presence of this unknown navigation data introduces random phase rotations (i.e. $[0, \pi]$) that manifest into a finite spectral dispersion of around T_b^{-1} Hz. Recognizing the coherent accumulation as a low pass filtering, the minimum cut-off frequency of such a filter should be greater than T_b^{-1} Hz. Hence, the maximum coherent integration time cannot exceed T_b seconds in the presence of unknown data modulation. Unfortunately, the maximum coherent integration time is further limited due to the lack of bit synchronization. The effect of data modulation appears as an attenuation of the correlation power. The correlation power loss can then be given by (O' Driscoll [2007]),

$$L_D(\tau) = \left| 1 - \frac{2\tau}{N_r N_c} \right|^2, \ \tau = 0, 1, \ldots, N_r N_c. \tag{3.44}$$

Thus, the data modulation exerts its maximum effect when the transition occurs in the middle of coherent integration (i.e $\tau = 0.5NN_c$). However, one has to take into account the probability of data transition occurring within coherent integration. Hence, the average mean attenuation due to data modulation can be expressed as (Davisson and Flikkemama [1988]),

$$L_D(N_r) \approx \begin{cases} \left| 1 - \frac{N_r}{3N_D} \right|^2 & N_r < N_D \\ \left| \frac{N_D}{N_r} \left(1 - \frac{D}{3N_r} \right) \right|^2 & N_r \geq N_D \end{cases} \tag{3.45}$$

where $N_D = T_b T_r^{-1}$ and $N_r = TT_r^{-1}$. There exists a trade-off between the loss due to data modulation and gain due to noise suppression in terms of coherent integration time. Typically, the maximum coherent integration is limited to within 10 ms (i.e. N $\leq (0.5N_D - 1)$) in the presence of unknown data modulation.

Residual Carrier

The residual carrier affects the matched filter in terms of residual phase offset (ϕ_0), frequency error (ΔF) and its drift (ϖ). In the absence of residual frequency error and

its drift, we can express the matched filter output in the absence of noise, navigation data and code phase error as,

$$\Psi_{MF}(\hat{\theta}) = N_r N_c \sqrt{\frac{C}{2}} e^{j\phi_0} \tag{3.46}$$

From (3.46), it is observed that the matched filter detector output is no longer real due to the presence of residual phase offset. Moreover, the correlation power is distributed between inphase and quadrature channels depending on ϕ_0. On the other hand, in the presence of constant residual frequency error, the matched filter output is given by,

$$\Psi_{MF}(\hat{\theta}) = \frac{1}{N_r} \sum_{r=0}^{N_r-1} \sqrt{\frac{C}{2}} sinc(\pi \Delta F_{err} T_r) e^{j\left(2\pi \Delta F_{err}\left[rN_c + \frac{N_c-1}{2}\right]T_c + \phi_0\right)} \tag{3.47}$$

From (3.47), it is apparent that the detection output still undergoes phase rotation due to the residual frequency error. The effective power attenuation introduced by the constant residual frequency error is plotted in Figure 3.3. The plot also shows the effect of different coherent integration time (i.e. $T_{COH} = N_r T_r$). From figure 3.3, the
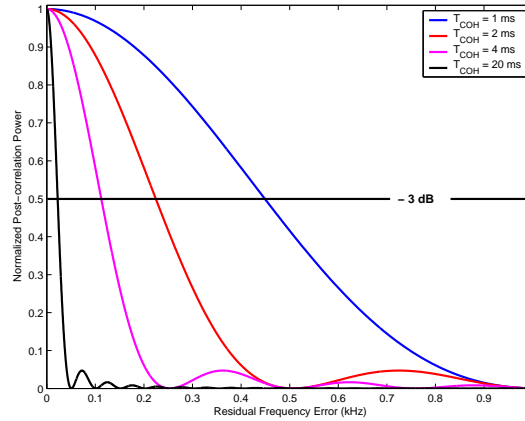
Figure 3.3: Correlation Power Loss as a Function of Constant Residual Frequency Error

sensitivity to frequency error increases drastically with a relative increase in coherent integration time. For instance, to ensure that power attenuation is less than 3 dB, the frequency error should be constrained by,

$$\Delta F_{err} \leq \frac{0.44}{T_{COH}} \tag{3.48}$$

The frequency search bin size, ΔF, is typically related to the aforementioned residual frequency error as $\Delta F = 2\Delta F_{err}$. Thus, increasing coherent integration time necessitates a more stringent frequency estimation during acquisition. Based on (3.48), the number of frequency search bins is given by,

$$N_F = \left\lfloor \frac{2F_D}{\Delta f} \right\rfloor \tag{3.49}$$

where Δf is the frequency search bin size and F_D is the frequency search range (i.e. $F_D = \pm 10$ kHz). $\lfloor a \rfloor$ rounds a towards positive infinity. As mentioned earlier, the frequency search bin size is primarily influenced by the coherent integration period. For example, an increase in coherent integration time from nominal 1 ms to 10 ms reduces the frequency search bin size from 880 Hz down to 88 Hz and thereby resulting in a ten fold increase in frequency search bins. Under frequency drift conditions, the matched filter output is given by,

$$\Psi_{MF}(\hat{\theta}) = \frac{1}{N_r} \sum_{r=0}^{N_r-1} \sqrt{\frac{C}{2}} sinc(\pi \Delta F_{err}(r) T_r) e^{j\left(2\pi \Delta F_{err}(r)\left[rN_c + \frac{N_c-1}{2}\right]T_c + \phi_0\right)} \tag{3.50}$$

The presence of frequency drift (ϖ) introduces a linear variation in the residual frequency error. That is,

$$\Delta F_{err}(r) = \Delta F_{err}(r-1) + \varpi T_r \tag{3.51}$$

The constant frequency drift introduces a linear (or uniform) variation in the residual frequency offset. Thus, the net effect of frequency drift can be approximated by taking the mean of the correlation power (i.e. $sinc^2(\bullet)$). The effective correlation power loss depends not only on the frequency drift but is equally influenced by the maximum coherent integration period and the total observation period as well. Moreover, the type of detection (coherent or noncoherent) also influences the net effect of constant frequency drift during acquisition.

Residual Code Phase Error

There exists a trade-off between the correlation power loss and code search space. Typically, code phase is incremented in steps of $\Delta\tau = 0.5T_c$, which results in a worst case correlation power loss of approximately 3 dB. Note that the worst case correlation suppression for the C/A code is approximately 21.6 dB, which still provides a comfortable margin of around 18 dB in terms of correlation suppression. Finally, the presence of residual frequency error will also manifest in residual code phase error. The time varying code phase error is given by,

$$\tau_{err}(k) = \tau_0 - \frac{\Delta F_{err}(k)}{F_{L1}} \tag{3.52}$$

where $\Delta F_{err}(k)$ is the net residual frequency error that includes the effect of frequency drift. For example, a residual frequency error of 500 Hz would translate into a code Doppler of 0.32 chips/second. The residual frequency error during acquisition is readily influenced by the search bin size and the maximum coherent integration period.

3.3.3 Limitations of Matched Filter Detector

Even though the matched filter implementation achieves optimal detection performance, it can still be limited by a number of factors. The relevant factors limiting the detection performance of a matched filter detector are briefly summarized below:

1. The detection output (or SNR) of a matched filter incurs degradation in the presence of residual signal effects. However, there exists a trade-off between choosing higher search resolution in code phase/frequency offset and the computational complexity. The search step in code phase (δt) and frequency offset (δF) is set typically as follows:

$$\delta t \leq 0.5T_c$$
$$\delta f \leq \frac{2}{3T_{COH}} \tag{3.53}$$

2. High acquisition sensitivity mandates significant processing gain, which is accomplished by increasing the coherent integration period. However, increasing the coherent integration period concentrates the signal energy into finer frequency bins and thereby necessitates finer frequency resolution. The number of cells needed to be searched can be related to the coherent integration as,

$$N_{cells} \approx \left(N_c \frac{T_c}{\delta t} \right) \left(\frac{2F_D}{\delta F} \right) = (2N_c) \left(3F_D T_{COH} \right) \tag{3.54}$$

3. The navigation data modulation limits the maximum coherent integration time down to 10 ms in the absence of bit synchronization. Furthermore, the gain in the SNR through extended coherent integration time comes at the expense of significant computational complexity due to the increased search space.

4. Finally, the matched filter implementation is only optimal in the presence of Gaussian noise and its performance degrades substantially if the noise is non-Gaussian as in the case of narrow band interference.

3.4   Optimal Detection – Unknown Signal Parameters

In the previous section, the GLRT was shown to be equivalent to a *matched filter* under completely known deterministic signal condition. The matched filter detected the presence of the PRN code signal through the change in mean statistics under the Gaussian assumption. Nevertheless, it is critically influenced by the presence of unknown signal parameters such as residual carrier and navigation data modulation. Hence, the matched filter detector mandates the estimation of these unknown parameters to incur minimal SNR loss. As stated earlier, AGPS receivers overcome this limitation through external aiding. On the other hand, non-AGPS receivers are readily limited by the presence of unknown navigation data and residual frequency errors. Even AGPS receivers can be limited by residual carrier due to the receiver clock offset. Hence, the presence of

unknown navigation data and residual carrier can be more aptly modelled as unknown even in the presence of known PRN code signal. Accordingly, the optimum detector based on Neyman-Pearson lemma for a deterministic PRN code signal with unknown signal parameters can be obtained using the GLRT as expressed in (3.12).

To derive the GLRT under an unknown signal model, we consider a general detection problem,

$$
\begin{aligned}
H_0 &: x(k) = w(k) && k = 0, 1, ..., N-1. \\
H_1 &: x(k) = s(k) + w(n) && k = 0, 1, ..., N-1.
\end{aligned}
\tag{3.55}
$$

where $s(k)$ is deterministic and completely unknown and $w(k)$ is a complex AWGN with variance σ^2. A GLRT would decide on signal presence (or H_1), if

$$
L(\mathbf{x}) = \frac{p\left(\mathbf{x}; \hat{s}(0), ..., \hat{s}(N-1), H_1\right)}{p\left(\mathbf{x}; H_0\right)} > \gamma
\tag{3.56}
$$

where $\hat{s}(n)$ is the MLE of $s(n)$ under H_1. To determine the MLE, we maximize the likelihood function

$$
p\left(\mathbf{x}; s(0), ..., s(N-1), H_1\right) = \frac{1}{\left(2\pi\sigma^2\right)^{N/2}} e^{\left[-\frac{1}{2\sigma^2}\sum_{k=0}^{N-1}|x(k)-s(k)|^2\right]}
\tag{3.57}
$$

over the signal samples. Under a completely unknown signal, we have the MLE as $\hat{s}(n) = x(n)$ (Kay [1993b]). Thus, from (3.56)

$$
\frac{\frac{1}{(2\pi\sigma^2)^{N/2}}}{\frac{1}{(2\pi\sigma^2)^{N/2}}\left(-\frac{1}{2\sigma^2}\sum_{k=0}^{N-1}|x(k)|^2\right)}
\tag{3.58}
$$

Taking logarithms produces

$$
\frac{1}{2\sigma^2}\sum_{k=0}^{N-1}|x(k)|^2 > ln\ \gamma
\tag{3.59}
$$

Thus, the sufficient test statistic is,

$$
T(\mathbf{x}) = \sum_{k=0}^{N-1}|x(k)|^2 = \sum_{k=0}^{N-1}x(k)\hat{s}^*(k) > \ln\gamma, \ \ \hat{s}(n) = x(n)
\tag{3.60}
$$

The above expression is similar to that of an *energy detector*, which can also be obtained by modelling the signal as a white Gaussian random process (Kay [1993a]).

Figure 3.4 shows the structure of the GLRT for deterministic and completely unknown signal. Interestingly, it also follows the estimator-correlator form although its detection performance will differ from the well-known *estimator-correlator* (Kay [1993a]).
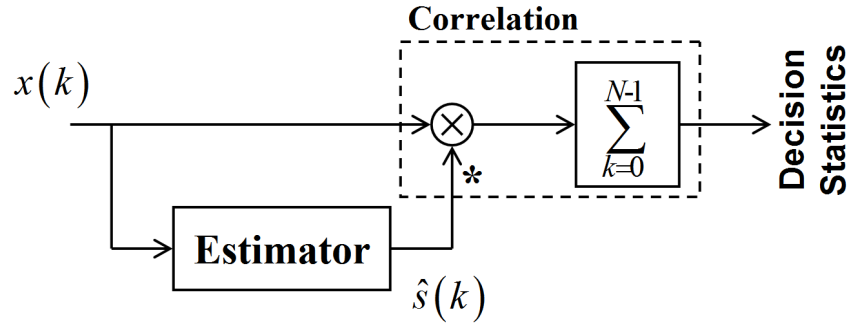
Figure 3.4: GLRT Structure for Deterministic and Completely Unknown Signal

The expression in (3.60) is fundamental to the development of various detection algorithms that are currently utilized in GPS signal acquisition. The GLRT structure shown in Figure 3.4 can be applied prior to or after the matched filtering based on the *a priori* information. In the subsequent sections, we will establish the following widely considered detection schemes as specialized forms of the GLRT structure as defined by (3.60):

1. Incoherent Matched Filter Detector

2. Post-correlation Non-coherent Detector

3. Post-correlation Differential Detector

4. Pre-correlation Differential Detector

More importantly, the unification of these various detectors using a common framework aids in a deeper understanding of these schemes. For instance, in Section 3.5, we introduce an asymptotic version of the GLRT that is shown to be equivalent to the *estimator-correlator*. The developed asymptotic structure is attractive in terms of

enhanced noise suppression and robust fine frequency estimation (Shanmugam et al. [2007b]).

3.4.1 Incoherent Matched Filter

The matched filter detector introduced in Section 3.3.1 can be considered optimal under the deterministic known signal model. The perfectly known signal assumption is merely the case in theory. Hence, it is more reasonable to assume some aspect of the signal model to be unknown or random. To start with, let us consider the received signal with unknown initial phase. That is,

$$
\begin{aligned}
H_0 &: x(k) = w(k) & k = 0, 1, ..., N - 1. \\
H_1 &: x(k) = s(k)e^{j\phi_0} + w(k) & k = 0, 1, ..., N - 1.
\end{aligned}
\tag{3.61}
$$

where ϕ_0 is the unknown initial phase and is uniformly distributed over $[0, 2\pi)$ and is independent of $s(k)$. While the PDF of H_0 is unchanged, the PDF under H_1 is now explicitly parametrized by ϕ_0. The unknown phase can be averaged out from the GLRT, resulting in an *energy detector* (Kay [1993a]). In the presence of perfect code and carrier estimate besides the unknown initial code phase, the corresponding test statistics based on GLRT can be derived as,

$$
T(\mathbf{x}) = \left| \frac{1}{N} \sum_{k=0}^{N-1} x(k)e^{-j2\pi\Delta\hat{F}k}c(k - \hat{\tau})\hat{d}(k - \hat{\tau}) \right|^2, \ N = TT_s^{-1} = N_r N_c N_s.
\tag{3.62}
$$

The above test statistic is often referred to as the *incoherent matched filter*, since the inphase and quadrature matched filter outputs are combined incoherently. The GLRT structure for the received signal with unknown initial phase is shown in Figure 3.5. Interestingly, the above GLRT structure can be derived using the *estimator-correlator* formulations (Refer Chapter 5 in Kay [1993a]) and the structure shown in Figure 3.5 is also referred to as the *periodogram detector*. For example, let us consider the code and data is known perfectly and is removed prior to the residual carrier. Then, (3.62) can

be further reduce to,

$$T(\mathbf{x}) = \left| \frac{1}{N} \sum_{k=0}^{N-1} x(k) e^{-j2\pi\Delta\hat{F}k} \right|^2 \qquad (3.63)$$

From the above equation, we see that the $T(\mathbf{x})$ is obtained by initially computing the Fourier transform, which is followed by a magnitude square operation. The aforementioned structure can also be viewed as a PSD estimator (Kay [1993b]), since the power will be concentrated at a known frequency (i.e. ΔF) in case of the signal being present.
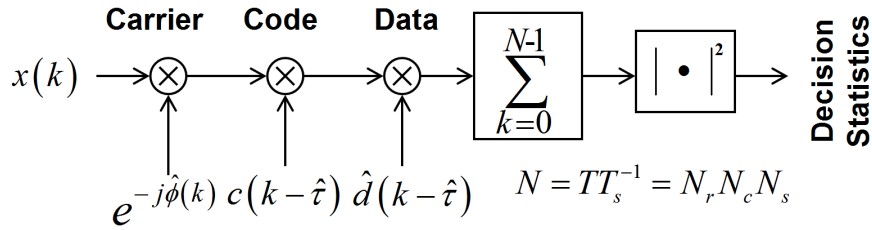
Figure 3.5: Incoherent Matched Filter Detector Implementation

The ICMF detector only suppresses the unknown phase rotation and can still be influenced by residual code phase, carrier phase, and navigation data modulation. For example, the influence of residual frequency error on ICMF output can readily be deduced from (3.42) as,

$$\Psi_{ICMF} = CNR^2_{\tau_{err}} sinc^2 \left(\pi \Delta F_{err} T \right) \qquad (3.64)$$

Ignoring the effects of residual carrier, an approximation for the influence of navigation data modulation can be obtained as (Davisson and Flikkemama [1988]; O' Driscoll [2007]),

$$L_D \approx \begin{cases} \left| 1 - \frac{N_r}{3N_D} \right|^2 & N_r < N_D \\ \frac{N_D}{N_r} \left(1 - \frac{N_D}{3N_r} \right) & N_r \geq N_D \end{cases} \qquad (3.65)$$

where $N_r = TT^{-1}_{COH}$ and $N_D = T_b(N_c T_c)^{-1}$. In contrast to CMF, the ICMF involves the noise terms from both inphase and quadrature channels. Compared to the CMF in (3.22), the ICMF requires higher SNR to accomplish the same detection performance.

This extra SNR, known as the detector loss, is the price paid for not knowing the signal phase.

3.4.2 Post-correlation Noncoherent Detector

The performance of a matched filter as well as the incoherent matched filter detector can be severely degraded in the presence of unknown phase variations. The unknown phase variations introduced by the navigation data modulation and residual carrier can be averaged out from the GLRT, resulting in an *energy detector*. Interestingly, the squared magnitude operation in (3.60) eliminates the phase information and the corresponding magnitude sampled are combined to implement the well-known *non-coherent integration*. The post-correlation non-coherent detector (PCND) is a hybrid detection, wherein both coherent matched filtering and the energy detection are applied. The corresponding test statistic can be derived as (Kaplan and Hegarty [2006]),

$$T(\mathbf{x}) = \frac{1}{N_r} \sum_{r=0}^{N_r-1} |y(r)|^2 \tag{3.66}$$

where $y(r)$ is the coherent matched filter output with an coherent integration period of T_{COH} (i.e. $T_{COH} = N_c T_c$) as expressed in (3.32). Figure 3.6 shows the GLRT structure of the PCND scheme.
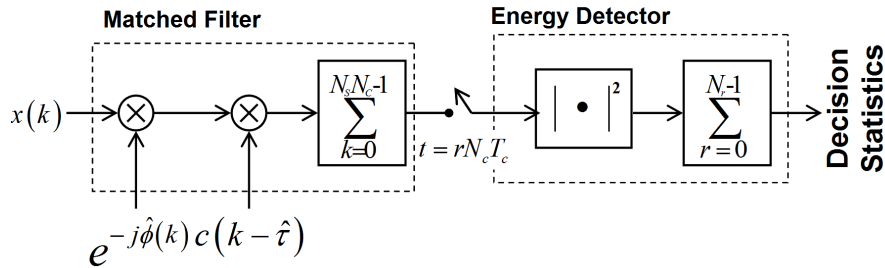
Figure 3.6: Post-correlation Noncoherent Detector Implementation

The influence of residual carrier on PCND is similar to that of ICMF and can be derived as,

$$\Psi_{PCND}(\hat{\theta}) = CNR_{\tau_{err}}^2 sinc^2 \left(\pi \Delta F_{err} T_{COH} \right) \tag{3.67}$$

Comparing (3.66) with that of (3.64) readily shows the robustness of the PCND over the ICMF detector in the presence of residual frequency error. In other words, using PCND, we can extend the total observation interval, without reducing the size of frequency search bins. However, the presence of residual frequency drift can still affect the PCND detection output. O' Driscoll [2007] derived the influence of the navigation data modulation on the PCND structure as,

$$L_D \approx 1 - \frac{N_r}{N_D} \left[\frac{cot \frac{\pi \Delta F_{err} T_{COH}}{2}}{\frac{\pi \Delta F_{err} T_{COH}}{2}} - cot^2 \frac{\pi \Delta F_{err} T_{COH}}{2} \right] \tag{3.68}$$

In contrast to CMF and the ICMF detector, the PCND incoherently combines the initial coherently detected samples. A coherent combination reduces the noise more rapidly then noncoherent combination. Accordingly, the PCND requires more SNR to accomplish a similar detection performance as that of the CMF and the ICMF detectors. The noncoherent accumulation can be increased to compensate for this SNR loss (i.e. *squaring loss*). Finally, the PCND implementation can be effectively applied when there are significant mismatches in signal phase due to residual frequency error and unknown navigation data modulation (Kaplan and Hegarty [2006]).

3.4.3 Post-correlation Differential Detector

The post-correlation differential detector (PCDD) utilizes the phase relationship to suppress the residual phase variations. Owing to the periodicity of the underlying GPS PRN code signal we have,

$$
\begin{aligned}
H_0 &: y(r) \neq y(r - N_c T_c) \quad r = 0, 1, ..., N_r - 1. \\
H_1 &: y(r) \approx y(r - N_c T_c) \quad r = 0, 1, ..., N_r - 1.
\end{aligned}
\tag{3.69}
$$

where $y(r)$ is the coherent correlation output (i.e. $T_{COH} = N_c T_c$). The PCND introduced in the previous section utilized the instantaneous samples for its MLE estimation (i.e. $\hat{s}(r) = y(r)$). In PCDD, the delayed version of the coherently detected samples is

utilized during estimation process. That is,

$$T(\mathbf{x}) = \frac{1}{N_r} \sum_{r=0}^{N_r-1} y(r)y^*(r - N_cT_c) \tag{3.70}$$

Hence, the receiver based on (3.70) correlates the received signal with a noisy and delayed estimate of the received signal. Note that the estimate, $\hat{s}(r) = y(r - N_cT_c)$, is no longer the maximum likelihood estimate of $s(r)$ in the presence of navigation data and residual carrier. Interestingly, it can also be viewed as a form of *differential phase detection*, wherein the current phase estimate is derived from the previous coherent integration output. Differential detection is attractive as the detection output is obtained from the product of independent but identically distributed variables. In a noncoherent detector, the detection output is obtained by squaring the same variable. Figure 3.7 shows the block diagram of the post-correlation differential detector.
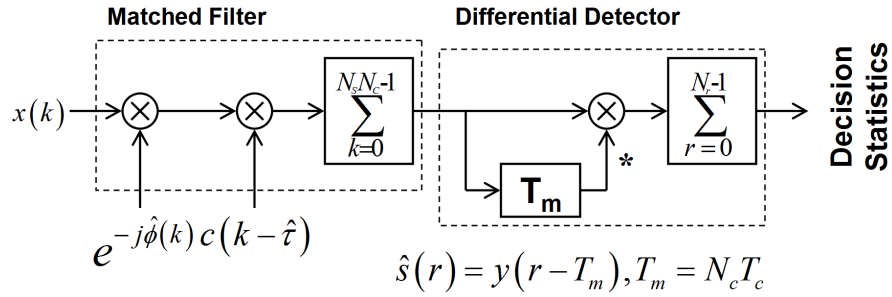
Figure 3.7: Post-correlation Differential Detector Implementation

The test statistic $T(\mathbf{x})$ as expressed in (3.70) is still complex and requires the incoherent combination of inphase and quadrature of components. The impact of residual frequency errors and that of data modulation can be determined by analyzing the detection output in the absence of noise. That is,

$$\Psi_{PCDD}(\hat{\theta}) = CR_{\tau_{err}}^2 sinc^2(\pi\Delta F_{err}N_cT_c) \left| \sum_{r=0}^{N_r-1} d(r)d(r - N_cT_c) \right|^2 \tag{3.71}$$

The differential detection incurs a finite power loss due to the decorrelation of $d(r)$ over N_cT_c seconds. More importantly, we can notice the decorrelation of navigation data

in the above expression over $N_c T_c$ seconds. For instance, Schmid and Neubauer [2004] reported that the power loss due to the navigation data decorrelation for a delay of $N_c T_c$ seconds is approximately 0.45 dB. The power loss due to this navigation data decorrelation over an arbitrary delay T_m (i.e. $T_m = m N_c T_c$, $m = 1, 2, ..$) is given by,

$$L_D(T_m) = E\left[\left(\sum_{r=0}^{N_r-1} d(r)d(r - T_m)\right)^2\right] \tag{3.72}$$

The above expression can be further approximated using the fact that $d(r)$ is highly correlated for $T_m < T_b$. Therefore, we have for $N_r \to \infty$,

$$L_D(T_m) = E\left[\left(\sum_{r=0}^{N_r-1} d(r)d(r - T_m)\right)\right]^2 + Var\left[\left(\sum_{r=0}^{N_r-1} d(r)d(r - T_m)\right)\right] \tag{3.73}$$
$$\approx E\left[\left(\sum_{r=0}^{N_r-1} d(r)d(r - T_m)\right)\right]^2$$

The above approximation was obtained by ignoring the variance term. This approximation holds good as the navigation data modulation is correlated within the navigation data bit duration. That is,

$$Var\left[\left(\sum_{r=0}^{N_r-1} d(r)d(r - T_m)\right)\right] \approx 0, \; T_m < T_b \tag{3.74}$$

Assuming equiprobable data symbols and letting $T_m < T_b$, for $N_r \to \infty$, the loss due to the navigation data modulation based on rectangular pulse shape assumption of navigation data is given by,

$$L_D(T_m) \approx E\left(\sum_{r=0}^{N_r-1} d(r)d(r - T_m)\right)^2 \tag{3.75}$$
$$= \left|1 - \frac{T_m}{T_b}\right|^2, \; T_m < T_b, \; T_m = m N_c T_c, m = 1, 2, ...,$$

Figure 3.8 depicts the effect of navigation modulation as a function of differential delay m. From the figure, it can readily be understood that the loss due to navigation data modulation is significant for large values of m. Hence, the value of m is kept minimal (i.e. $m = N_c T_c$ seconds), not only to minimize the power loss due to data modulation but also to minimize the effect of residual frequency errors. Figure 3.8 shows the theoretical loss due to the navigation data modulation (Black Square) from
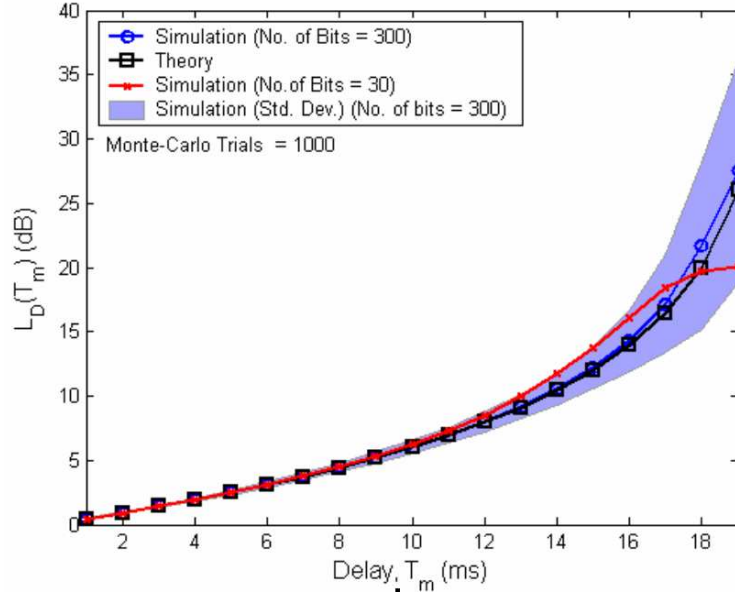
Figure 3.8: Effect of Data Modulation on Post-correlation Differential Detection

(3.75) and the numerical simulation results for 30 (Red Cross) and 300 (Blue Circle) navigation data bits. In Figure 3.8, we see that for $N_r = 600$ (30 navigation data bits), the theoretical and numerical computed loss increasingly differs for T_m ¿ 12 ms. However, the approximation in (3.75) is well validated up to $T_m = 19$ ms in the case of $N_r = 6000$ (300 bits). The results shown in Figure 3.8 utilized the asymptotic assumption to characterize the average loss due to navigation modulation. However, the actual loss due to navigation data modulation for a given observation period can differ substantially as shown by the standard deviation for large T_m. Figure 3.8 readily shows the inherent limitation of the differential detection approach in the presence of navigation data modulation. For example, the detection performance of PCDD is expected to degrade significantly with increased coherent integration. This does not come as a surprise as the underlying assumption of phase correlation in PCDD no longer holds true for $T_m \geq T_b$ due to the random phase transition introduced by navigation data. A tighter bound on the effect of navigation data modulation on the PCDD scheme can be found in O' Driscoll [2007].

Fine Frequency Estimation

For a constant frequency offset, we can express the phase at the output of differential detection as,

$$\psi(r)\psi^*(r-1) = sinc^2(\pi\Delta F_{err}T_r)e^{j2\pi\Delta F_{err}N_cT_c} \qquad (3.76)$$

The exponential term in (3.76) essentially reflects the phase difference over the interval $T_m = N_cT_c$. One can readily notice that the above differential operation on residual carrier is similar to that of a frequency discriminator. Thus, one can estimate the residual frequency error by utilizing the angle information. That is,

$$\Delta\hat{F}_{err} = \frac{\angle\left(\sum_{r=0}^{N_r-1}\psi(n)\psi^*(r-1)\right)}{2\pi N_cT_c} \qquad (3.77)$$

Elders-Boll and Dettmar [2004] utilized the above approach to aid in fine frequency estimation and later Schmid and Neubauer [2005] developed an adaptive phase correction loop using the above fine frequency estimation. It should be noted here that the estimation performance of the corresponding frequency estimation technique would be critically effected by the C/N$_0$, the observation period and the differential delay (due to the presence of navigation data). On the other hand, one can utilize a longer observation period to minimize the effect of noise so as to obtain a better estimate of residual frequency error (Schmid and Neubauer [2005]) for lower C/N$_0$ conditions.

3.4.4 Pre-correlation Differential Detector

The major limitation with post-correlation noncoherent and differential detector stems from the residual frequency offset. These differential detection schemes estimate both code phase and frequency offset through two-dimensional search that necessitates a certain computational complexity. Interestingly, the search space and hence the computational complexity can be significantly reduced by eliminating either the code or residual carrier from the received signal. For example, the GLRT structure in (3.70)

can be applied at the chip-level to estimate both the navigation data and the residual carrier. The choice of delay critically affects the subsequent implementation of this pre-correlation differential detector (PDD). For example, letting the delay T_m be less than T_c effectively removes the PRN code signal as implemented in Lin and Tsui [2000] and can lead to poor correlation characteristics of the modified PRN code signal [6]. Coenen and Van Nee [1992] proposed a better PDD structure utilizing the *delay-and-multiply* property of the underlying PRN code signal. The DAM property introduced in Section 2.2.3 yields a modified PRN code with similar correlation characteristics as long as the original PRN code is multiplied with its chip delayed version. Recognizing that the data and residual carrier are highly correlated over T_c, a more reasonable estimate can be obtained by letting $\hat{s}(k) = x(k - T_m)$, where $T_m = mT_c, m = 1, 2, ..$ [7]. Substituting this estimate in (3.60) and upon further manipulation, we have the following decision statistics,

$$T(\mathbf{x}) = \frac{1}{N} \sum_{k=0}^{N-1} \tilde{x}(k)\tilde{c}(k), \ \ N = TT_s^{-1} = N_r N_c N_s. \tag{3.78}$$

where $\tilde{x}(k) = x(k)x^*(k - T_m)$ and $\tilde{c}(k) = c(k)c(k - T_m)$. To further understand the PDD scheme, we expand upon (3.78) as,

$$T(\mathbf{x}) = \frac{1}{N} \sum_{k=0}^{N-1} [\tilde{x}_{ss}(k) + \tilde{x}_{sw}(k) + \tilde{x}_{ww}(k)] \tilde{c}(k - \hat{\tau}) \tag{3.79}$$

The individual terms are given by,

$$\tilde{x}_{ss}(k) = \tilde{d}(k - \tau)\tilde{c}(k - \tau)e^{j2\pi\Delta F T_m}$$
$$\tilde{x}_{sw}(k) = s(k)w^*(k - T_m) + w(k)s^*(k - T_m) \tag{3.80}$$
$$\tilde{x}_{ww}(k) = w(k)w^*(k - T_m)$$

where $\tilde{d}(k) = d(k)d(k - T_m)$. The choice of T_m is of critical influence on the detection performance of the pre-correlation differential detector. For instance, the PDD scheme introduced by Lin and Tsui [1998] essentially translated the received complex signal

---

[6]As the PRN code signal is correlated within T_c)
[7]Besides, $mod(T_m, N_c T_c) \neq 0$

into real by performing the differential detection over T_m. The choice of T_m in their approach was assumed to be less than the chip duration (i.e. $T_m = 0.41T_c$), so as to minimize the loss due to residual phase rotation. However, this choice of delay will result in a correlation performance degradation due to the signal correlation. Recalling that the C/A code is nearly uncorrelated for $T_m \geq T_c$, the delay T_m can be safely assumed to take integer multiples of chip duration (i.e. $T_m = mT_c$, $m = 1, 2, ..$). It should be emphasized here that the differential operation largely eliminates the effect of the time varying phase introduced by the residual frequency offset and that of navigation data under the following constraints,

$$T_m << \Delta F^{-1}$$
$$T_m << T_b$$

(3.81)

Once again, (3.78) can be viewed as an extreme form of differential phase detection, wherein the current phase estimate is derived from the previous chip duration. The above structure is often called pre-correlation differential detection (Coenen and Van Nee [1992]) or chip level differential detection (Chung [1995]). Figure 3.9 illustrates the pre-correlation differential detector structure. The influence of residual signal effects
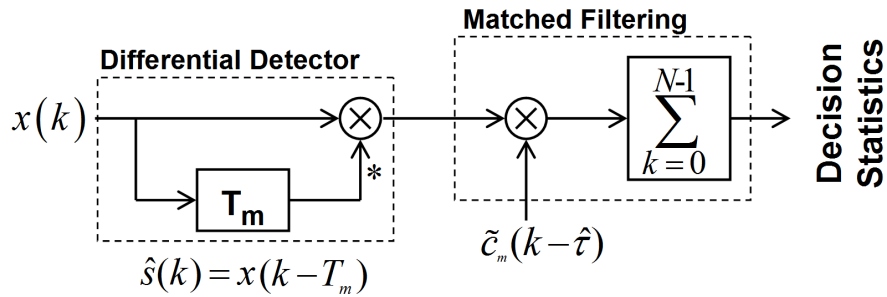
Figure 3.9: Pre-correlation Differential Detector Implementation

can be well understood by analyzing the signal component of the detection output. The detection output in the absence of the noise is given by,

$$\Psi_{PDD}(\hat{\tau}) = CR_{\tau_{err}} \sum_{k=0}^{N-1} d(k)d(k - T_m)e^{j2\pi\Delta F T_m}$$

(3.82)

From (3.82), it is apparent that the effect of constant frequency offset is nearly eliminated due to the differential detection. However, the presence of constant frequency drift will manifest itself as a constant frequency offset at the output of differential detection. Comparing (3.71) with (3.82), one can notice that the effect of data modulation on pre-correlation differential detection is similar to that of post-correlation differential detection. However, the loss should be negligible due to smaller differential delay selection. Following a similar analysis, we can derive the loss due to navigation data modulation for PDD scheme as,

$$L_D(T_m) = \left| 1 - \frac{mT_c}{T_b} \right|^2, \ T_m << T_b, m = 1, 2, ...,$$ (3.83)

Pre-correlation differential detection is of interest not only from it ability to suppress time varying phase (from data and residual carrier) but also for its reduced complexity in implementation. Utilizing the C/A code periodicity, we can rearrange the order of the summation in (3.82) and from (3.78) we have,

$$\Psi_{PDD}(\hat{\tau}) = \frac{1}{N_s N_c} \sum_{k=0}^{N_c N_s - 1} \left(\frac{1}{N_r} \sum_{r=0}^{N_r - 1} \tilde{x}(k - rN_c) \right) \tilde{c}(k - \hat{\tau})$$ (3.84)

From the above equation, the accumulation now precedes the matched filtering process and is shown as a recursive filter implementation as in Figure 3.10. The above expression is only valid for constant Doppler [8] and is critically limited in the presence of residual frequency drift. Besides, the presence of navigation data will also affect the above coherent accumulation as predicted by (3.83). The above characteristics of the pre-correlation differential detector, although promptly pointed by Coenen and Van Nee [1992], were never utilized in the later implementations introduced by Lin and Tsui [2000] and Chung [1995]. Figure 3.10 shows the recursive implementation of (3.84) originally introduced by Coenen and Van Nee [1992].

---

[8]As constant Doppler manifests as a constant complex phase rotation after differential detection.
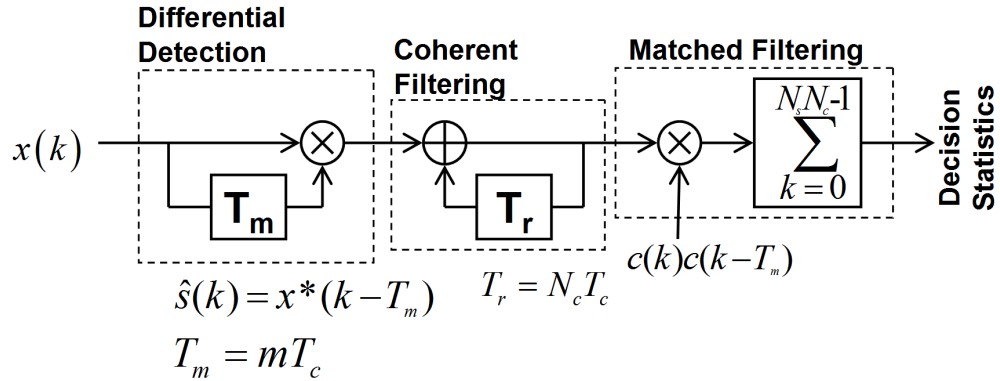
Figure 3.10: Reduced Complexity Implementation of Pre-correlation Differential Detection

Fine Frequency Estimation

The pre-correlation differential detection nearly eliminates the residual carrier, which is undesirable since it can be utilized for velocity information. However, one can utilize the approach adopted in post-correlation differential detection to aid in fine residual carrier estimation. For instance, an estimate of the residual carrier can be obtained as follows:

$$\Delta \hat{F} = \frac{\angle \left(\sum_{k=0}^{N-1} \tilde{x}(k)\tilde{c}(k - \hat{\tau}) \right)}{2\pi T_m} \tag{3.85}$$

Thus, for the correct code phase offset, the above expression yields the estimate of residual frequency offset. However, this frequency estimate will be far less accurate compared to the frequency estimate obtained through the post-correlation differential detector due to the significant noise enhancement. The PDD scheme suffers the most from the squaring loss as the differential detection is applied prior to any kind of matched filtering. The PDD scheme is more attractive to high dynamics scenarios as it effectively suppresses the phase variations through chip-level differential detection.

3.4.5 GPS Signal Acquisition – Detector Trade offs

Having reviewed the various detectors utilized for GPS signal acquisition, one can readily discern the inherent limitations of the respective detectors when applied to GPS

signal acquisition. For instance, the coherent approach although optimal in terms of noise suppression is crucially limited by the time-varying phase. In contrast, the non-coherent and the differential approaches readily alleviate the problem of time-varying phase but are decisively suboptimal in terms of detection performance. Figure 3.11 summarizes the inherent trade offs of various detection approaches as applied to the problem of GPS signal acquisition. As shown in Figure 3.11, minimal noise enhancement and utmost resilience to time-varying phase are highly desirable for detectors applied to GPS signal acquisition.
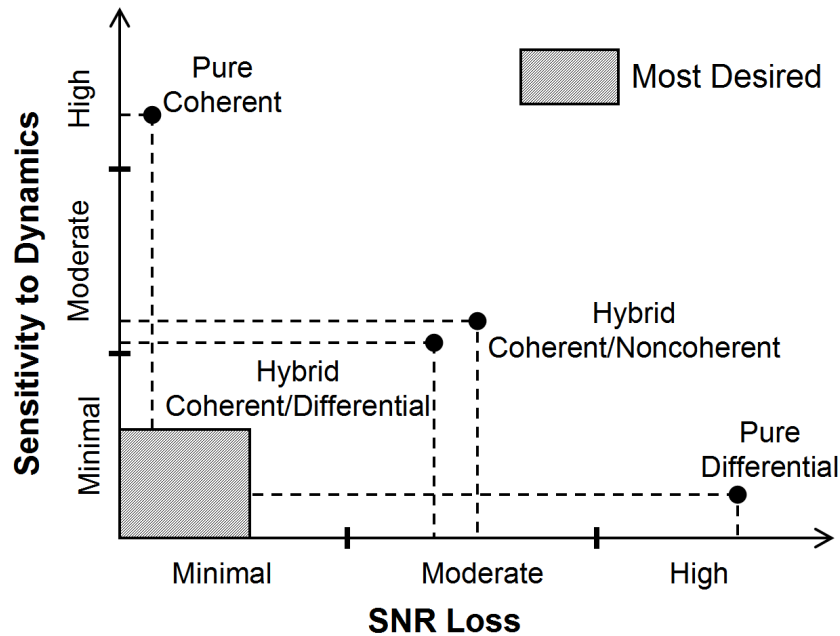
Figure 3.11: GPS Signal Detection – Trade offs

Motivated by the aforementioned constraints, a novel detection algorithm known as the *generalized post-correlation differential detection* (GPCDD) is proposed for the problem of enhanced GPS signal acquisition. The developed detector can be viewed as the generalized form that comprises both PCDD and PCND as its specialized forms. As with PCDD, the GPCDD scheme also utilizes the periodicity of the underlying GPS PRN code signal in its implementation.

3.5 New Generalized Post-Correlation Differential Detector

To derive the decision statistics for GPCDD, we model the output of the coherent matched filter output as,

$$H_0 : y(r) = w(r) \qquad r = 0, 1, 2, \ldots, N_r - 1$$
$$H_1 : y(r) = s(r) + w(r) \quad r = 0, 1, 2, \ldots, N_r - 1 \tag{3.86}$$

where $y(r)$ is the coherent matched filter output (with $T_{COH} = N_c T_c$) that is sampled every code period (i.e. $t = r N_c T_c$, $r = 0, 1, 2..$). The signal component of the coherent matched filter $(s(r))$ is given by,

$$s(r) \approx \sqrt{C} d(r) R_{\tau_{err}}(r) sinc(\pi \Delta F_{err} N_c T_c) e^{j\left(2\pi \Delta F_{err}\left[r N_c + \frac{N_c - 1}{2}\right] T_c + \phi_0\right)} \tag{3.87}$$

Recognizing the periodic property of the GPS PRN code signal, we can obtain an ensemble of estimates as

$$\hat{s}(r) = y(r - T_m), \ T_m = m N_c T_c, \ m = 1, 2, \ldots \tag{3.88}$$

Substituting for $\hat{s}(r)$ from (3.88) in the original test statistic of (3.60) and averaging over m, we have

$$T(\mathbf{x}) = \frac{1}{M} \sum_{m=1}^{M} \frac{1}{N_r - m} \sum_{r=m}^{N_r - 1} y(r) y^*(r - m N_c T_c), \ M < N_r \tag{3.89}$$

From (3.89), the current matched filter output is correlated with an ensemble of earlier matched filter outputs. Moreover, the above structure can be viewed as a generalization of both a post-correlation differential detector by letting $M = 1$ and $m = 1$ and a post-correlation noncoherent detector by letting $M = 1$ and $m = 0$. The above GLRT structure is very similar to that of an auto-correlation estimate (ACE) utilized for signal detection in radar signal processing (Wirth [1995]). It should be noted that the $s(r)$ is correlated over r, whereas the noise $w(r)$ is not. Thus, the coherent summation across m is expected to suppress noise and thereby alleviate the squaring loss incurred during

the initial differential operation. Nevertheless, it is important to analyze the impact of residual carrier and that of navigation data modulation on the developed detector. The following sections discusses the influence of these signal effects on the developed detector.

3.5.1 Loss Due to Data Modulation

To derive an expression for the effect of navigation data on the proposed GPCDD structure, we ignore the effect of other residual errors and AWGN. Hence, we can rewrite (3.89) as,

$$T(\mathbf{x}) = \frac{1}{M} \sum_{m=1}^{M} \frac{1}{N_r - m} \sum_{r=m}^{N_r - 1} d(r)d(r - mN_cT_c) \qquad (3.90)$$

Figure 3.12 shows the output of the individual differential detectors in the presence of navigation data transition (at 32 ms). While the original data is marked in Red (dashed), the detection outputs for delays $T_m = 1$ ms and 19 ms are highlighted in Blue (Solid) and Green (dash-dot) respectively. As can be seen in Figure 3.12, for $T_m = 1$ ms, the effect of navigation data bit transition is pronounced only over a millisecond (31 ms). For $T_m = 19$ ms, the same data transition is pronounced over a longer period (13 ms to 31 ms). In other words, the residual effect due to navigation data is increasingly pronounced at the output of differential detection for increasing delays. However, our goal is to determine the net effect of data on the final detection output.

As the final detection output is formed by summing the individual differential detection outputs, the final expression can be obtained by summing (3.75) over the range of delays. That is,

$$L_D(M) = E\left[\frac{1}{M} \sum_{m=1}^{M} \left| 1 - \frac{mT_r}{T_b} \right|^2 \right], \ T_r = N_cT_c \qquad (3.91)$$

Once again, letting $N_r \to \infty$ and ignoring the variance of $L_D(M)$, we can further
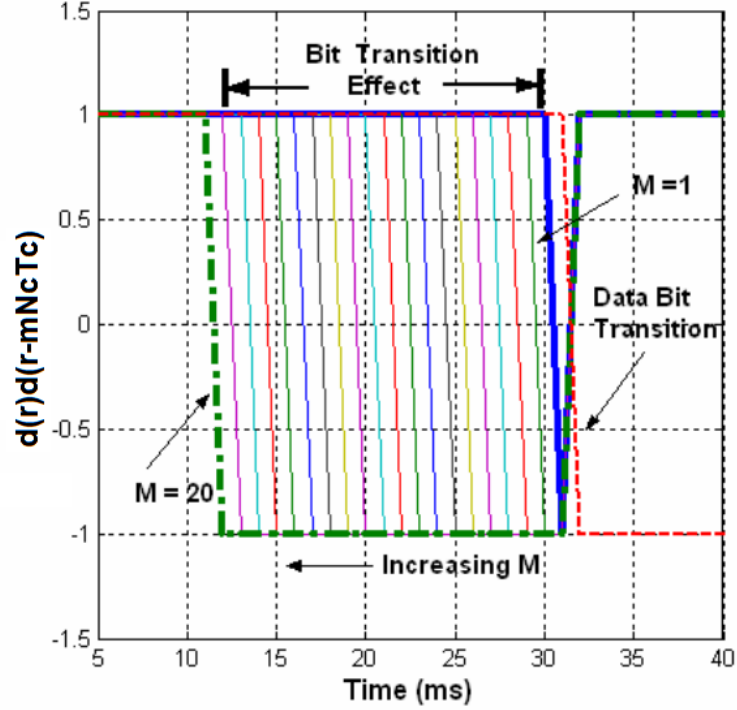
Figure 3.12: Effect of Navigation Data Bit Transition on GPCDD Output

simplify the above expression using the summation identity as,

$$L_D(M) = \left|1 - \frac{(M+1)N_cT_c}{2T_b}\right|^2, \ M < N_r, \ M < T_b(N_cT_c)^{-1} \tag{3.92}$$

It should be noted here that the above expression is only an approximation due to (3.75). Figure 4 shows the theoretical power loss (Black Square) due to navigation data modulation as a function of the number of branches, M. The numerical simulation for the power loss due to navigation data (Blue circle) averaged over 1000 independent trials is also plotted. Figure 3.13 shows the theoretical power loss as a function of correlation summations or branches (M). It should be noted that the above analysis is based on the coherent summation across the differential detection outputs, which is crucially affected by the presence of residual carrier. In the next section, we characterize the influence of residual carrier on the GPCDD structure. In particular, we show how the aforementioned structure can be incorporated with FFT to provide an estimation of the residual carrier frequency offset.
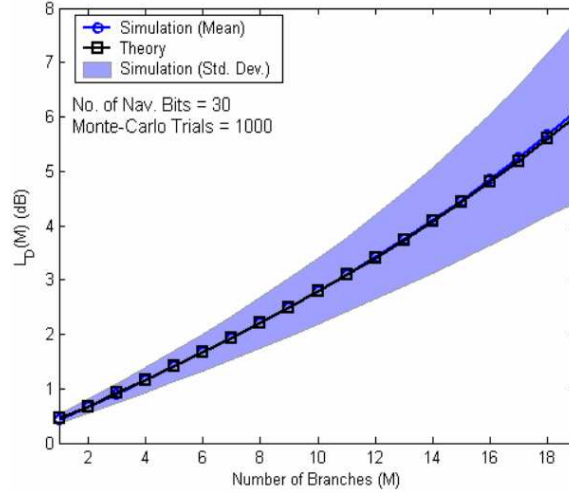
Figure 3.13: Power Loss due to Navigation Data in Generalized Post-correlation Differential Detection (Solid: Theory, {Circle,Diamond,Square}:Simulation)

3.5.2 Effect of Residual Carrier

To characterize the effect of residual carrier on the developed GPCDD structure, we express the detector output in the absence of AWGN and that of navigation data modulation as,

$$T(\mathbf{x}) = sinc^2(\pi \Delta F_{err} N_c T_c) R_{\tau_{err}}^2 \sum_{m=1}^{M} \sum_{r=0}^{N_r-(m+1)} e^{j2\pi \Delta F_{err} m N_c T_c} \qquad (3.93)$$

In the above equation, the gain achieved by the GPCDD structure can be limited by residual carrier even in the absence of navigation data modulation. Interestingly, the influence of residual carrier on GPCDD can be alleviated with non-coherent or differential combining of the individual branch outputs. Unfortunately, the subsequent noise suppression through non-coherent or differential combining is less significant to that of coherent combining. Nevertheless, the same periodic property of the underlying PRN code signal can be utilized to allow for finer frequency estimation in the developed GPCDD structure. For example, the complex phase rotation across the individual branches is related to the residual frequency offset and the corresponding branch delay. Thus, the individual complex phase rotations collectively embody the sampled residual carrier. Hence, for correct code phase, the residual carrier can be estimated by applying

a M-pt FFT across the differential detection outputs. Moreover, the FFT based combining also accomplishes coherent combining. Figure 3.14 illustrates the GPCDD structure utilizing M-pt FFT based residual frequency offset estimation and coherent combining. In Figure 3.14, the use of recursive filtering to implement coherent averaging in individual differential detector branches, which works effectively in the absence of residual frequency drifts. The proposed frequency estimation technique involves an additional gain of $10log_{10}\sqrt{M}$ over the frequency estimation methods proposed by Elders-Boll and Dettmar [2004] and that of Schmid and Neubauer [2005]. As the input sampling rate to the FFT is $T_{COH} = T_r = N_cT_c$, the corresponding bandwidth and the resolution of the FFT based frequency estimation is given by,

$$\Gamma_{BW} = \frac{1}{N_cT_c}$$
$$\Gamma_{RES} = \pm\frac{1}{MN_cT_c}$$

(3.94)

For example, with M = 20, the above estimator achieves a minimum resolution of approximately $\Gamma_{RES} = 50$ Hz. Note that the FFT estimator will be able to correctly estimate residual frequencies that fall between T_r^{-1} or 500 Hz. Thus, a residual frequency offset greater than 500 Hz introduces an integer frequency ambiguity due to spectral wrapping over the input sampling rate. Nevertheless, the complex phase rotations are still compensated for even in the presence of this integer frequency ambiguity. A more reasonable choice for the number of branches is around 16 based on the data decorrelation loss and FFT implementation efficiency. For $M = 16$, any residual frequency offset within 500 Hz can be estimated with an accuracy of around 62.5 Hz. In summary, the proposed GPCDD structure accomplishes both noise suppression as well as robust frequency estimation for weak GPS signal acquisition. However, the performance of GPCDD structure can be degraded significantly, for $T_m \rightarrow T_b$ due to the phase decorrelation caused by the navigation data.
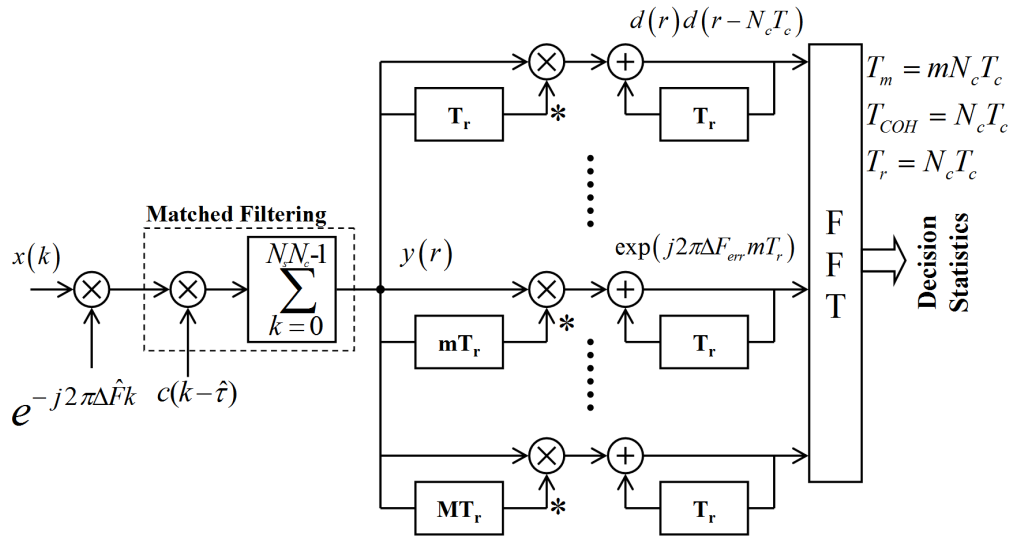
Figure 3.14: Generalized Post-correlation Differential Detector Structure

3.6   Detection Performance

The previous sections established the optimal detector structures in the presence of a known deterministic signal or its absence. Moreover, it also established the relation between the popular GPS detection schemes to GLRT processing. This section deals with the derivation of the detection performance for these detectors. It should be emphasized here that various authors have derived the close form expression for many of these detectors using the well known Gaussian approximation. For example, the detection performance of post-correlation noncoherent (van Dierendonck [1996]), differential (Schmid and Neubauer [2004]) and pre-correlation differential (Chung [1995]) detectors were derived invoking the central limit theorem. The readers are referred to O' Driscoll [2007] for a more detailed treatment of the derivation of detection performance in terms of probability of false alarm and detection, deflection coefficient and related performance bounds. The first step towards characterizing the detection performance of a particular detector is to determine the conditional PDF's, $P(x|H_0)$ and $P(x|H_1)$ so as to obtain the decision statistics PDF's, denoted by $P(\Psi|H_0)$ and $P(\Psi|H_1)$ respectively.

Accordingly, we can determine the probability of detection (P_D) as

$$P_D = \int_\alpha^{+\infty} P(\Psi|H_1)d\Psi \tag{3.95}$$

and the probability of false alarm s P_{FA} as,

$$P_{FA} = \int_\alpha^{+\infty} P(\Psi|H_0)d\Psi \tag{3.96}$$

where the threshold α can be solved from (3.96) for a fixed upper limit on false alarm rate.

3.6.1 Coherent Matched Filter

The coherent matched filter detector operates with perfect knowledge of the signal parameters. The ensuing detection performance analysis assumes that $x(k)$ is Gaussian for both the hypotheses and hence the test statistic $T(\mathbf{x})$ is also Gaussian. Accordingly, the detection problem reduces to a mean-shifted Gauss-Gauss problem and requires only the first two central moments to derive an expression for P_{FA} and P_D. Therefore, we can express the decision statistic as,

$$T(\mathbf{x}) = \begin{cases} \mathcal{N}\left(0, \sigma_I^2 \varepsilon\right) & H_0 \\ \mathcal{N}\left(\varepsilon, \sigma_I^2 \varepsilon\right) & H_1 \end{cases} \tag{3.97}$$

where ε is the total energy in the expected signal $s(k)$ (i.e. $\varepsilon = E\left[s^2(k)\right]$). The noise power is reduced by half in the above expression as the power of the AWGN is evenly split between the inphase and quadrature channels (i.e. $P(\mathbf{x}|H_0) = \mathcal{N}(0, \sigma_w^2 \varepsilon)$). In other words, only half of the noise power enters in the sufficient statistic. The test statistic $T(\mathbf{x})$ is Gaussian distributed with the two central moments as defined in (3.97). The following expression for probability of detection and false alarm can be established (Kay

[1993a]):

$$P_{FA} = \frac{1}{2}\left[1 - \Phi\left(\frac{\alpha}{\sqrt{\sigma_I^2 \varepsilon}}\right)\right]$$

$$P_D = \frac{1}{2}Q\left[Q^{-1}\left(P_{FA}\right) - \sqrt{\frac{\varepsilon}{\sigma_I^2}}\right] \tag{3.98}$$

$$\alpha = \Phi^{-1}\left(1 - P_{FA}\right)\sqrt{\sigma_I^2 \varepsilon}$$

where $Q(\bullet)$ is the Q-function is related to the the error function $\Phi(z)$ as

$$Q(z) = \frac{1}{\sqrt{2\pi}}\int_z^{+\infty} e^{-\frac{z^2}{2}}dz$$

$$= 1 - \Phi(z) \tag{3.99}$$

Another useful measure to characterize the CMF detector performance is the processing gain (G). The processing gain (G) of the coherent matched filter is defined as the ration of output SNR to the SNR at the input of the matched filter. That is,

$$G = \frac{(SNR)_{out}}{(SNR)_{in}} \tag{3.100}$$

For the coherent matched filter, the signal power after the coherent averaging is εN^2 whereas the noise variance is $\sigma_I^2 N$. Therefore,

$$G = \frac{(N^2\varepsilon/N\sigma_I^2)}{(\varepsilon/\sigma_I^2)} = N \tag{3.101}$$

Hence, the coherent matched filtering improves the detection performance by a factor of N for a given pre-detection SNR using coherent observation of $N = TT_c^{-1}$ samples. Similarly, we can also express the SNR at the output of the coherent matched filter or the post-correlation SNR (PSNR) using the method presented in Kay [1993a] and arrive at,

$$PSNR = \frac{(E\left[T(\mathbf{x}); H_1\right] - E\left[T(\mathbf{x}); H_0\right])^2}{Var\left[T(\mathbf{x}); H_0\right]} \tag{3.102}$$

For the coherent matched filter, we have

$$E\left[T(\mathbf{x}; H_0)\right] \approx 0$$

$$Var\left[T(\mathbf{x}; H_0)\right] = \frac{\sigma_I^2}{N} \tag{3.103}$$

$$E\left[T(\mathbf{x}; H_1)\right] = \sqrt{\frac{C}{2}}$$

Substituting the values from the above equation in (3.102), we have

$$PSNR_{CMF} = \frac{C/2}{\sigma_I^2/N} = N\left(\frac{C}{2\sigma_I^2}\right) \tag{3.104}$$

Once again, $(C/2\sigma_I^2)$ is the pre-detection SNR and is related to the C/N$_0$ as $SNR_{in} = C/(N_0 B_{IF})$[9], where B_{IF} is the IF bandwidth. The coherent matched filter improves the SNR and hence the detection performance by a factor of N using a coherent observation of T seconds.

3.6.2 Incoherent Matched Filter

In contrast to the CMF detector, the ICMF detector combines the inphase and quadrature channels and thereby integrates the noise power completely. Under H_0, the decision statistics $T(\mathbf{x})$ is Rayleigh distributed and can be expressed as,

$$P(\lambda_{ICMF}|H_0) = \begin{cases} \frac{\lambda_{ICMF}}{\varepsilon\sigma_w^2}e^{-\frac{\lambda_{ICMF}^2}{2\varepsilon\sigma_w^2}} & \lambda_{ICMF} \geq 0 \\ 0 & \lambda_{ICMF} < 0 \end{cases} \tag{3.105}$$

where $\lambda_{ICMF} = T(\mathbf{x}); H_0)$. Under H_1, λ_{ICMF} is Rician distributed:

$$P(\Psi_{ICMF}|H_1) = \begin{cases} \frac{\Psi_{ICMF}}{\varepsilon\sigma_w^2}e^{-\frac{\lambda_{ICMF}^2+\varepsilon^2}{2\varepsilon\sigma_w^2}}I_0\left(\frac{\lambda_{ICMF}}{\sigma_w^2}\right) & \Psi_{ICMF} \geq 0 \\ 0 & \lambda_{ICMF} < 0 \end{cases} \tag{3.106}$$

where $I_0(\bullet)$ is the Bessel function and is given by,

$$I_0(z) = \frac{1}{2\pi}\int_0^{2\pi}e^{z\cos(\theta)}d\theta \tag{3.107}$$

From (3.105) and (3.96), the probability of false alarm can be calculated as,

$$P_{FA} = e^{\left(\frac{-\alpha^2}{\varepsilon\sigma_w^2}\right)} \tag{3.108}$$

The detection threshold can be readily obtained by inverting the above equation. That is,

$$\alpha = \sqrt{-\varepsilon\sigma_w^2 ln P_{FA}} \tag{3.109}$$

---

[9]$\sigma_w^2 = N_0 B_{IF}$

Similarly, we can also obtain the expression for probability of detection from (3.95) and (3.106) as,

$$P_D = Q_M \left(\sqrt{\frac{\varepsilon}{\sigma_w^2}}, \sqrt{\frac{\alpha^2}{\varepsilon\sigma_w^2}} \right) \tag{3.110}$$

where $Q_M(\bullet, \bullet)$ is the Marcum's Q-function and is defined as (Proakis [2001]),

$$Q_M(\beta, \tau) = \int_\tau^{+\infty} t e^{-\frac{1}{2}(t^2 + \beta^2)} I_0(\beta t) dt \tag{3.111}$$

3.6.3 Post-correlation Noncoherent Detector

In contrast to the CMF and ICMF, the PCND involves the accumulation of squared magnitude values and is hence less efficient at suppressing noise. The detection performance of the PCND can be determined approximately by calculating the loss in noncoherent accumulation in comparison to the ideal coherent matched filtering. The loss factor (or the squaring loss) is given by,

$$L_{PCND} = \frac{SNR_{CMF}}{SNR_{PCND}} \tag{3.112}$$

The SNR at the output of the coherent matched filter is summarized in (3.104). For $N_r >> 1$, then the PCND decision statistics, as defined in (3.66), can be approximated by a Gaussian random variable since it is the sum of N_r independent and identically distributed random variables. Thus, we need only to find the first two moments to characterize the detection performance. The PDF of the decision statistics of (3.66) can be characterized by,

$$T(\mathbf{x}) = \begin{cases} \chi^2_{N_r} & H_0 \\ \chi'^2_{N_r}(\lambda_{PCND}) & H_1 \end{cases} \tag{3.113}$$

where, $\lambda_{PCND} = (1/N_r) \sum_{r=0}^{N_r - 1} s^2(r)$ and $s(r)$ is the signal component of coherent matched filter output that is sampled at $N_c T_c$. χ^2 is the central chi-squared and χ'^2 is the non-central chi-squared distribution with non-centrality parameter λ_{PCND} (Papoulis

[1984]). Using the properties of chi-squared random variables we have (Kay [1993a]),

$$E\left[T(\mathbf{x}; H_0)\right] \approx 2\sigma_Y^2$$

$$Var\left[T(\mathbf{x}; H_0)\right] \approx 8\sigma_Y^4/N_r \qquad (3.114)$$

$$E\left[T(\mathbf{x}; H_1)\right] \approx C + 2\sigma_Y^2$$

where σ_Y^2 is the noise variance at the output of the initial coherent matched filtering, which is sampled at $N_c T_c$ seconds . In the above equation, we see that the decision statistics actually measures the power due to the squared magnitude operation. Thus, the expression (3.102) cannot be applied directly. Accordingly, one can utilize the modified version that utilizes the standard deviation of noise statistics, which is given by,

$$PSNR = \frac{(E\left[T(\mathbf{x}); H_1\right] - E\left[T(\mathbf{x}); H_0\right])}{\sqrt{Var\left[T(\mathbf{x}); H_0\right]}} \qquad (3.115)$$

Therefore we have,

$$PSNR_{PCND} = \frac{C}{\sqrt{2N_r}2\sigma_Y^2} = \sqrt{\frac{N_r}{2}}\frac{C}{2\sigma_Y^2} \qquad (3.116)$$

The PSNR expression in (3.104) can be rewritten as,

$$PSNR_{CMF} = N_r\frac{C}{2\sigma_Y^2} \qquad (3.117)$$

Substituting for (3.104) and (3.116) in (3.112) we have

$$L_{PCND} = \sqrt{2N_r} \qquad (3.118)$$

The above loss factor expression for the PCND scheme is only an approximation. Moreover, similar approximations for the PCND loss factor are reported in Curry [2001] and DiFranco and Rubin [1980]. The authors are referred to O' Driscoll [2007] for an accurate evaluation of the probabilities of detection and false alarm.

3.6.4 Post-Correlation Differential Detector

In contrast to the PCND scheme, the PCDD scheme involves the product of two independent noise samples. Accordingly, the noise variance at the output of PCDD detector

is less than that of the noise variance at the output of the PCND detector (Zarrabizadeh and Sousa [1997]). However, the PCDD still experiences a loss in comparison to the ideal coherent matched filter. Hence, the detection performance of PCDD scheme can be determined approximately by calculating the loss experienced in the PCDD scheme in comparison to the ideal coherent matched filtering. The loss factor for the PCDD scheme is given by,

$$L_{PCDD} = \frac{SNR_{CMF}}{SNR_{PCDD}} \tag{3.119}$$

The SNR at the output of the coherent matched filter is summarized in (3.104). Following a similar analysis, the first two moments of the decision statistics can be obtained as (Yang et al. [2007]),

$$E\left[T(\mathbf{x}; H_0)\right] \approx 0$$
$$Var\left[T(\mathbf{x}; H_0)\right] \approx 4\sigma_Y^4(N_r - 1) \tag{3.120}$$
$$E\left[T(\mathbf{x}; H_1)\right] \approx C(N_r - 1)$$

Similar to PCND, the decision statistics for PCDD also measures the power due to the squared magnitude operation. Therefore, utilizing the modified statistics as previously defined for PCND scheme in (3.115), we have the PSNR for the PCDD scheme as

$$PSNR_{PCDD} = \frac{C(N_r - 1)}{2\sigma_Y^2\sqrt{N_r - 1}} = \sqrt{N_r - 1}\frac{C}{2\sigma_Y^2} \tag{3.121}$$

Substituting (3.121) and (3.104) in (3.119) we have the loss factor for the PCDD scheme as

$$L_{PCDD} \approx \sqrt{N_r}, \ N_r \gg 1 \tag{3.122}$$

From (3.122) and (3.118), we see that the PCDD scheme accomplishes a gain of around 1.5 dB over the PCND scheme. However, it still experiences a loss of approximately $\sqrt{N_r}$. This performance improvement is consistent with the estimates reported earlier by Schmid and Neubauer [2004] and Yu [2006].

3.6.5 Pre-Correlation Differential Detector

In contrast to post-correlation schemes, the PDD scheme involves the differential operation prior to any kind of coherent matched filtering. Thus, the PDD scheme experienced huge loss in comparison to the post-correlation schemes. In contrast to PCDD, the differential detection is applied at the chip level for the PDD scheme. In Section 3.6.1, it was shown that the coherent matched filtering simply scaled the input SNR by a factor of N and retained a similar PDF as its output. Hence, the PDF of the decision statistics for PDD and that of PCDD are similar except for the inherent coherent matched filtering gain. Following a similar analysis, the first two moments of the decision statistics can be obtained as (Chung [1995]),

$$
\begin{aligned}
E\left[T(\mathbf{x}; H_0)\right] &\approx 0 \\
Var\left[T(\mathbf{x}; H_0)\right] &\approx 4\sigma_I^4(N_c N_r - 1) \\
E\left[T(\mathbf{x}; H_1)\right] &\approx C(N_c N_r - 1)
\end{aligned}
\tag{3.123}
$$

Once again, using (3.115) we can obtain the PSNR for the PDD scheme as,

$$
PSNR_{PDD} = \frac{C(N_c N_r - 1)}{2\sigma_I^2 \sqrt{N_c N_r - 1}} = \sqrt{N_c N_r - 1}\frac{C}{\sigma_w^2}
\tag{3.124}
$$

The loss factor for the PDD scheme can be obtained by comparing the above equation with the (3.104). That is

$$
L_{PDD} \approx \sqrt{N_c N_r}
\tag{3.125}
$$

From (3.122) and (3.125), we see that the PDD scheme involves a further loss of $\sqrt{N_c}$ in comparison to the PCDD scheme. This additional loss of $\sqrt{N_c}$ in the PDD scheme is caused by the absence of initial coherent matched filtering. Thus, the PDD scheme accomplishes better resilience to dynamics at the expense of large SNR loss. The readers are referred to Chung [1995], for a detailed probability of detection and false alarm analysis of the PDD scheme.

3.6.6 Generalized Post-Correlation Differential Detector

In the proposed GPCDD scheme, the decision statistic is based on the differential detection of coherent matched filter outputs taken over a range of delays. Since the noise at the output of the coherent matched filter output can be considered independent over these delays, he decision statistics across the individual differential detectors is similar to that of the PCDD scheme and is defined by (3.120). Moreover, the final decision statistics is obtained by coherent accumulation (i.e. via FFT operation). Thus, the first two moments of the GPCDD decision statistics are given by,

$$
\begin{aligned}
&E\left[T(\mathbf{x}; H_0)\right] \approx 0 \\
&Var\left[T(\mathbf{x}; H_0)\right] \approx 4\sigma_Y^4 \sum_{m=1}^{M}(N_r - m) = 4\sigma_Y^4 M\left[N_r - \tfrac{(M+1)}{2}\right] \\
&E\left[T(\mathbf{x}; H_1)\right] \approx CM\left[N_r - \tfrac{(M+1)}{2}\right]
\end{aligned}
\tag{3.126}
$$

As expected, substituting $M = 1$ in the above equation leads to the decision statistics of that of PCDD as defined in (3.120). Following a similar analysis, we can derive the PSNR at the output of GPCDD as,

$$
PSNR_{GPCDD} = \frac{CM\left[N_r - \frac{(M+1)}{2}\right]}{2\sigma_Y^2 \sqrt{M\left[N_r - \frac{(M+1)}{2}\right]}} = \sqrt{M\left[N_r - \frac{(M+1)}{2}\right]} \frac{C}{2\sigma_Y^2}
\tag{3.127}
$$

Accordingly, we can derive the loss factor for the proposed GPCDD scheme as,

$$
L_{GPCDD} \approx \sqrt{M\left[N_r - \frac{(M+1)}{2}\right]}
\tag{3.128}
$$

However, it should be noted here that the GPCDD also incurs loss due to random navigation data modulation as expressed in (3.92). Moreover, the noise across the output of the individual differential detectors is not entirely independent and the central limit theorem was not applied in the strictest sense to derive the decision statistics. Interestingly, it can be shown that the decision statistics of the proposed GPCDD scheme can be approximated by the well-known ICMF statistics for $M \rightarrow N_r$. To do that, we consider a simplistic model of the received signal with no residual carrier and

navigation data modulation. Accordingly, the coherent matched filter output (with $T_{COH} = N_c T_c$) that is sampled every $N_c T_c$ (i.e. $y(r - mN_c T_c)$) is be given by,

$$y(r) = \sqrt{\frac{C}{2}} + w(r), \ r = 0, 1, ..., N_r - 1. \tag{3.129}$$

where $w(r)$ is defined by (3.41). Substituting for $y(r)$ from the above equation in (3.89) we have,

$$T_{GPCDD}(\mathbf{x}) = \frac{1}{M} \sum_{m=1}^{M} \frac{1}{N_r - m} \sum_{r=m}^{N_r - 1} \left(\sqrt{\frac{C}{2}} + w(r) \right) \left(\sqrt{\frac{C}{2}} + w(r - m) \right)^* \tag{3.130}$$

On further expansion we have

$$T_{GPCDD}(\mathbf{x}) = \frac{1}{M} \sum_{m=1}^{M} \frac{1}{N_r - m} \sum_{r=m}^{N_r - 1} \left[\frac{C}{2} + \sqrt{\frac{C}{2}} \left(w(r) + w^*(r - m) \right) + w(r)w^*(r - m) \right] \tag{3.131}$$

Form $m = 1$, the inner summation of the noise product term $w(r)w^*(r - m)$ can be expanded as,

$$\sum_{r=0}^{N_r - 2} w(r)w^*(r - 1) = w(0)w^*(-1) + w(1)w^*(0) + \ldots + w(N_r - 3)w^*(N_r - 4)$$
$$+ w(N_r - 2)w^*(N_r - 3) \tag{3.132}$$

Similarly, for $m = 2$, we have the inner summation of the noise product term $w(r)w^*(r - m)$ as,

$$\sum_{r=0}^{N_r - 3} w(r)w^*(r - 2) = w(0)w^*(-2) + w(1)w^*(-1) + \ldots + w(N_r - 4)w^*(N_r - 5)$$
$$+ w(N_r - 3)w^*(N_r - 4) \tag{3.133}$$

Accordingly, the noise product terms over the summations r and m can be compactly written in matrix form as,

$$
\begin{bmatrix}
\underbrace{w(0)}\, w^*(-1) & \underbrace{w(1)}\, w^*(0) & \cdots & \underbrace{w(N_r - 3)}\, w^*(N_r - 4) & w(N_r - 2)w^*(N_r - 3) \\
\underbrace{w(0)}\, w^*(-2) & \underbrace{w(1)}\, w^*(-1) & \cdots & \underbrace{w(N_r - 3)}\, w^*(N_r - 5) & 0 \\
\underbrace{w(0)}\, w^*(-3) & \underbrace{w(1)}\, w^*(-2) & \cdots & 0 & 0 \\
\underbrace{w(0)}\, w^*(-(M+1)) & 0 & \cdots & 0 & 0
\end{bmatrix}
\tag{3.134}
$$

In the above matrix, the summation across rows readily represents the inner summation across r (i.e. from $r = 0$ to $r = N_r - (m + 1)$). Note that the final result is independent of the order of summation. For convenience, let us consider that the summation across m (i.e. across differential detectors) precedes the summation across r (i.e. temporal summation). Note that the terms highlighted with under braces are the same across columns and can be taken out of the summation. Therefore, we can express the summations of noise product terms as,

$$\sum_{m=1}^{M} \sum_{r=0}^{N_r-(m+1)} = w(0) \left[w(-1) + w(-2) + \ldots + w(-(M+1)) \right]^*$$
$$+ w(1) \left[w(-1) + w(-2) + \ldots + w(-M) \right]^* + w(N_r - 3) \left[w(N_r - 4) + w(N_r - 5) + \ldots \right]^* +$$
$$+ \ldots + w(N_r - 2) \left[w(N_r - 3) + \ldots \right]^* \tag{3.135}$$

Interchanging the order of the summations and upon further manipulation, we have

$$\frac{1}{M} \sum_{m=1}^{M} \frac{1}{N_r - m} \sum_{r=m}^{N_r-1} w(r)w^*(r - m) \approx \frac{1}{N_r} \sum_{r=0}^{N_r-1} w(r) \frac{1}{M - r} \sum_{m=(r+1)}^{M} w^*(r - m) \tag{3.136}$$

As $w(r)$ are AWGN samples, they can be considered wide sense stationary[10]. Hence, the following approximation can be utilized

$$\lim_{M \to \infty} \sum_{m=0}^{M} w^*(r - (m+1)) \approx \sum_{m=0}^{M-1} w^*(-m) \tag{3.137}$$

From the above approximation, we have the summation of noise product terms as,

$$\frac{1}{M} \sum_{m=1}^{M} \frac{1}{N_r - m} \sum_{r=m}^{N_r-1} w(r)w^*(r - m) \approx \left(\frac{1}{N_r} \sum_{r=0}^{N_r-1} w(r) \right) \left(\frac{1}{M} \sum_{m=0}^{M} w^*(-(m+1)) \right) \tag{3.138}$$

The above approximation hold only for $M \gg 1$. Finally, we can approximate the first term in the signal-noise product term in (3.131), for $M \gg 1$ and $N_r \gg 1$ as,

$$\sum_{m=1}^{M} \sum_{r=m}^{N_r-1} w(r) \approx \sum_{r=0}^{N_r-1} w(r) \tag{3.139}$$

---

[10]For wide sense stationary process, the first two moments is independent of time or time-lag

The above approximation is possible as $w(r)$ is AWGN and hence wide sense stationary. The index m can be brought inside (r). That is

$$\lim_{N_r \to \infty} \sum_{r=0}^{N_r-1} w(r - m) \approx \sum_{r=0}^{N_r-1} w(r) \tag{3.140}$$

Similarly, the summation of the second term in the signal-noise product terms in (3.131) can be approximated as

$$\sum_{m=1}^{M} \sum_{r=m}^{N_r-1} w^*(r - m) \approx \sum_{r=0}^{N_r-1} w^*(r) \tag{3.141}$$

As $w(r)$ is wide sense stationary, the summation (or the mean) of $w(r)$ converges to its mean value and can be considered a constant. Hence, the outer summation over m is dropped owing to the wide sense stationarity of $w(r)$. From (3.138), (3.139) and (3.141) and letting $M = N_r$, we have the decision statistics of the GPCDD as,

$$T_{GPCDD}(\mathbf{x}) \approx \frac{C}{2} + \sqrt{\frac{C}{2}} \frac{1}{N_r} \left(\sum_{r=0}^{N_r-1} w(r) + \sum_{r=0}^{N_r-1} w^*(r) \right) + \left(\frac{1}{N_r} \sum_{r=0}^{N_r-1} w(r) \right) \left(\frac{1}{N_r} \sum_{r=0}^{N_r-1} w^*(r) \right)$$
$$\tag{3.142}$$

The above equation can be further simplified as,

$$T_{GPCDD}(\mathbf{x}) \approx \left| \sqrt{\frac{C}{2}} + \frac{1}{N_r} \sum_{r=0}^{N_r-1} w(r) \right|^2 \tag{3.143}$$

From the above equation, we see that the GPCDD scheme can accomplish similar detection performance as that of incoherent matched filter for $M \to N_r$. Besides, the above structure is also similar to that of an estimator-correlator. Thus, the GLRT structure pertaining to that of GPCDD scheme is essentially similar to an estimator-correlator as $M \to N_r$. However, the final result is only an approximation and requires further validation in terms of probability of detection and false alarm analysis. Interestingly, Yang et al. [2007] demonstrated this asymptotic property of the GPCDD scheme (referred to as the semi-coherent scheme with $N_r/2$ lags) for GPS L1 C/A code acquisition.

3.7 Acquisition Performance Evaluation

Having derived the various detection schemes theoretically, we now turn to empirical tests to validate the developed theory. These tests consist of software-based analysis of IF samples from two signal sources: a hardware GPS simulator, and live signals from the GPS constellation. Furthermore, the average acquisition performance was also calculated based on a MATLAB based IF signal simulator (Psiaki [2007]). The developed acquisition schemes based on the various detection algorithms established earlier were implemented in a MATLAB environment to evaluate their performance. The basic hardware front-end setup and the subsequent processing is detailed in Section 2.4 and illustrated in Figure 2.6. For basic acquisition sensitivity tests, hardware simulated data has been used to carefully control the received C/N_0 with the Spirent GSS 7700 simulator controlled by SimGEN software. The acquisition performance analysis involved the usage of resampled GPS data (from 20 MHz to 2.046 MHz). To validate the technique further, live GPS data were also collected with variable attenuation (to control the pre-detection SNR) to validate the acquisition schemes. Monte-Carlo simulations were also carried out using the MATLAB software simulator reported in Psiaki [2007] to obtain average performance results.

For all sets of simulated data, most error sources including multipath, atmospheric effects, and orbital errors were set to zero. Thus, the sensitivity analysis were targeted only for the controlled variable of absolute C/N_0. Data from both the live GPS constellation and the GSS 7700 hardware simulator were collected. The receiver's C/N_0 estimate of a high-elevation GPS satellite was used as a baseline for defining the "nominal" hardware simulator levels, from which attenuated levels were then defined. The Euro-3M card was driven by an external rubidium reference oscillator during the data collections (Riley [1999]).

3.7.1   Fine Frequency Estimation Performance

In the previous sections, it was shown that the *differential detection* approach can potentially enable fine frequency estimation. The differential operation performed in the developed detectors can be readily inferred as a phase discrimination [11] . Accordingly, the frequency estimate can be obtained as (Kaplan and Hegarty [2006]),

$$\Delta \hat{F} = \text{atan2} \left(\frac{\Im \left\{ R(\hat{\tau} = \tau) \right\}}{\Re \left\{ R(\hat{\tau} = \tau) \right\}} \right) (2\pi T)^{-1} \tag{3.144}$$

The delay T essentially reflects the differential delay adopted in the developed differential detectors. For example, for the pre-correlation differential detection, the value of T assumes integer multiples of chip duration (i.e. $T = mT_c$). On the other hand, the delay T assumes an integer multiple of coherent integration period for post-correlation differential detection (i.e. $T = mN_cT_c$).

Pre-correlation Differential Detection

Figure 3.15 shows the frequency estimation performance of the pre-correlation differential detector as a function of differential delay. The result was based on the live GPS data collection and the PRN 1 had a C/N_0 level of approximately 50 dB-Hz. The observation time was set to 100 ms, and resulted in an average PSNR of approximately 27 dB. Hence, one can expect a good frequency estimation performance for this SNR level. From Figure 3.15, the frequency estimate is close to the expected 836.6 Hz for the PRN1 signal. For small differential delays, the noise is enhanced due to factor $(2\pi T_m)^{-1}, T_m = mT_c$. In the presence of residual Doppler, we can observe a change in sign of the frequency estimate (i.e. around $T_m = 600T_c$). The sign change is caused by the phase wrapping and occurs every 2π or the inverse of the residual Doppler. It can readily be compensated for by changing the absolute values greater than pi to their 2π complement. In summary, pre-correlation differential detection can be adopted for fine

---

[11] $\Delta \hat{F} = \frac{\phi(k) - \phi(k-T)}{2\pi T}$
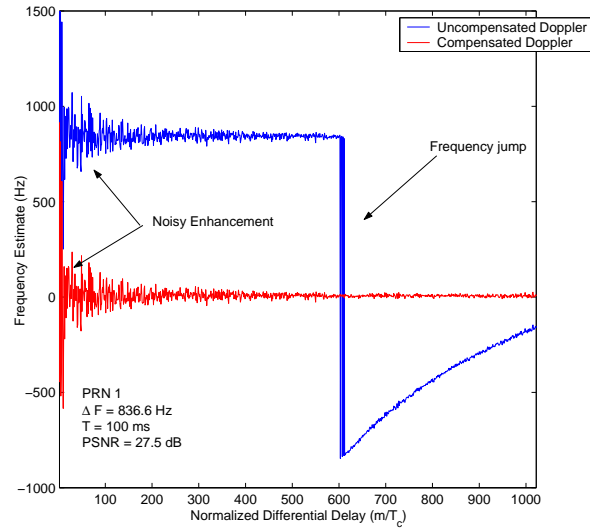
Figure 3.15: Fine Frequency Estimation Using Pre-correlation Differential Detector (C/N_0 = 50 dB-Hz, ΔF = 836 Hz, T = 100 ms)

frequency estimation for good C/N_0 levels. The frequency estimation performance is directly related to the PSNR, which is critically influenced by the detection performance besides the C/N_0. There exists a trade-off in the selection of differential delay times for fine frequency estimation. While smaller differential delays are immune to frequency jumps, they are critically limited by the noise enhancement.

Post-correlation Differential Detection

The major drawback with pre-correlation differential detector based fine frequency estimation stems from its inferior SNR performance. In contrast, the post-correlation differential detector boosts the PSNR through coherent matched filtering and thereby enhancing the frequency estimation performance. Figure 3.16 shows the convergence of frequency estimation as a function of observation period. The detector utilized a coherent integration time of 1 ms, which was followed by 100 accumulations resulting in a total observation period of 100 ms. The residual Doppler of PRN 14 was approximately 254 Hz. From the plot, we can see a strong convergence for moderate to high C/N_0 levels. For low C/N_0 levels, the frequency estimation performance degraded substantially

due to the inherent degradation in PSNR.
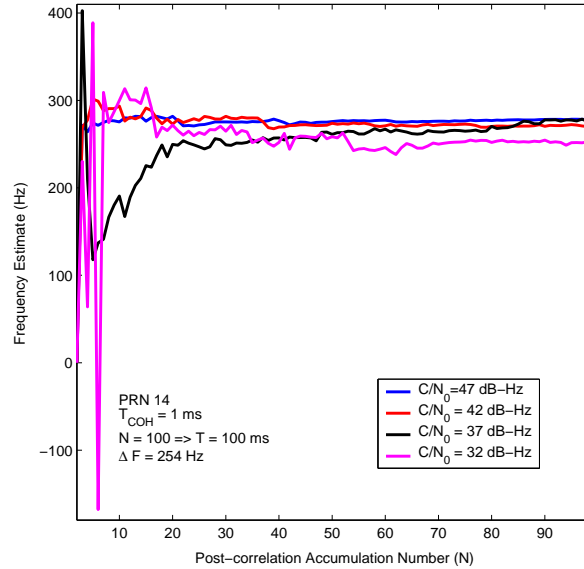
Figure 3.16: Fine Frequency Estimation Performance of Post-correlation Differential Detector

Generalized Post-correlation Differential Detection

The generalized post-correlation differential detection performs the frequency estimation using an ensemble of observations. Consequently, the generalized post-correlation differential detector achieves superior frequency estimation performance due to the additional gain obtained through coherent summation (i.e. FFT combining). Monte-Carlo simulations were performed in MATLAB as an initial step to assess the frequency estimation performance of the proposed detector structure. The frequency estimation technique in the proposed detector essentially averaged the frequency estimates obtained across individual branches for the correct code phase estimation. That is,

$$\Delta \hat{F}_{err}(M) = \frac{1}{M} \sum_{m=1}^{M} \left[\frac{\angle \left(\frac{1}{N_r - m} \sum_{r=0}^{N_r - (m+1)} y(r) y^*(r - mN_cT_c) \right)}{2\pi m (N_cT_c)^{-1}} \right] \tag{3.145}$$

where $\angle(\bullet)$ is the phase angle estimate. From the above equation, we see that for $M = 1$, the frequency estimation decomposes to the method introduced in Elders-Boll and Dettmar [2004] and that of Schmid and Neubauer [2005]. Table 3.2 summarizes the

frequency estimation performance for different M vales under different C/N_0 conditions. The frequency estimation results were averaged over 250 independent simulations for different PRN's, Dopplers and code phases. While the coherent integration period was set to 1 ms, the total observation period was increased correspondingly for decreasing C/N_0 levels. The proposed detector (for M = 4) demonstrated substantial improvement in terms of frequency estimation under low C/N_0 conditions due to its enhanced noise suppression via coherent combining across branches. The FFT based frequency estimation approach was also verified using hardware simulated GPS data for 25 dB-Hz C/N_0 data. The proposed detector utilized 1 ms coherent integration and a 400 ms observation period with M = 16. Figure 3.17 shows the normalized FFT output for the developed GPCDD detector structure for various PRN's in the case of 25 dB-Hz C/N_0 data. The coherent integration period was set to 1 ms with a 400 ms total observation period.

C/N_0 (dB-Hz)	T (ms)	Frequency Estimation Error, $\delta F_{err} = \left| \Delta F_{err} - \Delta \hat{F}_{err} \right|$ (Hz)							
		M = 1		M = 2		M = 3		M = 4	
		Mean	STD	Mean	STD	Mean	STD	Mean	STD
48	20	1.8	1.8	1.4	1.5	1.2	1.4	1.0	1.4
43	40	2.4	2.1	1.9	1.7	1.6	1.6	1.4	1.3
38	75	3.4	2.8	2.3	2.1	2.0	1.8	1.8	1.6
33	150	5.6	4.8	3.8	2.9	3.0	2.3	2.5	1.9
28	300	12.6	10.1	7.9	5.9	4.6	3.6	3.9	31
23	600	26.1	21.8	16.0	12.6	12.1	9.8	10.1	10.6

Table 3.2: GPCDD – Fine Frequency Estimation Performance

The FFT based frequency estimation performance can potentially be degraded for large M values. To illustrate this, we plotted the normalized FFT output in Figure 3.18 as a function of M. The result pertains to PRN 14 received at a C/N_0 of 47 dB-Hz with a residual Doppler of approximately 254 Hz. The coherent integration time was set to 1 ms, which was followed by 100 accumulations resulting in a total observation period
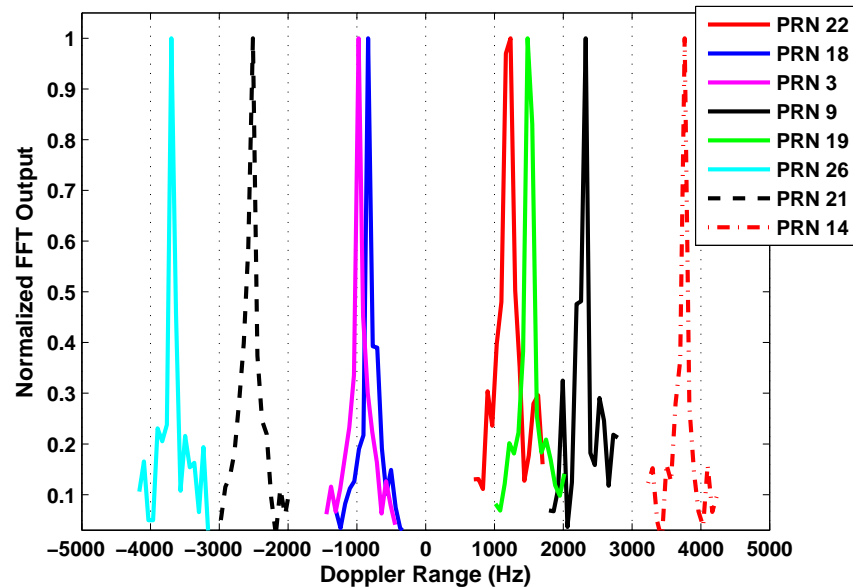
Figure 3.17: GPCDD/FFT Based Residual Doppler Estimation (C/N$_0$ = 25 dB-Hz, T$_{COH}$ = 1 ms, T = 400 ms, M = 16) (Hardware simulated GPS IF Data)

of 100 ms. Note that a 1024 point FFT was utilized to obtain a smoothened spectrum. Figure 3.18 readily confirms the fact that the frequency resolution can be increased by increasing the correlation branches (as we increase the observation period). It should be emphasized here that the larger values of M not only improve the resolution but also suppress the unwanted side-lobe (which can be clearly noticed in the plot) to allow for better estimation performance. One of the limitations of this frequency estimation technique is its inability to estimate frequencies beyond its bandwidth, which in this case is 500 Hz. To illustrate this effect, an additional error of 250 Hz was added to the original frequency offset resulting in a net frequency error of around 504 Hz. Figure 3.19 shows normalized FFT output as a function of M. In Figure 3.19, the wrapping of 504 Hz frequency error over the FFT bandwidth of 1 kHz is noted and thereby results a peak at -496 Hz. The secondary peak around 500 Hz (specifically at 504 Hz) is caused by the periodicity of the spectrum over the sampling frequency which is again 1 kHz. While there is a disadvantage of integer frequency ambiguity for frequency errors exceeding the
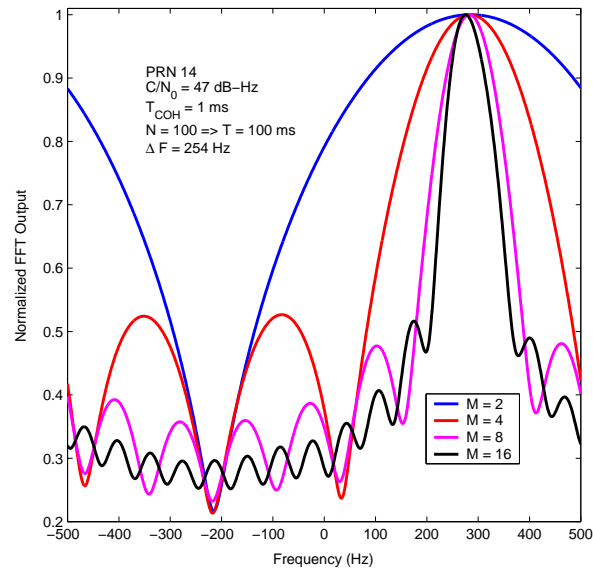
Figure 3.18: Fine Frequency Estimation Using Generalized Post-correlation Differential Detector
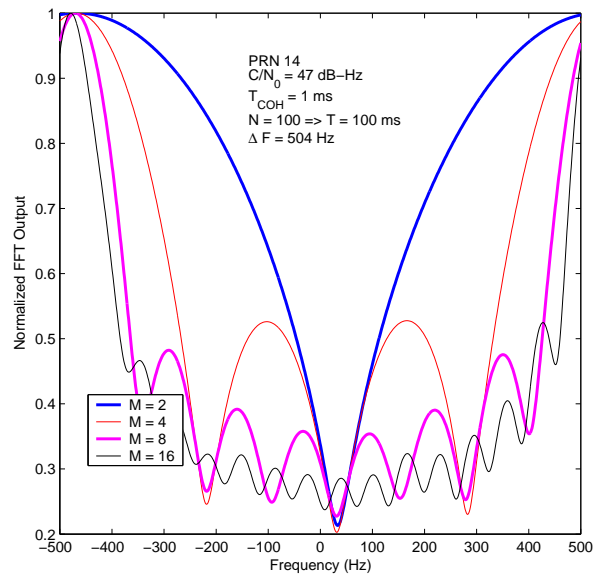
Figure 3.19: Frequency Ambiguity Limitation of Generalized Post-correlation Differential Detection

FFT bandwidth, there is also an advantage in that the uncompensated frequency errors do not incur a SNR loss[12] in the generalized post-correlation differential detection.

To further validate this notion, GPCDD based acquisition was carried out for large M. The PRN 3 signal was received at a 50 dB-Hz C/N_0 level with the residual frequency of around 1.6 kHz. The signal was then processed by the generalized post-correlation differential detector with a 1 ms coherent integration and 100 post-correlation accumulations. The residual carrier was only compensated partly leaving a frequency error of around -254 Hz. Figure 3.20 shows the effect of navigation data modulation on the generalized GPCDD scheme. In Figure 3.20, we can readily observe the split spectrum
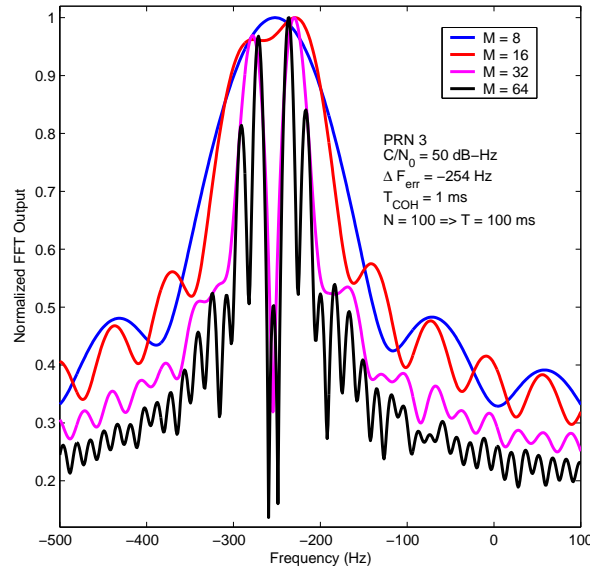
Figure 3.20: Effect of Navigation Data Modulation on Generalized Post-correlation Differential Detection

with the null occurring at the expected frequency offset. The split spectrum can readily be attributed to the phase reversal occurring for the differential detection branches (due to the data bit phase transition) with delays exceeding the data bit duration. Moreover, the spectrum shown in Figure 3.20 also closely resembles the spectrum that arises as a result of binary offset carrier modulation (Betz [2001-2002]). The binary offset carrier

---

[12]However, there is still a loss incurred in coherent matched filter due to the original frequency error

modulation (BOC) is a square subcarrier modulation, whereby the original carrier or signal is further modulated with a subcarrier that splits the spectrum of the signal into equal parts.

3.7.2 Acquisition Sensitivity Tests

To evaluate the acquisition sensitivity of the detection schemes, IF data were collected for different C/N_0 levels from 47 dB-Hz down to 22 dB-Hz in steps of 5 dB-Hz. Each detection technique was tested to compare their acquisition sensitivities in terms of the resulting PSNR, both as a function of the processing technique and as a function of various parameters such as C/N_0, coherent integration time, observation period, and differential delay. Figure 3.21 shows the acquisition sensitivity of the PDD scheme as a function of individual differential delays. The C/N_0 was set to 47 dB-Hz and the PRN 14 signal was acquired for an observation period of 100 ms with an average PSNR estimate of 21.7 dB. The PSNR estimates varied for differential delays due to the underlying noise statistics. Note that the PSNR performance is unaffected by the residual frequency offset due to the envelope detection. On the other hand, the detection output can be significantly effected if only the real part is considered as reported in Lin and Tsui [2000].

As discussed earlier, the performance of the PDD scheme was severely limited by the large SNR loss arising from the pre-correlation differential operation. Thus, the acquisition sensitivity performance of the PDD scheme was not carried out for lower C/N_0 conditions. However, it should be noted here that the PDD scheme does offer excellent immunity towards frequency errors as is further illustrated in subsequent section. Therefore, the acquisition sensitivity performance was mainly focused on the post-correlation schemes, namely the PCND (with $T_{COH} = 1$ ms, and 2 ms) and the GPCDD scheme (with M = 1 and M = 10 branches). Table 3.3 shows the average ac-
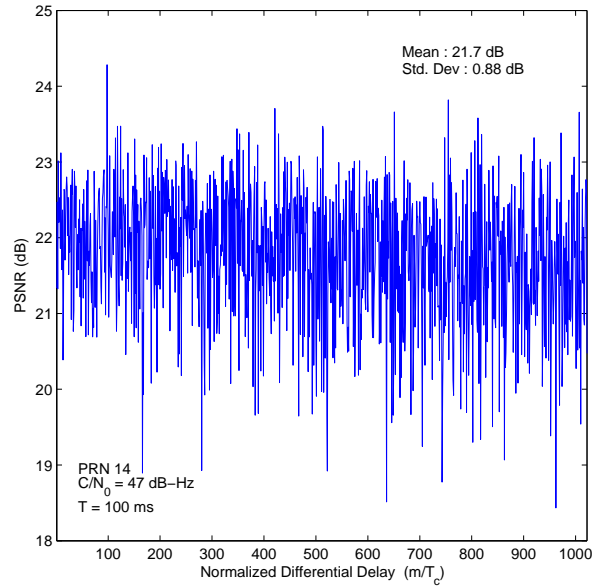
Figure 3.21: Effect of Differential Delay Selection on Pre-correlation Differential Detection Acquisition Performance

quisition sensitivity performance obtained through 250 independent trials for different C/N_0 levels. The observation period was increased accordingly with decreasing C/N_0 values to ensure proper detection performance. The GPCDD based acquisition with $M = 10$ demonstrated an average performance improvement of approximately 7 dB in comparison to $M = 1$. Similarly, the PCND with 10 ms coherent integration readily resulted in an 8 dB improvement over 1 ms coherent integration for the same observation period.

Under low C/N_0 conditions, for instance 20 dB-Hz, the detection performance of PCND with 1 ms coherent integration and that of PCDD ($M = 1$) are severely degraded resulting in an increased false acquisition. On the other hand, the noise suppression in PCND with 10 ms coherent integration and that of GPCDD with $M = 10$ resulted in minimal false acquisition conditions. Additionally, the influence of M for noise suppression under various C/N_0 conditions was also evaluated. Figure 3.22 shows the convergence of the deflection coefficient as a function of M for various C/N_0 levels. As expected, under higher to moderate C/N_0 conditions, the convergence is

C/N$_0$ (dB-Hz)	T (ms)	PSNR (dB)							
		PCND				GPCDD			
		$T_{COH} = 1$ ms		$T_{COH} = 10$ ms		M = 1		M = 10	
		Mean	STD	Mean	STD	Mean	STD	Mean	STD
45	30	42.5	1.5	48.5	2.1	48.0	1.5	50.7	2.3
40	40	34.1	1.3	41.8	2.1	39.9	1.4	45.3	2.6
35	80	27.2	1.7	35.2	1.9	32.9	1.8	39.4	2.7
30	150	20.1	1.8	28.5	2.3	25.6	1.9	33.3	2.2
25	300	12.2	2.9	21.5	2.4	17.3	3.0	26.0	2.3
20	450	3.0	7.5	13.3	3.9	3.4	9.8	16.7	4.4

Table 3.3: Acquisition Sensitivity Performance of Various Post-correlation Detection Schemes

not apparent for large values of M. On the other hand, the use of large values of M is readily apparent for low C/N$_0$ conditions. However, the incremental noise suppression decreases with M due to the presence of navigation data. Figure 3.23 shows the average acquisition sensitivity performance for various C/N$_0$ levels in the case of different detection algorithms. The final PSNR results were obtained by averaging the individual PSNR for different PRN satellites (8 in total) that were transmitted with equal power levels. As expected, the PCND with 10 ms coherent integration and the GPCDD with M=10 performed better than the PCND and PCDD schemes with 1 ms coherent integration period. Figure 3.24 shows the average PSNR convergence for the proposed GPCDD based acquisition as a function of M. As expected the plot in Figure 3.24 was consistent with the result obtained through the MATLAB based Monte-Carlo simulation as shown in Figure 3.22.

3.7.3   Acquisition Sensitivity – Blind Data Test

The previous subsections dealt with the average acquisition sensitivity performance of various detection schemes for C/N$_0$'s ranging from 45 dB-Hz to 20 dB-Hz. To further validate the acquisition sensitivity performance of the conventional and the proposed GPCDD scheme, blind tests were conducted for C/N$_0$'s 20, 18 and 16 dB-Hz. The
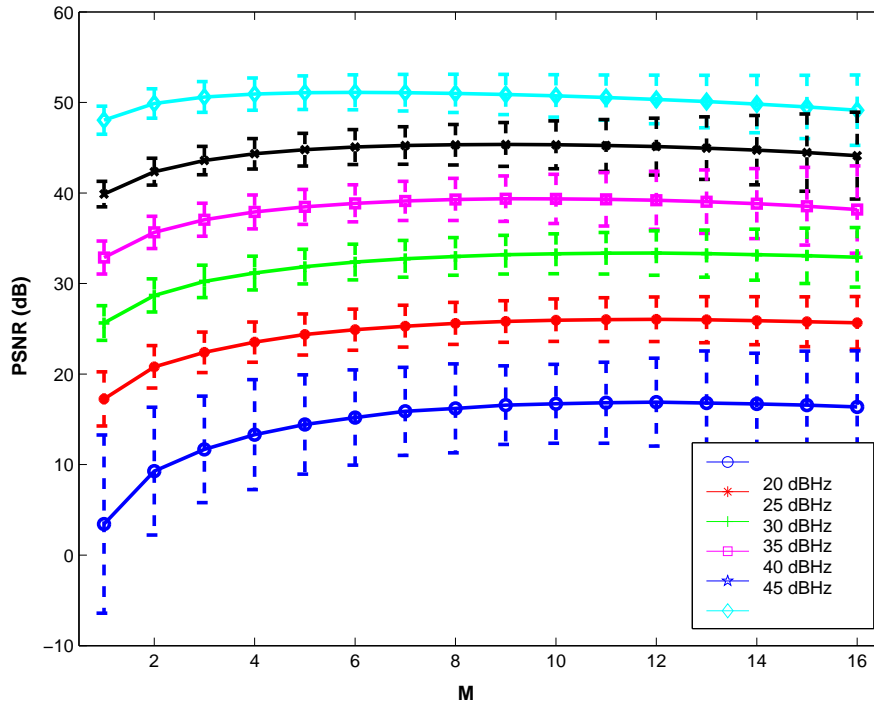
Figure 3.22: Convergence of PSNR in GPCDD based Acquisition (Averaged Result)
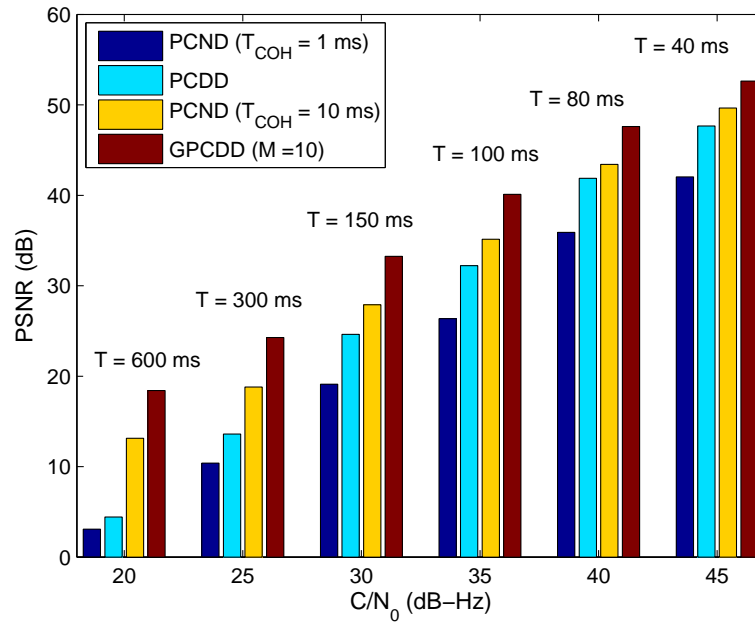
Figure 3.23: Average Acquisition Sensitivity Performance of Post-correlation Detection Schemes (Hardware Simulated GPS IF Data)
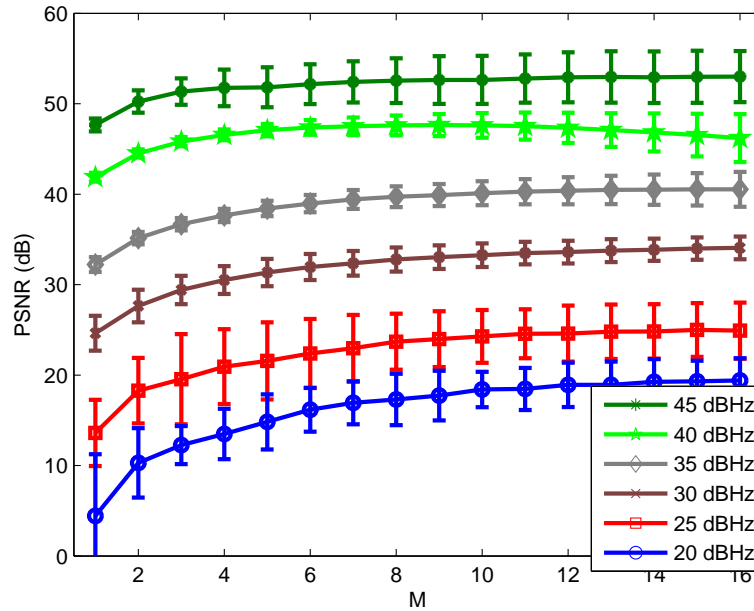
Figure 3.24: Convergence of PSNR in GPCDD based Acquisition (Averaged Result, Hardware Simulated GPS IF Data)

author was provided with IF samples of GPS L1 C/A signal, PRN information and a coarse Doppler estimate with an accuracy of $\pm$ 500 Hz. The processed results were compared to the true Doppler estimation and code phase estimation by a third party. The results of this comparison are presented in this section. The parameters pertaining to the blind data set are summarized in Table 3.4.

Parameters	Values
Centre Frequency	2 MHz
IF Bandwidth	5 MHz
C/N_0 Levels	20, 18 and 16 dB-Hz
Simulation Time	1 s
No. of PRN's	7 or 8
Doppler Uncertainty	$\pm$ 500 Hz

Table 3.4: Blind Data Test – GPS IF Data Parameters

A number of detection schemes were applied to the blind data sets and their corresponding code phase and PSNR measures were obtained. In addition, the FFT based frequency estimation of the proposed GPCDD scheme was also evaluated. The per-

formance of PCDD and PCND was also evaluated for 1 ms and 10 ms coherent integration period. The PRN Doppler estimation was carried out using the FFT/GPCDD algorithm. Subsequently, this Doppler estimate was utilized for all of the detection algorithms. The code phase estimation was rudimentary as the code phase pertaining to the strongest correlation peak is declared as the correct code phase estimation. All the detection schemes assumed no *a priori* knowledge about the navigation data phase and bit transition boundaries. Table 3.5 lists the actual, coarse and the estimated Doppler offsets for various PRNS for different C/N_0 values. The observation period was set to 1 s and the GPCDD scheme utilized an M of 10.

	C/N_0 (dB-Hz)	Doppler (Hz)							
PRN	20	1	3	10	14	22	23	25	28
Coarse	20	-4500	1000	-5000	-1500	0	500	2000	-4500
Estimated	20	-4292	825	-4970	-1225	122	-724	1969	-4482
Truth	20	-4296	826	-4965	-1252	126	-718	1958	-4477
PRN	18	3	7	10	12	13	17	19	25
Coarse	18	-2500	1500	-3500	500	5000	4000	1000	2500
Estimated	18	-2574	1614	(-3805)	512	4868	3881	1200	2294
Truth	18	-2567	1615	-3550	519	4870	3903	1178	2286
PRN	16	10	13	14	18	24	27	28	–
Coarse	16	-1000	-5000	0	0	4000	-3000	-2000	–
Estimated	16	(-1005)	(-5005)	(100)	92	4140	-3081	(-2100)	–
Truth	16	-829	-4756	-145	75	4131	-3106	-1824	–

Table 3.5: Blind Data Test – FFT/GPCDD Frequency Estimation Performance (T = 1 s, M = 10, T_{COH} = 1 ms, Values within brackets indicate false acquisition)

For a C/N_0 of 20 dB-Hz, the FFT/GPCDD successfully acquired all the PRN's and the corresponding Doppler estimates fairly accurately. The accuracy with which the Doppler can be estimated in the FFT/GPCDD scheme is determined by the value of M and the individual differential delay. For the 18 dB-Hz trial, the GPCDD was still able to acquire 7 out of 8 PRN's with good Doppler estimation. At 16 dB-Hz level, the GPCDD failed to detect 4 out of 7 PRN's. Thus, the Doppler estimates for PRN's 1,

3, 10, and 25 are actually due to false peak acquisition and cannot be used to evaluate the frequency estimation performance of the FFT/GPCDD algorithm.

Having analyzed the Doppler estimation performance of the proposed FFT/GPCDD scheme, the code phase estimation (and thus the detection) performance of the individual detection schemes was evaluated. Table 3.6 lists the true code phase as well as the estimated code phase of various detection schemes for different PRN's. The total observation period was set to 1 s and the GPCDD scheme utilized a M of 10. With 5 PRN's missed out of 8, the PCND scheme with 1 ms coherent integration demonstrated the worst performance in terms of correct code phase estimation. By increasing the coherent integration from 1 to 10 ms for the PCND scheme the performance was made better. The proposed GPCDD scheme was also able to estimate the code phase accurately for all the PRNs.

PRN No.	True Code Phase (chips)	Estimated Code Phase (chips)				
		PCND		PCDD		GPCDD
		$T_{COH} = 1$ ms	$T_{COH} = 10$ ms	$T_{COH} = 1$ ms	$T_{COH} = 1$ ms	$M = 10$
1	667.1	667.2	667.2	667.2	667.2	667.2
3	55.9	56.1	56.1	56.1	56.1	56.1
10	545.0	(256.8)	545.3	545.3	545.3	545.3
14	190.0	(427.2)	190.1	(160.1)	190.1	190.3
22	343.9	(445.4)	344.1	344.1	344.1	344.1
23	19.2	19.4	19.4	19.4	19.4	19.4
25	206.0	(926.2)	206.2	206.2	(42.8)	206.2
28	245.0	(101.3)	245.3	245.3	245.1	245.3

Table 3.6: Code Phase Estimation of Various Detection Algorithms ($C/N_0 = 20$ dB-Hz, T = 1 s, Values within braces indicate false acquisition)

Figure 3.25 shows the detection statistics for the PCDD and PCND schemes for 1 ms and 10 ms coherent integration period for PRN 14. Both the PCND and PCDD with 1 ms coherent integration were limited by the large squaring type loss, but resulted in improved performance with 10 ms coherent integration. While the PCND with 10 ms coherent integration resulted in correct code phase estimation, the reliability of the estimation can still be an issue. A limitation of the PCND scheme is the squaring

operation results in the mean of the noise samples being non-zero. This effect can readily be observed in Figure 3.25. The PCDD with 10 ms coherent integration resulted in a more reliable code phase estimation. While the PCDD scheme is attractive because noise samples remain zero mean after differential operations, it can still be limited by the unknown navigation data modulation. Finally, the GPCDD scheme also resulted in a more reliable code phase estimation. The corresponding detection statistics are plotted in Figure 3.26.
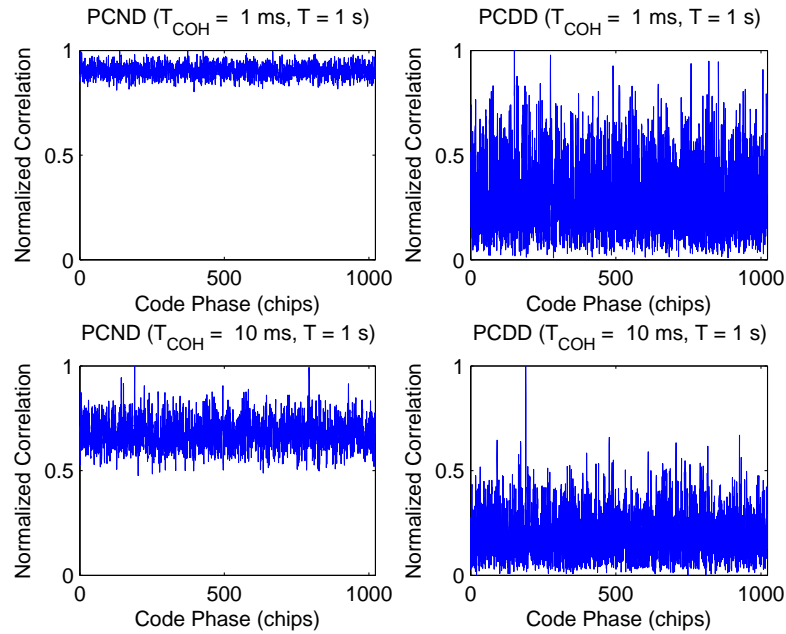
Figure 3.25: Detection Statistic of PCDD and PCND Schemes for PRN 14

For PRN 25, the PCDD scheme with 10 ms coherent integration resulted in wrong code phase estimation. However, PRN 25 was successfully acquired using PCDD with 1 ms coherent integration. Figure 3.27 shows the detection statistics as a function of the code phase for PRN 25. The apparent degradation in PCDD with 10 ms coherent integration can be attributed to the navigation data modulation. The absence of truth data does not allow any further conclusions to be drawn.

The various detection algorithms were utilized to acquire PRN's present in the 18
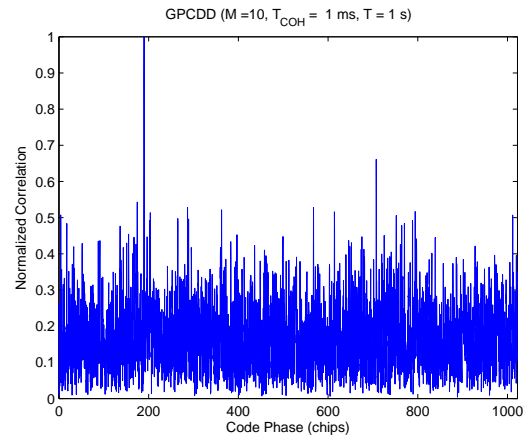
Figure 3.26: Detection Statistic of GPCDD Scheme for PRN 14
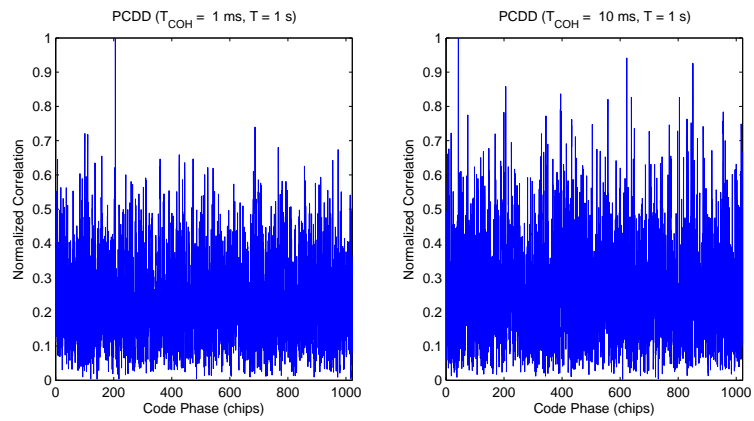
Figure 3.27: Detection Statistic of PCDD Scheme for PRN 25

dB-Hz data set. The same acquisition parameters were also utilized for this case. Table 3.7 lists the individual code phase estimates of different detection schemes for all PRN's. From Table 3.7, the limitations of utilizing for short coherent integration while using PCND or PCDD schemes with 1 ms coherent integration are apparent. The PCND scheme with 1 ms coherent integration was only able to acquire 1 out of 8 PRN's. The PCDD scheme with 1 ms coherent integration performed better with 2 successful PRN acquisitions. On the other hand, increasing the coherent integration to 10 ms resulted in 6 and 7 successful PRN acquisitions for PCND and PCDD schemes, respectively. Similarly, the GPCDD scheme was able to acquire all but one of the PRN's in the 18 dB-Hz data set.

PRN No.	True Code Phase (chips)	Estimated Code Phase (chips)				
		PCND		PCDD		GPCDD
		T_{COH} = 1 ms	T_{COH} = 10 ms	T_{COH} = 1 ms	T_{COH} = 1 ms	M =10
3	945.8	(815.3)	945.9	(613.0)	945.9	945.9
7	836.5	836.8	836.8	(975.3)	836.8	836.8
10	59.1	(683.2)	(638.1)	(167.8)	(738.0)	(393.7)
12	6.0	(251.0)	6.3	(18.2)	6.1	6.1
13	912.0	(177.4)	912.1	(564.7)	912.1	912.1
17	326.0	(386.1)	326.1	326.1	326.3	326.1
19	909.7	(313.7)	901.9	901.9	901.9	901.9
25	764.5	(759.5)	(101.7)	(336.0)	764.8	764.8

Table 3.7: Code Phase Estimation of Various Detection Algorithms (C/N$_0$ = 18 dB-Hz, T = 1 s, Values within braces indicate false acquisition)

The detection algorithms failed to acquire PRN 10 because the proposed GPCDD/FFT scheme estimated the wrong Doppler information. For instance, the GPCDD/FFT method estimated the Doppler to be -3.8 kHz, while the actual Doppler was only around -3.6 kHz. Hence, the Doppler error of 250 Hz critically attenuated the correlation power for the 10 ms coherent integration. The detection statistics for PRN 10 with estimated and truth Doppler is plotted in Figure 3.28. The detection statistics corresponding to the true Doppler case readily shows the strongest correlation peak for the correct code phase as 59.1 chips.
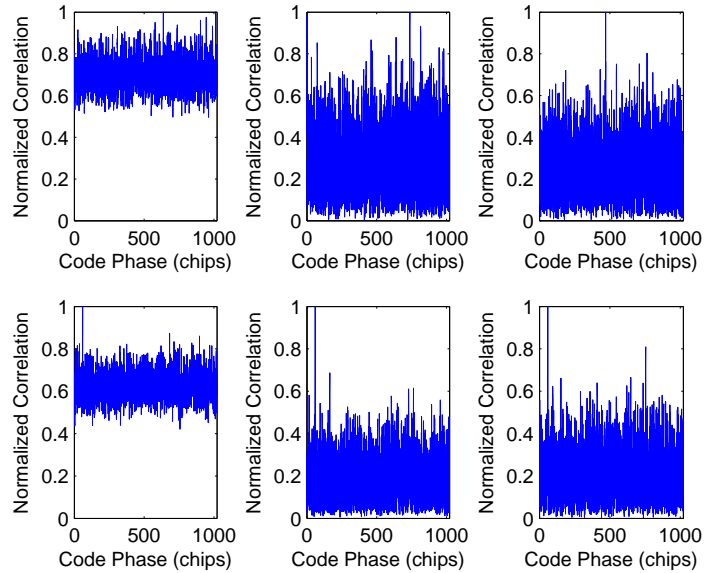
Figure 3.28: Detection Statistic of PRN 10. Top: With Estimated Doppler, Bottom: With True Doppler

Finally, the detection algorithms were applied to acquire the PRN's in the worst case, 16 dB-Hz data set. As expected, the PCND and PCDD with short coherent integration failed to acquire any of the PRN's. The PCDD scheme, even with 10 ms coherent integration was able to acquire only 1 out of 7 PRN's. The PCND with 10 ms coherent integration and the GPCDD scheme demonstrated better performance with the acquisition of 3 out of 7 PRN's. Interestingly, for PRN's 14 and 28, both these schemes yielded similar, yet incorrect, code phase estimates.

PRN No.	True Code Phase (chips)	Estimated Code Phase (chips)				
		PCND		PCDD		GPCDD
		$T_{COH} = 1$ ms	$T_{COH} = 10$ ms	$T_{COH} = 1$ ms	$T_{COH} = 1$ ms	M =10
10	488.8	(10.6)	(143.4)	(677.4)	(448.5)	(216.5)
13	738.2	(587.8)	(768.1)	(862.6)	(670.5)	(947.3)
14	947.2	(42.4)	(870.2)	(814.1)	(834.5)	(869.6)
18	633.0	(855.1)	633.2	(283.0)	(766.0)	633.2
24	1008.0	(244.3)	1008.3	(715.7)	1008.3	1008.3
27	145.9	(669.2)	146.1	(97.2)	(748.0)	146.1
28	43.6	(632.6)	(395.1)	(510.1)	(729.2)	(395.1)

Table 3.8: Code Phase Estimation of Various Detection Algorithms (C/N$_0$ = 16 dB-Hz, T = 1 s, Values within braces indicate false acquisition)

The detection statistics for successfully acquired PRN's are plotted in Figure 3.29. Note that the PCDD scheme with 10 ms coherent integration successfully acquired only PRN 24. The detection statistic for PCDD scheme was included in Figure 3.29 for completion. Comparing the individual detection statistics of the PCND and GPCDD schemes, the improved performance of the GPCDD scheme is clear. However, the reliability of the individual code phase estimation can still be an issue for these detection schemes under very low C/N_0 conditions.
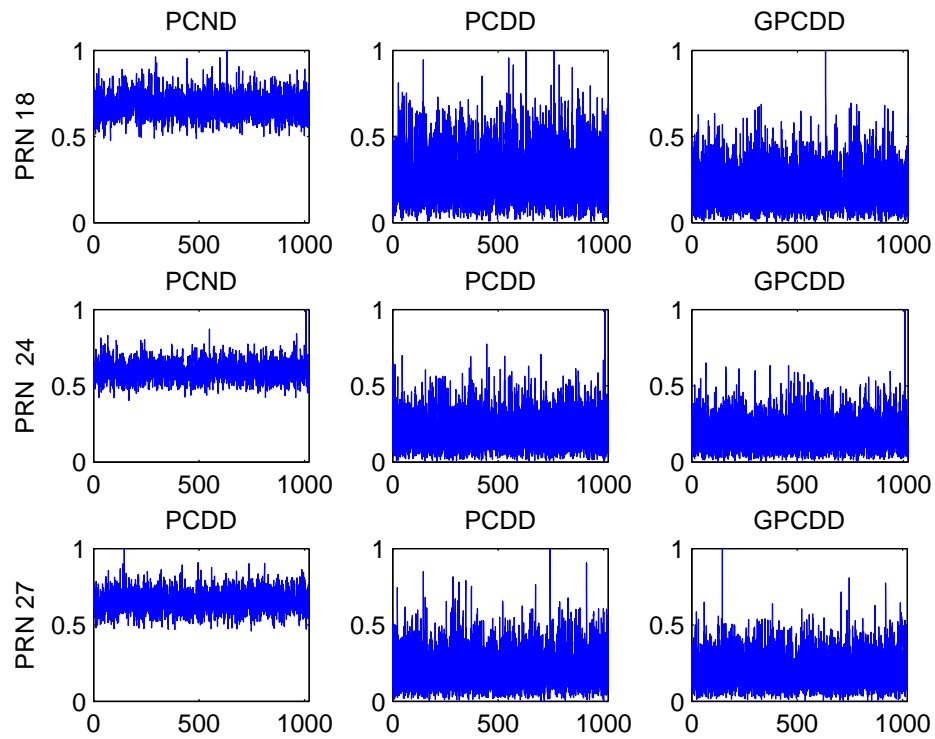
Figure 3.29: Detection Statistics Successful PRN Acquisitions (C/N_0 = 16 dB-Hz, x-axis: Code Phase (chips) y-axis: Detection Statistic)

The GPCDD algorithm proposed herein for unaided acquisition scenarios performs well but cannot evidently outperfrom the 20 ms coherent integration method followed by non-coherent integration for the case of knowing the data bit boundaries a priori. The Neyman-Pearson lemma would otherwise be violated. The GPCDD algorithm was developed under the assumption of no a priori information about the data bit boundary

or the phase of the navigation data. Even in the absence of navigation data modulation, the GPCDD algorithm could not yield better detection performance. This is because for a given fixed observation period, increasing M increases the differential delay and thus, the number of samples processed by individual detectors. Hence, for large values of M, the GPCDD algorithm follows the law of diminishing gain.

The GPCDD algorithm has many advantages however. The scheme was set herein to utilize an initial coherent integration of 1 ms, which significantly reduces the time/frequency search cells during unaided acquisition. The complex phase rotation, which is considered constant in the absence of frequency drift across individual differential detection branches in the GPCDD algorithm corresponds to the residual carrier. Utilizing the FFT to combine the individual branch outputs accomplishes both fine frequency estimation as well as coherent integration. The choice of M is typically limited by navigation data modulation and Figure 3.24 shows the convergence of the PSNR as a function of M. It can be seen that the GPCDD algorithm becomes saturated in terms of PSNR for moderate values of M. While the GPCDD algorithm shows better performance than the PCND/PCDD schemes with 1 ms coherent integration, additional analysis is required to assess the noise performance and the computational complexity in terms of gate counts.

3.7.4 Frequency Sensitivity Tests

To examine the practical tolerance of the acquisition schemes to residual frequency offset and drifts, these errors were artificially introduced during the acquisition process. The average acquisition sensitivity performance was also evaluated under the frequency drift conditions using Monte-Carlo simulations. The initial coherent matched filtering readily limited the acquisition sensitivity of the post-correlation schemes in the presence of frequency offset and drift. Initially, the influence of residual frequency offset on

the acquisition sensitivity of post-correlation schemes was evaluated by deliberately introducing a large frequency offset. The frequency offset was varied between 0 and 1.5 kHz in steps of 50 Hz. While this frequency offset range corresponds to a 0.1 ppm accuracy at GPS L1 frequency, a typical crystal oscillator will have much larger values. Figure 3.30 shows the impact of residual frequency error on the acquisition performance of different detection schemes by presenting resultant PSNR. A theoretical sinc-squared function normalized to the maximum deflection coefficient of the post-correlation noncoherent detector is also plotted. It can be readily observed that the frequency sensitivity follows the expected sinc-squared function. For instance, the first null in the PSNR was observed at a frequency of approximately T_{COH}^{-1}, as defined by the well known sinc-squared nature of this effect.
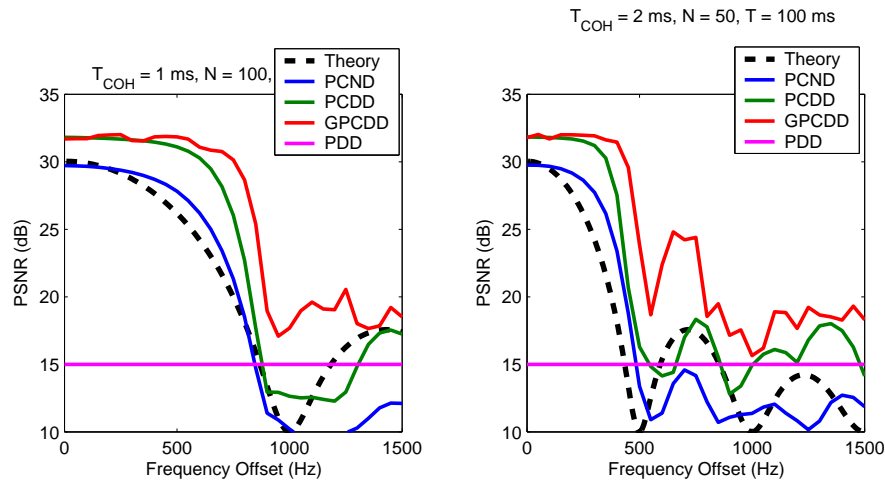
Figure 3.30: Effect of Residual Frequency Offset on Acquisition Sensitivity

The influence of residual frequency drift was also evaluated using numerical simulation. The acquisition sensitivity performance of the post-correlation schemes is tabulated in Table 3.9. The acquisition sensitivity results were obtained via 100 independent trials. The C/N_0 was fixed to 25 dB-Hz and the total observation period was set to 400 ms. The PCND with 1 ms coherent integration and GPCDD with M= 1 based acquisition demonstrated the least degradation in terms of frequency drift. PCND based

Freq.Drift (Hz/s)	PSNR (dB)							
	PCND				GPCDD			
	$T_{COH} = 1$ ms		$T_{COH} = 10$ ms		$M = 1$		$M = 10$	
	Mean	STD	Mean	STD	Mean	STD	Mean	STD
0	12.2	2.9	21.5	2.4	17.3	3.0	26.0	2.3
25	12.6	3.0	21.2	2.3	16.7	3.6	25.7	2.3
50	12.4	2.7	20.7	2.2	16.3	3.3	25.1	2.1
100	12.2	2.9	20.4	2.4	15.7	3.5	24.8	2.4
300	11.7	2.9	15.6	2.7	15.4	4.0	18.7	3.9

Table 3.9: Acquisition Sensitivity Performance of Various Post-correlation Detection Schemes

acquisition with 10 ms coherent integration degraded by 10 dB for 400 Hz/s frequency drift. GPCDD based acquisition with M = 10 experienced the worst-case degradation of around 12 dB. Figure 3.31 shows the influence of frequency drift on the acquisition sensitivity as a function of M. In Figure 3.31, the improvement in deflection coefficient with increasing M in the absence of frequency drift is observable. On the other hand, the presence of frequency drift readily degrades the deflection coefficient for large M . The frequency drift essentially manifests into a frequency offset at the output of the differential detector. Accordingly, the coherent summation (recursive filtering) in Figure 3.14 incurs a loss due the residual frequency drift. In other words, branches with longer differential delays incur more loss due to the increased residual frequency offset occurring due to the frequency drift. Therefore, it is highly desirable to use small values of M in the presence of large frequency drifts.

For pre-correlation differential detection, a constant frequency drift will manifest itself as a constant frequency offset at the output of the differential detection. The magnitude of this frequency offset is directly related to the underlying differential delays. The pre-correlation differential scheme applies coherent accumulation after the differential detection and thus the effect of constant frequency offset should appear as a sinc-squared function over the differential delays. Hence, one can expect a performance
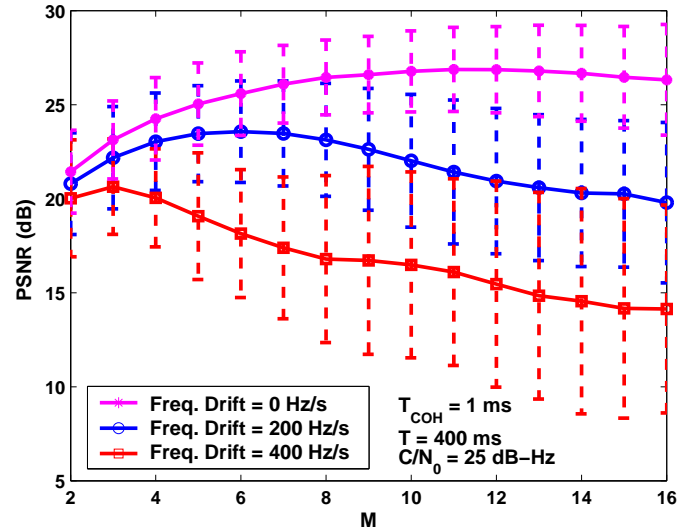
Figure 3.31: Effect of Residual Frequency Drift on GPCDD Based Acquisition

degradation for differential delays which yield a residual offset greater than the inverse of the total observation period. Figure 3.32 shows the effect of residual frequency drift on the PSNR performance of the pre-correlation differential scheme as a function of differential delay times. The total observation period was set to 200 ms. The effect of
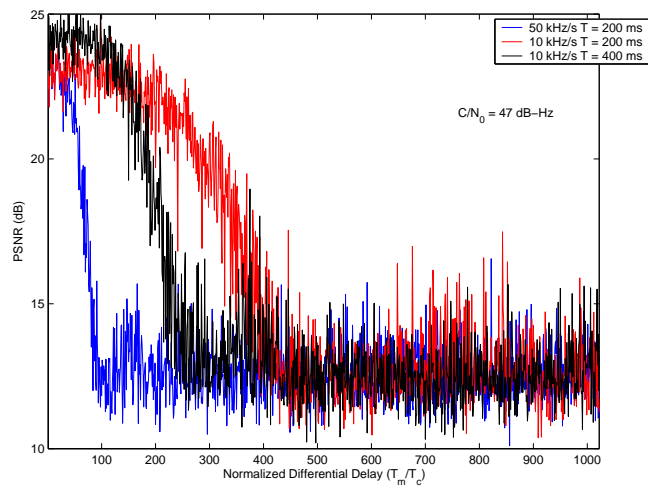
Figure 3.32: Effect of Residual Frequency Drift on Pre-correlation Differential Detection

residual frequency drift indeed followed a sinc-squared form as predicted by the theory. Moreover, the PSNR declined sharply around 100 T_c and 450 T_c for the 10 and 50 kHz

drifts, respectively. To further understand this phenomenon, let us first express the phase at the output of differential detector as,

$$\phi_m(k) = \left[\phi_t(0) + \omega k + \frac{1}{2}\varpi k^2\right] - \left[\phi_t(0) + \omega(k - T_m) + \frac{1}{2}\varpi(k - T_m)^2\right] \tag{3.146}$$

where ϖ is the Doppler drift of the frequency drift. On further expansion, the above equation can be rearranged as,

$$\phi_m(k) = T_m\left(\omega + \varpi k - \frac{\varpi T_m}{2}\right) \tag{3.147}$$

From the above equation, it is readily apparent that the effect of frequency drift translates to that of a frequency offset at the output of differential detection. Note that the differential detection output is supplied to a coherent filtering as expressed in (3.84), whose output can be represented as,

$$\begin{aligned}
\bar{\psi}(k) &= (1/N)\sum_{n=0}^{N-1} e^{j\phi_m(k - nN_cT_c)} \\
&= (1/N)\sum_{n=0}^{N-1} e^{j\phi_m(k)}e^{-j\varpi T_m nT_r}
\end{aligned} \tag{3.148}$$

The output of the coherent accumulator is readily characterized by the well known sinc-function as,

$$\bar{\psi}(k) \approx sinc(\pi\varpi T_m N N_c T_c)e^{j(\phi_m(k) - \varphi)} \tag{3.149}$$

where $\varphi = \varpi T_m(N-1)N_cT_c/2$. Thus, ignoring the noise term, the output of the matched filter including the above residual phase is given by,

$$\Psi_{PDD} = \frac{1}{N_c}\sum_{k=0}^{N_c-1} \tilde{c}_m(k)sinc(\pi\varpi T_m N N_c T_c)e^{j(\varpi k T_m + \varphi_0)}\tilde{c}_m(k - \hat{\tau}) \tag{3.150}$$

where $\varphi_0 = T_m(\omega - \frac{\varpi T_m}{2}) - \varphi$. The output of the above equation is given by,

$$\Psi_{PDD} = R_{\tau_{err}}sinc(\pi\varpi T_m N N_c T_c)sinc(\pi\varpi T_m N_c T_c)e^{j\left(\varpi\left[\frac{N_c-1}{2}\right]T_m T_c + \varphi_0\right)} \tag{3.151}$$

Thus, the effect of residual frequency drift essentially results in two sinc functions corresponding to the coherent filtering over nN_cT_c and over k. A frequency drift of 10

kHz/s over a differential delay of 450 T_c would result in a maximum frequency offset of around 4.4 Hz. Note that a coherent accumulation over 200 ms would result in a frequency null at 5 Hz. A coherent accumulation over 200 ms with 4.4 Hz would result in a severe attenuation as shown in Figure 3.32. To further validate this phenomenon, the figure also includes the PSNR performance with 5 kHz/s drift but with 400 ms observation. A coherent accumulation over 400 ms would result in a null at 2.5 Hz, which allows only for delays up to 250 T_c as they would result in a residual frequency offset of around 2.5 Hz. Similar results were obtained for the 50 kHz/s frequency drift and 200 ms observation, which would result in a residual frequency offset of 5 Hz for differential delays around 100 T_c.

3.8   Discussion

This chapter mainly focused on the enhanced acquisition of GPS C/A code signals at the pre and post-correlation levels. The GPS signal acquisition was initially introduced in the context of detection/estimation problem. The generic GLRT detection processing was shown to established a number of subsequent detection schemes practically implementable in GPS receivers for signal acquisition. Accordingly, the GLRT structure was shown to be equivalent to a *matched filter* detector for an assumed, completely known, deterministic signal. The influence of residual signals was analyzed by characterizing the output of a matched filter detector. The use of a matched filter detector can be readily found in the context of AGPS technology as it involves the carrier, code and data wipe-off through assistance information.

For a received GPS signal with unknown signal parameters, the GLRT decomposed to an *energy detector*. Moreover, the energy detector was shown to establish the well-known *incoherent matched filter detector* and the widely used *post-correlation noncoherent detector*. The incoherent matched filter introduced here is essentially an

estimator-correlator as it involves the noisy estimate of the unknown complex phase rotation at the output of the initial coherent matched filter. A limitation with these detectors is the SNR loss incurred as a result of noisy estimation of signal parameters.

Interestingly, the *post-correlation differential detector* utilized the underlying periodicity of the GPS PRN code signal to reduce this SNR loss. Accordingly, theoretical analysis established a gain of around 1.5 dB for the post-correlation differential detector over the post-correlation noncoherent detector. At the pre-correlation, the GLRT structure reduces to a *pre-correlation differential detection* in the presence of unknown carrier and navigation data modulation. In contrast to post-correlation differential detection, the pre-correlation differential detection applies the differential operation at chip-level. Consequently, it nearly suppresses the influence of the unknown residual carrier and that of navigation data modulation. The noisy estimation of signal parameters without any kind of coherent matched filtering results in a large SNR loss and thus limits the application of pre-correlation differential detection even for moderate C/N_0 conditions.

Finally, the *generalized post-correlation differential detection* was introduced and shown to comprise the well-known post-correlation noncoherent and the differential detectors. More importantly, it was shown that the asymptotic version of the GLRT is equivalent to an estimator correlator (i.e. the incoherent matched filter). The major benefit of the developed detector structure stems from its enhanced noise suppression and the ability to allow for fine frequency estimation. Most importantly, adequate noise suppression is achievable without increasing the coherent integration period. The limitations of the proposed detector structure in terms of navigation data and frequency drift was analyzed. Finally, the achievable acquisition sensitivity improvements based on the proposed detection algorithm were demonstrated using both numerical simulations and hardware simulated GPS data.

Unfortunately, the developed detectors can still be limited in some ways when ap-

plied to HS GPS acquisition. For instance, the pre-correlation differential detector although attractive in terms of robustness to residual frequency errors is severely limited due to the inherent SNR loss arising from the differencing operation. On the other hand, the post-correlation techniques, although demonstrated substantial acquisition sensitivity, are critically limited by the sensitivity to residual frequency errors.

Chapter 4

A Novel Pre-Filtering/Multi-correlation Differential Detection

Based Robust GPS C/A Code Acquisition

In the previous chapter, we considered the various forms of detectors for enhanced sensitivity GPS signal acquisition. The matched filter detector offered the best noise suppression performance but can be severely limited in terms of residual frequency errors. The post-correlation noncoherent and the differential schemes accomplished a trade-off between noise suppression and sensitivity to dynamics. However, they can still be limited due to the presence of the initial coherent matched filtering. On the other end, the pre-correlation differential detection offered the best resilience to the frequency errors but incurred huge SNR loss in the process. Consequently, the application of pre-correlation differential detection was limited to high C/N_0 environments.

This chapter begins by introducing the conflicting nature of noise suppression and frequency sensitivity. The use of a coherent pre-filtering (PF) technique to accomplish the noise suppression is presented. The effect of pre-filtering on the previously developed detector structures is discussed. It is then followed by the introduction of a *multi-correlator differential detector* (MCDD), which is the generalization of the pre-correlation differential scheme discussed in Section 3.4.4. The PRN code properties described in Section 2.2.3 of Chapter 2, are revisited in the light of MCDD. More importantly, the developed pre-filtering/multi-correlation differential detector is shown to be equivalent to the fundamental estimator-correlator. The developed PF/MCDD based acquisition and its various aspects are validated using live GPS data.

4.1   Pre-correlation Noise Suppression

Traditional matched filter theory relies on signal parameter estimation for subsequent noise suppression. For example, the matched filter allows for noise suppression through extended coherent integration. However, it also necessitates the estimation of a correct code/frequency offset so as to prevent any signal loss, which is indeed effected by the background noise. Alternatively, one can also utilize the periodicity of the underlying C/A code to perform a kind of coherent pre-filtering prior to correlation. For instance, the coherent summation of the received GPS signal with its delayed versions can potentially enhance the signal while suppressing the noise. That is,

$$\bar{x}(k) = \frac{1}{L} \sum_{l=0}^{L-1} x(k - lT_r), \ L \geq 1, \ T_r = N_c T_c. \tag{4.1}$$

where $x(k)$ is the received GPS signal that is sampled at a chip rate. For $L = 1$, the pre-filtering operation is simply disabled outputting the original samples. Substituting for the $y(k)$ from (3.4) in Chapter 3 , we have,

$$\bar{x}(k) = \sqrt{\frac{C}{2}} c(k - \tau) \left(\frac{1}{L} \sum_{l=0}^{L-1} d(k - lT_r) e^{j(2\pi \Delta F(k - lT_r) + \phi_0)} \right) + \bar{w}(k) \tag{4.2}$$

where $\bar{w}(k) = 1/L \sum_{l=0}^{L-1} w(k - lT_r)$. The C/A code $c(k)$ can be taken out of the summation as it is periodic over T_r (i.e. $c(k) = c(k - lT_r)$). Therefore, the above averaging operation enhances the signal components by suppressing the noise components. Figure 4.1 depicts the implementation of the aforementioned pre-filter using a tapped delayed line structure. In (4.2), we readily notice the effect of pre-filtering as an averaging operation on both the navigation data and the residual carrier. Hence, it is critical to analyze the influence of these residual signals on the pre-filtering to determine its applicability for pre-correlation noise suppression. The following subsections deal with the characterization of the navigation data and that of residual carrier at the output of pre-filtering.
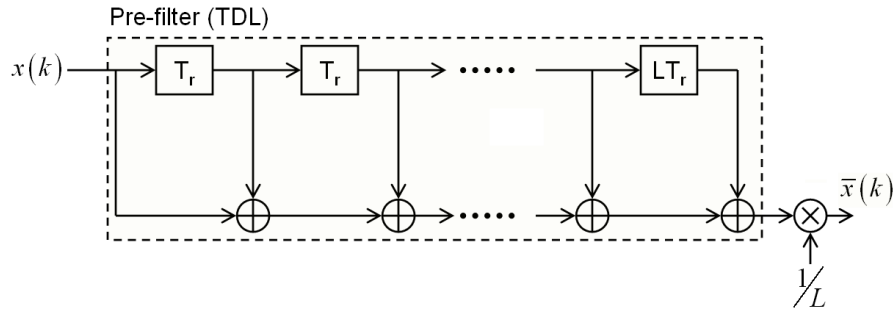
Figure 4.1: Tapped Delayed Line Implementation of Coherent Pre-Filtering

4.1.1 Effect of Residual Frequency Offset

It should be emphasized that the pre-filtering process is a linear operation and the sum of sinusoidal signals with the same frequency results in a similar sinusoid with a different phase offset. Hence, the residual carrier will still not be affected by pre-filtering although there would be a finite spectral dispersion. Ignoring the effect of data modulation, the summation in (4.2) can be written as,

$$\psi_{PF}(k) = e^{j(2\pi\Delta Fk+\phi_0)} \left(\frac{1}{L} \sum_{l=0}^{L-1} e^{j2\pi\Delta FlT_r} \right) \tag{4.3}$$

Invoking the summation identity[1] and taking $e^{j\pi\Delta FT_rL}$ from the numerator and $e^{j\pi\Delta FT_r}$ from the denominator produces,

$$\frac{1}{L} \sum_{l=0}^{L-1} \left(e^{j2\pi\Delta FT_r} \right)^l = e^{j\pi\Delta FT_r(L-1)} \left(\frac{1}{L} \frac{e^{j\pi\Delta FT_rL} - e^{-j\pi\Delta FN_cT_cL}}{e^{j\pi\Delta FT_r} - e^{-j\pi\Delta FT_r}} \right) \tag{4.4}$$

We can readily approximate the expression within the braces using the well known *sine cardinal* function (i.e. sinc(x)). Therefore, we can express (4.3) as,

$$\psi_{PF}(k) \approx e^{j(2\pi\Delta Fk+\varphi)} sinc(\pi\Delta FLT_r) \tag{4.5}$$

where $\varphi = \pi\Delta F(L-1)T_r + \phi_0$. The filtering operation expressed in (4.2) can also be viewed as a moving average process. That is,

$$\bar{x}(k) = \sum_{l=0}^{L-1} x(k)h(k - lT_r) \tag{4.6}$$

---

[1] $\sum_{i=0}^{L-1} e^i = (1 - e^L)/(1 - e)$

where $h(l)$ is the filter response and is given by,

$$h(l) = \begin{cases} \frac{1}{L} & 0 \leq l \leq L-1 \\ \\ 0 & elsewhere \end{cases} \tag{4.7}$$

The frequency response of $H(f)$ of the above filter can be written as,

$$H(f) = \frac{1}{L} \left(\frac{1 - e^{j2\pi fL}}{1 - e^{j2\pi f}} \right) \tag{4.8}$$

Figure 4.2 shows the magnitude response of $H(f)$. The pre-filter's frequency response readily followed the sinc-squared function as predicted by (4.5). More importantly, the response is periodic over 1 kHz, which is the sampling frequency of the filter itself. For example, the samples are fed to the filter at the rate of $T_r = N_c T_c$. Thus, the frequency response wraps around this sampling frequency. This result is of critical interest to the
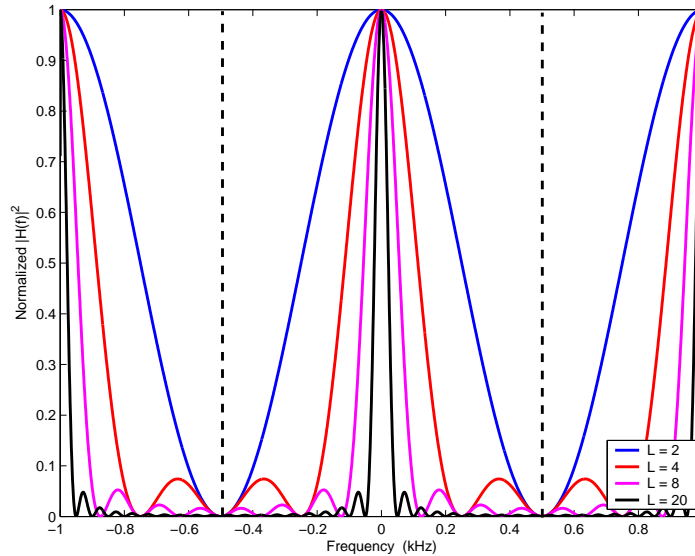
Figure 4.2: Frequency Response of Pre-Filter

development of pre-correlation noise suppression. For instance, the pre-filter's output is insensitive to frequency shifts that are integer multiples of its sampling frequency. That is,

$$H(f) = H(f + nT_r^{-1}), \ n = 0, 1, 2.. \tag{4.9}$$

Accordingly, the output of the convolution sum (4.6) should be insensitive for residual frequency offsets taking integer multiples of T_r^{-1}. For example, with a residual frequency offset of 2 kHz, we would expect the phase at the beginning of every millisecond or T_r^{-1} to take a similar value and thus add coherently. On the other hand, a 2.5 kHz residual frequency offset would be exactly out-of-phase every millisecond resulting in complete signal cancellation. This property of pre-filtering is further illustrated in Figure 4.3. The
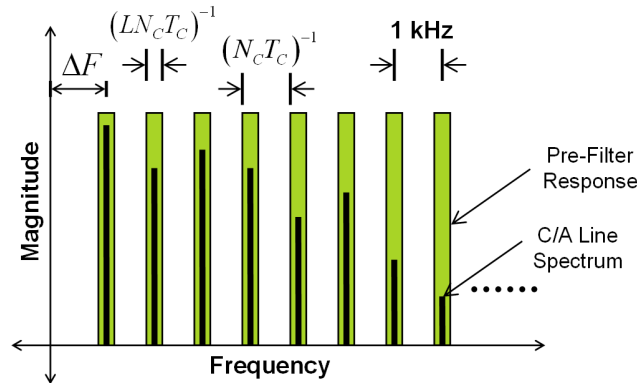
Figure 4.3: GPS C/A Code Line Spectrum and Pre-Filter's Frequency Response

spectrum of received C/A code is comprised of discrete spectral lines spaced T_r^{-1} apart but with a finite dispersion of $T_b^{-1} + \Delta F_c$ caused by the navigation data modulation and code Doppler (ΔF_c). Furthermore, the spectrum is shifted by ΔF, the residual frequency offset. The bandwidth of the pre-filter is readily determined by its maximum delay $T_L = L T_r$ and hence by the pre-filter order. Thus, the maximum filter order that could be tolerated is,

$$L_{max} \leq \frac{T_b + \Delta F_c^{-1}}{T_r} \tag{4.10}$$

From the above equation, we see that the maximum filter order is limited critically by the data modulation, which is expected based on the summation in (4.6). Owing to the periodic response (i.e. $(N_c T_c)^{-1}$ Hz), the frequency offset compensation can be accomplished with a limited frequency search within $\pm (N_c T_c)^{-1}$ Hz (i.e. $\pm$ 500 Hz) rather than the entire frequency range. However, the frequency offset is not completely

removed as the pre-filter is simply unaffected by the integer T_r^{-1} (or kilo-hertz) frequency offset. Hence, this integer frequency ambiguity should be compensated prior to any kind of correlation processing.

4.1.2 Effect of Navigation Data Modulation

In the previous section, it was observed that the maximum filter delay and hence the pre-filter order cannot exceed the navigation data bit duration (i.e. $LT_r \leq T_b$). Nevertheless, the navigation data bit transitions within the pre-filter delay will still affect the pre-filter output. To derive an expression for the loss due to data modulation, it would be initially desirable to observe the effect of pre-filtering on the navigation data. Assuming equiprobable data symbols, we can express the loss due to data modulation as a function of pre-filter delay as,

$$L_D(l) = \left|1 - \frac{T_l}{2T_b}\right|^2, \ T_l < N_D \tag{4.11}$$

where $T_l = lT_r$ is the pre-filter delay. However, we are interested in finding the net effect of pre-filtering on navigation data rather than effect due to individual delays. To determine the effect of pre-filtering on the navigation data modulation, we have to average $L_D(l)$ over l. That is,

$$L_D(L) = E\left[\frac{1}{L}\sum_{l=0}^{L-1}\left|1 - \frac{lT_r}{2T_b}\right|^2\right] \tag{4.12}$$

For $N_r >> 1$ and ignoring the variance of $L_D(L)$, we can simplify the above expression of loss incurred in pre-filtering as result of the navigation data modulation as,

$$L_D(L) = \left|1 - \frac{(L-1)T_r}{4T_b}\right|^2, \ LT_r \leq T_b \tag{4.13}$$

Figure 4.4 shows the average loss incurred in the pre-filtering process as a result of the navigation data modulation. The simulation result was obtained by averaging over 100 independent trials with 100 navigation data bits. From the plot, we can could readily

observe the maximum loss due to pre-filtering with 20-taps is around 2.5 dB as was promptly predicted in the aforementioned discussion.
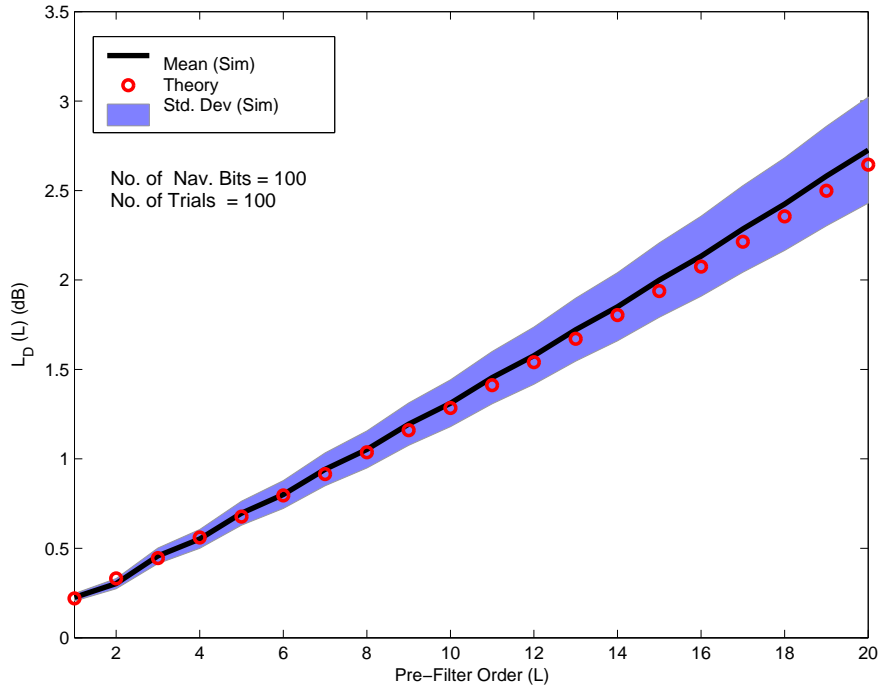
Figure 4.4: Effect of Navigation Data Modulation on Pre-Filtering – Loss Factor

The pre-filter operation introduced above not only suppresses noise but also interference. Let us consider a CW interference with the center frequency ΔF_{CW} that lies within the received C/A code spectrum. The resulting CW interference will be attenuated by the pre-filter as long as,

$$\Delta F_{CW} = \frac{n(N_c T_c)^{-1}}{2}, \; n = 0, 1, 2, \ldots \tag{4.14}$$

For instance, a CW interference with a relative center frequency (with respect to GPS L1) of around 2.5 kHz applied to pre-filter input will get canceled completely as the phase will be out-of-phase over integer millisecond durations. A similar observation can be extended to self-interference from other PRN satellites as well.

4.1.3 Effect of Pre-Filtering on Standard Detectors

Having inferred the significance of pre-filtering, it would be naturally desirable to evaluate its effect on the previously developed detectors. Instead of analyzing the pre-filtering effect on the individual detectors, we shall focus on our analysis in terms of pre-correlation and post-correlation techniques. For the post-correlation techniques, it is desirable to initially model the effect of pre-filtering at the output of coherent matched filtering. First, we shall express the pre-filter output as,

$$\bar{x}(k) \approx \sqrt{\frac{C}{2}}\bar{d}(k)c(k-\tau)sinc(\pi\Delta FLT_r)e^{j(2\pi\Delta Fk+\varphi)} + \bar{w}(k) \tag{4.15}$$

where $\varphi = \pi\Delta F(L-1)T_r+\phi_0$ and $\bar{d}(k) = 1/L\sum_{l=0}^{L-1} d(k-lT_r)$ is the averaged navigation data output. The above expression decomposes to the classical matched filter output as expressed earlier in (3.31) for $L = 1$, as the pre-filtering is eliminated[2]. Furthermore, the coherent matched filter output with the pre-filter output as its input is given by,

$$\bar{y}(n) = \frac{1}{N_cN_s} \sum_{k=nN_sN_c}^{(n+1)N_sN_c-1} \sqrt{\frac{C}{2}}\bar{d}(k)c(k-\tau)c(k-\hat{\tau})sinc(\pi\Delta FLT_r)e^{j(2\pi\Delta F_{err}k+\varphi)}+\bar{w}(k)c(k-\hat{\tau}), \tag{4.16}$$

Following a similar analysis to that of Section 3.3.2 of Chapter 3, we model the matched filter output with the pre-filter output as its input as,

$$\bar{y}(n) = \sqrt{\frac{C}{2}}\bar{d}(n)R(\tau_{err})\bar{\psi}_{\Delta F_{err}}(n) + \bar{w}(n) \tag{4.17}$$

where,

$$\bar{d}(n) = \sum_{k=nN_sN_c}^{(n+1)N_sN_c} \bar{d}(k) \tag{4.18}$$

$$\bar{w}(n) = \frac{1}{N_sN_c} \sum_{k=nN_sN_c}^{(n+1)N_sN_c} \bar{w}(k)c(k - \hat{\tau})e^{-j\left(2\pi\Delta\hat{F}k+\phi_r(0)\right)} \tag{4.19}$$

The integrated phase at the output is given by,

$$\bar{\psi}_{\Delta F_{err}}(n) = sinc(\pi\Delta FLT_r)sinc(\pi\Delta F_{err}T_r)e^{j\left(2\pi\Delta F_{err}\left[nN_c+\frac{N_c-1}{2}\right]T_c+\varphi\right)} \tag{4.20}$$

---

[2]The sinc-approximation is no longer valid for L=1. However, we have $\frac{sin(\pi\Delta FLT_r)/\pi\Delta FLT_r}{sin(\pi\Delta FT_r)/\pi\Delta LT_r} = 1$ for L=1

The above expression readily decomposes to a conventional matched filter output as derived earlier in (3.31) for $L = 1$, which is the case of no pre-filtering. Figure 4.5 shows the frequency response of the pre-filter with order $L = 2$ and that of a matched filter with a coherent integration period of 1 ms. The matched filter's response is readily characterized by the coherent integrator which also assumes a sinc-function.
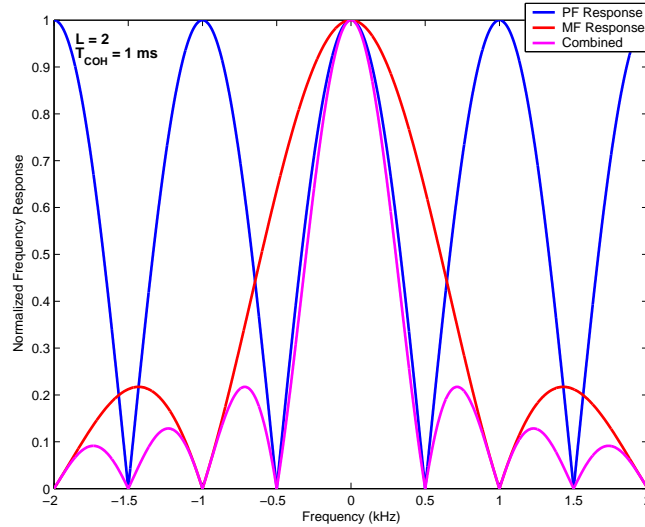
Figure 4.5: Frequency Response of Pre-Filter and that of Matched Filter

Recall that the pre-filter's response is periodic over its sampling period $(N_cT_c)^{-1}$. On the other hand, a matched filter's response is periodic over its sampling frequency T_c^{-1}. The combined (or the product) response of a pre-filter and that of a matched filter is also plotted (magenta) in Figure 4.5. As expected, the resultant response is no longer periodic over $(N_cT_c)^{-1}$. Besides, it can be noticed that the combined response is very similar to the response obtained for a 2 ms coherent integration with matched filtering. To further illustrate this, we shall express (4.16) as,

$$\bar{y}(n) = \frac{1}{N_s N_c} \sum_{k=nN_sN_c}^{(n+1)N_sN_c-1} \left(\frac{1}{L} \sum_{l=0}^{L-1} \sqrt{\frac{C}{2}} d(k)c(k-\tau)c(k-\hat{\tau})e^{j(2\pi\Delta F_{err}k+\phi_0)} + w(k)c(k-\hat{\tau}) \right)$$

$$(4.21)$$

In (4.21), the code and carrier removal processes precede the pre-filtering. This is possible because pre-filtering is a linear process and the C/A code is periodic over

N_cT_c, which is the input sampling rate of the pre-filter. Since the summations are linear processes, we can rearrange the order of the summations as well and arrive at,

$$\bar{y}(n) = \frac{1}{L}\sum_{l=0}^{L-1}\left(\frac{1}{N_sN_c}\sum_{k=nN_sN_c}^{(n+1)N_sN_c-1}\sqrt{\frac{C}{2}}d(k)c(k-\tau)c(k-\hat{\tau})e^{j(2\pi\Delta F_{err}k+\phi_0)} + w(k)c(k-\hat{\tau})\right) \tag{4.22}$$

The expression within the braces is simply the coherent matched filter output as expressed in (3.31). Therefore,

$$\bar{y}(n) = \frac{1}{L}\sum_{l=0}^{L-1}y(n) \tag{4.23}$$

Comparing the above equation with that of (3.22), we see that the $\bar{y}(n)$ is similar to the output obtained using matched filter with a coherent integration period, $T_{COH} = N_rN_cT_c$, where $N = L$. Hence, a coherent matched filter with an observation period of N_cT_c alongside a pre-filter of L is essentially similar to that of a matched filter with a coherent observation period of LN_cT_c. Therefore, the notion of pre-filtering is not critically appealing to the post-correlation techniques.

Having modelled the effect of pre-filtering on post-correlation techniques, we shall focus on the pre-filtering effect on pre-correlation techniques and thus the pre-correlation differential scheme. First, let us express the signal term at the output of pre-correlation differential detection with the pre-filter output as its input,

$$\tilde{\bar{x}}_m^S(k) = \frac{1}{N_sN_c}\sum_{k=nN_sN_c}^{(n+1)N_sN_c-1}C\tilde{\bar{d}}_m(k)\tilde{c}_m(k-\tau)sinc^2(\pi\Delta FLT_r)e^{j2\pi\Delta FmT_c} \tag{4.24}$$

where $\tilde{\bar{d}}_m(k) = \bar{d}(k)\bar{d}(k-mT_c)$. Similarly, we can express the noise and signal-noise cross terms respectively as,

$$\tilde{\bar{x}}_m^W(k) = \frac{\sqrt{0.5C}}{N_sN_c}\sum_{k=nN_c}^{(n+1)N_sN_c-1}\bar{d}(k)c(k)\psi_{PF}(k)\bar{w}^*(k-mT_c)$$
$$+\frac{\sqrt{0.5C}}{N_sN_c}\sum_{k=nN_sN_c}^{(n+1)N_sN_c-1}\bar{d}(k-mT_c)c(k-\tau-mT_c)\psi_{PF}^*(k-mT_c)(k)\bar{w}(k) \tag{4.25}$$
$$+\sum_{k=nN_sN_c}^{(n+1)N_sN_c-1}\bar{w}(k)\bar{w}^*(k-mT_c)$$

where $\psi_{PF}(k)$ is given by (4.5). From (4.24) and (4.24), we can readily make the following two observations: first, the pre-correlation differential scheme still effectively

removes the residual carrier. However, the detection output is now critically influenced by the $sinc^2(\pi\Delta FLN_cT_c)$ term arising from the pre-filtering operation. Hence, one has to compensate the residual carrier ΔF so as to minimize the loss stemming from the $sinc^2(\pi\Delta FLN_cT_c)$ term. Secondly, the pre-correlation differential scheme no longer allows frequency independent code phase acquisition as a consequence of using pre-filtering.

Employing pre-filtering can provide the necessary SNR gain to compensate for the inherent squaring type loss in the pre-correlation differential scheme. Recall that the pre-filter's response is periodic over $(N_cT_c)^{-1}$. Accordingly, the term $sinc^2(\pi\Delta FLN_cT_c)$ is also periodic over $(N_cT_c)^{-1}$. Thus, it is insensitive to residual frequency error that are integer multiples of $(N_cT_c)^{-1}$ (i.e. $\Delta F_{err} = n(N_cT_c)^{-1}$), where $|\Delta F - \Delta\hat{F}| = \Delta F_{err}$. Consequently, the response of the pre-filtering/pre-correlation differential scheme is periodic over $(N_cT_c)^{-1}$ in the frequency domain. Therefore, one has to search within $(N_cT_c)^{-1}$, or 1 kHz in our case, to incur minimal loss due to the frequency selectivity of the pre-filter. By performing this limited search, the pre-correlation differential scheme allows for a finer frequency estimation although an integer ambiguity n still exists. Note that the residual carrier can still be estimated using the differential phase $e^{j2\pi\Delta FmT_c}$ as described in Section 3.4.4 of Chapter 3. More importantly, the background noise is suppressed by a factor of L which is significant to the performance of the pre-correlation differential scheme.

In summary, the pre-correlation suppression utilizing a coherent pre-filtering can provide a substantial advantage to the pre-correlation differential although it simply implements an extended coherent integration for the post-correlation schemes. Interestingly, the pre-filtering/pre-correlation differential combination offers a flexible trade-off between the noise suppression and residual frequency sensitivity.

4.1.4 Multi-correlation Differential Detector

In Section 3.4.4 of Chapter 3, it was inferred that a GLRT structure at the pre-correlation level reduces to the pre-correlation differential detection. Furthermore, the decision statistics for the pre-correlation differential scheme did not utilize the maximum likelihood estimate so as to allow for code phase estimation. It accomplished the code phase estimation by choosing delays greater than the chip duration so that the resulting PRN code signal was no longer correlated. On the other hand, the navigation data modulation and the residual carrier were highly correlated over this delay and were effectively removed through differential detection. Consequently, the GPS signal acquisition resulted in a one-dimensional search in code phase. However, the noisy estimation was performed prior to any coherent filtering and thus resulted in a large SNR loss.

This section introduces the *multi-correlation differential detection*, which can readily be considered the generalization of the aforementioned pre-correlation differential detection. The MCDD scheme similar to the post-correlation generalization scheme, the GPCDD structure, utilizes an ensemble of delayed signal estimates and multiple correlations to suppress the inherent SNR loss. In order to develop the decision statistics of the proposed MCDD scheme, we shall model the detection of GPS signal as:

$$
\begin{aligned}
H_0 : x(k) &= w(k) & k &= 0, 1, 2, \ldots NN_s - 1. \\
H_1 : x(k) &= s(k) + w(k) & k &= 0, 1, 2, \ldots NN_s - 1.
\end{aligned}
\tag{4.26}
$$

where $s(k) = \sqrt{C/2}d(k-\tau)c(k-\tau)e^{j(2\pi\Delta Fk+\phi_0)}$. The signal is being observed over a duration of $N = TT_s^{-1}$ samples, wherein it is assumed that $s(k)$ is periodic over N_c as the underlying code $c(k)$ is periodic over N_c. Alternatively, we can also view that the receiver has N_r observations of $s(k)$ of length N_sN_c. While the above assumption is only an approximation, the issue will be addressed later during the analysis of residual signal effects. From Section 3.4.4 of Chapter 3, we have the ensemble estimates (but

adhoc) of the received PRN code signal as,

$$\hat{s}(k) = x(k - T_m)$$
$$= \sqrt{\tfrac{C}{2}} d(k - \tau - T_m)c(k - \tau - T_m)e^{j(2\pi \Delta F(k - T_m) + \phi_0)} \ m = 1, 2, ..., \ m \neq N_c \tag{4.27}$$

Interestingly, we can exploit the fundamental characteristics of $s(k)$ to let the code or the carrier component be correlated or decorrelated. For example, in the case of a received GPS signal, the code is correlated within T_c and the correlation is periodic over T_r. Thus, we can either accomplish code and carrier suppression by equating the delay T_m to:

$$T_m = \begin{cases} mT_c, & 1 \leq m \leq N_c, \ m \neq N_c \\ mN_cT_c & m = 1, 2, \ldots \end{cases} \tag{4.28}$$

For the received GPS signal, the first choice essentially eliminates the residual carrier and that of data modulation as it is correlated over the delay. On the other hand, the second choice suppresses the code completely, and the residual carrier and navigation data to a certain extent. However, we can estimate the residual carrier using the complex phase rotation arising at the output as discussed in Section 3.4.4 of Chapter 3 and further summarized in (3.85). Substituting, for $\hat{s}(k)$ from (4.27) in the original test statistic (3.60) of Chapter 3 and upon further summing across the pre-correlation differential delays (m) produces,

$$T_{MCDD}(\mathbf{x}) = \frac{1}{M} \sum_{m=1}^{M} \frac{1}{N - mN_s} \sum_{k=m}^{N-1} [x(k)x^*(k - mT_c)] [c(k - \hat{\tau})c(k - \hat{\tau} - mT_c)] \tag{4.29}$$

From the above equation, we can see that the developed MCDD scheme allows for an additional gain of $10\log_{10}(\text{M})$ due to the summation across m. This additional gain can compensate for the SNR loss incurred during the individual differential operations. Moreover, the number of correlation branches is not limited by N_c as the code is periodic over N_c. However, the residual signal influence is not entirely eliminated and their effect on the final decision statistics should be characterized prior to any detection

performance analysis. Substituting $M = 1$ in the above decision statistics decomposes to that of the pre-correlation differential detection one as defined in (3.78) of Chapter 3. The above decision statistics can be further expanded as,

$$T_{MCDD}(\mathbf{x}) = \frac{1}{M} \sum_{m=1}^{M} \frac{1}{N - mN_s} \sum_{k=0}^{N-m} \left[x_m^{ss}(k) + \tilde{x}_m^{ww}(k) + \tilde{x}_m^{sw}(k) \right] \tilde{c}_m(k - \hat{\tau}) \qquad (4.30)$$

The individual terms $x_m^{ss}(k)$, $x_m^{sw}(k)$, and $x_m^{ww}(k)$ are given by

$$
\begin{aligned}
x_m^{ss}(k) &= \tfrac{C}{2} \tilde{d}_m(k - \tau) \tilde{c}_m(k - \tau) e^{j2\pi\Delta F m T_c} \\
x_m^{sw}(k) &= \sqrt{\tfrac{C}{2}} d(k - \tau) c(k - \tau) e^{j(2\pi\Delta F k + \phi_0)} w^*(k - mT_c) \\
&\quad + \sqrt{\tfrac{C}{2}} d(k - \tau - mT_c) c(k - \tau - mT_c) e^{j(2\pi\Delta F(k - mT_c) + \phi_0)} w(k) \\
x_m^{ww}(k) &= w(k) w^*(k - mT_c)
\end{aligned}
\qquad (4.31)
$$

where $\tilde{d}_m(k) = d(k)d(k - mT_c)$ and $\tilde{c}_m(k) = c(k)c(k - mT_c)$.

4.1.5   Residual Signal Effects

The MCDD structure is of critical interest as it involves a substantial additional gain due to the accumulation of multiple correlations (i.e. across m). Thus, it would be desirable to evaluate the influence of various signal effects on the developed detector. The following sections characterize the influence of the residual carrier and that of navigation data modulation on the proposed MCDD structure.

Robust Frequency Estimation

The influence of residual carrier on the developed detector can be understood by analyzing the signal component alone at the output of the detector (i.e. $x_m^{ss}(k)$). Ignoring the effect of navigation data modulation, we can express the detection output for the correct code phase by

$$\Psi_{MCDD}(\tau) = \frac{1}{M} \sum_{m=1}^{M} \frac{1}{N - m} \sum_{k=m}^{N_r N_c - 1} \frac{C}{2} e^{j2\pi\Delta F m T_c} \qquad (4.32)$$

From the above equation, we see that the differential detection over T_m transforms the time varying residual phase into a complex phase rotation that is coherently related to

the residual frequency offset (ΔF) and the differential delay (T_m). Interestingly, the above expression can be further simplified as,

$$\Psi_{MCDD}(\tau) \approx \frac{MN_sC}{2}\left[N_rN_c - \frac{(M+1)}{2}\right]sinc(\pi\Delta FMT_c) \qquad (4.33)$$

From the above equation, we see that the MCDD detection output can still be influenced by residual carrier and the corresponding loss follows the well-known sinc function. Interestingly, the complex phase rotations in (4.32) collectively embody the original residual carrier. However, the residual carrier is now sampled at the basic chip rate T_c due to chip differential delay selection. Accordingly, we can utilize an FFT based combining of the individual differential detection outputs as discussed earlier in Section 3.5.2 for the GPCDD scheme. For uniform chip-differential delay selection, we have the bandwidth and the resolution of the FFT based estimator as

$$\begin{aligned}\Gamma_{BW} &= \frac{1}{T_c} \\ \Gamma_{RES} &= \pm\frac{1}{MN_cT_c}\end{aligned} \qquad (4.34)$$

Hence, the bandwidth of the FFT based estimator is $\Gamma_{BW} = 1.023$ MHz. Accordingly, the developed estimator will readily acquire GPS signals as long as the residual carrier offset (ΔF) is within a staggering ± 511.5 kHz. This result is of critical significance in applications where the receiver experiences significant clock offset. The resolution of the resulting FFT based estimator is 2 kHz or ± 1 kHz. Note that the resolution can be further improved by either increasing M or by reducing the sampling rate by choosing an integer multiple of the chip duration for differential delay. Figure 4.6 depicts the proposed multi-correlation differential detection scheme, wherein the FFT based estimator/combiner was utilized.

Loss Due to Data Modulation

One of the central advantages of pre-correlation schemes is the ability to nearly elimi-nate the data modulation effects as established in Section 3.4.4 for the pre-correlation
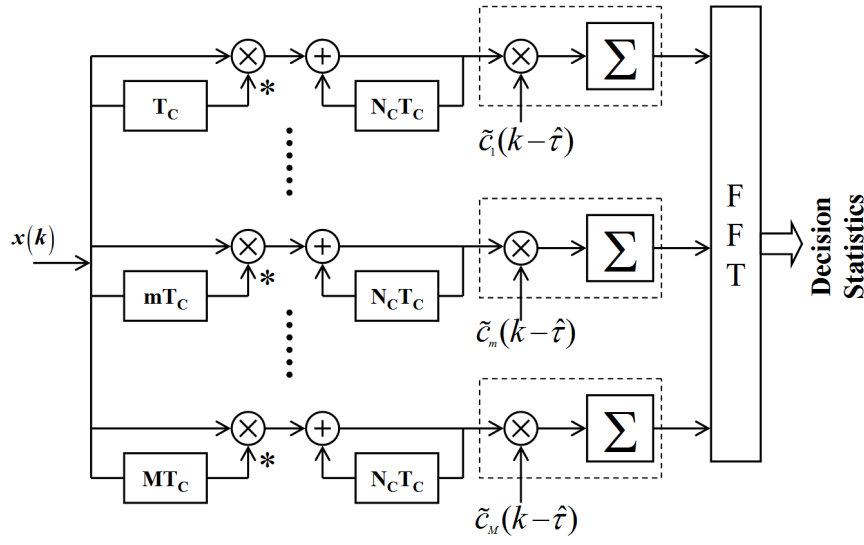
Figure 4.6: Multi-correlator Differential Detector Implementation with FFT Based Estimation/Combining

differential detector. The effect of data modulation for a specific differential delay was derived in Section 3.4.4 and is rewritten here as,

$$L_D(T_m) = \left|1 - \frac{T_m}{T_b}\right|^2, \ T_m = mT_c, \ T_m < T_b \tag{4.35}$$

The above loss expression was obtained as an approximation for the pre-correlation differential detector with a corresponding delay of T_m. However, we are interested in the net effect of navigation data modulation on the MCDD scheme. Accordingly, the loss expression in (4.35) is integrated over m to obtain the loss in the MCDD scheme due to navigation data modulation. As the navigation data is correlated for $T_m << T_b$, the following approximation is applicable,

$$L_D(M) \approx E\left[\frac{1}{M}\sum_{m=1}^{M}\left|1 - \frac{mT_c}{T_b}\right|^2\right] \tag{4.36}$$

The above loss expression

$$L_D(M) = \left|1 - \frac{(M+1)T_c}{2T_b}\right|^2, \ MT_c < T_b \tag{4.37}$$

Figure 4.7 shows the power loss due to data modulation for the developed multi-correlation differential detector. From the plot, we readily observe that $L_D(M)$ is

practically zero for $MT_c << T_b$. The multi-correlator differential detector incurs a loss of around 0.45 dB for a delay of $M = N_c$ (and hence a maximum delay of 1 ms), which is consistent with the loss estimates obtained for the GPCDD scheme with millisecond differential delay. Thus, we can see that the developed multi-correlation differential detector is capable of providing substantial gain while incuring a minimal loss due to data modulation.
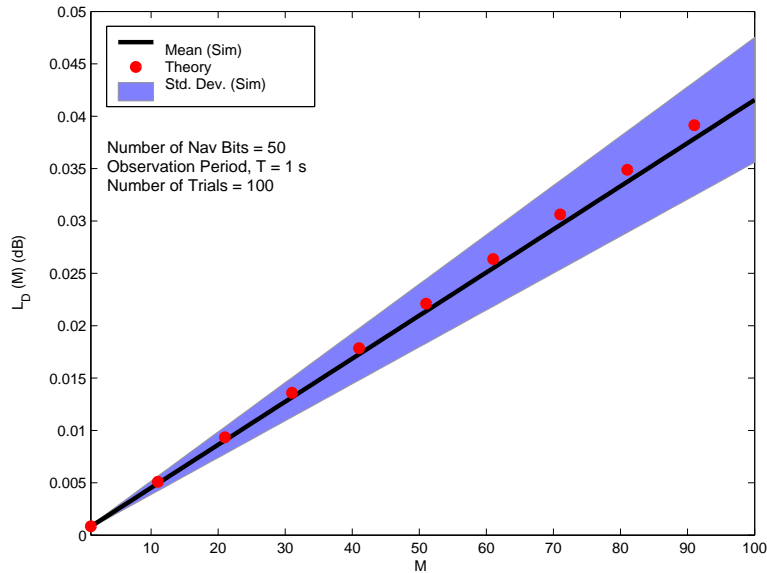
Figure 4.7: Power Loss Due to Navigation Data bit Transitions

4.1.6   Correlation Performance

The effect of the delay-and-multiply operation on GPS C/A codes and thus Gold codes were established in Section 2.2.3. There it was noted that the effect of the DAM operation on the Gold sequence results in an another Gold sequence from the family of $N_c + 1$ Gold sequences. Thus, the differential detection output across the individual branches in Figure 4.6 can be considered a different Gold sequences. Hence, it is importat to analyze the overall correlation performance of multi-correlator differential detector. First let us express the correlation output considering only the C/A code as the input to the

multi-correlator differential detector as,

$$R_M(\tau) = \sum_{m=1}^{N_c-1} R_m(\tau), \ \tau = 0, 1, 2, \ldots, N_c - 1. \tag{4.38}$$

where $R_m(\tau)$ is the individual correlation output of the mth branch and is promptly given by,

$$R_m(\tau) = \sum_{k=0}^{N_c-1} \tilde{c}_m(k)\tilde{c}_m(k-\tau), \ \tau = 0, 1, 2, \ldots, N_c - 1 \tag{4.39}$$

where $\tilde{c}_m(k) = c(k)c(k-m)$. In Section 2.2.3, it was proved that $\tilde{c}_m(k), m \neq N_c$ is indeed a Gold sequence. Thus, the correlation function can be represented using the three-level cross and four-level auto-correlation function as expressed in (2.8) of Section 2.2.2 in Chapter 2 and rewritten here as,

$$R_m^{AC}(\tau) = \begin{cases} 1 & \tau = 0 \\ \left\{ \frac{63}{1023}, \frac{-1}{1023}, \frac{-65}{1023} \right\} & \tau \neq 0 \end{cases}$$

$$R_m^{CC}(\tau) \in \left\{ \frac{63}{1023}, \frac{-1}{1023}, \frac{-65}{1023} \right\} \tag{4.40}$$

where $R_m^{AC}(\tau)$ and $R_m^{CC}(\tau)$ are the respective auto-correlation of $c_m(k)$ and cross-correlation of $c_m(k)$ with $c_n(k)$ $n \neq m$. Accordingly, adding individual correlation outputs $R_m(\tau)$ coherently can potentially result in cancellation of auto-correlation side-peaks and cross-correlation. Figure 4.8 shows the auto-correlation output for the PRN 1 C/A code signal and cross-correlation output of PRN 1 C/A code signal with that of PRN 24 (red) for MCDD based correlation with $M = N_c - 1$. The plot also includes the correlation output with a standard correlation technique (blue). Figure 4.8 readily shows the auto-correlation side-peak and cross-correlation peak cancellation in the developed MCDD scheme. The MCDD based correlation resulted in a peak to side-lobe ratio (PSLR) of around 50.1 dB, a 26.2 dB improvement over the 23.9 dB obtained with standard correlation. The PSLR is readily defined by,

$$PSLR = 10\log_{10} \frac{|R(\tau = 0)|^2}{max\,|R(\tau \neq 0)|^2} \tag{4.41}$$
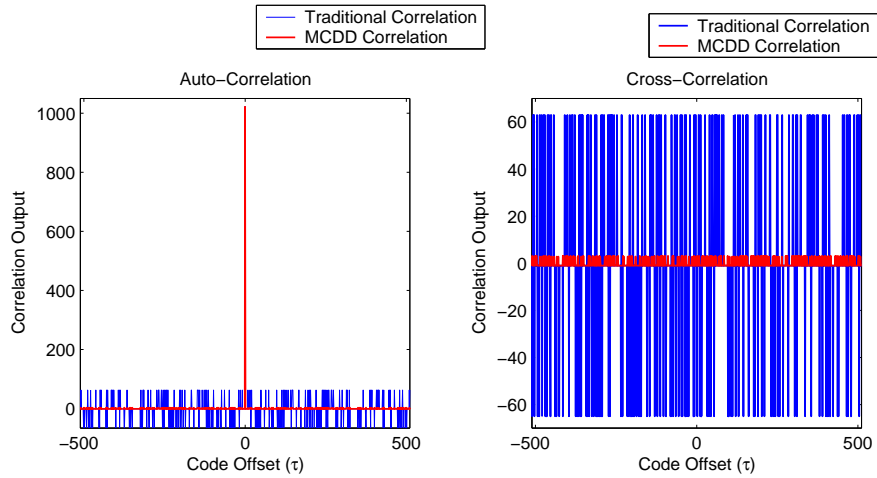
Figure 4.8: Auto-correlation and Cross-correlation Outputs for Standard Correlation and MCDD Scheme

The aforementioned gain of around 26.2 dB is accomplished through MCDD by setting $M = N_c - 1$. However, in many applications, the large number of correlations is not required. Hence, it would be desirable to assess the effect and thus convergence of PSLR as a function of correlation summations. Figure 4.9 shows the auto-correlation and cross-correlation suppression PSLR performance of MCDD scheme as a function of correlation summations. The auto-correlation plot includes all the PRN's from 1 to 37 and the cross-correlation includes their combinations. The plot readily shows the convergence of both auto and cross-correlation performance for all the GPS PRN C/A codes. Interestingly, the cross-correlation between PRN 34 and 37 resulted in 0 dB, which was surprising. The simple fact that PRN 34 and 37 are one and the same was overlooked during the analysis, which resulted in this unexpected result.

The plot also shows theoretical convergence based on the central limit theorem (Solid Black) as the auto-correlation side-peaks and cross-correlation peaks are assumed to be independent but identically distributed. The theoretical convergence closely approximates the result for a larger number of correlation summations as predicted by theory. Interestingly, the maximum correlation suppression was achieved initially at $M = 512$ and then followed by $M = 1022$. Furthermore, there exists a degradation immediately
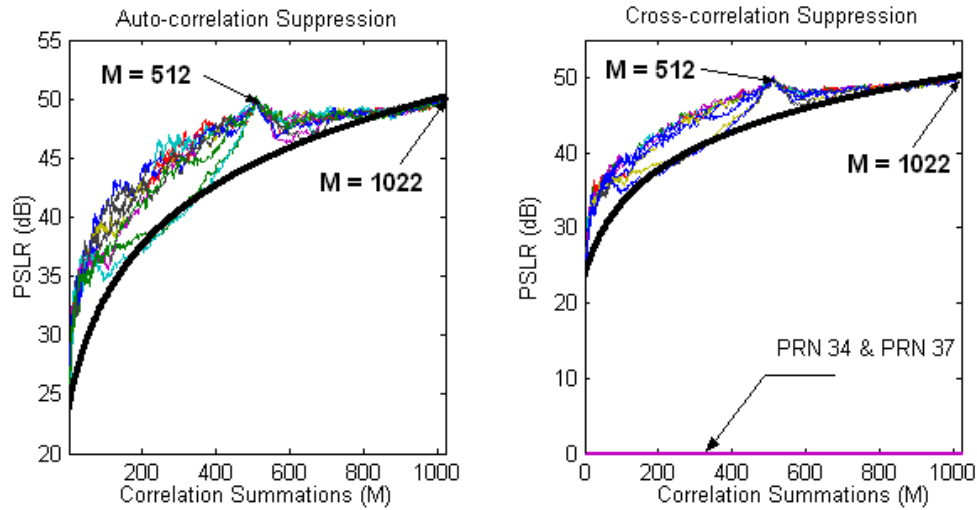
Figure 4.9: PSLR Performance of Standard Correlation and MCDD Scheme (Left) Auto-correlation (Right) Cross-correlation (Solid Black:Theory)

after $M = 512$ followed by a gradual increase that eventually peaks at $M = 1022$. The degradation after $M = 512$, readily indicates that the process in no longer independent, which means that out-of-phase auto-correlation and cross-correlation no longer cancel each other. To further investigate this phenomenon, the cross-correlation between $\tilde{c}_{512}(k)$ and $\tilde{c}_{511}(k)$ is plotted in Figure 4.10.
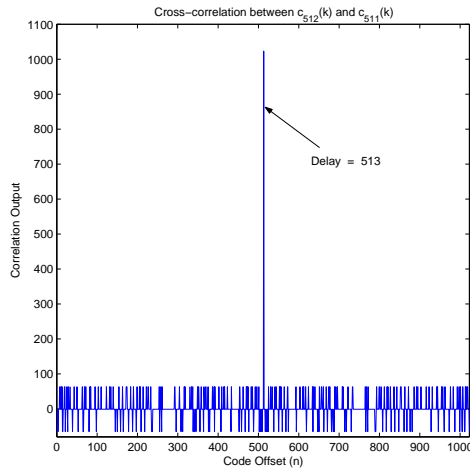
Figure 4.10: Cross-correlation Between $\tilde{c}_{512}(k)$ and $\tilde{c}_{511}(k)$

The cross-correlation plot in Figure 4.10 is essentially an auto-correlation, as we see the perfect four-level correlation between the $\tilde{c}_{512}(k)$ and $\tilde{c}_{511}(k)$. Hence, the code

sequence generated by choosing delays $m_1 = 511$ and $m_2 = 512$ resulted in the same modified sequence. However, there was a delay of $\tau_m = 512$ or 513 depending on whether $\tilde{c}_{511}(k)$ is correlated with $\tilde{c}_{511}(k)$ or vice-versa. On further investigation, it was found that the phenomenon was actually a resultant of code periodicity. To further understand this phenomenon, let us consider the effect of choosing different delays on the SAM operation. For example, Figure 4.11 shows the SAM output for two different delays $m_1 = 1$ and $m_2 = 1022$. In the case of $\tilde{c}_1(k)$, the first chip would be multiplied by the second one and the 1022 chip will be multiplied by the 1023rd chip. Similarly, the first chip will be multiplied by 1023rd chip for $\tilde{c}_{1022}(k)$. On the other hand, the 1023rd chip of $\tilde{c}_{1022}(k)$ will be multiplied with 2045th chip. But, we know the the code $\tilde{c}(k)$ is periodic over N_c. Hence, the product $c(1023)c(2045)$ is equivalent to $c(1023)c(1022)$, which is of course the one chip delayed version of $c_1(k)$. Thus, it can be inferred that the resultant of delay-and-multiply operation over m_1 is similar to the output obtained with the delay $N_c - m$.
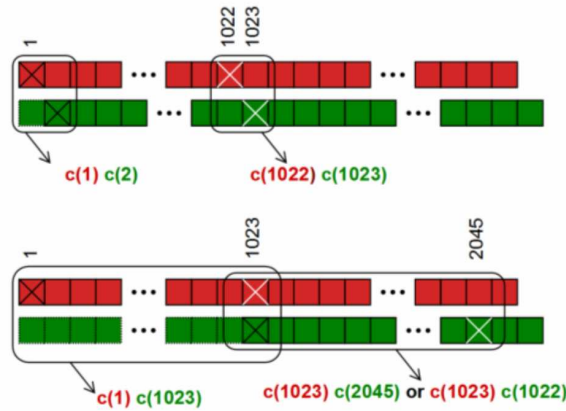
Figure 4.11: Shift-and-multiply Outputs for $m_1 = 1$ and $m_2 = 1022$

To prove this prediction, let us write the correlation of the modified code obtained by choosing m_1 as,

$$R_{m_1}(\tau) = \sum_{k=0}^{N_c-1} \left[c(k)c(k - m_1) \right] \left[c(k - \tau)c(k - m_1 - \tau) \right] \quad \tau = 0, 1, 2, \ldots, N_c - 1. \quad (4.42)$$

Replacing $k - m_1$ by a dummy variable k' in the above correlation produces

$$R_{m_1}(\tau) = \sum_{k'=-m_1}^{N_c-1-m_1} \Big[c(k'+m_1)c(k')\Big]\Big[c(k'+m_1-\tau)c(k'-\tau)\Big] \qquad (4.43)$$

Invoking the code periodicity, we have

$$R_{m_1}(\tau) = \sum_{k'=-m_1}^{N_c-1-m_1} \Big[c(k'-(N_c-m_1))c(k')\Big]\Big[c(k'-\tau+(N_c-m_1))c(k'-\tau))\Big] \qquad (4.44)$$

Replacing $\tau + (N_c - m_1)$ by a dummy variable τ', we have,

$$R_{m_1}(\tau'-m_1) = \sum_{k'=-m_1}^{N_c-1-m_1} \Big[c(k'-(N_c-m_1))c(k')\Big]\Big[c(k'-\tau')c(k'-\tau'-(N_c-m_1))\Big] \qquad (4.45)$$

Since $c(k')$ is periodic over N_c we can readily omit $-m_1$ from the summation. Therefore,

$$R_{m_1}(\tau'-m_1) = \sum_{k'=0}^{N_c-1} \Big[c(k')c(k'-(N_c-m_1))\Big]\Big[c(k'-\tau')c(k'-(N_c-m_1)-\tau')\Big] \qquad (4.46)$$

The right hand side of the above equation can be represented by $R_{N_c-m_1}(\tau)$. That is

$$R_{m_1}(\tau'-m_1) = R_{N_c-m_1}(\tau') \qquad (4.47)$$

Equivalently,

$$c_{m_1}(\tau'-m_1) = c_{N_c-m_1}(\tau') \qquad (4.48)$$

This result is important to the developed MCDD scheme. The result essentially implies that there are only $(N_c - 1)/2$ distinct modified C/A codes that are obtained through delay-and-multiply operation. On the other hand, we need to generate only $(N_c - 1)/2$ codes, as the other sequences can be obtained by delaying their corresponding counterparts. The PSLR convergence plot shown in Figure 4.9 indicates that the number of correlations (M) can be reduced at the expense of some correlation performance degradation. Furthermore, the modified C/A codes obtained through the delay-and-multiply operation, employing delays m_1 and $N_c - m_1$, can be added coherently for a slowly varying residual carrier. Figure 4.12 shows an implementation that combines two individual differential detectors' output based on the derived result.
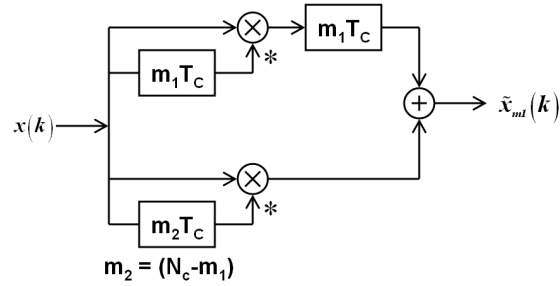
Figure 4.12: Differential Detection Output Combining Technique

Correlation Performance − MCDD vs. Conventional Correlator

In the previous section, the correlation characteristics of the multi-correlator differential detector was established. However, it would be desirable to relate the performance of the multi-correlator differential with that of a conventional correlator. In this section, it will be shown that the correlation output of MCDD is essentially similar to the squared magnitude of conventional correlator. To derive the performance comparison, let us express the correlation output for the developed MCDD scheme in a more general fashion,

$$R_M(\tau) = \sum_{m=1}^{M-1} \sum_{k=0}^{N_c-1} \left[c(k)c(k-m) \right] \left[c(k-\tau)c(k-m-\tau) \right], \ \tau = 0, 1, 2, \ldots, N_c - 1.$$
(4.49)

In the above equation, we can readily interchange the order of the multiplication as the C/A code assume biphase values (i.e. $c(k), c_m(k) = \pm 1$), and the multiplication operation is associative over the binary field $\{+1, -1\}$. Hence, we have

$$R_M(\tau) = \sum_{m=1}^{M} \sum_{k=0}^{N_c-1} \left[c(k)c(k-\tau) \right] \left[c(k-m)c(k-m-\tau) \right]$$
(4.50)

Replacing $k - m$ with a dummy variable k', where $k = k' + m$ and letting $M = N_c$ produces,

$$R_M(\tau) = \sum_{k'=1-k}^{N_c-k} \sum_{k=0}^{N_c-1} \left[c(k)c(k-\tau) \right] \left[c(k')c(k'-\tau) \right]$$
(4.51)

Recall that $c(k)$ and thus $c(k')$ is periodic over N_c and thus we can readily leave the variable k in the outer summation. Hence, we can rewrite the above equation as,

$$R_M(\tau) = \sum_{k'=0}^{N_c-1} c(k')c(k'-\tau) \sum_{k=0}^{N_c-1} c(k)c(k-\tau) \tag{4.52}$$

The two summations readily result in the correlation output $R(\tau)$. Therefore, the final correlation output is given by,

$$R_M(\tau) = R^2(\tau) = \left| \sum_{k=0}^{N_c-1} c(k)c(k-\tau) \right|^2 , \ \tau = 0, 1, 2, \ldots, N_c - 1. \tag{4.53}$$

This result is of critical significance. The final expression in (4.53) fundamentally implies that the output of the multi-correlation differential detector is essentially similar to that of the squared magnitude output of a conventional correlator (or coherent matched filter) in the absence of noise. To further validate the theory, the magnitude output of $|R(\tau)|$ for conventional correlation and that of $\sqrt{|R_M(\tau)|}$ for MCDD is shown in Figure 4.13 for the PRN 1 C/A code. The magnitude output was utilized instead of the squared magnitude in order to provide a better comparison. Thus, the substantial correlation suppression gain observed in Figure 4.8 in Section 4.1.6 can readily be summarized by (4.53).
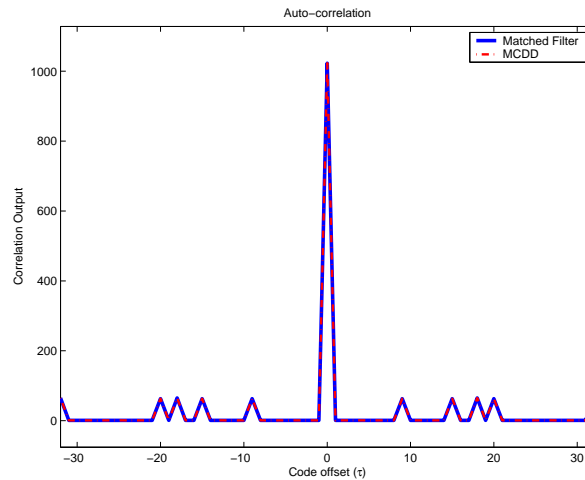
Figure 4.13: Magnitude Output for Conventional Correlation and MCDD Sceheme

In summary, we started with the extension of the delay-and-multiply property to the proposed multi-correlator differential detector. Moreover, we observed substantial gains in the auto and cross correlation suppression performance. The phenomenon behind MCDD achieving a maximal correlation suppression for $M = (Nc + 1)/2$ was also established. This can readily be utilized to combine the individual differential outputs in the absence of residual carrier or over delays where its impact is least pronounced. Finally, we found that the correlation output of the developed MCDD is essentially similar to the squared magnitude output of a conventional correlator for $M \rightarrow N_c$. In other words, the MCDD decision statistics are asymptotically equivalent to that of an incoherent matched filter in the absence of noise.

4.2   Detection Performance

In Section 3.6.5 of Chapter 3, the detection performance of the PDD scheme was established by deriving the loss factor in the PDD scheme in comparision to the ideal coherent matched filter. Similarly, we can define the loss factor for the proposed MCDD scheme as,

$$L_{MCDD} = \frac{SNR_{CMF}}{SNR_{MCDD}} \tag{4.54}$$

To determine the SNR at the output of the MCDD, we can follow a similar analysis to that of Section 3.6.5. Therefore, we can express the first two moments of the MCDD detection output as,

$$
\begin{aligned}
E\left[T(\mathbf{x}; H_0)\right] &\approx 0 \\
Var\left[T(\mathbf{x}; H_0)\right] &\approx 4\sigma_I^4 M\left[N_r N_c - \tfrac{(M+1)}{2}\right] \\
E\left[T(\mathbf{x}; H_1)\right] &\approx CM\left[N_r N_c - \tfrac{(M+1)}{2}\right]
\end{aligned}
\tag{4.55}
$$

Accordingly, we have the PSNR measure for the MCDD scheme as,

$$PSNR_{MCDD} \approx \frac{CM\left[N_rN_c - \frac{(M+1)}{2}\right]}{2\sigma_I^2\sqrt{M\left[N_rN_c - \frac{(M+1)}{2}\right]}} = \sqrt{M\left[N_rN_c - \frac{(M+1)}{2}\right]}\frac{C}{\sigma_w^2} \qquad (4.56)$$

The SNR at the output of the coherent matched filter is expressed in (3.104) and is rewritten here as

$$PSNR_{CMF} = \frac{C}{\sigma_w^2} \qquad (4.57)$$

Hence, the loss factor can be given by,

$$L_{MCDD} = \sqrt{M\left[N_rN_c - \frac{(M+1)}{2}\right]} \qquad (4.58)$$

From the above equation, we see that the SNR loss in MCDD can be reduced significantly as $M \rightarrow N_rN_c$. While this result is encouraging, in practice, the number of parallel correlations and hence M can be critically limited by a number of factors. For example, the proposed MCDD detection scheme requires M = 10230 to compensate for squaring type loss and to achieve a detection performance similar to that of a coherent matched filter with $T_{COH} = 10$ ms. On the other hand, it requires M = 1023 to achieve a detection performance similar to that of the PCDD scheme with $T_{COH} = 1$ ms. Moreover, the convergence of the loss factor in MCDD could prove crucial for a practical choice of M. Alternatively, the loss factor can be reduced by utilizing coherent pre-filtering prior to the multi-correlation differential detection. However, as discussed earlier, the use of coherent pre-filtering necessitates a limited frequency search.

In Section 3.6.6 of Chapter 3, it was shown that the GPCDD structure decomposes to an incoherent matched filter for $M \rightarrow N_c$. In the following sections, a similar proof will be established for the proposed MCDD scheme as well. In other words, it will be shown that the MCDD and that of the PF/MCDD structure decomposes to that of an incoherent matched filter for $M \rightarrow N_rN_c$ and thus equivalent to an estimator-correlator. The detection performance in the presence of AWGN is derived under two conditions.

Initially, we derive the performance of multi-correlation differential detection considering only a coherent integration period of $T_{COH} = N_c T_c$. Then, we incorporate the pre-filtering approach with that of mutli-correlation differential detection for a coherent integration period beyond one code period. However, in both the cases, it will be shown that the final test statistic is equivalent to that of the incoherent matched filter for $M \rightarrow N_c N_r$.

4.2.1 Multi-correlation Differential Detector

As discussed earlier, the detection performance is derived considering only an observation period of $T = T_{COH} = 1$ ms. Accordingly,the decision statistic for the developed MCDD scheme can be expressed as

$$T(\mathbf{x}) = \frac{1}{MN_cN_s} \sum_{m=1}^{M} \sum_{k=0}^{N_c-1} \tilde{x}_m(k)\tilde{c}_m(k-\tau) \tag{4.59}$$

where $\tilde{x}_m(k) = x(k)x^*(k-m)$ and $x(k) = \sqrt{2C}d(k)c(k)e^{j(2\pi\Delta Fk+\phi_0)} + w(k)$. Note that the influence of residual signal effects were already modelled in Section 4.1.5 and will be ignored in $x(k)$ from now onwards. Furthermore, we can express $\tilde{x}_m(k)$ into signal, noise and cross terms arising from the multiplication of signal and noise components as,

$$
\begin{aligned}
\tilde{x}_m^{ss}(k) &= \tilde{c}_m(k) \\
\tilde{x}_m^{sw}(k) &= c(k)w^*(k-m) + c(k-m)w(k) \\
\tilde{x}_m^{ww}(k) &= w(k)w^*(k-m)
\end{aligned}
\tag{4.60}
$$

where $\tilde{x}_m(k) = \tilde{x}_m^{ss}(k) + \tilde{x}_m^{sw}(k) + \tilde{x}_m^{ww}(k)$. Thus, the signal part of the above test statistic is given by,

$$T^{ss}(\mathbf{x}) = \frac{1}{MN_c} \sum_{m=1}^{M} \sum_{k=0}^{N_c-1} \tilde{c}_m(k)\tilde{c}_m(k-\tau) \tag{4.61}$$

The final part of Section 4.1.6 clearly indicated that the output of multi-correlation differential detection is similar to the squared magnitude output in conventional coherent

matched filter. Utilizing the final result as given in (4.53), and letting $M = N_c$, we can write the signal component of the test statistic as,

$$T^{ss}(\mathbf{x}) \approx \left| \frac{1}{MN_c} \sum_{k=0}^{N_c-1} c(k)c(k-\tau) \right|^2 = R^2(\tau), \ \tau = 0, 1, 2, \ldots, N_c - 1. \tag{4.62}$$

The above expression is only an approximation because we ignored the residual signal effects. Similarly, we can express the part of the test statistic arising from signal and noise cross terms as,

$$T^{sw}(\mathbf{x}) = \frac{1}{MN_c} \sum_{m=1}^{M} \sum_{k=0}^{N_c-1} \Big(c(k)w^*(k-m) + c(k-m)w(k) \Big) \tilde{c}_m(k-\tau) \tag{4.63}$$

Invoking the periodicity and bringing in $c_m(k-\tau)$ in its expanded form produces,

$$\begin{aligned} T^{sw}(\mathbf{x}) = \frac{1}{MN_c} \sum_{m=1}^{M} \sum_{k=0}^{N_c-1} \underline{c(k)c(k-\tau)}c(k-m-\tau)w^*(k-m) \\ + \frac{1}{MN_c} \sum_{m=1}^{M} \sum_{k=0}^{N_c-1} +c(k-\tau)\underline{c(k-m)c(k-m-\tau)}w(k) \end{aligned} \tag{4.64}$$

One can readily notice the correlation of $c(k)$ in the first summation and $c(k-m)$ in the second summation within the braces. Thus, we can rewrite the above equation as,

$$T^{sw}(\mathbf{x}) \approx R(\tau)\frac{1}{MN_c} \sum_{m=1}^{M} \sum_{k=0}^{N_s N_c-1} w^*(k-m)c(k-m-\tau) + w(k-nN_c)c(k-\tau) \tag{4.65}$$

Note that the second term no longer includes the outer summation over m as $c(k-\tau)\bar{w}(k)$ is independent of m. Replacing $k-m$ by a dummy variable k' in the first term on the right hand side produces

$$T^{sw}(\mathbf{x}) \approx R(\tau)\frac{1}{MN_c} \left(\sum_{m=1}^{M} \sum_{k'=-m}^{N_c-1-m} c(k'-\tau)w^*(k') + \sum_{k=0}^{N_c-1} c(k-\tau)w(k) \right) \tag{4.66}$$

Note that $w(k')$ is wide sense stationary (i.e. $E[w(k)] \approx E[w(k-m)]$) and hence summation over k' converges to its mean value especially for $N_c >> 1$. Besides, $c(k'-\tau)$ is also periodic over N_c. Figure 4.14 shows the variance of the $\sum_{k'=-m}^{N_c-1-m} c(k'-\tau)w^*(k')$ over m. From the plot, it is apparent the convergence is strong especially for large M (i.e. $M = 10N_c$), which is the case for GPS signal acquisition. Note that the variance estimate is unbiased as it has been scaled by N_c.
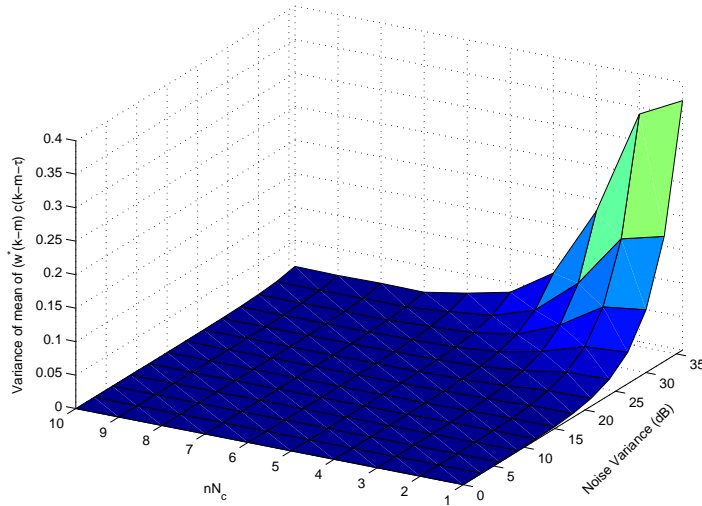
Figure 4.14: Variance of $\sum_{k=0}^{N_c-1} c(k - m - \tau)w^*(k - m)$

Accordingly, the effect of second summation over m hardly effects the output of the inner summation over k'. Thus, dropping the first summation over m and replacing the dummy variable yields

$$T^{sw}(\mathbf{x}) \approx R(\tau)\frac{1}{N_c}\sum_{k=0}^{N_c-1} c(k - \tau)w^*(k) + R(\tau)\frac{1}{N_c}\sum_{k=0}^{N_c-1} c(k - \tau)w(k) \qquad (4.67)$$

Finally, we express the part of test statistic pertaining to the noise product term as,

$$T^{ww}(\mathbf{x}) = \frac{1}{MN_c}\sum_{m=1}^{M}\sum_{k=0}^{N_c-1} w(k)w^*(k - m)c_m(k - \tau) \qquad (4.68)$$

The order of summation can be rearranged as $w(k)w^*(k-m)$ is jointly ergodic. Further, by letting $M = N_c$ and expanding $c_m(k - \tau)$ produces

$$T^{ww}(\mathbf{x}) \approx \frac{1}{MN_c}\sum_{k=0}^{N_c-1} w(k)\left(\sum_{m=0}^{N_c-1} w^*(k - (m + 1))c(k - (m + 1) - \tau)\right)c(k - \tau) \quad (4.69)$$

Replacing $k - m$ by a dummy variable $k - k'$ and letting $M = N_c$ produces

$$T^{ww}(\mathbf{x}) \approx \left(\frac{1}{N_c}\sum_{k=0}^{N_c-1} w(k)c(k - \tau)\right)\left(\frac{1}{N_c}\sum_{k'=k+1}^{N_cN_s+k} w^*(k')c(k' - \tau)\right) \qquad (4.70)$$

In the above equation, we can consider the second summation to be independent of the first one. This assumption is already validated during the previous analysis in regards

to signal and noise cross terms and shown in Figure 4.14. Finally, dropping the dummy variable yields,

$$T^{ww}(\mathbf{x}) \approx \left(\frac{1}{N_c} \sum_{k=0}^{N_c-1} w(k)c(k-\tau) \right) \left(\frac{1}{N_c} \sum_{k=0}^{N_c-1} w^*(k)c(k-\tau) \right) \quad (4.71)$$

From (4.62), (4.67) and (4.71), we have

$$T_{MCDD}(\mathbf{x}) = R^2(\tau) + R(\tau)\frac{1}{N_c}\left(\sum_{k=0}^{N_c-1} c(k-\tau)w^*(k) \right.$$
$$\left. + \sum_{k=0}^{N_c-1} c(k-\tau)w(k) \right) + \frac{1}{N_c}\left(\sum_{k=0}^{N_c-1} w(k)c(k-\tau) \right)\left(\frac{1}{N_c}\sum_{k=0}^{N_c-1} w^*(k)c(k-\tau) \right)$$
$$(4.72)$$

In Section 3.4.1 in Chapter 3, the decision statistic for an incoherent matched filter is summarized in (3.62) and is rewritten here as,

$$T_{ICMF}(\mathbf{x}) = \left| \frac{1}{N_c} \sum_{k=0}^{N_c-1} \left(c(k) + w(k) \right)c(k-\tau) \right|^2 \quad (4.73)$$

Taking the squared magnitude of $T_{ICMF}(\mathbf{x})$ and upon further expansion yields,

$$T_{ICMF}(\mathbf{x}) = R^2(\tau) + R(\tau)\frac{1}{N_c}\sum_{k=0}^{N_c-1} c(k-\tau)w^*(k)$$
$$+ R(\tau)\frac{1}{N_c}\sum_{k=0}^{N_c-1} c(k-\tau)w(k) + \left(\frac{1}{N_c}\sum_{k=0}^{N_c-1} w(k)c(k-\tau) \right)\left(\frac{1}{N_c}\sum_{k=0}^{N_c-1} w^*(k)c(k-\tau) \right)$$
$$(4.74)$$

Comparing (4.74) with (4.72), we see that the decision statistics of MCDD is reduces to that of the incoherent matched filter for $M \rightarrow N_c$. That is,

$$\lim_{M \rightarrow N} T_{MCDD}(\mathbf{x}) \approx T_{ICMF}(\mathbf{x}) \quad (4.75)$$

Figure 4.15 shows the distribution of $\Re\{T(\mathbf{x})\}$ for the incoherent matched filter and that of the multi-correlation differential detector. While a coherent integration period of $T_{COH} = 1$ ms was assumed for the incoherent matched filter, the multi-correlation differential detector utilized $M = 1022$ correlation summations.

The PDF of MCDD closely approximates the Gaussian distribution although it involves the product of two Gaussian distributed variates. The convergence to a Gaussian distribution in multi-correlation differential detector is in accordance to the central limit
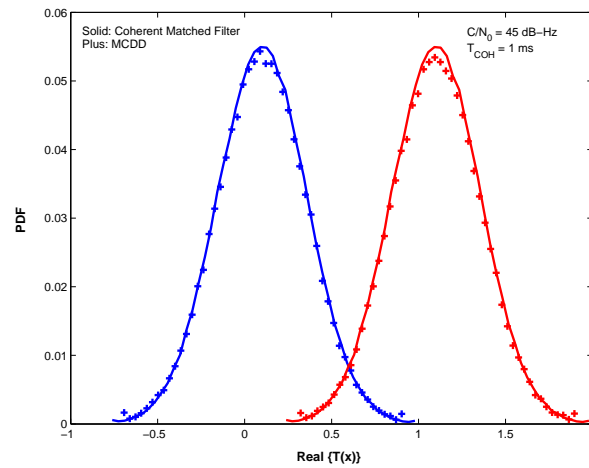
Figure 4.15: PDF of $\Re\{T_{ICMF}(\mathbf{x})\}$ (Solid) and $\Re\{T_{MCDD}(\mathbf{x})\}$ (Plus)

theorem as a large number of summations (i.e. $M >> 1$) is being employed. Accordingly, one can extend this analysis to characterize the SNR loss in a multi-correlation differential detector with respect to a coherent matched filter as a function of M. Figure 4.16 shows the convergence of SNR loss in multi-correlation differential detection as a function of M. The plot also includes the theoretical convergence rate of $M^{-1/2}$
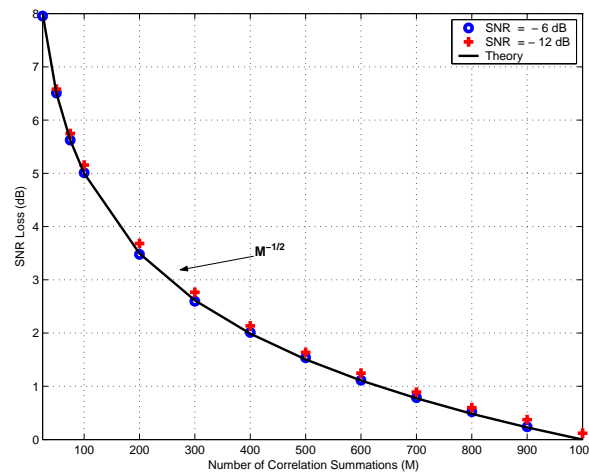
Figure 4.16: Convergence of SNR Loss in Multi-correlation Differential Detection as a function of M

based on the central limit theorem (Papoulis [1984]). Figure 4.16 essentially implies that the gain accomplished by increasing M follows a diminishing return. For instance, the reduction in SNR loss between $M = 10$ to $M = 500$ is around 6.5 dB. On the other

hand, increasing or doubling M from 500 to 1000 resulted only in a further reduction of around 1.5 dB. Hence, increasing the number of M may not always result in improved detection performance. Alternatively, substantial reduction can be achieved by selecting a moderate M at the expense of SNR loss.

4.3   Acquisition Performance Evaluation

Having derived the theory for the pre-filtering and multi-correlation differential detection, we now turn to empirical tests to validate the developed theory. These tests consist of software-based analysis of IF samples from hardware simulated GPS signals. The same data sets utilized for the analysis in Chapter 3 has been utilized here to allow for coherent comparisons. The real data analysis primarily focuses on validation of various concepts proposed in the earlier sections.

4.3.1   Pre-correlation Noise Suppression Performance

In Section 4.1, it was demonstrated that the pre-filtering in conjunction with post-correlation techniques basically accomplishes similar performance improvements to that of the original post-correlation detector with extended coherent integration. To further verify this theory, the detection performance, in terms of PSNR, was evaluated for a post-correlation noncoherent technique with and without pre-filtering. Figure 4.17 shows the PSNR performance as a function of residual frequency offset for both cases. While the post-correlation noncoherent scheme utilized a coherent integration period $T_{COH} = LN_cT_c$, the pre-filter/post-correlation noncoherent combination utilized a $T_{COH} = N_cT_c$ but with a pre-filter order of L. Figure 4.17 shows the acquisition results for pre-filter orders of $L = 2$ and $L = 4$. The plot also includes the results from post-correlation noncoherent detection alone. In all the cases, the total observation period was set to 80 ms. From Figure 4.17, it is readily apparent that pre-filtering
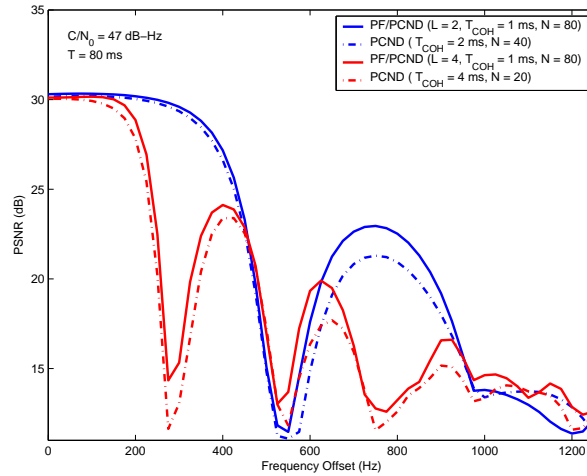
Figure 4.17: PSNR Performance of Pre-Filtering/Post-correlation Noncoherent Technique

essentially accomplishes extended coherent integration.

A more interesting conjecture of pre-correlation noise suppression is the incorporation of pre-filtering with the pre-correlation differential detector. There it was proposed that the use of pre-filtering enhances the pre-detection SNR thereby minimizing the inherent SNR loss incurred during the differential detection. Moreover, it was reported that the use of pre-filtering with pre-correlation differential detection is no longer insensitive to frequency offset. To validate these predictions, the originally developed pre-correlation differential detector was augmented with the pre-filtering unit. Subsequently, the effect of C/N_0 and residual frequency offset were evaluated for both the cases of with and without pre-filtering in the pre-correlation differential detector.

Figure 4.18 shows the convergence of PSNR as a function of pre-filter order and observation period. The pre-filter order of 2 resulted in a 3 dB gain compared to the no pre-filtering case as predicted by the theory. However, the PSNR gain with $L = 8$ was around 6.5 dB, which is 1.5 dB less than the PSNR predicted by theory. Alternatively, it took only an observation period of around $T = 32$ ms for the $L = 8$ case to exceed the minimum detection threshold of 16 dB and thereby resulting in a gain of around 7 dB in comparison to the no pre-filtering case. Thus, there still exists an improvement

over choosing larger pre-filter orders.
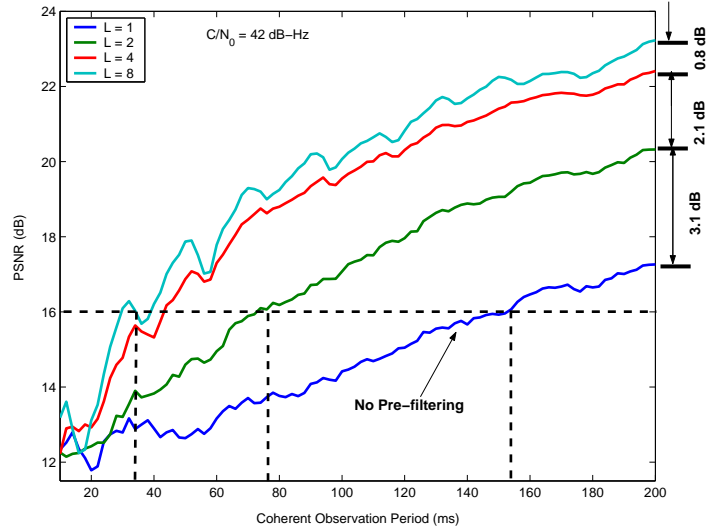
Figure 4.18: PSNR Convergence of Pre-Filtering/Pre-correlation Differential Technique

The PSNR performance of the pre-filtering/pre-correlation differential detector as a function of C/N_0 is plotted in Figure 4.19. The use of pre-filtering indeed resulted in better PSNR performance although the gain started to diminish with decreasing C/N_0. For example, the pre-filter order of $L = 4$ and $L = 8$ still aided the pre-correlation differential detector and obtained a PSNR that exceeded the minimum threshold of 16 dB. However, the pre-filter resulted in no improvement for C/N_0 around 32 dB-Hz even with an order of $L = 8$. This is rather disappointing as we expected the pre-filter to boost the SNR so as to minimize the SNR loss due to pre-correlation differential detection. However, this does not come at a surprise as the pre-filter gain is effectively canceled by the substantial SNR loss. For instance, a C/N_0 of 32 dB-Hz would result in a pre-detection SNR of around -31 dB. Accordingly, the SNR at the output of pre-filter would be around -24 dB, which would still yield a substantial SNR loss.

The frequency sensitivity of the developed pre-filtering/pre-correlation differential scheme was also evaluated as function of residual frequency offset and is shown in Figure 4.20. The residual frequency offset was incremented in steps of 50 Hz up to 4
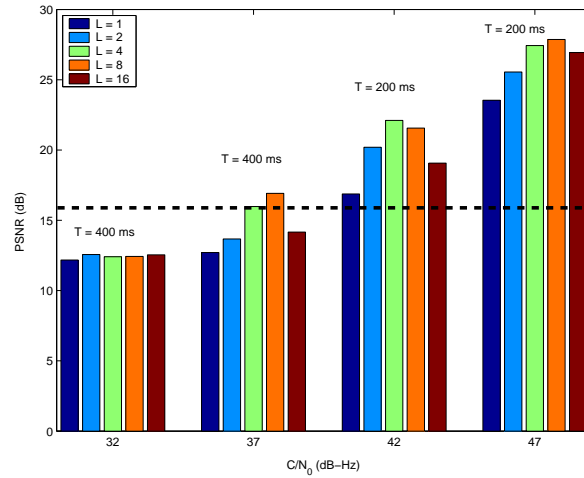
Figure 4.19: PSNR Performance of Pre-Filtering/Pre-correlation Differential Technique as a Function of C/N_0

kHz. Figure 4.20 confirms the theory that stated that the sensitivity is periodic over 1 kHz. Note that the pre-correlation differential scheme nearly suppresses the residual carrier. The PSNR plot shown in Figure 4.20 readily follows the pre-filter's frequency response. Moreover, it also clearly shows the integer kilo-hertz ambiguity arising from pre-filtering. However, it should be recalled that the integer ambiguity can be resolved using the fine frequency estimation descried earlier in Section 3.4.4 of Chapter 3. Figure 4.21 further extends the analysis by increasing the resolution from 50 Hz to 5 Hz and limiting the frequency offset to 500 Hz. The effect of pre-filtering with various orders can be clearly seen in Figure 4.21.

4.3.2   Multi-correlation Differential Detection Performance

The following analysis primarily focuses on demonstrating the abilities of multi-correlation differential detection in terms of code and frequency acquisition. The PF/MCDD scheme alongside its various forms was implemented in a MATLAB environment. Initially the MCDD based code/frequency acquisition was validated using the 47 dB-Hz C/N_0 data set. The total observation time was set to 10 ms with the MCDD using 1022 correlation branches. Figure 4.22 shows the convergence of PSNR for different
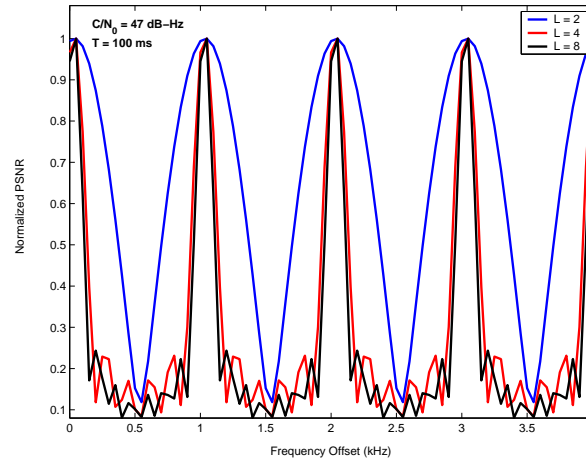
Figure 4.20: PSNR Performance of Pre-Filtering/Pre-correlation Differential Technique as a Function of Residual Frequency Offset
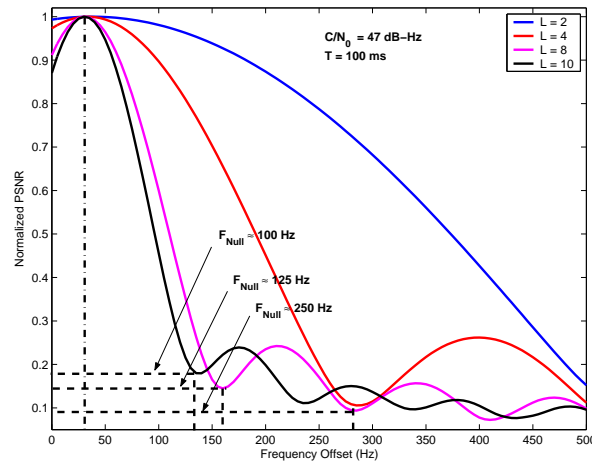
Figure 4.21: Frequency Selectivity of Pre-Filtering/Pre-correlation Differential Technique as a Function of Pre-Filter Order

correlation combining techniques as a function of correlation summations. While the FFT based and differential combining resulted in a final PSNR of around 31 dB, the noncoherent combining yielded 29.4 dB. The coherent combining owing to the presence of residual carrier resulted in a maximum PSNR of 29 dB for M around 100 and declined for subsequent increases in M.
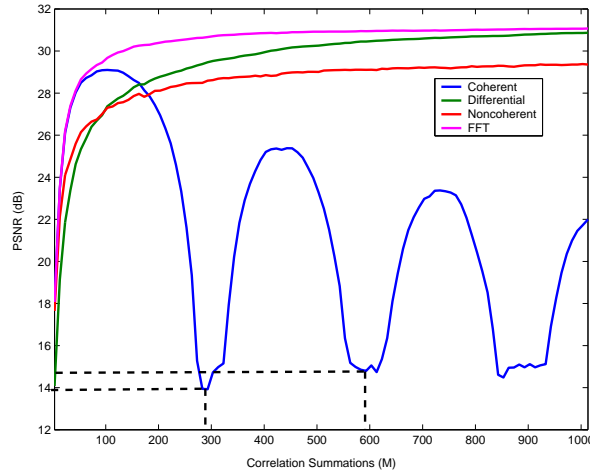
Figure 4.22: PSNR Convergence as a Function of Correlation Summations

From Figure 4.22, it can still be seen that the convergence occurred at a faster rate for coherent and FFT based combining, which are, of course, one and the same in the absence of residual carrier. Interestingly, the effect of residual carrier can be be clearly observed in the PSNR of coherent combining. For example, the PSNR gain exhibited a null at every 300 T_c or every 3.41 kHz, wherein the uncompensated residual carrier had a frequency of 3.45 kHz. Thus, the total number of correlation summations for coherent combining in the presence of residual carrier is given by,

$$M \approx \frac{1}{4\Delta F T_c} \tag{4.76}$$

Therefore, the maximum number of correlation summations is limited within 25 T_c assuming a 10 kHz residual carrier, which still provides a gain of around 14 dB. Alternatively, one can combine N number of correlation outputs coherently out of M correlations and combining the resulting M/N in a noncoherent fashion.

Frequency Estimation Performance

Earlier it was shown that the developed multi-correlation differential detection is capable of estimating residual carrier within a much wider range. More importantly, the range and the resolution of FFT based frequency estimation is flexible to accommodate either wider frequency ranges or finer resolution. The quintessential fact behind FFT based estimation is that the output of individual branches in MCDD collectively embodies the residual carrier for the correct code phase. To further validate this assumption, the real and imaginary parts of the the final detection output in MCDD for code phase is plotted in Figure 4.23. The residual carrier for this particular case was around -3.45 kHz.
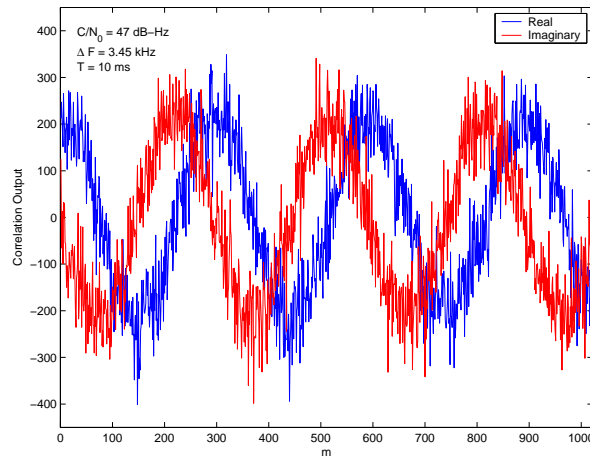
Figure 4.23: Final Detection Output of MCDD for Correct Code phase as a Function of m

From Figure 4.23, it is immediately apparent that the complex phase rotations across the individual branches indeed represent the residual carrier in a collective fashion. However, the residual carrier is now being sampled at T_c rather than T_s. As described earlier, the resolution of the resulting FFT based estimator critically depends on the bandwidth (and hence the input sampling rate) and the number of observation points (M). Figure 4.24 shows the FFT output for a different number of correlation branches while keeping the sampling rate or the individual differential delays at T_c.

The bandwidth of the ensuing FFT based estimator is 1.023 MHz extending between 511.5 kHz on either side. Accordingly, the resolution can be halved for every doubling in M as shown in Figure 4.24.
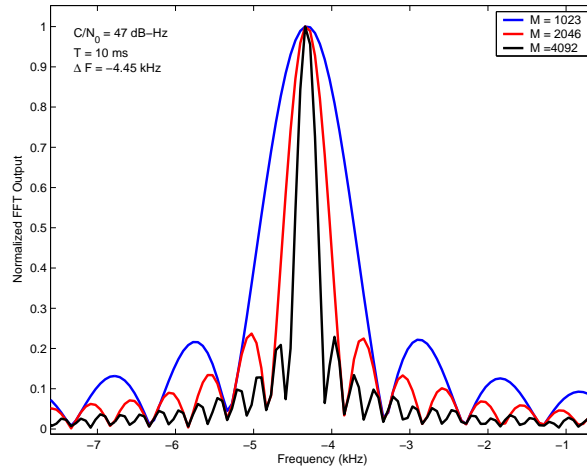
Figure 4.24: Frequency Estimation Performance of MCDD/FFT based Scheme as a Function of M

Alternatively, one can also improve the frequency resolution at the expense of FFT bandwidth and thus frequency range. For example, the resolution can be halved for the same M by halving the sampling rate. For instance, Figure 4.25 shows the frequency offset estimation performance for a fixed value of M but with different sampling rates. The resolution improved with decreasing sampling rate although the bandwidth of the FFT estimator is also correspondingly reduced.Thus, the required sampling rate to have a frequency estimation range of ± 10 kHz is around $50\,T_c$. In other words, the differential delay should be incremented by $50\,T_c$ over consecutive branches. Correspondingly, an M for this input FFT sampling rate of around 1000 will yield a frequency resolution of about 40 Hz.

Frequency Sensitivity Performance

Having analyzed the frequency estimation performance, we now turn to the frequency sensitivity analysis of the developed multi-correlation differential detection. The robust-
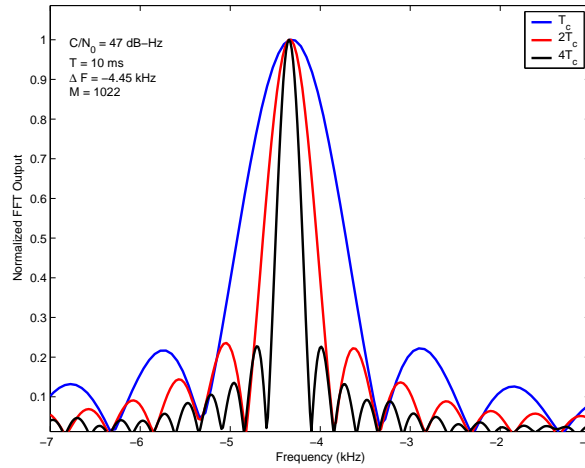
Figure 4.25: Frequency Estimation Performance of MCDD/FFT based Scheme as a Function of Input Sampling Rate

ness of the pre-correlation differential scheme to residual frequency errors was already established in Section 3.7.4 of Chapter 3. The main motivation behind the resilience of the multi-correlation differential detector is the chosen differential delay literally translates the residual carrier into a complex phase rotation, which is readily compensated during the FFT based combining. However, the residual code Doppler can be of some significance in the presence of large frequency offsets. The effect of residual code Doppler on the outputs of individual differential detectors is given by,

$$\Delta F_c = \frac{\Delta F T_m}{\eta} \ (chips), \ \eta = L_1 T_c^{-1} = 1540 \tag{4.77}$$

For example, a residual frequency offset of 154 kHz would result in a residual code Doppler of around 100 Hz. Accordingly, this residual code Doppler would manifest into a drift of 0.1 chips over the differential delay of $T_m = N_c T_c$. Hence, the effect of 154 kHz residual frequency offset would translate into a 5% power loss in the multi-correlation differential detection with a uniform delay selection and $M = N_c$.

The frequency drift, on the other hand, has a significant impact on multi-correlation differential detection especially for large differential delays. For instance, Figure 4.26 shows the normalized FFT output for 50 and 100 kHz/s frequency drifts. The FFT

output without any frequency drift is also plotted for comparison. In Figure 4.26, one
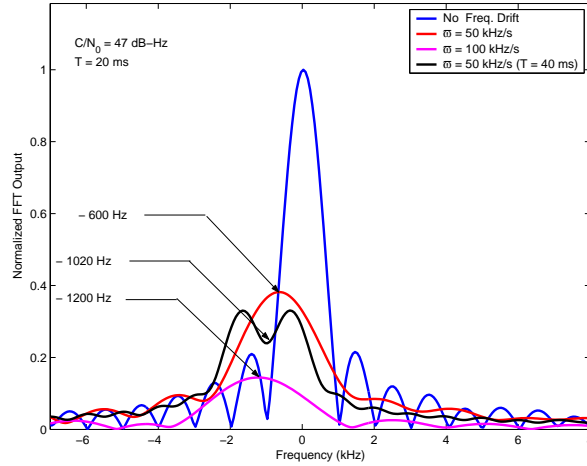
Figure 4.26: FFT Output of Multi-correlation Differential Detector with Frequency Drift

can clearly observe the frequency dispersion incurred due to the presence of frequency drift. To further understand the phenomenon, let us express the output of the individual differential detectors for the correct code phase as,

$$y(m) = sinc(\pi\varpi T_m N N_c T_c) sinc(\pi\varpi T_m N_c T_c) e^{j\left(\varpi\left[\frac{N_c-1}{2}\right]T_m T_c+\varphi_0\right)} \tag{4.78}$$

where $\varphi_0 = T_m(\omega - \frac{\varpi T_m}{2}) - \varpi T_m(N-1)N_c T_c/2$, $T_m = mT_c$ and ϖ is the frequency drift. Substituting for φ_0 and rearranging the above equation yields,

$$y(m) = sinc(\pi\varpi T_m N N_c T_c) sinc(\pi\varpi T_m N_c T_c) e^{j\left(\left(\omega - T_c\frac{\varpi(N-1)N_c+\varpi}{2}\right)T_m + \frac{\varpi T_m^2}{2}\right)} \tag{4.79}$$

Note the above equation was directly obtained from (3.151) of Chapter 3, wherein the effect of frequency drift on a particular differential delay was analyzed. Upon close observation of 4.79, the manifestation of frequency drift across m can be observed in the term $\varpi T_m^2/2$. However, the effect of the this frequency drift would be felt over $N_c T_c$ and thus can be marginalized. More importantly, the frequency offset introduced by the frequency drift can be observed in the term $0.5T_c(\varpi(N-1)N_c + \varpi)$. Hence, increasing either ϖ or N would correspondingly increase the observed frequency offset.

Acquisition Sensitivity Performance

To evaluate the acquisition sensitivity of the multi-correlation differential detection and that of pre-filtering, the same data sets (with C/N_0's ranging from 22 dB-Hz to 47 dB-Hz), which was utilized in analyzing the acquisition schemes was used here as well. Initially, the effectiveness of different correlation combining techniques was evaluated under varying C/N_0 conditions. Figure 4.27 shows the PSNR performance of coherent, differential and that of noncoherent correlation combining in multi-correlation differential detection. The number of correlation branches was set to 1022 and thus we would expect substantial gain. The PSNR performance at least in the case of differential
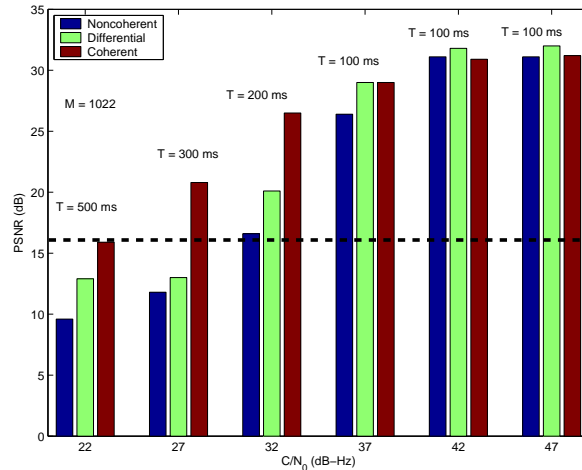
Figure 4.27: PSNR Performance of Different Correlation Combining Techniques in Multi-correlation Differential Detection (M =1022)

combining resulted in no degradation up until 37 dB-Hz. Accordingly, one could very well utilize these noncoherent or differential correlation combining even for moderate C/N_0 levels. However, the significance of coherent combining is clearly apparent with low C/N_0 conditions as the noise enhancement is substantial in the noncoherent and differential combining. Even the coherent combining barely managed to exceed the 16 dB PSNR threshold for the lowest C/N_0 of 22 dB-Hz.

While the number of correlation branches was set to the maximum of $M = 1022$ in the previous analysis, it may not require that many correlation branches to converge to

the final PSNR. Hence, it would be highly desirable to analyze the effect of correlation summations in terms of PSNR convergence. Figure 4.28 shows the PSNR convergence with coherent correlation combining as a function of correlation summations for various C/N_0 levels. From Figure 4.28, one can readily notice the strong convergence at least
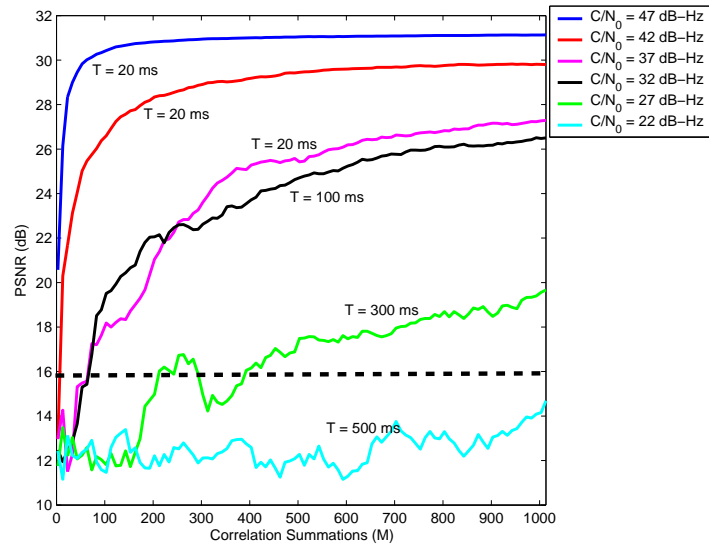
Figure 4.28: Effect of Coherent Correlation Summations on PSNR Convergence

for nominal C/N_0 conditions. For instance, it only took an $M = 75$ and an observation period of $T = 20$ ms to converge to the final PSNR of 30.8 dB. On the other hand, the rate of convergence declined with decreasing C/N_0 levels as there was significant noise enhancement that had to be suppressed. Unfortunately, the convergence for the 22 dB-Hz C/N_0, was meager and it would have required a lot more correlation summations. Thus, the multi-correlation differential detection although desirable from its resilience to frequency errors, is still deficient in combating weak signal conditions.

The major limitation with multi-correlation differential detection under weak signal conditions is the substantial noise enhancement that incurs during the pre-correlation differential process. Intuitively, one can infer that by enhancing the SNR prior to performing the differential operation can aid in further improvements. Accordingly, we can equip the multi-correlation differential detection with that of coherent pre-

filtering to deal with weak signal conditions. However, the price of accomplishing this enhancement in PSNR is the requirement of limiting the frequency search. To further evaluate the significance of pre-filtering, the 22 dB-Hz C/N_0 data was processed again using the PF/MCDD technique with different pre-filter order's. Figure 4.29 shows the convergence of PSNR with the PF/MCDD scheme for different pre-filter order's as a function of correlation summations. The PSNR convergence with no pre-filtering is
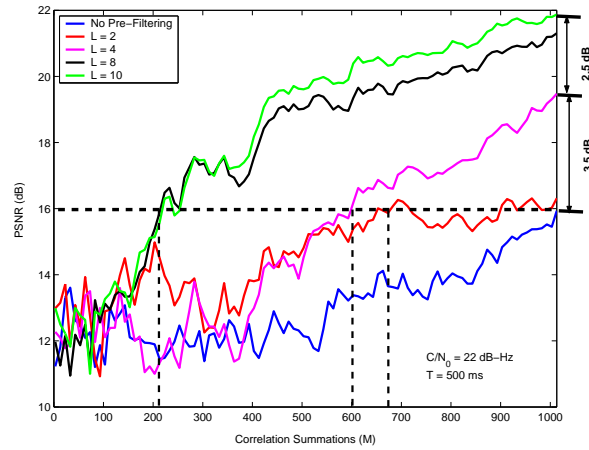
Figure 4.29: Effect of Pre-Filtering on Multi-correlation Differential Detector's PSNR Performance

also included in the plot for the sake of comparison. The PSNR performance and its convergence generally improved with increasing pre-filter order. Moreover, it is interesting to note the PSNR almost unaffected by the pre-filter order at least for $M <$ 150 under these degraded signal conditions. However, the advantage of selecting higher pre-filter order is readily apparent for larger correlation summations. For instance, a pre-filter order of $L = 8$ resulted in a final PSNR gain of around 6 dB when compared to the case of no pre-filtering. Besides, it also resulted in a faster convergence as it took only a M of 200 to exceed the 16 dB PSNR threshold. It should also be noted that the pre-filter order resulted in no apparent PSNR improvement in comparison to no pre-filtering for $M = 1022$, it did result in better convergence over the no pre-filtering case. Therefore, the use of pre-filtering in conjunction with multi-correlation differential

detection can provide necessary ammunition to combat weak signal conditions at the expense of increased computational complexity.

The PSNR performance of all the acquisition schemes developed during this research are plotted in Figure 4.30 as a function of C/N_0. The multi-correlation differential scheme utilized 1022 correlation branches for all the cases but also utilized a pre-filtering with an order $L = 8$ for the 22 dB-Hz C/N_0. Similarly, the post-correlation noncoherent and differential schemes utilized a coherent integration of 4 ms for the 22 dB-Hz C/N_0. From Figure 4.30, it is clearly apparent that the best overall PSNR performance was achieved by the generalized post-correlation differential detection. Moreover, it is even more attractive as it accomplished this PSNR gain while still maintaining a coherent integration of 1 ms. However, one has to bear in mind that the PSNR gain is critically influenced by the residual frequency error stemming from the initial coherent integration. On the other hand, the multi-correlation differential detector yielded the second best performance in terms of PSNR but also achieved this gain without the need for initial frequency search. However, it still required some kind of limited frequency search for the worst case C/N_0 of 22 dB-Hz to accomplish similar PSNR levels to that of generalized post-correlation differential scheme.
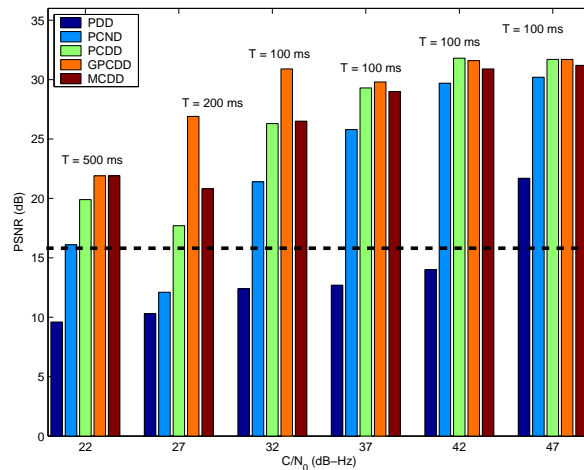
Figure 4.30: PSNR Performance of Different Acquisition Schemes as a Function of C/N_0

4.4   Discussion

In Section 4.1, a pre-correlation noise suppression scheme was introduced. The developed pre-filtering scheme utilized the C/A code periodicity for its implementation. The equivalence of coherent pre-filtering and extended coherent integration in post-correlation detectors was established. More importantly, the advantage and the complementary characteristics of pre-filtering and pre-correlation differential detector were highlighted. In Section 4.1.4, the generalization of pre-correlation differential detection namely the *multi-correlation differential detection* was established.

The effect of navigation data and a novel robust fine frequency estimation scheme using FFT and MCDD was described in Section 4.1.5. The DAM property was further utilized to characterize the correlation performance of a C/A code as a consequence of MCDD. It was noted that the delay-and-multiply operation on a code of length N_c yielded only $(N_c - 1)/2$ unique codes with the remaining being the time-shifted versions of the original codes. More importantly, the correlation output of MCDD was established as the squared magnitude output of a coherent matched filter and summarized in (4.53). It should be emphasized here that both the GPCDD scheme developed earlier and the MCDD scheme proposed in this chapter are asymptotically equivalent to that of an estimator-correlator.

Chapter 5

Multi-Correlation Differential Detection Based Interference Detection and Suppression

Acquisition under strong RFI is more difficult as the GPS receiver has no prior knowledge of both signal and interference parameters. Moreover, many commercial receivers are equipped with no or at most a basic level of protection against in-band RFI. This chapter begins by giving a brief introduction of various RFI sources and types. The effect of RFI at various stages of GPS receiver signal processing is succinctly reviewed. The vulnerability of GPS C/A code detection to various RFI is also detailed. The effect of RFI on the proposed multi-correlation differential detection is analyzed. Consequently, a simple but effective continuous wave (CW) interference detection, estimation, and suppression scheme based on MCDD is introduced. The remainder of the chapter is focused on the detection performance evaluation of the various acquisition schemes under *narrow band interference* (NBI) environments. Besides, the use of frequency excision and its effect on the developed detectors is also demonstrated.

5.1   RF Interference – Sources and Types

The widespread proliferation of GPS technology in commercial sector often comprises of safety critical applications (Carroll [2003]). For instance, Emergency 911 in North America and Emergency 112 in Europe largely rely on GPS for mobile user locationing. Nevertheless, many commercial receivers are equipped with minimal or basic levels of protection towards external RFI (Spilker and Natali [1996]). The GPS system, being a spread spectrum system, does offer some resistance to external RFI in comparison

to a narrowband system, however, the GPS signal undergoes significant attenuation before it reaches the receiver which permits even relatively low power RFI to mask the weak GPS signals. Potential interference largely emanates from unintentional sources although intentional jamming and spoofing of GPS signals is also anticipated (Ward [1995]). Figure 5.1 summarizes the various type of RF interference. Interference is normally classified as either *narrowband* or *wideband* depending on the ratio of the interfering signal bandwidth to that of the GPS signal bandwidth.
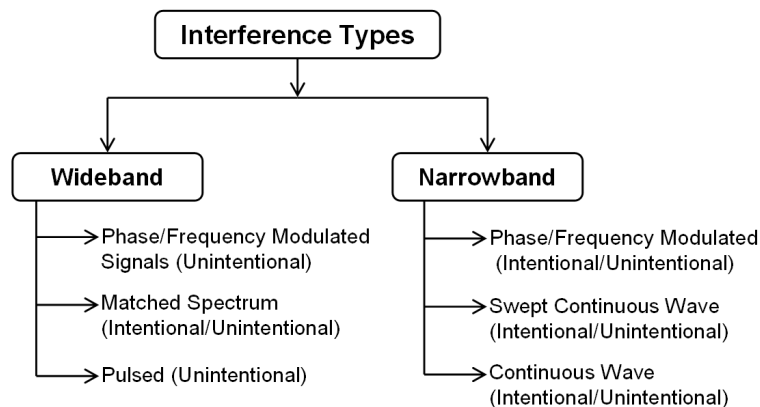
Figure 5.1: RFI Types (Ref: Spilker and Natali [1996])

The extreme form of narrowband interference is a signal consisting of a pure tone (single) often referred to as *continuous wave* interference (CWI). The potential source of CWI may typically include intentional CW jammers or unmodulated carriers (or its harmonics) in the vicinity of the receiver. Later, it will be shown that the CWI can induce substantial performance degradation despite having very small bandwidth. Another form of CWI is the swept continuous wave interference (SCWI) arising primarily from the harmonics generated by the frequency modulation (FM) transmitters or from swept CW jammers. Phase/frequency modulated signals or their harmonics produced from amplitude modulation (AM) transmitters or intentional chirp jammers also constitute a form of narrowband interference.

Wideband interference encompasses a range of interference sources of varying characteristics. For instance, the mutual interference experienced by the GNSS signals from different satellite vehicles are wideband and generally referred to as *self interference* or *intra-system interference*. On the other hand, the mutual interference experienced by the GNSS signals pertaining to different GNSS systems (i.e. GPS and Galileo) is often referred as *inter-system interference*. A wideband interference with similar spectral characteristics such as similar bandwidth and center frequency is called *matched spectrum interference*, which are characteristic of intentional jamming and spoofing and in many cases the pseudolites. Alternatively, the interference generated from pseudolites or from stronger GPS signals (in indoor scenarios) toward's weak GPS signals is referred as *near-far interference*. Burst transmission systems such as ultra wideband (UWB) systems and radar system result in a type of interference known as *pulsed interference*, which are also wideband but are characterized by strong spectral lines. Finally, the phase/frequency modulated signals (or their harmonics) from television transmitters and microwave link transmitters also introduces a form of wideband interference.

5.2   RF Interference Effects and Receiver Trade-offs

The RF interference effects on the GPS receiver performance critically depends on the design of the various stages of the GPS receiver. The low power transmission in conjunction with substantial signal attenuation requires a considerable gain in the front-end stages. Hence, many commercial receivers typically employ small dynamic range that may not be able to accommodate gain variations induced by the interference. Furthermore, there exists a fundamental trade-off in terms of front-end bandwidth. For instance, the receiver bandwidth is usually set as wide as 20 MHz to suppress the AWGN (i.e. narrow correlator). On the other hand, smaller bandwidth on the order of 2 MHz is more desirable to tackle out-of-band interference. RF filtering also plays a vital

role in preventing the out-of-band interference from saturating the LNA and image frequency problems in the down mixers. The major objective of the automatic gain control (AGC) is to adaptively weigh the RMS amplitude of the downconverted signal to remain constant at the input of analog-to-digital converter (ADC). Interestingly, the same mechanism can also be utilized to implement an interference detector or most commonly referred as jamming-to-noise ratio (J/N) meter (Ward and Betz [2006]).

Signal sampling and quantization primarily constitute the ADC process. It is interesting to note that the sampling process inadvertly introduces aliasing noise into the subsequent digitized signal that manifests as a wideband interference. It should be emphasized here that both anti-aliasing filtering and sampling rate should be appropriately selected to minimize the aliasing noise. Low cost GPS chips typically employ a single-bit quantization as it no longer requires a AGC and the ADC can be simplified to a limiting operation. However, the ensuing receiver design is extremely vulnerable to even low levels of CWI. The use of multi-bit quantization alongside AGC is always beneficial in terms of resilience to CWI. The use of nonuniform quantization also aids in interference suppression although it follows a diminishing returns in terms of quantization levels (Amoroso [1983]). The performance of signal acquisition, tracking and that of data demodulation fundamentally depends on the signal-to-noise and interference ratio (SNIR) at the output of the individual correlator.

5.3   Interference Detection and Suppression

Interference detection and mitigation are central for protecting the GPS receiver against external RFI (Ward [1995]). Figure 5.2 provides a brief overview of various interference mitigation techniques that can be applied in a GPS receiver (Casbona and Rosen [1999]). Interference detection can be achieved by analyzing the residuals in the navigation solution as in the case of receiver autonomous integrity measurement (RAIM)

(Spilker and Natali [1996]). Nonetheless, the effectiveness of RAIM methods can still be restricted with limited satellite availability. The impact of narrowband interference can be detected by observing the tracking loop outputs using multi-correlator techniques (Macabiau et al. [2001]). However, the receiver should be tracking the signal in order to detect the presence of interference (Ward and Betz [2006]). Interference detection can also be accomplished in acquisition by analyzing the statistical properties. For instance, the distribution of the detection output tends to be non-Gaussian in the presence of narrowband interference (Cutright et al. [2003]). Other techniques include time-frequency analysis and statistical inference methods for interference detection (Balaei [2006] and Lijun et al. [2005]). Ward [1995] describes a simple approach to process the control signals of automatic gain control (AGC) to accomplish interference detection. Alternatively, transform domain processing (i.e. DFT) can also be used to reliably detect the presence of narrowband interference (Cutright et al. [2003]).
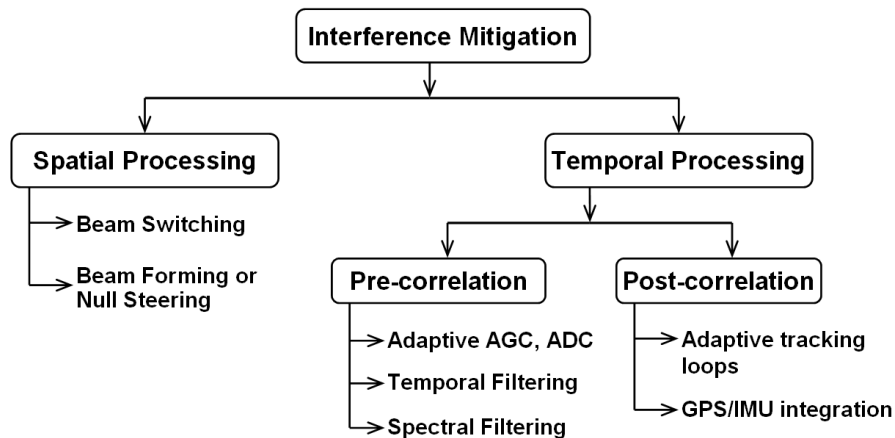
Figure 5.2: Overview of GPS Interference Mitigation Techniques

Judicious design of RF/IF stages, AGC loops, and A/D converters can protect a GPS receiver from external RFI (Spilker and Natali [1996]). On the other hand, specially designed receivers make use of advanced interference detection and mitigation techniques to detect and suppress the RFI. Interference mitigation techniques can be

carried out both spatially and temporally (Ward and Betz [2006]). Spatial processing such as adaptive null steering or beamforming offers significant interference suppression for a variety of RFI. However, the issue of system complexity, manufacturing cost and physical dimension largely limit the application of these techniques. Temporal processing such as temporal or spectral filtering can provide modest interference suppression performance with moderate levels of system complexity. Temporal processing can be performed prior to or after correlation detection. Adaptive notch filtering and frequency excision techniques are examples of pre-correlation techniques. Post-correlation techniques are usually referred to as adaptive code/carrier tracking loops, which utilize INS aiding data from external sensors such as IMUs.

To develop novel interference detection, estimation, and suppression algorithms, it is necessary to initially investigate the interference effects on the developed detectors. In the subsequent sections, the effect of RFI on the conventional correlator and that of the proposed MCDD scheme is performed by deriving their corresponding detection outputs.

5.4   Effect of Interference on Matched Filter Detector

Analyzing the effect of interference on the correlation detection output provides a means to characterize the influence of interference on GPS L1 C/A code acquisition. Recall that the spectrum of the received GPS signal is composed of periodic spectral C/A code line components with a finite dispersion caused by the navigation data. The sampled complex baseband representation of low-pass received signal in the presence of interference is given by,

$$x(k) = \sqrt{2C}d(k)c(k)e^{j(2\pi\Delta Fk+\phi_0)} + \sqrt{2I}p(k)e^{j(2\pi\Delta F_I k+\phi_0')} + w(k) \qquad (5.1)$$

where $x(k)$ is chip sampled output of the received baseband signal. C and I are the carrier and interference power respectively. $c(k)$ and $p(k)$ are the respective transmitted

C/A code signal and interference signal. The received signal is characterized by a residual frequency and phase offset of ΔF and ϕ_0. Similarly, the interference signal has a frequency offset of ΔF_I from the GPS L1 frequency and ϕ_0' being its phase offset. The characteristics of the interfering signal can be readily represented in $p(k)$. For example, $p(k)$ is typically assumed to be slowly varying with respect to $c(k)$ for narrowband interference and time invariant for CW interference. On the other hand, for wideband interference, $p(k)$ varies much more rapidly than $c(k)$. $w(k)$ denotes the complex AWGN with the zero mean and variance σ_w^2. Characterizing the interference at the output of a detector is of critical interest for the analysis of RF interference effects. For a particular $\hat{\theta} = [\Delta\hat{F}, \hat{\tau}]$, the received signal along with interference is multiplied by the locally generated residual carrier and PRN code. The output is typically integrated coherently over the C/A code period, which is further accumulated in a coherent or noncoherent fashion. The output of the matched filter in the presence of interference is given by,

$$y(n) = \sqrt{2C}d(n)R(\tau_{err})\psi_{\Delta F_{err}}(n) + \sqrt{2I}p'(n)\psi_{\Delta F_I'}(n) + w(n) \qquad (5.2)$$

where $y(n) = \sum_{k=nN_c}^{(n+1)N_c-1} x(k)c(k-\hat{\tau})e^{j2\pi\Delta\hat{F}k}$. $\psi_{\Delta F_{err}}(n)$ is the frequency ambiguity arising from the uncompensated residual frequency error. $\psi_{\Delta F_I'}(n)$ is the new center frequency of the interfering signal relative to the downconverted baseband GPS C/A code signal. Following a similar analysis, we can readily derive the signal and noise output as,

$$
\begin{aligned}
d(n) &= \sum_{k=nN_c}^{(n+1)N_c-1} d(k) \\
R(\tau_{err}) &= \sum_{k=0}^{N_c-1} c(k-\tau)c(k-\hat{\tau}) \\
\psi_{\Delta F_{err}}(n) &= sinc(\pi\Delta F_{err}N_cT_c)e^{j\left(2\pi\Delta F_{err}\left[nN_c+\frac{N_c-1}{2}\right]T_c+\phi_0\right)} \\
w(n) &= \sum_{k=nN_c}^{(n+1)N_c-1} w(k)c(k-\hat{\tau})e^{j(2\pi\Delta Fk+\phi_0)}
\end{aligned}
\qquad (5.3)
$$

where $\Delta F_{err} = \Delta F - \Delta \hat{F}$ and $\tau_{err} = \tau - \hat{\tau}$. Similarly, the interference at the output of matched filter detector is given by,

$$
\begin{aligned}
p'(n) &= \sum_{k=nN_c}^{(n+1)N_c-1} p(k)c(k-\hat{\tau}) \\
\psi_{\Delta F_I'}(n) &= sinc(\pi \Delta F_I' N_c T_c)e^{j\left(2\pi \Delta F_I'\left[nN_c + \frac{N_c-1}{2}\right]T_c + \phi_0'\right)}
\end{aligned}
\tag{5.4}
$$

where $\Delta F_I' = \Delta F_I - \Delta \hat{F}$. The effect of interfering signal on the GPS C/A code acquisition can be well understood by analyzing the Fourier transform of (5.2). During acquisition, one can readily notice that $p'(n)$ is essentially the correlation of the interfering signal $p(k)$ and that of the local PRN code signal $c(k)$ over τ. Accordingly, the spectrum of $p'(n)$ is the product of the individual spectrum's of $c(k)$ and $p(k)$. In other words, the Fourier transform of (5.4) readily yields the cross PSD of the local PRN code and that of interfering signal. Hence, the magnitude (or weight) of the specific C/A code spectral line affected by the interference signal crucially determines the impact of interference. The power level of the individual line components typically assumes levels around -30 dB below the code power although there exists individual lines with relatively higher powers. Table 5.1 lists the worst line frequencies and their corresponding amplitudes in reference to the nominal -30.1 dB for a set of GPS PRN codes.

C/A Code PRN Number	Worst Line Frequency (kHz)	Amplitude above Nominal Value (dB)
1	42	7.39
2	263	6.98
3	108	8.06
4	122	7.12
5	122	7.12
6	227	8.81

Table 5.1: Worst C/A Code Spectral Lines (Ref: Ward [1995])

For instance, the PRN 6 C/A code is characterized by a worst line frequency at around 227 kHz. If a CWI happens to fall on this spectral line, it is only scaled down by -21.59 dB rather than the nominal -30.1 dB, which puts the receiver in a more vulnerable

situation to the interference signal. Fortunately, the worst line frequency varies for every PRN code ensuring that other PRN's are less effected from a interference signal for a particular relative center frequency. More importantly, if a CWI signal falls in the vicinity of a C/A code spectral line, it will readily leak through the correlators. Figure 5.3 shows the imaginary component of the correlation output that comprises of the interference alone. The plot shows the correlation output of the CW interference signal with similar powers (i.e. SIR = 45 dB) but with different relative center frequencies. From Figure 5.3, one can readily notice the interference magnitude is substantially increased for the center frequency of 42 kHz in comparison to the 4 kHz center frequency. Note that, the PRN 1 C/A code was utilized for this scenario, which had the worst line frequency at 42 kHz as listed in Table 5.1. Therefore, the effect of CWI critically depends on its relative center frequency and the weights of the individual C/A code spectral lines that are in the vicinity of the CWI spectral line.
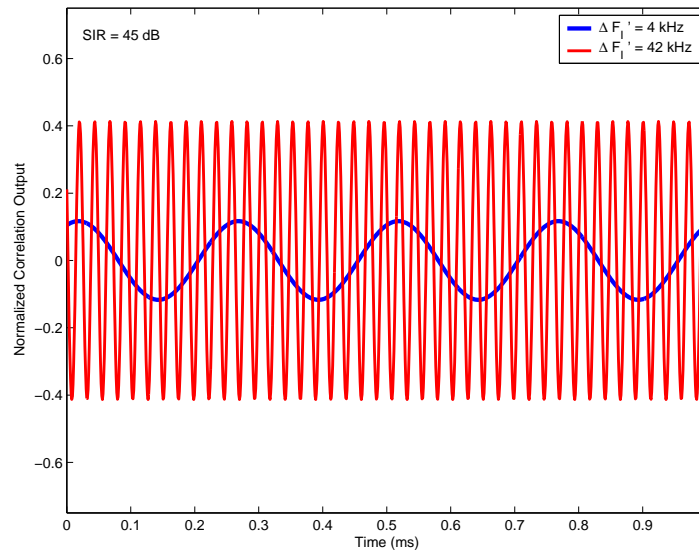
Figure 5.3: Effect of C/A Code Spectral Line on CW Interference Suppression

A narrowband signal with its center frequency taking one of the C/A reference line frequencies generates a comb of line components and eventually leak through the correlator as well (Spilker and Natali [1996]). A wideband interference exerts a uniform

degradation as the power is more or less evenly distributed over the entire interfering spectrum. Periodic wideband interference as in self-interference, can still severely degrade, if the spectral line of interfering signal aligns with the spectral lines of the signal of interest. Finally, it should be emphasized here that the probability that an interfering signal falling on the spectral line is relatively low. Moreover, the probability of multiple PRN's being affected by narrowband interference is even lower. A wideband interference, on the other hand, is more dangerous as it has the ability to effect all the PRN's. However, it requires much higher power than the power is being spread across the bandwidth.

The aforementioned analysis can be readily extended to assess the impact of interference on tracking as well. It should be noted that for interference for a specific code offset (i.e. tracking), the magnitude spectrum of (5.4) readily follows the convolution of an interference spectrum with the C/A code spectral lines. Consequently, the impact of CW interference can be seen as the convolution of impulse spectrum (centered on $\Delta F_I'$) with the C/A code spectral lines. For narrowband interference, the magnitude spectrum of (5.4) would become smoother if the bandwidth of the narrowband signal exceeds the C/A periodic repetition frequency (i.e. 500 Hz, assuming single-sided bandwidth).

5.5 Interference Effects on PF/MCDD technique

In contrast to a matched filter, the effect of interference on differential detection is yet to be investigated in the context of GPS signal detection. The differential detection, if utilized properly can be applied to detection, estimation and possibly the suppression of interference. However, it is necessary to initially characterize the effect of interference on the output of a differential detection for any subsequent development of interference detection and mitigation algorithms.

5.5.1 Multi-correlation Differential Detection

The quintessential operation of the MCDD is the differential detection, which was shown earlier as a modified implementation of a differential detector. The effect of interference can be readily characterized by deriving the MCDD output in the presence of interference. The output of the mth differential detector with (5.2) as its input is given by,

$$\tilde{y}_m(k) = \tilde{y}_m^{ss}(k) + \tilde{y}_m^{pp}(k) + \tilde{y}_m^{sp}(k) + \tilde{y}_m^{sw}(k) + \tilde{y}_m^{pw}(k) + \tilde{y}_m^{ww}(k) \tag{5.5}$$

where $\tilde{y}_m^{ss}(k)$, $\tilde{y}_m^{pp}(k)$, and $\tilde{y}_m^{ww}(k)$ are the signal, interference and noise product terms. The signal, noise and interference cross terms are represented by $\tilde{y}_m^{sp}(k)$, $\tilde{y}_m^{sw}(k)$ and $\tilde{y}_m^{pw}(k)$. The individual terms are given by,

$$\tilde{y}_m^{ss}(k) = 2Cd(k)d(k-m)c(k)c(k-m)e^{j2\pi\Delta F_{err}m}$$

$$\tilde{y}_m^{pp}(k) = 2Ip(k)p(k-m)e^{j2\pi\Delta F_I'm}$$

$$\tilde{y}_m^{ww}(k) = w(k)w^*(k-m)$$

$$\tilde{y}_m^{sp}(k) = \sqrt{2C}\sqrt{2I}\Big[d(k)p^*(k-m)c(k)e^{j\left(2\pi(\Delta F_{err}-\Delta F_I')k+\phi_0-\phi_0'\right)}e^{j2\pi\Delta F_I'm}$$
$$+ d(k-m)p(k)c(k-m)e^{j\left(2\pi(\Delta F_I'-\Delta F_{err})k+\phi_0'-\phi_0\right)}e^{j2\pi\Delta F_{err}m}\Big]$$

$$\tilde{y}_m^{sw}(k) = \sqrt{2C}\Big[d(k)c(k)w^*(k-m)e^{j(2\pi\Delta F_{err}k+\phi_0)} + d(k-m)c(k-m)w(k)e^{-j(2\pi\Delta F_{err}k+\phi_0)}\Big]$$

$$\tilde{y}_m^{pw}(k) = \sqrt{2I}\Big[p(k)w^*(k-m)e^{j(2\pi\Delta F_I'k+\phi_0')} + p^*(k-m)w(k)e^{-j(2\pi\Delta F_I'k+\phi_0')}\Big]$$
$$\tag{5.6}$$

In Section 4.2, the MCDD detection output was shown to be similar to the squared magnitude output of coherent matched filter detector. However, the modified implementation using MCDD can be utilized advantageously to implement intermediate frequency suppression techniques. For example, in (5.6), the interference at the output of differential detection is translated to baseband. This is of critical significance in terms of narrowband interference. For example, a CWI signal despite its center frequency will be translated to D.C. (or 0 Hz) and thus being attenuated significantly (30.1 dB). For narrowband interference, this alleviates the estimation of center frequency

and bandwidth. On the other hand, for wideband interference, the MCDD can still be advantageous for interference cancellation. For instance, traditional interference cancellation techniques require the estimation of the navigation data, $d(k)$, and residual carrier in addition to the amplitude of the interfering GPS C/A code signal (Madhani et al. [2003]). In contrast, the MCDD effectively suppresses time varying phase introduced by the residual carrier and that of data modulation and thereby eliminates the need for navigation data prediction and residual frequency offset estimation.

5.5.2 MCDD based CWI Detection, Estimation and Suppression

In the presence of a CWI signal, the term $y_m^{pp}(k)$ in (5.6) can readily be approximated by a constant $p(k)$ and is readily assumed to be time-invariant. Recognizing the fact that both the C/A code signal $c(k)$ and the background noise $w(k)$ is zero mean, the presence of CWI signal can be readily detected by estimating the mean of the differential detector and comparing it against a threshold. The mean value estimate is given by,

$$\Omega(m) = \frac{1}{NN_c} \sum_{k=0}^{NN_c-1} \tilde{y}_m(k) \tag{5.7}$$

Substituting for $\tilde{y}_m(k)$ and assuming the mean statistics of product terms arising from signal and noise multiplication to be zero (in the asymptotic sense) produces,

$$\Omega(m) \approx 2I\tilde{p}_m(k)e^{j2\pi\Delta F_I' m} \tag{5.8}$$

where $|\Omega(m)|$ readily yields the power of the interference signal. It should be emphasized that this approximation is valid only for $NN_c \gg 1$ and $p(k)$ is a constant or slowly varying with respect to $c(k)$. Therefore, the presence of a CWI signal can be detected by simply measuring the mean of the individual differential detector and comparing it against a pre-defined threshold. Besides, the mean $|\Omega(m)|$ can also be utilized as an indirect measure of the CW signal power. Figure 5.4 shows $|\Omega(m)|$ in the presence of the CW interference (LHS plot) and the performance of SIR estimator based on the same principle (RHS plot).
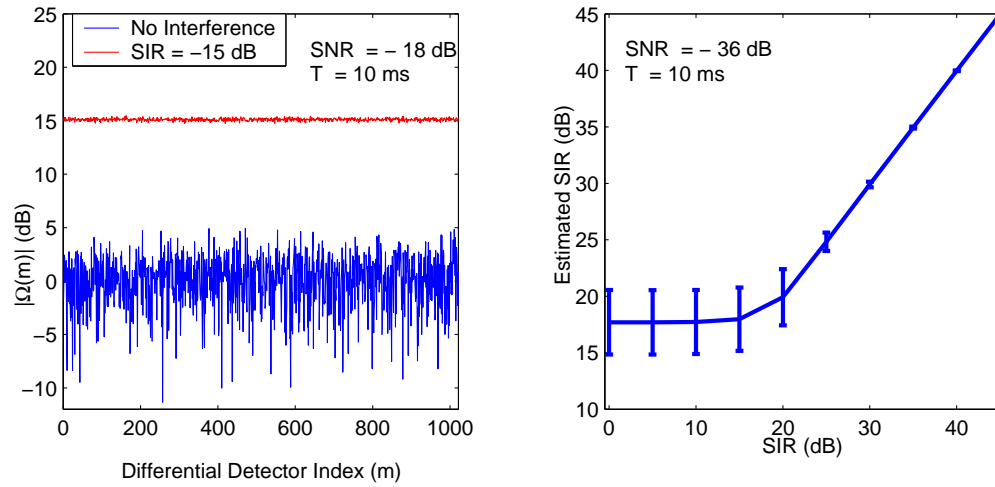
Figure 5.4: Detection of CW Interference Using MCDD Technique

From Figure 5.4, it is apparent that the accuracy of the SIR estimation improves with increasing SIR in accordance with theory. Note that the performance of the aforementioned SIR estimator can also be improved by averaging across the differential detector output using the envelope detection output. Moreover, it is also desirable to estimate the parameters of the interference signal to effectively cancel it in later stages. Interestingly, the complex phase rotations at the output of differential detector represented by $\Omega(m)$ collectively embody the CWI signal. For instance, we can utilize a simple FFT based frequency estimator to estimate the frequency of the CW interference. Note the developed frequency estimator should be capable of estimating multiple CW interference signals. Figure 5.5 shows the real and imaginary components of the differential detector output as a function of m.

The scenario includes two CW interferer's at 4 and 7 kHz with the relative interference power of 24 and 21 dB respectively. In the presence of multiple CW interferer's, the mean $\Omega(m)$ represents the summation of the individual but orthogonal CW interferer's. The normalized FFT output of $\Omega(m)$ is also plotted in Figure 5.5. The resolution and the bandwidth of the FFT based frequency estimator is given by $\Gamma_{BW} = T_c^{-1}$ and $\Gamma_{RES} = 2MT_c^{-1}$. Figure 5.6 illustrates the MCDD and FFT based CW interference
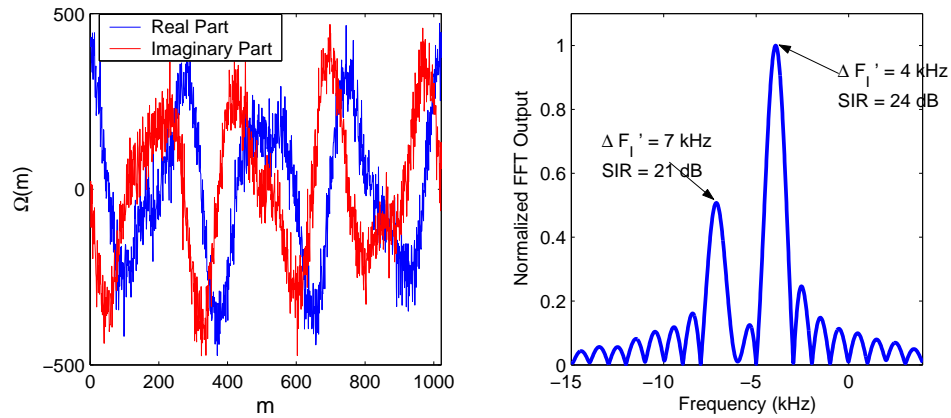
Figure 5.5: Detection of Multiple CW Interference Using MCDD and FFT Based Estimator

detection and estimation.
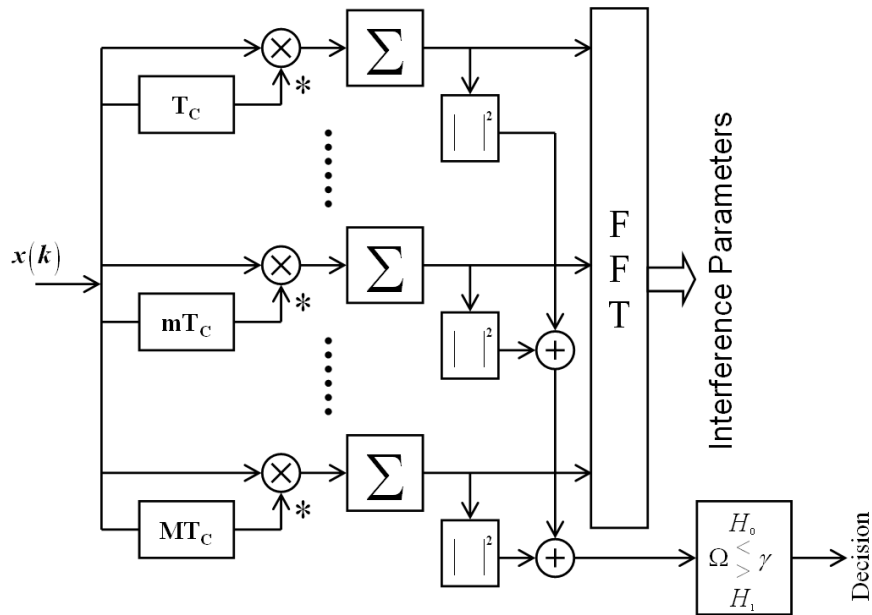
Figure 5.6: MCDD and FFT Based CW Interference Detection and Estimation

From (5.8) and (5.2), it can be readily inferred that removing the mean from (5.2) would effectively accomplish the process of interference suppression. Note that by removing the mean of the correlation output across the correlation branches does not

affect the final detection output. The CW interference suppressed output is given by,

$$\bar{y}_m(k) = \tilde{y}_m(k) - \frac{1}{N} \sum_{k=0}^{N-1} \tilde{y}_m(k) \tag{5.9}$$

where M is the observation period to estimate the mean value. Note that the summation operation in the above equation can be readily accomplished through a moving average filter. Figure 5.7 shows the convergence of $|\Omega(m)|$ as a function of observation period. The plot readily corroborates the convergence of $|\Omega(m)|$ for an observation period of 10 ms (or N = $10T_r T_s^{-1}$). Besides, the convergence is similar for various differential delays.
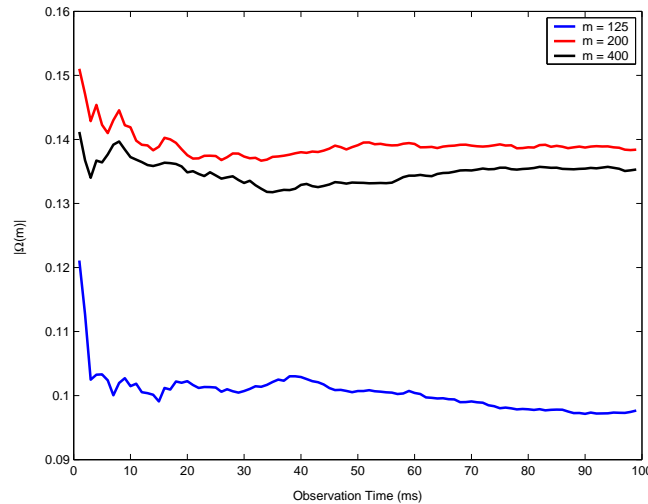
Figure 5.7: Convergence of $|\Omega(m)|$

Thus, the MCDD technique can be effectively adopted to detect, estimate and suppress CW interference with only moderate levels of complexity. However, it should be emphasized here that the CW interference suppression scheme may not be effective against multiple CW interferers as the differential detection output would also contain intermediate beat frequencies. The aforementioned interference detection and estimation can also be applied for narrowband interference with much smaller bandwidth. The developed MCDD scheme should be augmented with further interference suppression schemes to tackle the narrowband interference with larger bandwidths or multiple tone

CWI signals.

5.6 Acquisition Performance Evaluation

Having analyzed the effect of RF interference on the standard and multi-correlation differential detection, we now turn to real data analysis. The test setup utilized the hardware signal generator alongside a commercial off the shelf (COTS) arbitrary signal generator for emulating the CW and narrowband interference. The FFT based frequency excision algorithm was also developed and incorporated in the standard non-coherent and the multi-correlation differential detection for further performance evaluation.

5.6.1 Test Methodology

The developed test methodology utilized hardware simulated GPS signals to emulate controlled scenarios of interference environments. Figure 5.8 illustrates the test setup employed for the GPS data collection. The test setup included the Spirent GSS7700 GPS L1 signal generator, Agilent ESG E4413B for interference signal generation and Spirent GSS4766 interference combiner unit. The GPS signal generator and the interference combined was controlled by the SimGEN software. The output of the interference combiner output was pre-amplified by an LNA (30 dB gain) and subsequently supplied to the front-end NovAtel Euro-3M GPS card modified to output raw IF samples at 40 MHz (20 MHz for combined I and Q). The IF data was then resampled to 2.046 MHz with and digitized to 3-bit values. The receiver's C/N_0 estimate of a high elevation satellite (PRN20) was used as a baseline for defining nominal hardware simulator levels.

The interference scenarios included CW interference with the relative offset of 1 kHz at power levels of 15 dB and 30 dB higher than the GPS nominal power level.
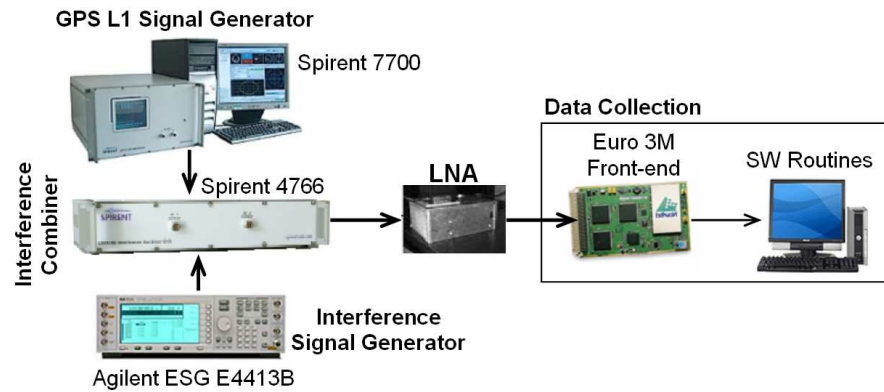
Figure 5.8: Interference Analysis – Test Setup

For narrowband interference, similar power levels were used alongside an interference bandwidth of 100 kHz (approximately 10% of GPS first null-to-null bandwidth). Figure 5.9 shows the spectrum of received GPS signal for the case of CW and narrowband interference. Note that the resultant spectrum was also characterized by additional CW spectral lines around 500 kHz.
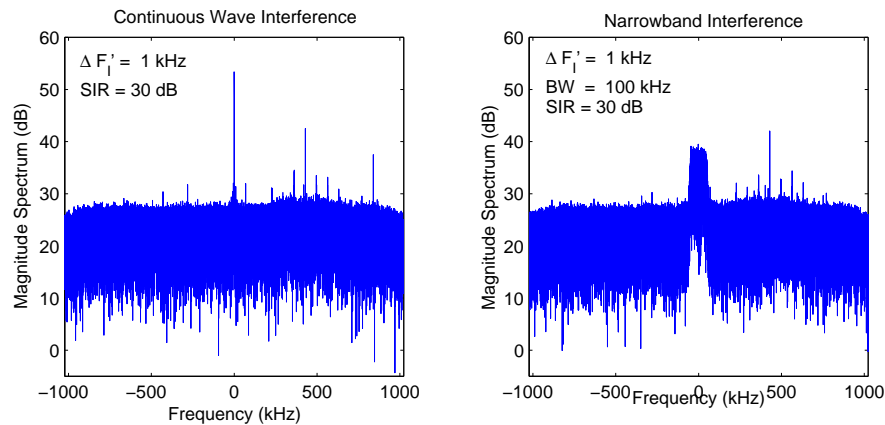
Figure 5.9: Magnitude spectrum of received GPS L1 signal. (LHS) CW interference (RHS) Narrowband interference

The benchmark performance of both the acquisition techniques was evaluated for the PRN 20, which had a C/N_0 of 47 dB-Hz. However, it is recognized that there would be finite power loss from the cables connecting the signal generator, LNA and the front-end. The post-correlation noncoherent, differential and generalized techniques

utilized one millisecond pre-detection integration period (i.e. $T_{COH} = 1$ ms). Besides, they also utilized an extended observation time of $T = 100$ ms. On the other hand, the MCDD technique with $M = 1022$ correlator branches with a similar total observation period of 100 ms. The same set of acquisition parameters had been consistently used to obtain the subsequent results.

In Section 5.4, it was reported that the CW interference can potentially leak through the correlator if its center frequency falls on the C/A code spectral lines. Macabiau et al. [2001] also utilized the same principle to develop a CW interference detection. To further validate, IF data in the presence of CW interference with a relative center frequency of 1 kHz with respect to the PRN 20 C/A code signal was collected and subsequently processed. Figure 5.10 shows the matched filter detector output in the presence of a 15 dB CW interferer with a relative center frequency of 1 kHz. The coherent integration time was set to 100 ms so as to clearly observe the effect of the CW interference. The plot clearly shows the presence of CW interference in the received
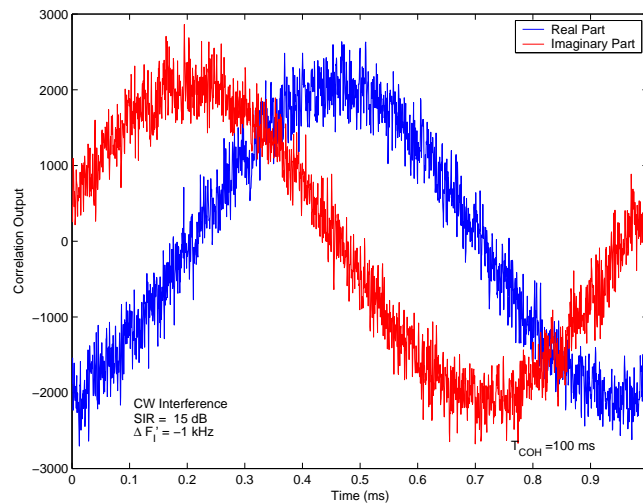
Figure 5.10: Matched Filter Detector Output in the Presence of CW Interference (SIR = 15 dB)

GPS C/A code signal. However, the receiver was still able to acquire the PRN 20 C/A code signal even in the presence of a 15 dB CW interference. A simple CW interference

detection based on analyzing the mean value at the output of the differential detector was introduced in Section 5.5.2. To validate the developed CW interference detector, the magnitude of $|\Omega(m)|$ is plotted in Figure 5.11 for various interference power levels as a function differential delays. The plot also includes the $|\Omega(m)|$ in the absence of CW interference.
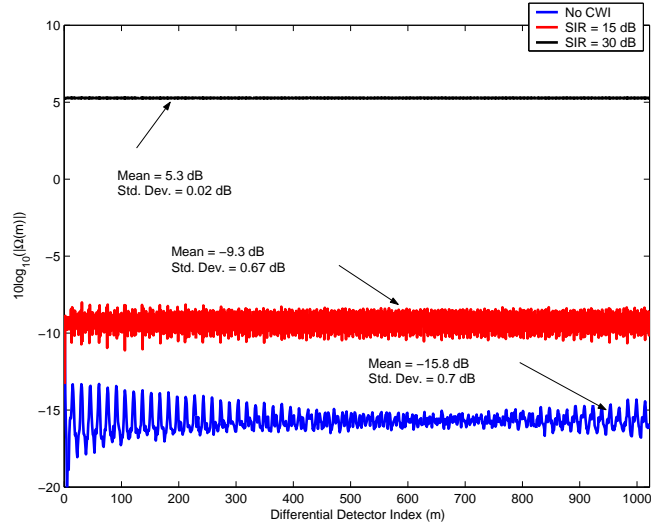
Figure 5.11: MCDD Based CW Interference Detection

From Figure 5.11, it can readily be noticed that $|\Omega(m)|$ tends to take higher values with increasing interference power levels. The relative values of $|\Omega(m)|$ for the 15 and 30 dB CW interference in regards to clean GPS signal were around 6.5 and 21 dB, respectively. The bias in the CW interference power estimation could be readily attributed to the additional CW interferer's around 500 kHz as shown in Figure 5.9. Interestingly, the mean $\Omega(m)$ also embodies the CW interferences as well. Hence, by analyzing $|\Omega(m)|$, we can readily determine the existence of CW interference and possibly provide an estimate of the values. Figure 5.12 shows the real and imaginary components of $\Omega(m)$ for the case of the 15 dB CWI signal.

The plot readily confirms the existence of a CW interference with a relative center frequency of around 1 kHz. The existence of a secondary CWI signal can also be
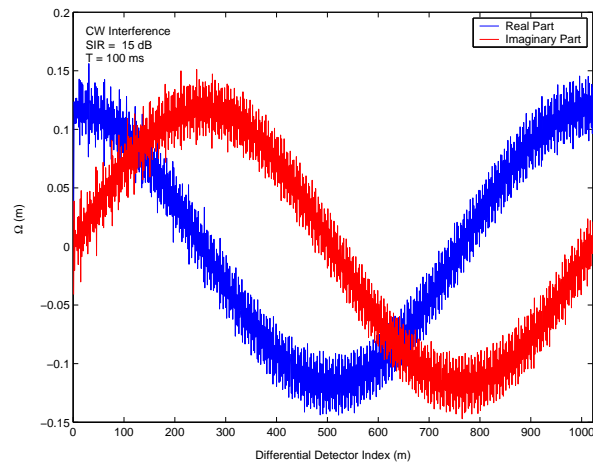
Figure 5.12: Real and Imaginary Components of $\Omega(m)$

observed in the form of high frequency periodic variations in $\Omega(m)$. Figure 5.13 shows the normalized FFT output of $\Omega(m)$ with T_c being the input sampling rate to the FFT estimator. The plot indicates the presence of strong CW interference around 1 kHz and -428 kHz. The interference at -428 kHz can also be observed in Figure 5.9. Furthermore, the CW interference had a 7 dB lower power compared to the stronger CW interference at 1 kHz but still sufficient to effect the weak GPS C/A code signal.
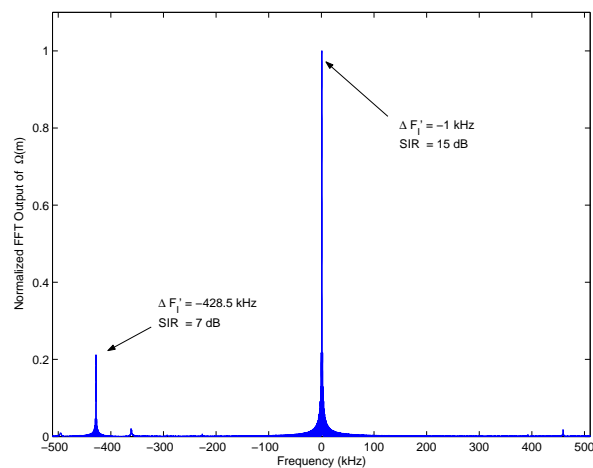
Figure 5.13: Normalized FFT Output of $\Omega(m)$

5.6.2   Acquisition Sensitivity Tests

The acquisition performance of various detectors in the presence of CW and narrow-band interference is tabulated in Table 5.2. The detection schemes performed well amidst of 15 dB CW and narrowband interference. However, almost all the detectors suffered a substantial degradation at 30 dB interference power levels. The developed MCDD technique was able to acquire the PRN 20 C/A code even with the 30 dB CW interference. It also barely managed to acquire the same PRN 20 C/A code for the 30 dB narrowband interference scenario. Nevertheless, there still exists some significant amount of degradation even with the MCDD scheme. It should be emphasized here that the MCDD technique basically suppresses the mean or the DC component and thus suppresses CW interference with line bandwidth. However, the bandwidth of the interference signal even for CW interference is finite. Secondly, the cross terms arising from the interference signal also substantially increases the noise floor that further degrades the MCDD acquisition performance.

Detector	CW Interference (dB)		Narrowband Interference (dB)	
Type	15	30	15	30
PCND	26.7	10.4	24.8	11.7
PCDD	31.1	13.1	27.1	11.3
GPCDD	32.2	15.8	31.4	10.3
MCDD	31.6	19.6	30.2	17.1

Table 5.2: PSNR Performance under CW and Narrowband Interference Environment

The use of the frequency excision technique will significantly enhance the acquisition performance especially at higher interference power levels (Peterson et al. [1996]). Recall that the matched filter detector is no longer optimal in the presence of non-Gaussian noise as in the case of narrowband interference. The traditional frequency excision technique essentially detects the non-Gaussian statistics of the received signal by observing the spectrum of the received GPS C/A code signal (Ndili and Enge [1998]). The spectrum is divided into number of frequency bins, wherein the magnitude of each

spectral bin is compared against a threshold (Dipietro [1989]). The threshold can either be fixed based on a priori knowledge or adaptive in which case, the threshold is typically set to the standard deviation of the spectrum (Jiang et al. [2004]). The spectral bin with magnitude exceeding the threshold can be simply set to zero (or a small value). It is recognized that the FFT based excision incurs interference spectral leakage due to the finite FFT process. However, the effect of this spectral leakage can be reduced by utilizing appropriate windowing methods (Jiang et al. [2004]).

The frequency suppression in the frequency domain can be readily understood as pre-whitening filtering, whereby the spectrum is made flat by removing part of the spectrum. Thus, the matched filter can be readily applied as the subsequent samples from the frequency excision unit are no longer non-Gaussian. However, the frequency excision process also eliminates the useful signal components and thus there would still be some degradation. In the presence of narrowband interference, the bandwidth should also be estimated to optimally excise the spectrum pertaining to the narrowband interference.

Figure 5.14 shows the PSNR improvement for the different detectors with frequency excision. The excision bandwidth was set to 1 kHz and the spectral bins exceeding the threshold were replaced by the standard deviation estimate of the spectrum. Note that the use of frequency excision resulted in further PSNR degradation for the 15 dB CW interference scenario. The degradation can be readily attributed to the frequency excision bandwidth of 1 kHz and in particular the removal of the stronger C/A code spectral line. On the other hand, significant improvements were observed for the stronger 30 dB CW interference scenario. The PSNR improvement for the MCDD is not significant in comparison to other detectors, as it utilized an inherent interference suppression mechanism. On the other hand, the PCDD and the GPCDD structure resulted in the maximum PSNR gain with the application of frequency excision. Be-

sides, the PCDD and GPCDD structures can also employ the CWI signal suppression mechanism proposed here in terms of MCDD.
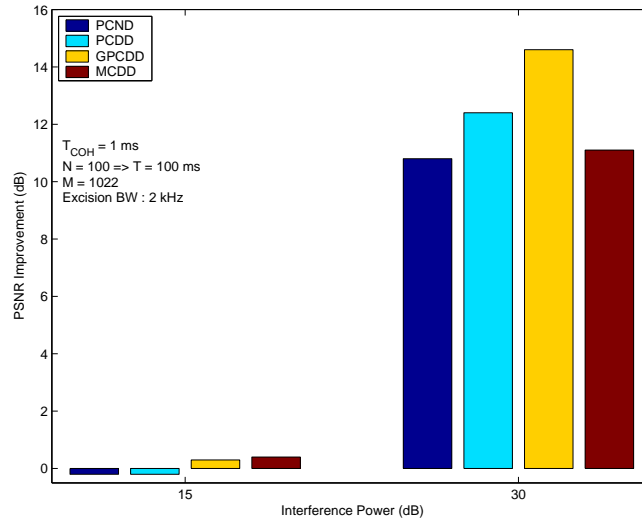
Figure 5.14: PSNR Performance Improvement with Frequency Excision Technique for CW Interference

Figure 5.15 shows the narrowband interference suppression in terms of the received and excised spectrum alongside their correlation outputs. The plot corresponds to the PCND with a coherent integration period of 1 ms and a total observation time of 100 ms. The interference signal had a received power level of around 30 dB and a bandwidth of 100 kHz centered around 1 kHz.

The plot readily confirms the significance of the frequency excision technique for narrowband interference suppression. One can also observe the pre-whitening of the received spectrum as a consequence of frequency excision. Figure 5.16 shows the PSNR performance as a function of frequency excision bandwidth. The saturation of PSNR around 100 kHz can be uniformly observed across all the detectors as the interference spectrum is completely excised.

Figure 5.17 shows the PSNR improvement with frequency excision for the narrowband interference. The interference excision bandwidth was set to 120 kHz for optimal interference suppression. The MCDD, due to its inherent interference suppression abil-
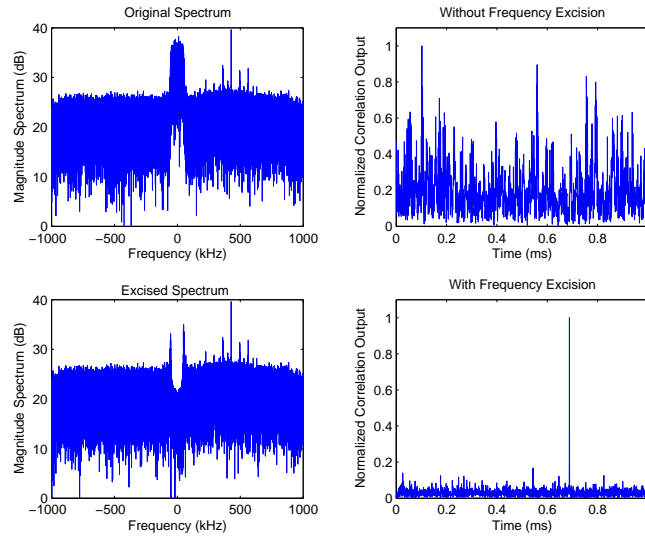
Figure 5.15: Narrowband Interference Suppression (Upper) Original Spectrum and Correlation Output (Lower) Excised Spectrum and Correlation Output
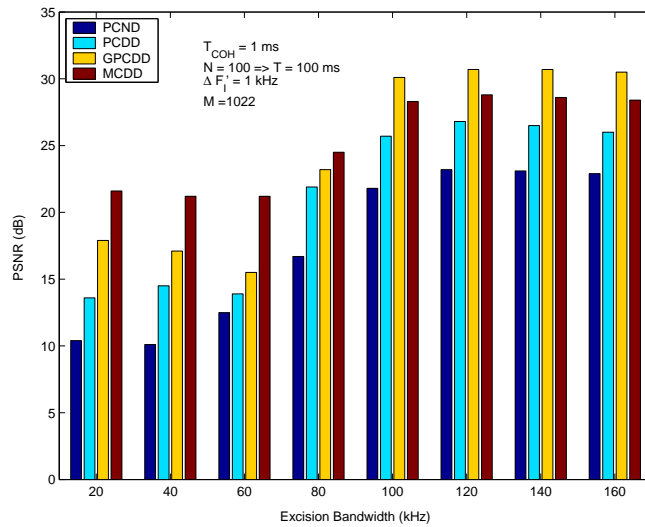
Figure 5.16: PSNR Performance as a function of Frequency Excision Bandwidth

ity, resulted in the least PSNR gain with the application of the frequency excision. It should be emphasized here that the proposed GPCDD and MCDD structure yielded superior detection performance over the traditional PCND and PCDD structures under RFI environment. The MCDD structure also offered a partial interference suppression through mean value suppression approach described in the context of CWI suppression.
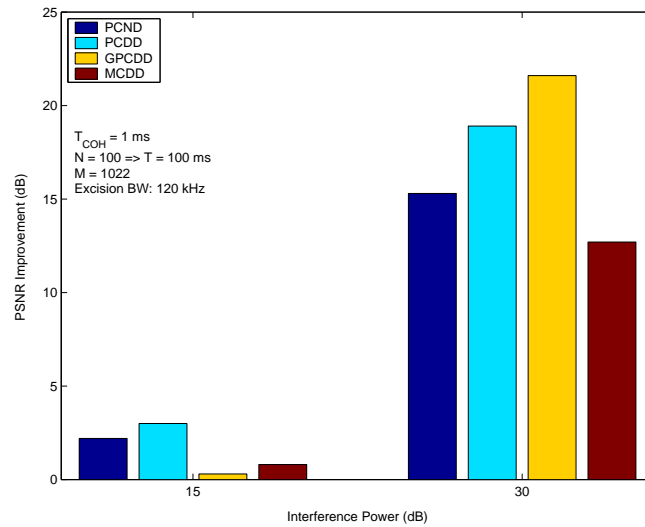
Figure 5.17: PSNR Performance Improvement with Frequency Excision Technique for Narrowband Interference

5.7 Discussion

Sections 5.1 and 5.2 briefly introduced the sources of different RFI and their effect on a conventional GPS receiver. In Section 5.4, we derived the matched filter output in the presence of interference. The detection output for the MCDD, in the presence of RFI, was derived in Section 5.5. The usefulness of the proposed structure in terms of interference suppression was succinctly introduced. Subsequently, a simple CWI detection scheme based on analyzing the mean value at the output of the differential detector was proposed. The scheme was further developed to estimate the CWI parameters such

as the center frequency and interference power. Finally, the acquisition performance of various detectors in the presence of CW and narrowband interference was analyzed in section 5.6. The MCDD structure generally proved to be robust against NBI even at stronger interference power levels. The significance of frequency excision techniques for interference suppression was also demonstrated in terms of real data analysis. It should be emphasized here that the research presented in this chapter is not comprehensive and was intended to demonstrate the use of differential detector sturctures for GPS signal detection under RFI.

Chapter 6

Modernized GPS Signal Acquisition – New Results

The commencement of GNSS modernization critically necessitates new acquisition algorithms to wholly utilize the innovative signal structure. A number of detection algorithms developed for the problem of legacy GPS C/A code acquisition were extended to modernized signal acquisition. Unfortunately, the new signal structure potentially limits the applications of these detectors to modernized GPS signal acquisition. Therefore, it is necessary to adapt the original detection algorithms for modernized GPS signal acquisition to achieve maximum benefit. In accordance with this objective, this chapter further develops the detection algorithms proposed in Chapters 3 and 4 for modernized GPS signal acquisition. This chapter begins by briefly introducing the modernized signal structure. A brief review of different acquisition schemes proposed in the literature for modernized GPS signal acquisition is presented. Consequently, a number of variants of the detectors/estimators developed in Chapters 3 and 4 are introduced for modernized GPS signal acquisition. The generalized post-correlation differential detector, in particular, is developed for the problem of GPS L2C code acquisition. The asymptotic optimality of the generalized post-correlation differential detection for the CL code detection is established. Similarly, the advantage of using multi-correlation differential detection for NH code detection in GPS L5 acquisition is established. Furthermore, the significance of judicious short synchronization code design is emphasized from the view point of NH code acquisition. Finally, the developed concepts are validated using the hardware simulated and live GPS signals side-by-side using detection performance comparisons.

6.1   Modernized Signal Structure

The block IIR-M satellites [1] transmit the modernized GPS L2C signals on the L2 signal in addition to the legacy GPS C/A code signal at L1. The modernized GPS L5 signals will be transmitted by block II-F satellites, which also transmit the C/A and L2C code signals on the L1 and L2 frequencies. The block IIR-M and II-F satellites also transmit the new military M-code signal on the L1 and L2 frequencies. Figure 6.1 shows the spectrum of legacy and of the modernized GPS signals (ICD-GPS-200C [2003]). The L2C signal is transmitted at -160 dBW, which is 2.3 dB lower compared to the -157.7 dBW L1 C/A signal (Fontana et al. [2001]). The allocated transmission bandwidth for the L2C signal is similar to that of L1 C/A, which is 20 MHz. On the other hand, the GPS L5 signal is transmitted at a -154 dBW level, 3.7 dB higher compared to the GPS L1 C/A signal (Van Dierendonck and Hegarty [2000]). The allocated transmission bandwidth for the GPS L5 signal is 24 MHz and thus the transmitted signal spectrum is limited to its first side-lobe. The M code signal utilizes the PRN that is chipped at 5.115 MHz and involves the binary offset carrier modulation, wherein the subcarrier is clocked at 10.23 MHz. The use of BOC modulation essentially splits the spectrum as shown in Figure 6.1 for spectral separation. The readers are referred to Barker et al. [2000] for a more detailed treatment of M code signal design and reception.
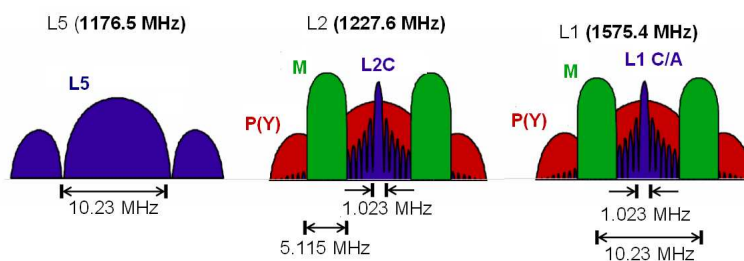
Figure 6.1: Spectral Allocation of Modernized GPS Signals (ICD-GPS-200C [2003])

---

[1]Currently, the L2C signals are being transmitted from PRN 7, 12 and 31 satellites

6.1.1 The L2C Signal

The L2C signal comprises of a time-multiplexed data and pilot channels to accommodate the military P(Y) signal. The readers are further referred to ICD-GPS-200C [2003] for L2C space and user interface documentation. Figure 6.2 shows the simplified block diagram of L2C signal generation in a block II-F satellite. The data component basically consists of the civil moderate (CM) code of length 10,230 in chips (i.e. $N_{cm} = 10230$) that is clocked at 511.5 kHz (i.e $T_{cm} = 2 T_c$, where T_c is the C/A code chip duration). Hence, the CM code signal is periodic over 20 ms (i.e. $N_{cm}T_{cm}$). The CM code is further modulated with the modernized navigation data (CNAV) that is generated at 25 bps (i.e. $T_b = 2N_{cm}T_{cm}$). However, the CNAV data is forward error control (FEC) coded with a rate 1/2 convolutional encoder that outputs symbols at 50 symbols-per-second. Thus, the symbol rate is kept similar to that of the L1 C/A data rate at 50 Hz (i.e. $T_{sym} = N_{cm}T_{cm}$). It is important to note that the transmitted power allocated to the L2C data signal is reduced by 3 dB but the use of advanced FEC coding provides a gain of around 5.6 dB. Note that the navigation data symbols are synchronized with that of the CM code period to facilitate data synchronization at the receiver end.
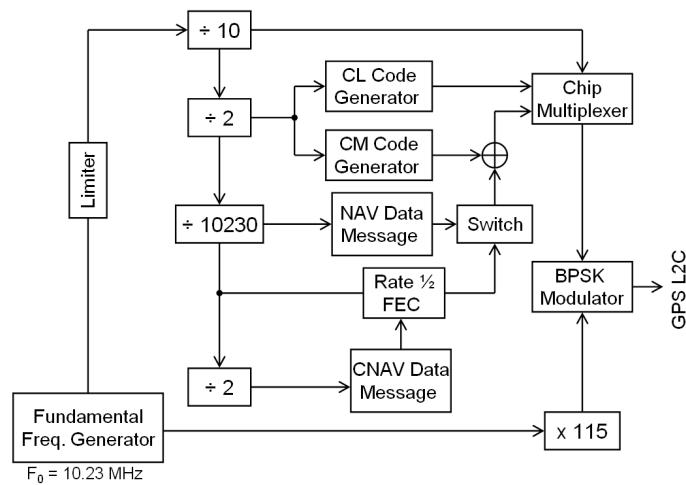
Figure 6.2: L2C Signal Generation in Block II-F Satellite

The pilot component of the L2C is essentially composed of the civil long (CL) code

of length 767, 250 in chips (i.e. $N_{cl} = 767250$), which is also clocked at 511.5 kHz (i.e $T_{cm} = 2\ T_c$). Hence, the CL code signal is periodic over 1.5 s, which is 75 times longer than the CM code signal (i.e. $N_{cl} = 75\ N_{cm}$). Furthermore, there is an additional advantage arising from the 1.5 s CL code period in the perspective of its relationship to the GPS Z-count. Finally, the modulated CM code signal and the CL code signal are chip-by-chip multiplexed to form the L2C signal. The L2C signal is then upconverted to 1227.6 MHz prior to transmission. It should be noted here that the block II-F satellites are capable of using either the legacy NAV or the modernized CNAV message as shown in Figure 6.2.

6.1.2   The L5 Signal

The L5 signal also consists of pilot and data components that are I/Q multiplexed due to the spectral availability around 1176.5 MHz (L5). The readers are further referred to ICD-GPS-705 [2002] for L5 space and user interface documentation. The data component is the inphase component, (often referred to as I5,) and contains the I5 code of length 10,230 in chips (i.e. $N_{I5} = 10230$) that is clocked at 10.23 MHz (i.e. $T_{I5} = T_c\ /10$, where T_c is the C/A code chip duration). Hence, the I5 signal is periodic over 1 ms (i.e. $T_r = N_{I5}T_{I5}$). The I5 code is modulated with the modernized CNAV data that is generated at 50 bps (i.e. $T_b = 20T_r$). However, the CNAV data is further processed through a rate 1/2 FEC convolutional coder to produce symbols at 100 symbols-per-second (i.e. $T_{sym} = 0.5T_b = 10T_r$). The pilot component, (often referred to as Q5,) occupies the quadrature of the L5 signal and contains the Q5 code. The Q5 code is also of length 10,230 in chips and is clocked at 10.23 MHz (i.e. $N_{Q5} = N_{I5}$ and $T_{Q5} = T_{I5}$). Figure 6.3 depicts a simplified block diagram of the GPS L5 signal generation (ICD-GPS-705 [2002]).

In contrast to the GPS L2C signal, the GPS L5 signal is characterized by a two-
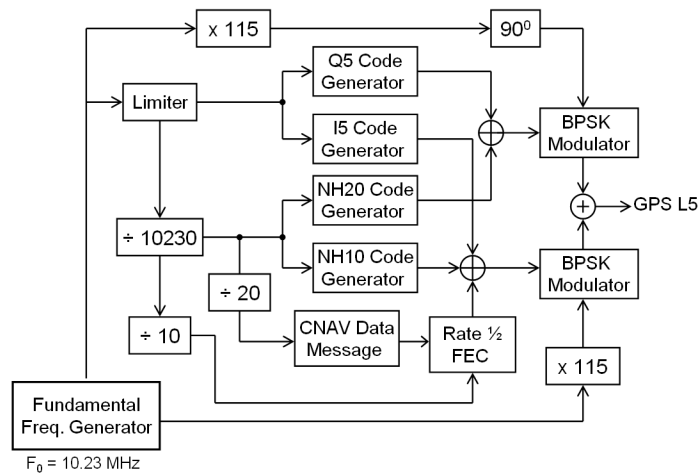
Figure 6.3: Modernized GPS L5 Signal Generation (ICD-GPS-705 [2002])

tiered code structure. The $I5$ and $Q5$ codes form the primary code and is utilized for spread-spectrum modulation. On the other hand, the secondary code is short and is mainly intended for data synchronization and interference suppression performance improvements. Thus, the I5 and Q5 codes are modulated with corresponding short synchronizations codes that are often referred as the NH codes (Neuman and Hofman [1971]). The NH codes are clocked at a much lower rate at around 1 kHz (i.e. $T_{NH} = T_{I5}N_{I5}$). While the data channel NH code is of length 10-bits (i.e. NH10), the pilot component NH code is of length 20-bits (i.e. NH20). The NH10 code is synchronized with the navigation data symbols and thus aid during data synchronization. Finally, the baseband I5 and Q5 signals are I/Q multiplexed using orthogonal carriers with the centre frequency of 1176.5 MHz prior to transmission.

6.1.3   Spectral and Correlation Characteristics

The essence of GPS receiver operation is readily embodied by the correlation detection (or matched filtering) operation. Hence, it is highly desirable to investigate the correlation properties of the underlying PRN code that is adopted for the modernized L2C and L5 signals. Additionally, the spectral properties can be well understood from

their corresponding correlation characteristics. This section briefly discusses the code generation, correlation and spectral characteristics of the PRN codes utilized in GPS L2C and L5 signals.

CM and CL Code Properties

The CM and CL codes are both generated from the same LFSR but with differential initial states. The shift register being used comprises of 27 stages with 12 feedback taps. The binary sequence generated by this shift register is periodic over 134217728 chips if not short cycled. However, the individual CM and CL codes are obtained by initializing the LFSR to specific initial states and short cycling back again to the same initial state after 10230 chips for CM code and 767,250 chips for the CL code. The same process can be performed by detecting the final state to short cycle back to initial state. A total of 100 CM and CL codes are generated in this fashion. The recursive representation of the CM and CL codes generator is given by (ICD-GPS-200C [2003]),

$$G(i) = G(i-27) \oplus G(i-24) \oplus G(i-21) \oplus G(i-19) \oplus G(i-16) \oplus G(i-13)$$
$$\oplus G(i-11) \oplus G(i-9) \oplus G(i-6) \oplus G(i-5) \oplus G(i-4) \oplus G(i-3)$$
$$\tag{6.1}$$

The octal representations of the initial and final states (of shift registers) for the first 37 CM and CL codes are defined in ICD-GPS-200C [2003]. The individual CM and CL codes are balanced with equal number of zeros and ones due to their implications in correlation and thus spectral characteristics. Figure 6.4 shows the spectrum of the legacy GPS C/A code aside from CM code (Left) and CL code (Right) spectrum. The CM code is periodic over 20 ms and thereby results in a periodic spectrum, wherein the individual spectral lines are separated by 50 Hz. The closely spaced spectral lines in CM code readily allows for better resilience against narrowband interference. Moreover, the time- multiplexed L2C signal is periodic over 1.5 s resulting in a much finer line spacing of 0.67 Hz and even better resilience against narrowband interference.
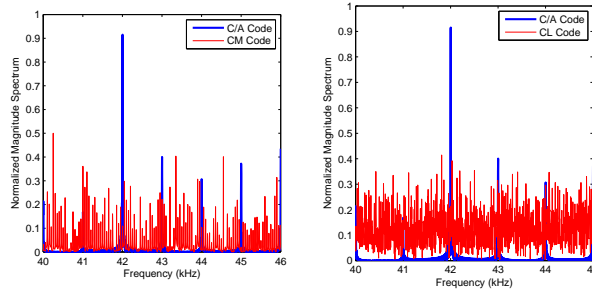
Figure 6.4: GPS L1 C/A and L2C CM and CL Code Spectrum (PRN 1)

I5/Q5 and NH Code Properties

The primary PRN codes, I5 and Q5, are derived from the family of codes that is often referred as *g-codes* (Spilker Jr and Van Dierendonck [2001]). The g-codes are generated from a pair of two different m-sequence generators, each consisting of 13 stages. The generator polynomial for the individual m-sequence generators are given by,

$$G1(i) = G(i-13) \oplus G(i-12) \oplus G(i-10) \oplus G(i-9)$$
$$G2(i) = G(i-13) \oplus G(i-12) \oplus G(i-8) \oplus G(i-7) \oplus G(i-6) \qquad (6.2)$$
$$\oplus G(i-4) \oplus G(i-3) \oplus G(i-1)$$

The m-sequences obtained from the generator polynomials $G1(i)$ and $G2(i)$ is commonly referred as preferred pairs, whose product forms the well known Gold sequence family. Note that the length of the m-sequences obtained from $G1(i)$ and $G2(i)$ are of length 8191 in chips. The I5 and Q5 codes of length 10,230 in chips are obtained from these primitive sequences generated by $G1(i)$ and $G2(i)$ in the following fashion. The code generated from $G1(i)$ is shortened by one chip and the resulting code is multiplied with the code produced from $G2(i)$, which results in the final code of length 8190 x 8191 = 67,084,290 chips in length. However, the m-sequence generators are reset every 10,230 chips to their initial states. In the case of $G1(i)$, the states are initialized by all 1's. For $G2(i)$, the states are initialized by the values corresponding to the PRN and I5 or Q5 states. The initial states to obtain the I5/Q5 PRN codes is listed in ICD-GPS-705 [2002]. Finally, I5/Q5 codes are obtained as the product of the codes generated by $G1(i)$

(shortened by one chip) and time offsetting the code generated from $G2(i)$. Hence, the number of unique codes that can be generated is readily limited by the length of the code obtained from $G1(i)$. Thus, one can generate only 4095 unique codes using the method described above. Finally, the NH10 and NH20 code is given by,

$$NH10 = [1, 1, 1, 1, -1, -1, 1, -1, 1, -1]$$

$$NH20 = [1, 1, 1, 1, 1, -1, 1, 1, -1, -1, 1, -1, 1, -1, 1, 1, -1, -1, -1, 1]$$

(6.3)

The same NH codes are utilized by every satellite as the primary I5 and Q5 codes readily provides the sufficient correlation separation. The correlation properties were slightly better with the inclusion of NH code. This does not come as a surprise as the NH codes are expected to have low correlation suppression performance due to the short code period. Figure 6.5 shows the auto-correlation function of NH10 and NH20 codes. As shown in Figure 6.5, the PSLR performance is around 14 dB for both the NH10 and NH20 codes. The presence of primary I5 and Q5 codes does provide maximal correlation suppression prior to NH code correlation. However, during acquisition, the presence of residual frequency errors will substantially degrade the NH code correlation performance. For instance, Macabiau et al. [2003] reported that the correlation suppression performance of NH20 code can be as low as 6.6 dB for worst case Doppler scenarios.
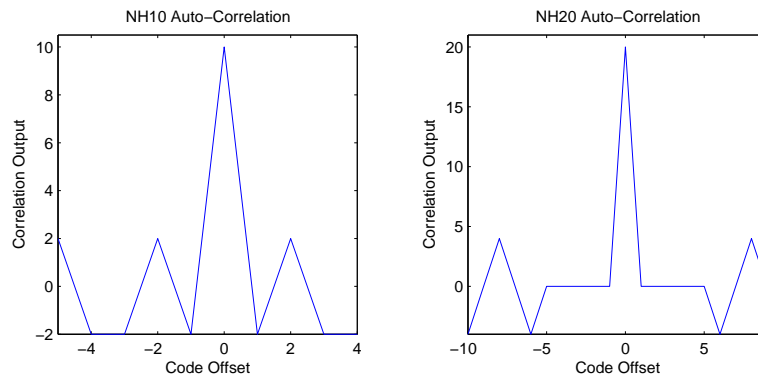
Figure 6.5: NH Code Correlation Properties

The magnitude spectrum of the L5 signal is readily obtained by applying Fourier

transform on the auto-correlation function of I5 and Q5 signal. While the individual codes are periodic over 1 ms, the presence of NH10 and NH20 codes further extends their code periodicity to 10 ms for I5 and 20 ms for the Q5 signal. Accordingly, the spectrum comprises of spectral lines that are spaced apart by 100 Hz for I5 signal and 50 Hz apart for Q5 signal. The finely spaced spectral lines are vital for the L5 signal's robustness to narrowband interference. Figure 6.6 shows the spectrum of the GPS L5 and that of legacy L1 signals.
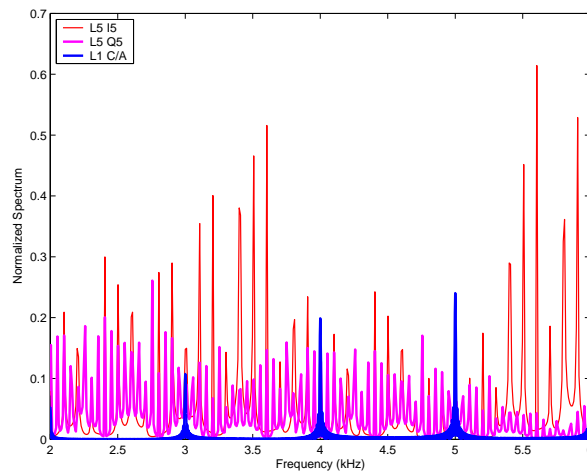
Figure 6.6: Spectrum of GPS L1 C/A and GPS L5 Signals

6.2   Modernized GPS Signal Acquisition

Acquisition of legacy GPS L1 C/A code signal is straightforward due to the simplicity of its signal structure. On the other hand, the acquisition process for the modernized signals is complicated due to the advanced signal design. For instance, the time-multiplexed data/pilot structure in L2C signal and the presence of NH code in L5 signal necessitates modified acquisition strategies. More specifically, the modernized GPS signal acquisition is usually carried out in two stages to deal with the complex nature of signal structure. The following sections briefly reviews the various detector/estimator structures reported in the literature for the problem of GPS L2C and L5

signal acquisition.

6.2.1   L2C Signal Acquisition

The acquisition of time multiplexed L2C code can be accomplished in two modes. The first mode involves the two-stage acquisition, wherein the CM code is first acquired and tracked. Since the CM code and CL code phases are related, the CL code phase search is limited to only 75 different code phases (where 75 is the number of CM code periods in one CL code period). Tran and Hegarty [2003] reviewed various local CM code generation and correlation methods for CM code acquisition. In CM code acquisition, the longer code correlation over 20 ms imposes stringent frequency estimation and thereby increases the computational complexity. For example, an increase in coherent integration from 1 ms to 20 ms correspondingly increases the frequency search bins from 30 to 600 (with a frequency bin size of $2/(3T_{COH})$). More importantly, the presence of unknown navigation data can potentially reduce the correlation power, when detected over its full period. Accordingly, Yang [2005] reported the utilization of zero padded double buffer correlation to overcome the effect of navigation data bit transitions. The performance gain is achieved at the expense of increased computational complexity due to the usage of a double buffer.

Psiaki [2004] further extended the block processing FFT algorithms reported earlier for GPS L1 C/A acquisition (Psiaki [2001]) to the problem of CM and CL code acquisition. Notably, Psiaki [2004] described means to acquire CM and CL codes through segmented FFT correlation techniques and the use of frequency-shifting for reducing complexity during the frequency search in FFT based correlation. Direct acquisition of the CL code is not practical even though possible, unless the receiver has a good initial time and frequency estimate. However, it can still be appealing for certain applications that mandate the acquisition of weak GPS signals (Psiaki [2004]). Yang [2005]

extended the segmented FFT based correlation approach and the absence of navigation data modulation in pilot channel for the direct CL code acquisition.

In contrast, Cho et al. [2004] presented a CM code acquisition technique that essentially utilized the post-correlation differential detector of Section 3.4.3 in Chapter 3. The method initially performs a short coherent integration in comparison to the CM code period (i.e. $T_{COH} = 0.2T_{cm}N_{cm}$), which is then followed by differential detection and noncoherent accumulations. In other words, CM code detection is performed through partial correlation, wherein the ensuing outputs are combined in a noncoherent or differential fashion. Hence, the stringent restriction on frequency estimation is relived due to the shorter coherent integration. Furthermore, it also alleviates the effect of unknown data transition. However, the shorter coherent detection critically influences the detection performance aside from correlation performance degradation.

Other techniques for direct CL code acquisition include the one reported by Moghaddam et al. [2006]. The CL acquisition scheme introduced by Moghaddam et al. [2006] can be viewed as an extension of the approach proposed by Yang et al. [1999] for P(Y) code acquisition. The acquisition scheme forms hyper codes (or subsequences) by adding shifted versions of the CL code segments (i.e. 20 ms), which are then correlated with the received samples. These unique time shifts readily yield the correct code offset and also the segment. The individual shifts should be selected judiciously to prevent any ambiguities that can arise from these time shifts and the actual code delay. Lim et al. [2006] utilized the correlation of errors between GPS L1 and L2C signal for a specific satellite and the receiver to perform L1 assisted L2C acquisition. This is made possible as the L1 C/A code and L2 CM code are phase aligned. Thus, one can perform CM code acquisition by searching only 10 code phases. However, this scheme requires the proper acquisition and possibly tracking of L1 C/A signal from the same satellite.

6.2.2   L5 Signal Acquisition

In contrast to L2C acquisition, L5 acquisition involves the acquisition of NH code in addition to the PRN code phase and residual carrier frequency offset. The L5 signal acquisition can also be performed in two different modes. The first method is a two-stage acquisition process involving the initial acquisition of I5/Q5 codes followed by NH code acquisition. The I5/Q5 codes are initially acquired through short coherent integration over one code period, which is often followed by a number of noncoherent accumulations. However, the coherent integration period is limited within 1 ms due to the presence of secondary NH code. The magnitude outputs of I5 and Q5 correlators can be further added resulting in an additional gain of around 2 dB (Tran and Hegarty [2003]). Even the coherent integration of one code period is vulnerable to NH code transitions, which can be alleviated through the double buffer FFT based correlation as reported in Yang [2005].

The NH code acquisition typically follows the initial coarse acquisition of I5/Q5 codes. After successful detection of I5/Q5 codes and estimation of their code start phases, the I5 and Q5 codes are stripped from the received samples. The output of the I5/Q5 correlator is dumped every code period to output the NH10 and NH20 samples. The presence of residual frequency errors from the initial coarse acquisition is compensated for prior to NH code acquisition in terms of fine frequency search. The NH code acquisition primarily relies on the detection of NH20 in the pilot channel. While the NH10 code can also be utilized, the presence of unknown navigation data critically effects its detection output. Zheng and Lachapelle [2004] described a rudimentary technique to remove residual carrier, NH code and that of navigation data, which is very similar to the pre-correlation differential scheme described in Section 3.4.4 of Chapter 3. As expected, the detection performance of the scheme degraded substantially for decreasing C/N_0 levels.

Under low C/N_0 conditions, the absence of navigation data in the quadrature channel and the fact that NH20 is completely deterministic allows for longer coherent integrations. Hegarty et al. [2003] described the direct acquisition of I5 and NH20 code through 20 ms coherent integration. However, the NH20 code detection can be severely degraded in the presence of Doppler uncertainty (Ries et al. [2002]). Macabiau et al. [2003] reported a better 20-bit code, but limited their investigation by introducing the code proposed by Mertens [1996]. While the search of short periodic code can be carried out exhaustively with contemporary computer hardware resources, a systematic analysis on the design of optimal short synchronization code could be much more beneficial.

6.3   Modernized GPS Signal Acquisition – Innovative Enhancements

The adoption of advanced signal structure offers tremendous opportunities even as the acquisition process has become more complicated. For instance, Psiaki [2004] and Yang [2005] emphasized this issue in the perspective of FFT based correlation for the GPS L2C code acquisition. FFT based techniques for long code acquisition is especially cumbersome as it requires longer storage buffer and the processor can potentially be overloaded during the data read in/read out process. Hence, segmented correlation techniques have been put forth for the problem of long CL and even CM code acquisition. The major limitations remaining is the fine frequency search requirements and the navigation data effects on CM code acquisition. The problem of frequency search and that of navigation data modulation effects can be eliminated, if one adopts the pre-correlation differential scheme as described in Section 3.4.4. The choice of differential delay is now selected as an even integer multiple of basic chip duration as the CM code is time multiplexed with CL code. Once again, the detection process is expected to degrade significantly at lower C/N_0 levels due to the substantial SNR loss incurred through the differential detection process. On the other hand, we can readily adopt

the multi-correlation differential detection to suppress the SNR loss with the additional advantage of fine frequency offset estimation. Unfortunately, the presence of long code structure can limit the use of pre-filtering because of longer tap delays. Therefore, the maximum advantage can be achieved only by means of coherent detection of CM and CL code. In this view point, the generalized post-correlation differential detection is more appealing for the problem of L2C CM and CL code acquisition. Furthermore, the generalized post-correlation differential detection is asymptotically optimal for CL code acquisition due to the absence of navigation data. Hence, in this chapter, we derive the decision statistics for the generalized post-correlation differential detector for CM and CL code detection.

The two major options for L5 acquisition is the two-stage acquisition using a post-correlation noncoherent detector and the direct acquisition of Q5 and NH20 code through longer coherent detection. The acquisition scheme reported by Zheng and Lachapelle [2004] can be readily extended in terms of multi-correlation differential detection, which not only allows for noise suppression but also aids in fine frequency estimation. Unfortunately, the presence of NH code limits the number of correlation branches and thus the noise suppression performance. On the other hand, maximal benefit can be accomplished by applying the multi-correlation differential detector for NH code acquisition. The multi-correlation differential detector based NH code detection can be applied in both two-stage and direct acquisition scenarios. Hence, in this chapter, the extension of the original multi-correlation differential for the problem of NH code acquisition will be developed. More importantly, the proposed NH code acquisition compensates for the residual carrier, which proved to be a significant problem in traditional NH code acquisition (Macabiau et al. [2003]). On a different note, the chapter investigates the critical performance measures for the design of short synchronization code for use in future GNSS systems. The analysis can reveal potential codes

or code designs that can minimize the vulnerability to residual frequency errors and thereby improves the NH code acquisition performance.

6.4 GPCDD Based L2C Signal Acquisition

6.4.1 Derivation of Decision Statistics

The use of generalized post-correlation differential detection in terms of noise suppression and fine frequency estimation was established in Section 3.5 of Chapter 3 for legacy GPS signal acquisition. The proposed detector is further extended here for the problem of CM and CL code acquisition. As shown in Figure 3.14, the matched filter output forms the input to the developed detector. Hence, it is desirable to derive the coherent matched filter output for the CM and CL code detection. Therefore, we can express the received complex pseudo baseband L2C signal in the presence of AWGN as,

$$x(k) = \sqrt{\frac{C}{2}} c(k - \tau) e^{j(2\pi \Delta F k + \phi_0)} + w(k) \tag{6.4}$$

where ΔF and ϕ_0 are the received residual frequency and phase offset respectively. $c(k)$ is the composite signal comprising of time-multiplexed CM and CL codes and is given by,

$$c(k) = d(k) cm(k) p_{cm}(k) + cl(k) p_{cl}(k) \tag{6.5}$$

where $p_{cm}(k)$ and $p_{cl}(k)$ are the pulse shaping function and is usually assumed to be a normalized rectangular function. The waveforms $p_{cm}(k)$ and $p_{cl}(k)$ are given by,

$$p_{cm}\left(k - \frac{t}{T_c}\right) = \begin{cases} 1 & 0 \leq t < T_c \\ 0 & T_c \leq t < 2T_c \end{cases} \tag{6.6}$$

$$p_{cl}\left(k - \frac{t}{T_c}\right) = \begin{cases} 0 & 0 \leq t < T_c \\ 1 & T_c \leq t < 2T_c \end{cases} \tag{6.7}$$

The waveform $p_{cl}(k)$ is simply the time-shifted version of $p_{cm}(k)$. Recall that $T_{cl} = T_{cm} = 2T_c$, as the CM code is generated at 511.5 kHz. Thus the multiplication of $cm(k)$ and $cl(k)$ with the waveforms $p_{cm}(k)$ and $p_{cl}(k)$ and their subsequent addition can be viewed as the time-multiplexing of the CM and CL codes. During acquisition, the receiver searches over the two-dimensional space in residual frequency offset $(\Delta \hat{F})$ and code phase $(\hat{\tau})$ to detect/estimate the received CM and/or CL code. Accordingly, the coherent matched filter output (over 20 ms to account for zero-padding in CM code) for a given $\hat{\theta} = [\Delta \hat{F}, \hat{\tau}]$ can be given by,

$$y(n) = \frac{1}{2N_{cm}} \sum_{k=2nN_{cm}}^{2(n+1)N_{cm}-1} x(k)\tilde{c}(k - \hat{\tau})e^{j2\pi\Delta\hat{F}k}, n = 0, 1, 2, \ldots, N - 1. \qquad (6.8)$$

where N is the number of extended accumulations and is related to the total observation period T as $N = TT_{COH}^{-1}$ ($T_{COH} = N_{cm}T_{cm}$). $\tilde{c}(k)$ is generated according to the specific mode of acquisition. The factor 2 essentially reflects the increase in CM code correlation as a consequence of the zero padding operation. As mentioned earlier, the L2C acquisition can be operated in two modes utilizing either CM or CL code signal. Accordingly, the locally generated code, $\tilde{c}(k)$, is given by,

$$\tilde{c}(k) = \begin{cases} cm(k)p_{cm}(k) & CM\ Acquisition \\ cl(k)p_{cl}(k) & CL\ Acquisition \end{cases} \qquad (6.9)$$

The matched filter output $y(n)$ can be expressed in terms of signal and noise components as, $y(n) = s(n) + w(n)$. The signal term $s(n)$ is given by,

$$s(n) = \begin{cases} \sqrt{\frac{C}{2}}d(n)R^{cm}(\tau_{err})\psi_{\Delta F_{err}}(n) \\ \sqrt{\frac{C}{2}}R_n^{cl}(\tau_{err})\psi_{\Delta F_{err}}(n) \end{cases} \qquad (6.10)$$

where $d(n)$ is the navigation data component at the output of the coherent matched filter. The CM code correlation output $R^{cm}(\tau_{err})$ is periodic over $2N_{cm}T_c$ and does not include the sample index n. On the other hand, the sample index n is included in the CL code correlation output, $R_n^{cm}(\tau_{err})$, as it varies (for $\tau_{err} \neq 0$) for every $2nN_{cm}T_c$, but

is periodic over $2N_{cl}T_c$ (i.e. $R_n^{cm}(\tau_{err}) = R_{n+N_{cl}/N_{cm}}^{cm}(\tau_{err})$). $\psi_{\Delta F_{err}}(n)$ is the frequency ambiguity function and is given by,

$$\psi_{\Delta F_{err}}(n) = sinc(2\pi\Delta F_{err}N_{cm}T_c)e^{j(2\pi\Delta F_{err}\left[2nN_{cm}+\frac{2N_{cm}-1}{2}\right]T_c+\phi_0)} \tag{6.11}$$

The navigation data component $d(n)$ at the output of the coherent matched filter is given by,

$$d(n) = \sum_{k=2nN_{cm}}^{2(n+1)N_{cm}-1} d(k) \tag{6.12}$$

The auto-correlation functions for the CM and CL codes are given by,

$$\begin{aligned} R^{cm}(\tau_{err}) &= \sum_{k=2nN_{cm}}^{2(n+1)N_{cm}} c(k-\tau)cm(k-\hat{\tau})p_{cm}(k), \ \hat{\tau} = 0, 1, 2, \ldots, N_{cm}-1. \\ R_n^{cl}(\tau_{err}) &= \sum_{k=2nN_{cm}}^{2(n+1)N_{cm}} c(k-\tau)cl(k-\hat{\tau})p_{cl}(k), \ \hat{\tau} = 0, 1, 2, \ldots, N_{cl}-1. \end{aligned} \tag{6.13}$$

Finally, the noise component of the coherent matched filter output is given by,

$$w(n) = \begin{cases} \sum_{k=2nN_{cm}}^{2(n+1)N_{cm}-1} w(k)zcm(k)e^{-j(2\pi\Delta\hat{F}k+\phi_0)} & CM\ Acquisition \\ \sum_{k=2nN_{cm}}^{2(n+1)N_{cm}-1} w(k)zcl(k)e^{-j(2\pi\Delta\hat{F}k+\phi_0)} & CL\ Acquisition \end{cases} \tag{6.14}$$

The final detection output utilizing various detectors are given by,

$$\Psi(\hat{\theta}) = \begin{cases} \left|\frac{1}{N}\sum_{n=0}^{N-1} y(n)\right|^2 & CMF \\ \frac{1}{N}\sum_{n=0}^{N-1} |y(n)|^2 & PCND \\ \left|\frac{1}{N}\sum_{n=0}^{N-1} y(n)y^*(n-1)\right|^2 & PCDD \end{cases} \tag{6.15}$$

The absence of navigation data in the pilot channel allows for the utilization of a coherent matched filter for CL code detection. However, it also mandates a finer frequency estimation depending on the coherent observation period. On the other hand, the presence of navigation data in the data channel limits the the use of coherent matched filtering for CM code detection. Moreover, the presence of a navigation data bit transition within a code coherent integration period during CM code detection can critically reduce the signal power at the output of the matched filter. However, one can utilize the DBZP technique reported in Psiaki [2004] and Yang [2005] to overcome the effects of

navigation data bit transition. Finally, the post-correlation differential detector, when applied to CM code detection, incurs a substantial SNR loss due to the combination of longer code period and navigation data transition. However, it can still be applied to CL code detection for marginalizing the effect of residual frequency errors.

Alternatively, short coherent integration followed by either noncoherent or differential accumulations as described in Cho et al. [2004] can also be utilized. The major benefits of this approach is the suppression of navigation data effects in CM code detection and less stringent frequency estimation. However, the approach can be limited under weak signal conditions as the partial correlation provides a modest suppression of noise. For partial correlation approach, the final decision statistics can be given by,

$$\Psi(\hat{\theta}) = \frac{1}{N} \sum_{n=0}^{N-1} y(n), \;\; n = 0, 1, 2, \ldots, N - 1. \tag{6.16}$$

The intermediate detection output $y(n)$ is further given by,

$$y(n) = \begin{cases} \frac{1}{L} \sum_{l=0}^{L-1} |y_s(l)|^2 & PCND \\ \left| \frac{1}{L} \sum_{l=0}^{L-1} y_s(l) y_s^*(l-1) \right|^2 & PCDD \end{cases} \tag{6.17}$$

where $L = N_{cm}/N_c$ is the number of partial correlations performed over a CM code period. The intermediate detection output $y_s(l)$ is further expressed as,

$$y_s(n-l) = \frac{1}{N_c} \sum_{k=lN_c}^{(l+1)N_c-1} x(k - 2nN_{cm})\tilde{c}(k - 2nN_{cm} - \hat{\tau})e^{-j2\pi\Delta\hat{F}k}, \;\; n = 0, 1, 2, \ldots, N - 1. \tag{6.18}$$

where $y_s(l)$ is the partial correlation output and N_c is the number of samples pertaining to this partial correlation period. The factor 2 is included to account for the zero-padding. Cho et al. [2004] utilized a partial correlation of 2 ms, which readily yields a N_C of 2046 for a chip sampled signal. The noncoherent and differential detection, when applied to the partial correlation output of (6.18) readily suppresses both the residual carrier as well as the navigation data. On the down side, the noise at the output of

partial correlation can be substantial due to the shorter coherent integration and thus ensue in significant SNR loss.

In summary, one can readily observe the trade-off between noise suppression and the influence of residual signals such as navigation data and residual carrier. The acquisition schemes reported in Psiaki [2004] and Yang [2005] allows for better noise suppression but requires finer frequency estimation. On the other side, the acquisition scheme introduced by Cho et al. [2004] alleviates the need for finer frequency estimation but is limited by SNR loss due to noise enhancement stemming from the noncoherent/differential operation. The generalized post-correlation differential detector developed in Section 3.5 of Chapter 3 readily offers a compromise between the schemes proposed by Psiaki [2004] and Cho et al. [2004]. More importantly, the proposed detector asymptotically achieves a similar performance to that of a coherent matched filter for CL code detection due to the absence of navigation data (refer Section 3.6.6 in Chapter 3).

The derivation of the final decision statistics for the generalized post-correlation differential detector is derived in Section 3.5 and will be utilized here for the problem of CM and CL code detection. Following the analysis in Section 3.5 of Chapter 3, we derive the intermediate detection output $y(n)$ as,

$$y(n) = \frac{1}{M} \sum_{m=1}^{M} \frac{1}{L} \sum_{l=0}^{L-1} y_s(n-l)y_s^*(n-l-m), \ n = 0, 1, 2, \ldots, N-1. \tag{6.19}$$

where M is the number of branches, which is upper bounded by $M \leq N_{cm}T_{cm}T_{COH}^{-1}$. The individual differential delays are selected as an integer multiple of the basic coherent integration period (i.e $T_m = mT_{COH}$). The input to the detector is the partial correlation output as summarized in (6.18). The output final decision statistics is obtained by substituting $y_s(l)$ from (6.19) in (6.16) and is given by,

$$\Psi_{cm}(\hat{\theta}) = \left| \frac{1}{NML} \sum_{n=0}^{N-1} \sum_{m=1}^{M} \sum_{l=0}^{L-1} y_s(n-l)y_s^*(n-l-m) \right|^2 \tag{6.20}$$

Similarly, we can derive the final decision statistic of the generalized post-correlation

differential detection for CL code acquisition as,

$$\Psi_{cl}(\hat{\theta}) = \left| \frac{1}{MN} \sum_{m=1}^{M} \sum_{n=0}^{N-1} y(n)y^*(n-m) \right|^2 \quad (6.21)$$

where $y(n)$ is the partial correlation output as expressed in (6.8) and expressed as, $y(n) = s(n) + w(n)$, where $s(n)$ is the signal component and is given by,

$$s(n) = 2CR_n^{cl}(\tau_{err})sinc(2\pi\Delta F_{err}N_{cm}T_c)e^{j(2\pi\Delta F_{err}\left[2nN_{cm}+\frac{2N_{cm}-1}{2}\right]T_c+\phi_0)} \quad (6.22)$$

where N_{cm} is the number of samples pertaining to the partial correlation period and is often assumed as the CM code period.

6.4.2 Residual Signal Effects

The influence of residual signals such as navigation data and residual carrier on the generalized post-correlation differential detector was analyzed in Sections 3.5.1 and 3.5.2 of Chapter 3 in the context of legacy GPS signal acquisition. The same analysis is further extended here in the context of CM and CL code detection.

For CM code detection, the residual carrier as well as the navigation data influence the developed generalized post-correlation differential detector. To further investigate, let us write the detection output in the absence of noise as,

$$\Psi_{cm}(\hat{\theta}) = \left| \sum_{n=0}^{N-1} \sum_{m=1}^{M} \sum_{l=0}^{L-1} 2Cd_m(l)R_{m,l}^{cm}(\tau_{err})sinc^2(\pi\Delta F_{err}T_{COH})e^{j2\pi\Delta F_{err}m} \right|^2 \quad (6.23)$$

where $d_m = d(l)d(l-m)$ is the product of the navigation data output with its delayed versions. ΔF_{err} and τ_{err} are the residual frequency and code phase errors at the output of the initial coherent matched filtering as summarized in (6.18). Note that the auto-correlation is a function of both m and l and not n as it is periodic over n. The loss due to navigation data modulation is derived earlier in Section 3.5.1 of Chapter 3 and is summarized in (3.92). On the other hand, the effect of residual frequency error can be alleviated using a FFT based coherent combining technique (refer to Section 3.5.2

in Chapter 3). For the CL code detection, the detection output is only influenced by the residual carrier due to the absence of navigation data. Hence, the corresponding detection output can be given by,

$$\Psi_{cl}(\hat{\theta}) = \left| \sum_{m=1}^{M} \sum_{n=0}^{N-1} 2C R_{m,n}^{cl}(\tau_{err}) sinc^2(\pi \Delta F_{err} T_{COH}) e^{j2\pi \Delta F_{err} m} \right|^2 \qquad (6.24)$$

The auto-correlation function includes m, n, and l due to its dependence on these variables. Once again, we can adopt a FFT based coherent combining technique to alleviate the effect of residual frequency errors on the developed generalized post-correlation differential detector.

6.4.3 Correlation Performance

A major limitation with short coherent integration is the degradation in correlation suppression performance. For instance, the CL code exhibits a nominal peak-to-sidelobe ratio (PSLR) performance of around 45 dB, when coherently correlated over its code period of 1.5 s.However, its PSLR performance can degrade with partial correlation (i.e. $T_{COH} \ll 1.5$ s) depending on the type of detector being utilized. The PSLR performance can be defined as,

$$PSLR = 10 \log_{10} \frac{|R(\tau = 0)|^2}{max \, |R(\tau \neq 0)|^2} \qquad (6.25)$$

For instance, noncoherent detection results in correlation performance degradation in comparison to coherent detection as the out-of-phase correlation values are noncoherently combined. Similarly, the use of differential detection can also degrade the correlation suppression performance. The choice of coherent integration period plays a vital role in terms of correlation suppression performance especially for the longer CL code. To further investigate this phenomenon, the PSLR performance as a function of coherent correlation period for CM and CL code was determined and is plotted in Figure 6.7. The PSLR performance shown in these plots was averaged across all the PRN's.
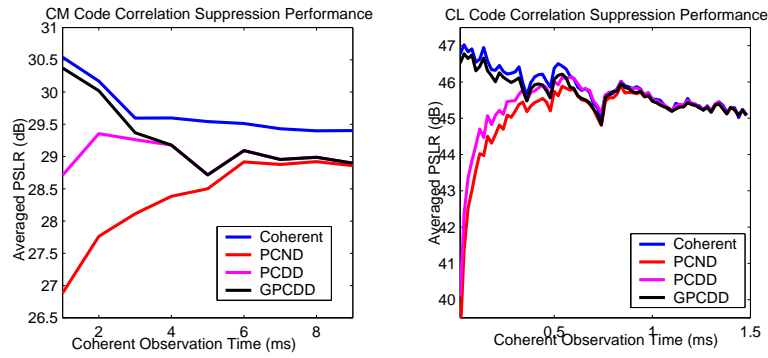
Figure 6.7: PSLR Performance of CM and CL Code as a Function of Coherent Observation Period

The average PLSR performance of all detector/estimators is expected to converge to a similar value when a received code is correlated over its period, which is around 10 ms (or 20 ms with zero padding) for the CM code. For partial correlations, the final PSLR performance is determined after coherent, noncoherent, and differential accumulations of partial correlations. As expected, the coherent accumulations of partial correlations resulted in the best PSLR performance.

The generalized post-correlation differential detection closely followed the performance obtained with coherent accumulations in the case of CL code correlation but incurred some degradation for CM code correlation. Although not shown in Figure 6.7, the CM code PSLR performance converged to 28.5 dB for all the detectors due to the code periodicity. The post-correlation differential detector showed considerable degradation for lower coherent integration periods especially for the CL code correlation. The post-correlation noncoherent detector demonstrated even larger degradation as the out-of-phase correlations are no longer zero-mean as a consequence of envelope detection. However, the correlation suppression performance of post-correlation noncoherent/differential recovered with a corresponding increase in coherent integration period.

6.5   MCDD based Enhanced GPS L5 NH Code Acquisition

In Section 4.1.4 of Chapter 4, the multi-correlation differential detection was introduced in the context of legacy C/A code acquisition. More importantly, it was shown to be asymptotically optimal by letting the number of branches M be similar to the number of samples in he coherent integration (i.e. $T_{COH}T_c^{-1}$). For example, in the case of NH20 code acquisition, the MCDD scheme with $M = 20$ branches is equivalent to a coherent integration of NH20 over one code period (i.e. $T_{COH} = 20$ ms). The following subsections deal with the derivation of the decision statistics of the MCDD based GPS L5 NH code acquisition. Figure 6.8 illustrates the simplified block diagram of the multi-correlation differential detector based NH code acquisition. As shown in the figure, the multi-correlation differential detector is applied to the output of the initial coherent matched filtering. The residual carrier and the PRN I5/Q5 codes are initially stripped and the corresponding accumulation output is sampled over its code period to produce the NH samples. The ensuing NH samples (sampled at kilo-hertz rate) are then fed to the multi-correlation differential detector and further processed to obtain the final decision statistics. The multi-correlation differential detector structure utilized in NH code acquisition is similar to the structure illustrated in Figure 4.6 of Chapter 4.
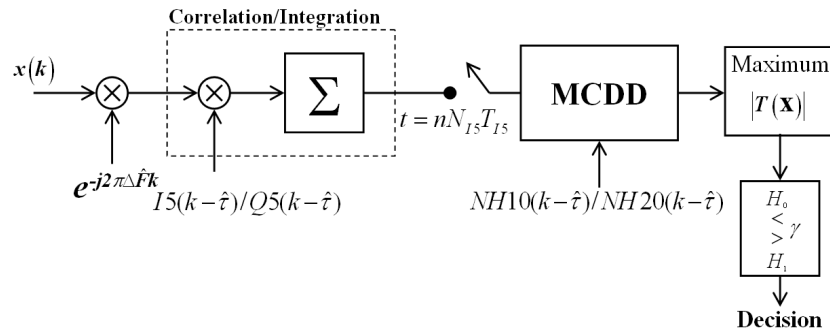
Figure 6.8: MCDD based GPS L5 NH Code Acquisition

In order to derive the final decision statistics, we begin by expressing the down-

converted, sampled GPS L5 samples by,

$$y(k) = \sqrt{2C}\Big[d(k)NH10(k)I5(k)cos(\phi(k)) + NH20(k)Q5(k)sin(\phi(k))\Big] + w(k) \quad (6.26)$$

where C is the carrier power of the transmitted signal that is assumed to be time invariant during acquisition. The inphase and quadrature primary PRN codes are denoted by $I5(k)$ and $Q5(k)$. $NH10(k)$ and $NH20(k)$ represents the secondary NH codes in the inphase and quadrature channels. The time varying phase $\phi(k)$ models the residual carrier and is given by $\phi(k) = 2\pi\Delta Fk + \phi_0$, where ϕ_0 is residual phase offset that embodies both received phase offset and that of the local oscillator. The 100 Hz navigation data symbols is denoted by $d(k)$.

Coarse Acquisition

As discussed earlier, the GPS L5 signal acquisition involves the detection of I5/Q5 PRN codes, NH10/NH20 codes and the estimation of their code phases in addition to the residual frequency offset. The phase of the individual PRN codes and the NH codes are coherently related, which can readily ease the detection process. Combined estimation of PRN and NH code phases is possible through the pilot (quadrature channel) but incurs significant computational complexity. Although it is recognized that such a detection is inevitable at very low C/N$_0$ levels. Traditional approaches rely on initial coarse acquisition of PRN code phase and approximate frequency offset, which is then followed by fine acquisition of NH code phases and residual frequency offset. We can readily express the sampled output (i.e. $T_r = nN_{I5}T_{I5} = nN_{Q5}T_{Q5}$) of initial coherent matched filtering by,

$$\begin{aligned}
y_D(n) &= \frac{1}{N_{I5}}\sum_{k=nN_{I5}}^{(n+1)N_{I5}-1} x(k)I5(k-\hat{\tau})e^{-j(2\pi\Delta\hat{F}k+\phi_0)} \\
y_P(n) &= j\frac{1}{N_{Q5}}\sum_{k=nN_{Q5}}^{(n+1)N_{Q5}-1} x(k)Q5(k-\hat{\tau})e^{-j(2\pi\Delta\hat{F}k+\phi_0)}
\end{aligned} \qquad (6.27)$$

where $y_D(n)$ and $y_P(n)$ are the correlation/integration outputs of the data and pilot channels respectively. The above correlation outputs can be critically effected from the

NH code transitions but can be alleviated using the DBZP correlation techniques (Yang [2005]; Psiaki [2001]).

$$y_D(n) = \sqrt{\tfrac{C}{2}}d(n)R_{I5}(\tau_{err})NH10(n)\psi_{\Delta F_{err}}(n) + w_D(n)$$
$$y_P(n) = j\sqrt{\tfrac{C}{2}}R_{Q5}(\tau_{err})NH20(n)\psi_{\Delta F_{err}}(n) + w_P(n)$$

(6.28)

The correlation function or the time ambiguity function $R_{I5}(\tau_{err})$ and $R_{I5}(\tau_{err})$ is given by,

$$R_{I5}(\tau_{err}) = \sum_{k=0}^{N_{I5}-1} I5(k-\tau)I5(k-\hat{\tau})$$
$$R_{Q5}(\tau_{err}) = \sum_{k=0}^{N_{Q5}-1} Q5(k-\tau)Q5(k-\hat{\tau})$$

(6.29)

The $R_{I5}(\tau_{err})$ and $R_{I5}(\tau_{err})$ is further related as,

$$R_{I5}(\tau_{err}) \approx R_{Q5}(\tau_{err}) \quad \tau_{err} = 0$$
$$R_{I5}(\tau_{err}) \neq R_{Q5}(\tau_{err}) \quad \tau_{err} \neq 0$$

(6.30)

The above equality is only an approximation in the presence of AWGN. Thus, the noncoherent combining of I5 and Q5 correlation/detection outputs further improves the correlation suppression. The navigation data output in the data channel is given by,

$$d(n) = \sum_{k=nN_{I5}}^{(n+1)N_{I5}} d(k)$$

(6.31)

The frequency ambiguity function is given by,

$$\psi_{\Delta F_{err}}(n) \approx sinc(\pi \Delta F_{err} T_P)e^{j\phi_{err}(n)}$$
$$\phi_{err}(n) = e^{j(2\pi \Delta F_{err}\left[nN_{I5}+\frac{N_{I5}-1}{2}\right]T_{I5}+\phi_0)}$$

(6.32)

Finally, the noise terms at the output of correlation/integration, $w_D(n)$ and $w_P(n)$ is given by,

$$w_D(n) = \tfrac{1}{N_{I5}} \sum_{k=nN_{I5}}^{(n+1)N_{I5}-1} w(k)I5(k-\hat{\tau})e^{-j(2\pi\Delta\hat{F}k+\phi_0)}$$
$$w_P(n) = \tfrac{1}{N_{Q5}} \sum_{k=nN_{Q5}}^{(n+1)N_{Q5}-1} w(k)Q5(k-\hat{\tau})e^{-j(2\pi\Delta\hat{F}k+\phi_0)}$$

(6.33)

Figure 6.9 shows the post-correlation noncoherent detector based I5/Q5 combined code acquisition. The envelope of the coherently detected outputs $y_D(n)$ and $y_P(n)$ is added

initially (which results in an additional gain of 2 dB) and later accumulated over several code periods. That is,

$$\Psi(\hat{\theta}) = \sum_{n=0}^{N-1} |y_D(n)|^2 + |y_P(n)|^2 \tag{6.34}$$
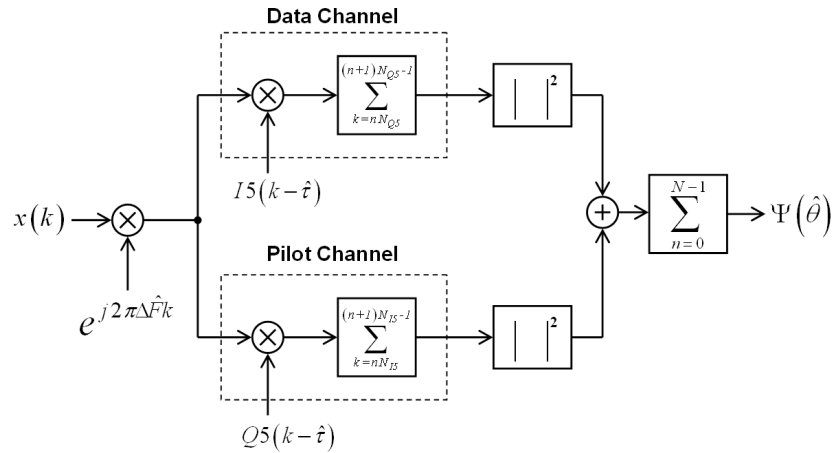
Figure 6.9: GPS L5 Code Acquisition using Combined I5/Q5 PCND

Fine Acquisition

Once the PRN I5/Q5 code is detected, the receiver typically strips off the PRN I5/Q5 code using the estimate of code phase and residual frequency offset, which is coherently accumulated over its code period to output the NH samples. Subsequently, the NH samples are processed via a multi-correlation differential detector to obtain the final decision statistics.

Derivation of Decision Statistics

In Section 4.1.4 of Chapter 4, we derived the asymptotically optimal estimator-correlator structure in the form of multi-correlation differential detector. Following the analysis in Section 4.1.4 of Chapter 4, we can derive the final decision statistics for NH code detection as,

$$\Psi(\hat{\theta}) = |Z_{MCDD}|^2 \tag{6.35}$$

where,

$$
Z_{MCDD} = \begin{cases} \sum_{m=1}^{M} \sum_{n=0}^{N-1} \left(y_P(n) y_P^*(n-m) \right) \left(NH20(n) NH20(n-m) \right) & NH20 \\ \sum_{m=1}^{M} \sum_{n=0}^{N-1} \left(y_D(n) y_D^*(n-m) \right) \left(NH20(n) NH20(n-m) \right) & NH10 \end{cases}
$$

$$(6.36)$$

Residual Signal Effects

The influence of residual signal such as the navigation data and residual carrier can be analyzed by expanding (6.35) in the absence of noise. That is,

$$
\Psi(\hat{\theta}) = \begin{cases} \left| \frac{C}{2} R_{I5}^2(\tau_{err}) \sum_{m=1}^{M-1} \sum_{n=0}^{N-1} RNH20_m(n) e^{j2\pi \Delta F_{err} m} \right|^2 & NH20 \\ \left| \frac{C}{2} R_{I5}^2(\tau_{err}) \sum_{m=1}^{M-1} \sum_{n=0}^{N-1} d_m(n) RNH10_m(n) e^{j2\pi \Delta F_{err} m} \right|^2 & NH10 \end{cases}
$$

$$(6.37)$$

The effect of data modulation on the MCDD output can be obtained following the analysis performed in Section 4.1.5 of Chapter 4. For the NH10 code acquisition, the number of branches is typically limited to half the NH10 code period (i.e. $M \leq N_{10}/2$). On the other hand, for NH20 code acquisition, the number of branches can take an arbitrary value owing to the absence of navigation data. As detailed in Section 4.1.5, the complex phase rotations across the individual branches readily embodies the uncompensated residual carrier during the coarse acquisition. An FFT based coherent combining can be utilized to accomplish NH code phase and fine frequency offset estimation. Alternatively, frequency independent NH code phase estimation can also be achieved by using noncoherent/differential combining of the individual branches at the expense of reduced acquisition sensitivity. The major advantage of utilizing MCDD based NH code acquisition arises from its implicit frequency offset compensation via FFT based combining. Thus, the correlation suppression performance of NH20 is maintained as a consequence of fine frequency compensation. Besides, MCDD also permits the usage of NH10 code during acquisition as the navigation data effect is nearly eliminated.

6.6 Acquisition Performance Enhancements via Short Synchronization Codes Design

6.6.1 NH Synchronization Codes – Limitations

A limitation arising due to the usage of short NH codes is the degradation in correlation suppression especially in the presence of frequency errors. The correlation performance of NH20 code is of utmost importance as it is the primary code for NH code synchronization. Macabiau et al. [2003] correctly identified this problem for NH code acquisition in the presence of Doppler uncertainty. To further illustrate, the NH20 correlation output, in the presence of 25 Hz Doppler error, is plotted in Figure 6.10 (LHS). Moreover, the NH20 correlation outputs for all the Doppler bins within $\pm$ 250 Hz (the bin size being 25 Hz) is also plotted in RHS of Figure 6.10. The residual frequency error in this case was around 12 Hz. From these plots, we can readily observe the substantial correlation performance degradation from the nominal 14 dB to 6.6 dB or even 4.8 dB under specific conditions.
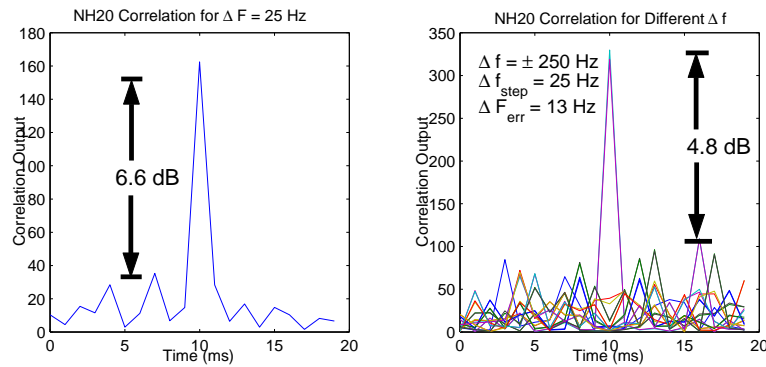
Figure 6.10: NH20 Acquisition Performance in the Presence of Residual Frequency Errors

Macabiau et al. [2003] also reported the existence of better 20-bit synchronization codes in comparison to standardized NH20 codes. More importantly, Lempel et al.

[1977] theoretically showed the correlation of *balanced* binary code as,

$$R(i) = \begin{cases} 2 \text{ or } -2 & \text{if } \frac{1}{2}(2^m - 1) \text{ is odd} \\ 0 \text{ or } -4 & \text{if } \frac{1}{2}(2^m - 1) \text{ is even, } i = 0, 1, 2, \ldots, N_c - 1. \end{cases} \tag{6.38}$$

where $R(i)$ is the cyclic auto-correlation of the binary code $c(k)$ whose length is given by $N_c = 2^m - 1, m = 2, 3, \ldots$. Analyzing the periodic correlation of NH codes using the above equation, we can readily observe the optimality of NH10 code but the sub optimality of NH20 code. On the other hand, both the NH10 and NH20 codes are not balanced (i.e. sum of individual code phases is not equal to zero) and thus (6.38) cannot be applied in a strict sense, but indicates the conditions for optimality. Later, it will be shown during the analysis that (6.38) holds true even for unbalanced codes such as the NH10 and NH20.

Macabiau et al. [2003] reported the existence of better synchronization codes limited their investigation by reporting an alternative 20-bit synchronization code that was originally proposed by Mertens [1996]. Given the critical significance of short synchronization codes in the current GPS L5 and more importantly in future GNSS systems, it would be highly desirable to conduct critical research into short synchronization code design. From this view point, the current research demonstrates the advantage of short synchronization code optimization in terms of acquisition performance. More specifically, the existence of better 10-bit and 20-bit synchronization codes over standardized NH codes are introduced. Furthermore, the relationship between systematic codes such as the Golay codes and optimal correlation are also identified.

6.6.2 Synchronization Code Optimization – Performance Measures

The code optimization can be performed readily via exhaustive search as the synchronization codes are of short code length. Additionally, the search technique utilized FFT based block processing to speed up the search process. More importantly, it would be

highly desirable to define a means to transform the auto-correlation into a measure or measures, which can be utilized to select the better codes. For instance, the desired code is expected to be optimal in terms of the following measures:

- Balance property (i.e. similar number of zeros and ones)

- Maximize peak-to-side lobe ratio

- Maximize Golay merit factor (GMF)

The first two properties are well known and does not require further explanation. However, the third criterion namely the GMF is of critical significance for optimizing auto-correlation of sequences. The GMF is defined as the ratio of main-lobe energy to that of side-lobes (Golay [1961]). That is,

$$GMF = \frac{\left|\sum_{k=0}^{N-1} c^2(k)\right|^2}{2\sum_{i=1}^{N-1} \left|\sum_{k=0}^{N-1} c(k)c(k-i)\right|^2}, k = 0, 1, 2, \ldots, N-1. \tag{6.39}$$

The GMF criterion readily embodies the other two criteria and was utilized in the exhaustive search to determine optimal 10 and 20 bit synchronization sequences.

6.6.3 Performance Analysis

An exhaustive search was carried for the case of 10-bit and 20-bit code sequences. The optimal 10-bit and 20-bit sequences are listed below:

$$
\begin{aligned}
S10 &= [1, -1, -1, -1, 1, 1, 1, 1, -1, 1] \\
S20_1 &= [-1, -1, 1, 1, 1, 1, -1, 1, -1, 1, 1, 1, 1, -1, 1, 1, -1, -1, 1, -1] \\
S20_2 &= [-1, 1, -1, -1, -1, -1, 1, -1, -1, -1, -1, 1, 1, -1, 1, 1, -1, -1, -1, 1] \\
S20_3 &= [1, 1, 1, -1, -1, 1, -1, -1, 1, -1, -1, 1, 1, 1, 1, -1, 1, -1, 1, -1]
\end{aligned}
\tag{6.40}
$$

The exhaustive search resulted in large number of sequences for both 10-bit and 20-bit synchronization codes. The large number of optimal sequence arise from the equivalence

classes. For instance, a sequence $c(k)$, its negated version and its cyclic shifts satisfy the aforementioned properties. Interestingly, the search resulted in multiple solutions for both 10-bit and the 20-bit cases, that were optimal under different conditions. Hence, the codes were further sorted based on their correlation suppression performance in the presence of frequency errors. The performance of the above mentioned sequences in regards to the optimization criteria is tabulated in Table 6.1.

Synchronization Sequence	Balance Property $\sum_{k=0}^{N-1} c(k)$	PSLR (dB)	GMF (dB)
NH10	2	14	1.4
NH20	4	14	2.5
S10	2	14	1.4
$S20_1$	4	14	2.5
$S20_2$	-6	14	3.1
$S20_3$	2	14	3.1

Table 6.1: Short Synchronization Code Properties

While the proposed 10-bit synchronization code, S10, had similar correlation performance to that of standardized NH10 code, it resulted in a better correlation suppression performance in the presence of residual frequency errors. For the 20-bit synchronization code, the search technique resulted in different codes that were optimal based on the performance measure. For instance, the codes, $S20_2$ and $S20_3$, showed a performance improvement in GMF when compared to $S20_1$ and NH20 codes. The performance improvement is readily attributed to the lower side-lobe energy. For example, both the $S20_2$ and $S20_3$ only had 4 non-zero out-of-phase correlations. More importantly, both $S20_2$ and $S20_3$ only had two distinct out-of-phase correlation values as predicted by Lempel et al. [1977] although they are not balanced either. On the other hand, both the $S20_1$, similar to the NH20, had 5 non-zero out-of-phase correlation values. Moreover, the code was also characterized by three distinct out-of-phase correlation values. Hence, the code $S20_2$ and $S20_3$ can be readily considered optimal in terms of GMF. More importantly, the codes $S20_2$ and $S20_3$ can be represented by a Golay complemen-

tary pair (Golay [1961]). A Golay complementary pair is defined as a pair of binary sequence whose auto-correlation function are complementary. Thus, the sum of their periodic correlation function assumes a perfect Dirac-delta function. For instance, the Golay pairs for $S20_2$ and $S20_3$ is given below,

$$
\begin{aligned}
G10^1_{S20_2} &= [-1, -1, -1, 1, -1, -1, 1, 1, -1, -1] \\
G10^2_{S20_2} &= [1, -1, -1, -1, -1, 1, -1, 1, -1, 1] \\
G10^1_{S20_3} &= [1, 1, -1, -1, 1, -1, 1, 1, 1, 1] \\
G10^2_{S20_3} &= [1, -1, 1, -1, -1, 1, 1, -1, -1, -1]
\end{aligned}
\tag{6.41}
$$

For example, the code $S20_2$ can be obtained by bit multiplexing $G10^1_{S20_2}$ and $G10^1_{S20_2}$. Interestingly, the 10-bit codes are all optimal and can very well be used for 10-bit synchronization codes. For example, it is sufficient to store only a 20-bit code, wherein the 10-bit code can be readily generated by decimating the 20-bit code. The aforementioned analysis clearly indicates the strong affinity between optimal binary codes and Golay complementary pairs. More importantly, one can utilize this relationship to generate moderate length binary sequences as Golay pairs can be easily generated in a recursive fashion. As mentioned earlier, the sum of the periodic correlation of $G10^1_{S20_2}$ and $G10^1_{S20_2}$ and that of $G10^1_{S20_3}$ and $tG10^1_{S20_3}$ results in a perfect correlation function (i.e. Dirac-delta function). That is,

$$
R_{S20_m}(i) = \sum_{k=0}^{N-1} S20_m(2k)S20_m(2k-i) + \sum_{k=0}^{N-1} S20_m(2k+1)S20_m(2k+1-i), \ m = 2, 3
\tag{6.42}
$$

where $R_{S20_m}(i) = \delta(i)$ and $\delta(\bullet)$ is the Dirac-delta function[2]. This property can be readily utilized for robust tracking of 20-bit synchronization code signal. During acquisition, there exists an ambiguity, whether the first bit corresponds to $G10^1_{S20_2}$ or $G10^2_{S20_2}$. Interestingly, the NH10 code and the first half of the NH20 code utilized by

---

[2] $\delta(i) = \begin{cases} 1 & i = 0 \\ 0 & elsewhere \end{cases}$

the GP L5 signal are Golay complementary pair. Unfortunately, the summation of the second half of the NH20 code with the NH10 code resulted in inferior auto-correlation. However, the above analysis indicates the significance of judicious code design that allow for innovative receiver and decoding implementations.

The PSLR performance of the standardized and the proposed codes in the presence of residual frequency error is shown in Figure 6.11. The proposed S10 code outperformed the conventional NH10 especially for worst case Doppler's. For example, a gain of around 3 dB can be obtained with the S10 code over NH10 code for a Doppler uncertainty of 25 Hz.
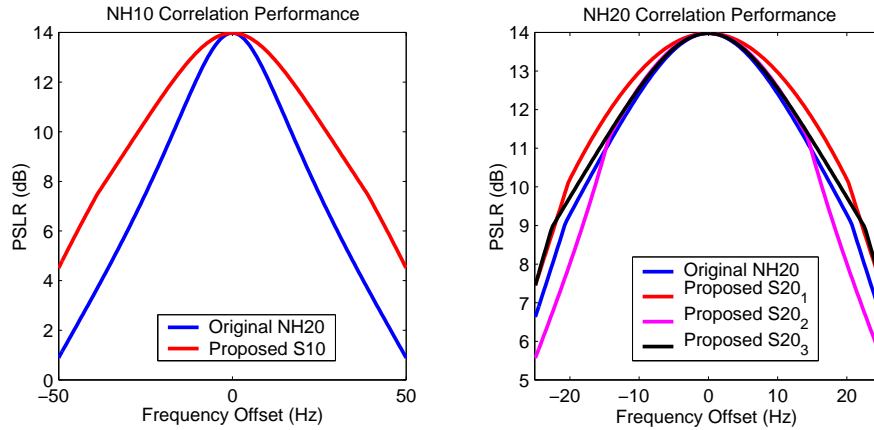
Figure 6.11: PSLR Performance of Standardized and Proposed Synchronization Codes (Left) 10-bit (Right) 20-bit

Among the various 20-bit codes, the worst case degradation in PSLR was observed in $S20_2$. The standardized NH20 code showed an improvement of 1 dB compared to the 5.6 dB PSLR obtained with $S20_2$. On the other hand, $S20_1$ and $S20_3$ showed a further improvement of 0.9 dB over the standardized NH20 code. However, $S20_1$ demonstrated the best PSLR performance among all the codes despite having inferior GMF.

The $S20_2$ code, despite showing inferior PSLR performance and balanced property, can still be desirable for its GMF properties. For example, the $S20_2$ code achieved a similar performance as that of the Merten's 20-bit code reported by Macabiau et al.

[2003]. Following Macabiau et al. [2003], we evaluated the correlation suppression performance over a range of frequency offsets (i.e. $\pm$ 250 Hz with a step size of 25 Hz). The uncompensated Doppler was around 12 Hz. The correlation suppression was measured using modified PSLR performance, which was defined as the ratio of main-lobe to the largest side-lobe across code and frequency offsets. Under these conditions, the standardized NH20 code showed a meagre 4.8 dB correlation isolation. The Merten 20-bit code and the $S20_2$ both demonstrated a correlation isolation of around 6.8 dB. On the other hand, the $S20_1$ and $S20_3$ showed a correlation isolation of about 5.1 and 5.6 dB, respectively.

In summary, the short synchronization code design is essentially a multiple objective optimization and often yield codes optimal for specific performance measures. More importantly, judicious design of short synchronization codes can offer optimal correlation suppression, efficient signal generation and also allow for innovative receiver implementation. The readers are further referred to Shanmugam et al. [2007a] for the the design of short synchronization codes for use in future GNSS signals.

6.7   Acquisition Performance Evaluation

Having shown the optimality of generalized post-correlation differential detection for GPS L2C code acquisition and that of multi-correlation differential detection for the GPS L5 NH code acquisition, we now proceed to empirical tests to validate the developed theory. These tests consist of software-based analysis of IF samples from hardware simulated GPS L2C and L5 signals. The test methodology initially involved the development of prototype GPS L2C and L5 acquisition module and successful validation using the hardware simulated GPS signals. Secondly, the original generalized post-correlation differential detection and multi-correlation differential detection were modified to process the GPS L2C and GPS L5 NH code signals. The basic hardware front-end setup

and the subsequent processing is detailed in Section 2.4 of Chapter 2.

6.7.1   GPS L2C Acquisition Results

The developed L2C code acquisition module was initially validated using the hardware simulated data. The PRN 1, which had an approximate C/N_0 of 50 dB-Hz was successfully acquired using a coherent integration of 20 ms (i.e. $T_{COH} = 20$ ms). The PRN 12 code signal had a residual frequency offset of 1.3 kHz. Furthermore, the CM assisted CL code and direct CL code acquisition was also validated. Figure 6.12 shows the CM and CL code correlation output for the correct Doppler bin for the PRN 12 code signal.
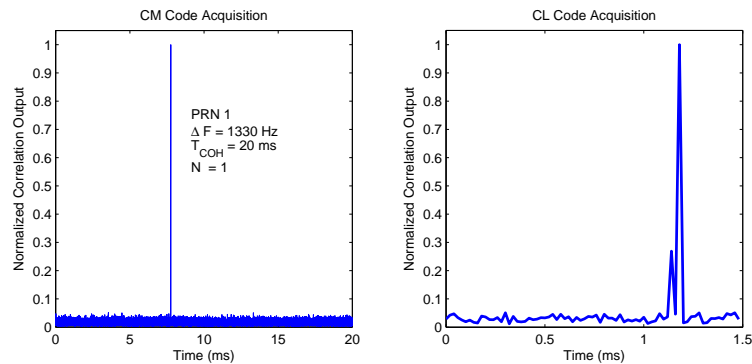
Figure 6.12: GPS L2C Code Acquisition. (Left) CM Code (Right) CL Code

The effect of navigation data transition on CM code acquisition was further investigated using the hardware simulated data. Figure 6.13 shows the CM code correlation output for a coherent matched filter, post-correlation differential and generalized differential detectors with and without data bit transition. The coherent matched filtering were obtained through post-correlation coherent accumulation. The partial correlation utilized a 2 ms coherent integration period (i.e. $T_{COH} = 2$ ms) followed by 10 non-coherent summations (i.e. $N = 10$). The coherent matched filter output was affected

severely as the bit transition occurred in the middle of the coherent integration. The post-correlation noncoherent detector resulted in a minuscule SNR loss as the effect of navigation data is removed during envelope detection. Finally, both the differential and the generalized differential detectors resulted in a 0.5 dB and 1.04 dB loss, respectively. The 0.5 dB loss in differential scheme corresponds closely to the theoretical loss of 0.45 dB. The generalized post-correlation detector should incur a loss of around -7.95 dB as it utilized $M = 5$ branches. On the other hand, it also accomplishes a gain of around 6.98 dB through coherent combining of individual correlation branches. Thus, the generalized post-correlation differential detector incurs a net loss of around 0.97 dB, which very well approximates the observed SNR loss of 1.04 dB.
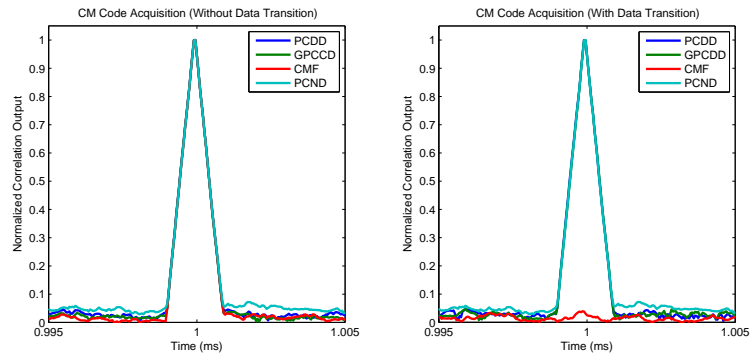
Figure 6.13: Effect of Navigation Data Bit Transition on CM Code Acquisition

One of the major advantages of GPCDD based acquisition lies in its ability to perform fine frequency estimation. The FFT based estimation/coherent combining technique is detailed in Section 3.5.2 of Chapter 3. For GPCDD based L2C acquisition, a coherent integration period of 2 ms and 10 branches was utilized, which resulted in a equivalent bandwidth and minimum resolution of $\pm$ 250 Hz and 50 Hz for the FFT based estimator. Figure 6.14 shows the fine frequency estimation obtained through GPCDD and FFT based estimator/combiner. The fine frequency estimation for both CM and CL code follows closely in accordance to the theory.
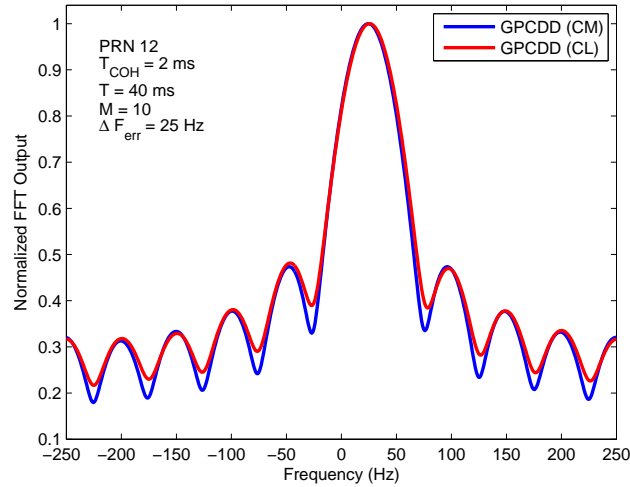
Figure 6.14: GPCDD/FFT based Fine Frequency Estimation

To evaluate the acquisition sensitivity of the detection schemes, IF data were collected for different C/N_0 levels from 50 dB-Hz down to 25 dB-Hz in steps of 5 dB-Hz. Each detection technique was tested to compare their acquisition sensitivities in terms of the resulting PSNR, both as a function of the processing technique and as a function C/N_0. The SNR threshold was kept to 16 dB for correct detection (Tsui [2000]). The PSNR was estimated for various algorithms for different C/N_0 values while keeping the coherent integration period of 2 ms but varying the accumulation number. The number of branches M was set to 10 for the GPCDD based acquisition. Figures 6.15 and 6.16 shows the PSNR performance of CM and CL code acquisition.

Higher PSNR values were observed for CM code acquisition over CL code acquisition with higher C/N_0 levels even though one would expect similar PSNR levels. The PSNR estimation during CL code acquisition was based on the 75 different code start phases whereas the PSNR estimation during CM code acquisition utilized 10230 samples corresponding to the 10230 code phases. The DBZP based FFT block acquisition demonstrated the best sensitivity performance amongst the various detectors. The GPCDD detector also showed PSNR levels similar to that of DBZP based acquisition.
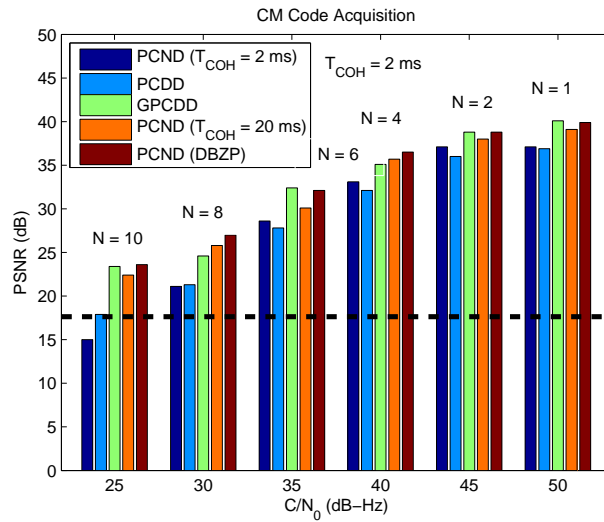
Figure 6.15: PSNR Performance of Various Detectors/Estimators for CM Code Acquisition

It should be noted here that the GPCDD scheme utilized a coherent integration of 2 ms and 10 branches, which is equivalent to coherent matched filtering technique with 20 ms coherent integration. Furthermore, the navigation data is also suppressed as a consequence of differential detection.
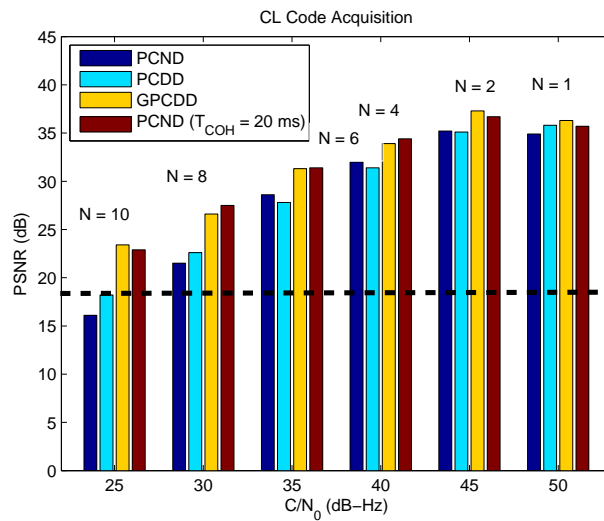
Figure 6.16: PSNR Performance of Various Detectors/Estimators for CL Code Acquisition

Finally, the post-correlation noncoherent/differential with a short coherent integra-

tion of 2 ms showed the least acquisition sensitivity and failed to acquire at 25 dB-Hz C/N_0 levels. On the other hand, they allow for considerable reduction in computational complexity owing to less stringent frequency estimation.

6.7.2 GPS L5 Acquisition Results

The various aspects of the developed L5 acquisition module was validated using hardware simulated data. The developed two-stage acquisition demonstrated consistent results in terms of PRN and NH code detection. Figure 6.17 shows the PRN code correlation outputs for PRN 9 (50 dB-Hz C/N_0) with and without NH code transitions. The coarse acquisition involved a coherent integration period of 1 ms with no additional noncoherent accumulations to illustrate the vulnerability of the NH code transitions.
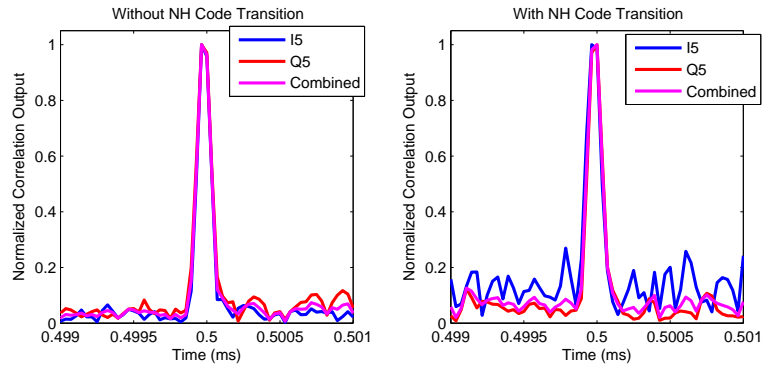
Figure 6.17: GPS L5 PRN Code Acquisition (LHS) Without NH Code Transition (RHS) With NH Code Transition

The PSNR for the data, pilot and combined cases were 33.2 dB, 32.2 dB, 35 dB respectively, in the absence of NH code transition. As reported in Hegarty et al. [2003], the combined detection resulted in an additional gain of around 2.3 dB in comparison to pure pilot or data channel acquisition. The RHS plot shows the normalized correlation output of the same in the presence of NH code transition. The PSNR values for the data, pilot and combined cases were 20.1 dB, 30.7 dB, 29.8 dB, respectively. Interestingly, the pilot-only acquisition resulted in the best PSNR due to the absence of NH code

transition. On the other hand, the data-only acquisition resulted in the worst case PSNR due to the presence of NH code transition. The combined detection of data and pilot channels also resulted in inferior PSNR in comparison to pilot-only acquisition. The reason for the apparent degradation is due to the addition of noisy data channel detection with that of pilot channel. It should be emphasized that the probability of NH code transition is around 0.5 for both pilot and data channels, and thus it is advantageous to still utilize the data/pilot combined detection. Moreover, the effect of NH code transitions can readily be alleviated through noncoherent accumulations or via DBZP technique (Yang [2005]) or through pre-correlation techniques (Zheng and Lachapelle [2004]; Shanmugam et al. [2005]).

The coarse acquisition is typically followed by the fine acquisition of NH code phases and frequency offset. While the NH10 code acquisition is limited by the navigation data transition, NH20 code acquisition can be limited by residual frequency error. Figure 6.18 shows the NH10 and NH20 code correlation outputs. Figure 6.18 also illustrates the influence of navigation data on NH10 code acquisition and the advantage of using NH20 code acquisition. The PSNR values for the NH10 and NH20 code were around 44 dB and 30.5 dB, respectively. The substantial difference in the PSNR values primarily stems from the PSNR estimation procedure. The PSNR essentially measures the ratio of the mean of the decision statistics in the presence of signal to the variance of decision statistics in the absence of signal. The variance of decision statistics is primarily influenced by the out-of-phase correlation values for high SNR values. The variance is nearly zero for NH10 code as its out-of-phase correlation assumes either +2 or -2 (or 2 if one considers enveloped detection). On the other hand, the NH20 out-of-phase correlation can assume -4, 0, or 4, which readily increases the variance and correspondingly decreases the PSNR value. The fine acquisition still utilizes the NH20 code detection due to the absence of navigation and longer code period. For instance, the correlation

output in the presence of navigation data transition (occurring at the middle of coherent integration) is also plotted in Figure 6.18. The NH10 code correlation output degraded substantially as the correlation power is completely cancelled by the navigation data bit transition. On the other hand, the NH20 correlation was consistent as there were no data bit transitions.
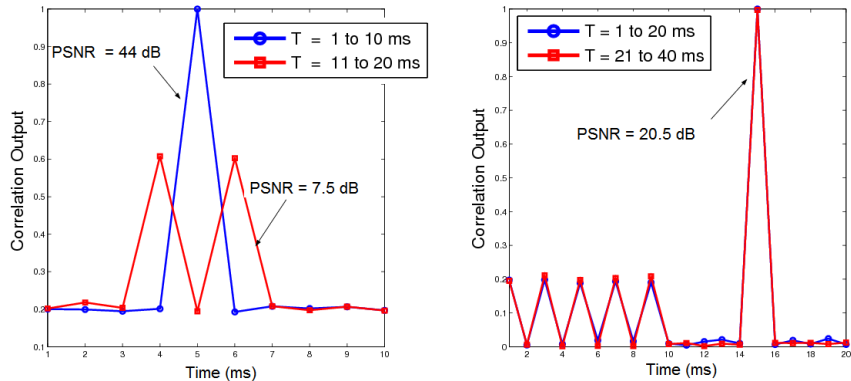
Figure 6.18: GPS L5 NH Code Acquisition

The asymptotic optimality of MCDD was proved in Section 4.1.4 of Chapter 4 and was basically extended to the problem of NH code acquisition in Section 6.5 in this chapter. To validate the theory, the NH code acquisition results using incoherent matched filter (as the magnitude output was assumed) and MCDD was obtained for the PRN 9 code signal, which has an approximate C/N_0 of 50 dB-Hz. The I5/Q5 code and the residual carrier was stripped prior to the NH code acquisition. The NH10 code was acquired using a coherent integration of 10 ms and the NH20 code was acquired using a 20 ms coherent integration period. Correspondingly, the MCDD scheme utilized 10 and 20 correlation branches for the NH10 and NH20 code acquisition. The normalized NH10 and NH20 code correlation outputs for the incoherent matched filter (circle) and MCDD (square) are plotted in Figure 6.19. The correlations plots readily confirms the asymptotic optimality of the MCDD scheme for NH code acquisition.

The major advantage behind using MCDD based NH code acquisition lies in its
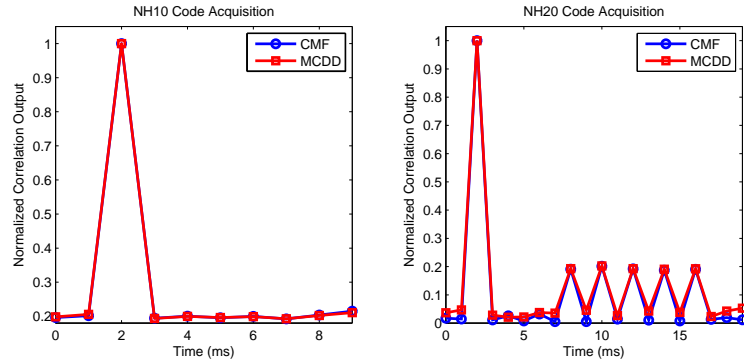
Figure 6.19: Normalized Detection Outputs of NH10 and NH20 Codes for CMF and MCDD based Acquisition Schemes

ability to compensate for residual frequency error through FFT based coherent combining. The correlation power loss due to residual frequency error can be minimized by reducing the frequency search step size. However, the number of code phase/frequency bins should be correspondingly increased due to the finer frequency resolution. On the other hand, the MCDD based NH code acquisition utilizes the inherent characteristics of the differential detector structure and FFT to compensate for the residual frequency error. To further illustrate the impact of residual frequency error, the NH10 and NH20 code acquisition was performed with a residual frequency error of 25 Hz. The NH20 acquisition is expected to degrade substantially due to the longer coherent integration period of 20 ms. Figure 6.20 shows the normalized code correlation outputs of NH10 and NH20 codes for coherent matched filtering and MCDD based NH code acquisition.

From Figure 6.20, one can readily notice the improved detection performance demonstrated by the NH code acquisition using NH10 code. The NH10 code acquisition utilized a short coherent integration period of 10 ms, which can tolerate a larger residual frequency error. However, it should be emphasized here that the code acquisition using NH10 code is severely limited by the navigation data transition and also, cannot
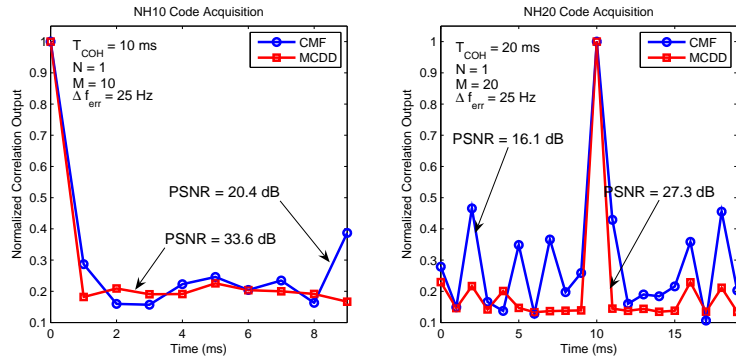
Figure 6.20: Impact of Residual Frequency Error on CMF and MCDD Based NH Code Acquisition

be reliably used for lower C/N_0 power levels. The MCDD based NH code acquisition consistently outperformed as the residual frequency error was readily compensated during the FFT based combining. Residual frequency errors exceeding the FFT estimator bandwidth (which was $\pm$ 500 Hz as the FFT input sampling rate was 1 ms) simply gets wrapped around the basic FFT input sampling frequency. While the frequency estimation using FFT in MCDD scheme becomes ambiguous, it still yields correct code phase estimation and was not affected by the apparent SNR loss due to residual frequency error. The detection performance of the NH code acquisition using the PCND and MCDD schemes was also evaluated as a function of C/N_0. Figure 6.21 shows the PSNR performance as a function of C/N_0 for NH10 (LHS) and NH20 (RHS) code acquisition.

The coherent integration period was set to 10 ms and 20 ms for the NH10 and NH20 code acquisition. The MCDD scheme utilized $M = 10$ and $M = 20$ for the NH10 and NH20 code acquisition to accomplish optimal PSNR performance. The total observation period was kept similar for both NH10 and NH20 code acquisition. The PSNR values for NH10 code acquisition were higher compared to that of NH20 due to the PSNR estimation procedure. Similarly, the substantial decline in PSNR values for NH10 code acquisition can be attributed to the noise induced out-of-phase correlation
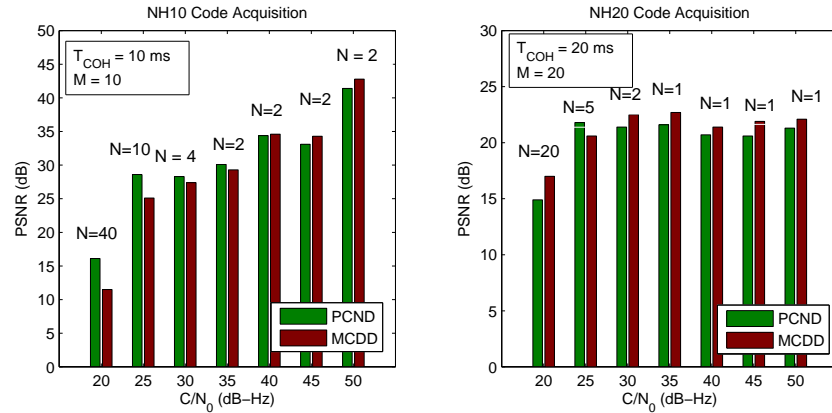
Figure 6.21: PSNR Performance of PCND and MCDD Based NH10/NH20 Code Acquisition

values. The MCDD scheme demonstrated inferior PSNR performance in comparison to PCND at lower C/N_0 levels. However, it should be emphasized here that the PCND is critically effected by residual frequency errors while MCDD is not. Hence, it would still be appealing to utilize MCDD based NH10 code acquisition.

In contrast to NH10 code acquisition, the degradation in PSNR for decreasing C/N_0 is not substantial due to the longer coherent integration. For NH20 code acquisition, the MCDD as well as the PCND based NH20 code acquisition resulted in a similar PSNR values. This does not come as a surprise as MCDD output reduces to that of incoherent matched filtering. Therefore, we can expect similar detection performance for both traditional PCND and proposed MCDD algorithms for NH code acquisition.

6.8 Discussions

The primary focus of this chapter was on the application of the detectors/estimators introduced in Chapters 3 and 4 to the problem of modernized GPS signal acquisition. The major outcome of the research presented in this chapter is summarized below:

1. A novel GPS L2C CM and CL code acquisition using the generalized post-

   correlation differential detection

2. A novel GPS L5 NH code acquisition using the multi-correlation differential detection

3. Design of new and improved short synchronization codes for future GNSS signals

The chapter briefly described the innovative signal structures utilized by the modernized GPS signals and their related correlation and spectral properties. A comprehensive review of various acquisition schemes reported in the literature for modernized GPS signal acquisition was carried out. Subsequently, we identified the various ways of extending the detectors introduced in Chapters 3 and 4 for modernized GPS signal acquisition. We also identified the critical appeal of generalized post-correlation differential detector and multi-correlation differential detector for GPS L2C and GPS L5 NH code acquisition. The correlation performance degradation with suboptimal post-correlation noncoherent/differential detectors was also identified. The two-stage acquisition process involving the initial coherent matched filtering and multi-correlation differential detection for GPS L5 acquisition was then introduced. The proposed MCDD scheme is not limited to two-stage acquisition strategy but can also be used in the direct acquisition of GPS L5 signals.

Chapter 7

Conclusions and Recommendations

This chapter summarizes the various aspects of the research presented in this dissertation. In the process, it also draws the seminal contributions of the thesis to the area of HS GPS signal detection. The chapter initially delineates the important results presented in the preceding chapters, which is followed by a list of functional recommendations to further the proposed research.

7.1 Synopsis

The main objective of this thesis was to gain a deeper understanding of the contemporary signal processing techniques utilized for enhanced GPS signal detection. By doing so, it also endeavoured to develop novel solutions that can potentially offer performance improvements over the existing solutions. The central objectives were systematically addressed in the preceding chapters and are further summarized succinctly here. Chapter 1 introduced the evolution of the GPS applications and thereby set the tone for the dissertation by foregrounding the need for HS GPS signal detection. Furthermore, it also reviewed the various solutions that were proposed in the literature for enhanced sensitivity detection of GPS signals. The scope of the research presented in this dissertation was also charted in Chapter 1. A brief review on the various aspects of legacy GPS systems was carried out in Chapter 2. The basic signal structure and related characteristics of the L1 C/A code was reviewed. More specifically, it identified the periodic property and successfully established the DAM property for the Gold sequences in theory. The basic receiver operations and limitations of GPS operations were addressed. Chapter 2 concluded by reviewing the HS GPS theory and its inherent limitations.

In Chapter 3, the GPS signal acquisition problem was treated from the perspective of *estimation theory*. The *MMSE estimator* was introduced as the one that minimizes the function, $E[(\theta - \hat{\theta})^2]$. Subsequently, the *maximum likelihood estimator* was introduced as a more practical approach, wherein the estimate $\hat{\theta} = [\hat{\tau}, \Delta\hat{F}]$ attempts to maximize the likelihood by searching over the discretized two-dimensional space θ. The GPS acquisition problem was also addressed from the view point of *detection theory*. Accordingly, the presence of the signal was determined by detecting the change in the known PDF (or its approximation). The primary approaches for hypothesis testing are based on the classical approach based on *Neyman-Pearson theorem* and the Bayesian approach based on minimization of *Bayes risk* and were summarized in (3.12) and in (3.15), respectively.

In this thesis, the analysis on the GPS signal acquisition problem was essentially based on the *detection/estimation* theory. The GPS signal acquisition was formulated as a joint detection/estimation problem, wherein the GPS receiver attempted not only to detect the transmitted PRN code signal, but also attempted to estimate the *code phase* and the *carrier frequency offset* pertaining to the detected PRN code signal (i.e. $\theta = [\tau, \Delta F]$). The detector analysis primarily utilized the Neyman-Pearson approach of maximizing the likelihood ratio. To this end, a variety of detectors, both optimal and suboptimal were introduced during the entirety of this thesis. The classification of these detectors was based on their relationship is illustrated in Figure 7.1.

The optimal detector (or the Neyman-Pearson) for a known signal (such as PRN code) in AWGN was derived as the *replica correlator*. The corresponding decision statistic is linear and is given by (3.22). The *matched filter* implementation of the replica correlator is given by (3.25) and subsequently used in (3.24). The frequency domain equivalent of the matched filter is given by (3.30), which essentially utilizes the fast Fourier transforms for its implementation. The detection performance of a matched
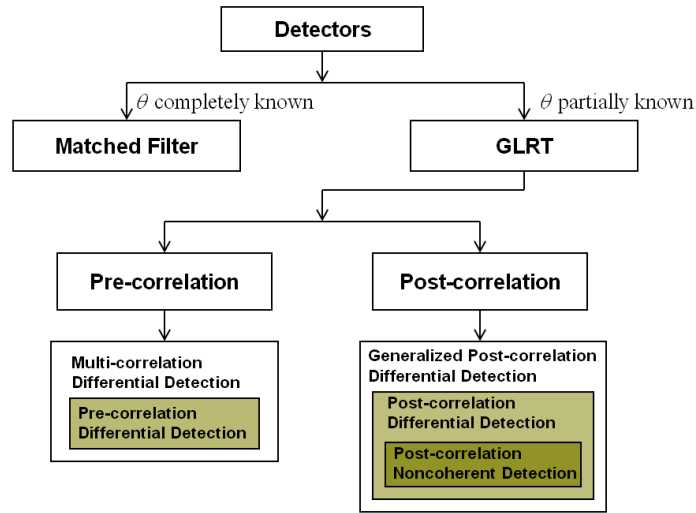
Figure 7.1: Developed Detectors/Estimators for GPS Signal Acquisition

filter is straight forward due to the Gaussian assumption and is analyzed in Section 3.6.1 of Chapter 3. More specifically, the relationship between the probability of detection and the pre-detection SNR (and thus C/N_0) for a given probability of false alarm is summarized in (3.98). The influence of the residual signals including the residual frequency errors, code phase errors and that of unknown navigation data modulation was characterized in Section 3.3.2 of Chapter 3. Subsequently, the limitations of the utilizing the matched filter in its original form was outlined in Section 3.3.3 in Chapter 3.

For a received signal with unknown signal parameters, the GLRT structure was established as an *energy detector* and the corresponding decision statistics were summarized in (3.60). The energy detector utilizes the *noisy estimate* of the transmitted signal in comparison to the *clean estimate* utilized in matched filtering during the correlation process. Therefore, the energy detector can be readily viewed as a suboptimal detector in terms of noise suppression although it is still optimal for deterministic signals with unknown parameters. In Chapter 3, it was also shown that several of the GPS signal acquisition schemes have utilized the GLRT structure of (3.60) in their special-

ized forms. Accordingly, the structure of (3.60) was established as the basic structure that readily encompasses the following detectors utilized in GPS signal acquisition.

1. Incoherent Matched Filter

2. Post-correlation Noncoherent Detector

3. Post-correlation Differential Detector

4. Pre-correlation Differential Detector

For unknown phase rotation, the GLRT structure of (3.60) reduced to an incoherent matched filter. The corresponding decision statistics are summarized in (3.62), which is essentially an estimator-correlator. The post-correlation noncoherent detector was readily established as the energy detector, whose decision statistics were summarized in (3.66). In contrast, the post-correlation differential detector utilizes the *previous sample* as the estimate (see (3.70)) during its estimation-correlation process. This is possible as the transmitted C/A code signal is periodic over 1 ms (however the noise is aperiodic). Besides, it approximates the time varying phase introduced by the navigation data and residual carrier to be time invariant over this delay. The SNR loss incurred due to navigation data bit transition is readily characterized by the *decorrelation* of the navigation data over the delay. The similarities between the differential detector and the *phase discriminator* were promptly summarized in (3.77). The post-correlation differential detection is attractive in terms of noise suppression as the noise samples are no longer correlated due to the usage of delayed samples in correlation, which also aided in fine frequency estimation.

In contrast, the pre-correlation applied the estimation-correlation process prior to matched filtering at the chip level (see (3.78)). The delay was judiciously selected as an integer multiple of basic chip duration (T_c) for two seminal reasons. The integer chip delay guarantees the decorrelation of the received C/A code signal. Furthermore, the

DAM property of Gold codes help retain similar correlation characteristics. Secondly, the navigation data and residual carrier were readily assumed to be time-invariant over the chip (or its multiple) duration. Moreover, it exploited the periodic property of the underlying C/A code to perform *comb filtering* prior to matched filtering. However, the incurred SNR loss is substantial as the estimation-correlation process is applied prior to matched filtering. The pre-correlation differential detection can also be utilized for fine frequency estimation although one would expect inferior estimation performance due to the poor input SNR values.

A novel GLRT structure, namely the *generalized post-correlation differential detector* was developed utilizing the periodicity of the underlying PRN code signal whose decision statistics are summarized in (3.89). It also exploited the basic C/A code periodicity to perform *comb filtering*, so as to enhance the SNR. Significant noise suppression was achieved by coherently combining the individual branch outputs via FFT processing. The second innovation pertaining to the generalized post-correlation differential detection lies in its ability to allow for fine frequency estimation. The complex phase rotations across the individual branches collectively embodies the residual carrier as expressed in (3.93). Accordingly, both coherent combining and fine frequency estimation can be accomplished through a simple FFT operation. The related performance measures of the FFT based fine frequency estimator is summarized in (3.94).

The detection performance of the individual detectors was derived theoretically in regards to coherent matched filtering in Section 3.6 of Chapter 3. Moreover, the the generalized post-correlation differential detector was shown to be asymptotically equivalent to that of incoherent matched filter and is summarized in (3.143). In Section 3.7, the various concepts developed in the Chapter 3 were validated alongside acquisition sensitivity and frequency sensitivity tests using hardware simulated and live GPS signals. The pre-correlation scheme showed the worst acquisition sensitivity but offered

the best resilience to residual signal effects. It also allowed for reduced complexity acquisition owing to the linear search in code phase alone. Additionally, it allowed for fine frequency estimation with limited estimation performance due to the inherent SNR loss. While the post-correlation noncoherent yielded a moderate acquisition sensitivity performance, the post-correlation differential yielded a better acquisition sensitivity performance over the noncoherent detector. Finally, the generalized post-correlation differential resulted in the best acquisition sensitivity performance in particular for low C/N_0 values. The post-correlation schemes were critically influenced by the residual frequency errors due to the usage of initial matched filtering. Thus, the developed detector schemes clearly demonstrated a trade-off between noise suppression and sensitivity to dynamics as originally predicted in Figure 1.2 in Chapter 1. The seminal findings of this chapter were presented in parts in Shanmugam et al. [2005] and Shanmugam et al. [2007b] and will be published in Shanmugam et al. [2007a].

Chapter 4, of this thesis, focused on the development of algorithms that achieve noise suppression and resilience to residual frequency errors. Once again, the fundamental periodic property of C/A code aided in the development of pre-correlation noise suppression through *coherent pre-filtering*. The pre-filter was implemented using a tapped delayed line structure as shown in Figure 4.1 and the corresponding filter output was given by (4.2). The influence of the residual signal effects on pre-filtering was promptly characterized in Sections 4.1.1 and 4.1.2. In Section 4.1.3, it was shown that the pre-filtering essentially accomplished the same effect as what extended coherent integration accomplished for post-correlation detectors. More importantly, it provided an excellent means to suppress the pre-correlation noise that critically enabled the application of pre-correlation differential detector. However, the use of pre-filtering necessitated a limited frequency search.

The generalization of pre-correlation differential detection, which is called *multi-*

correlation differential detector, was introduced in Section 4.1.4 and the corresponding decision statistic was summarized in (4.29). The influence of residual signal effects on the multi-correlation differential detector was analyzed in Section 4.1.5. Notably, the complex phase rotations across the individual branches was shown to collectively embody the residual carrier for correct code phase. Accordingly, the individual branch outputs was collectively processed by a FFT block to allow not only for coherent combining but also for fine frequency estimation. The related performance measures of the FFT based estimator were summarized in (4.34). The developed FFT based frequency estimator offered the robustness and the much desired flexibility. The analysis then turned to quantify the correlation performance of the C/A code signal detected via multi-correlation differential detection. It was observed that the out-of-phase correlation as well as cross-correlation values was randomly distributed, which yielded substantial correlation suppression as shown in Figure 4.8. Interestingly, the correlation suppression peaked for both $M = 512$ and $M = 1022$ as shown in Figure 4.9. Subsequent analysis revealed that the DAM operation yielded only $(N_c - 1)/2$ distinct codes and the remaining codes where essentially time shifted-versions of the same. The relationship between the DAM operation and the modified code was summarized in (4.48).

The essence of the multi-correlation differential detection was made known in the subsequent correlation performance analysis and is summarized in (4.53). The expression in (4.53), implied that the output of the multi-correlation differential detector is essentially similar to the output of a conventional correlator (matched filter). Armed with the preceding results, in Section 4.2.1, the detection performance of the multi-correlation differential detector was shown to be asymptotically equivalent to that of incoherent matched filtering and was summarized in (4.75). The multi-correlation differential detector can demonstrate optimal detection performance when the number of branches

M tends to N, where $N = T_{COH}T_s^{-1}$. However, the convergence of multi-correlation differential detection illustrated in Figure 4.16 signified the possibility of accomplishing significant reduction in the number of branches at the expense of suboptimal detection. The various system concepts developed in the preceding sections as well the acquisition performance was carried out in Section 4.3 of Chapter 4. There it was noted that the pre-filtering in conjunction with multi-correlation differential detection can provide the necessary processing gain to tackle weak signal conditions at the expense of limited frequency search. The generalized post-correlation differential detection and the multi-correlation differential detection, although varied in their respective implementations, essentially embody the different forms of the basic estimator-correlator structure. The major results pertaining to this chapter were presented in parts in Shanmugam et al. [2006b] and Shanmugam [2006] aside from a U.S. patent filing (Shanmugam et al. [2006a]).

In Chapter 5, the thesis further evolved to extend the algorithms developed in the preceding chapters for the problem of GPS signal detection under RFI. The chapter initially summarized the various interference types and their sources that are often encountered during GPS signal operation. Subsequently, the effect of interference, in particular, that of narrowband and continuous wave interference on a traditional matched filter detector was initially characterized. The vulnerability of a conventional matched filter detector to CW interference was outlined. In Section 5.5, the effect of interference on a multi-correlation differential detector was analyzed by characterizing the corresponding detection output. The multi-correlation differential detection was highlighted as an efficient detector to be used in conjunction with interference cancellation techniques to combat self-interference. More importantly, a simple yet efficient detection, estimation, and suppression scheme for CW interference based on multi-correlation differential detection was developed in Section 5.5.2. The test methodology for evaluating

the detection performance of the developed acquisition schemes in the presence of CW and narrowband interference was detailed. The various system concepts developed in the preceding sections was promptly validated using the interference corrupted GPS data. The acquisition sensitivity performance of the various detectors developed during the preceding chapters was summarized in Table 5.2. Finally, the use of a frequency excision technique for CW and narrowband interference suppression was readily emphasized in terms of detection performance analysis. The preliminary research findings in terms of multi-correlation differential detection performance under narrowband interference was presented in Shanmugam [2007].

Chapter 6 further extended the detectors developed in Chapters 3 and 4 to address the problem of modernized GPS signal acquisition. The innovative signal structure of modernized GPS L2C and L5 signals alongside their generation and the corresponding correlation and spectral characteristics was introduced in Section 6.1. We also reviewed the traditional coherent and post-correlation noncoherent detector algorithms proposed to address the problem of modernized GPS signal acquisition in Section 6.2. More importantly, in Section 6.3, the various possibilities of utilizing the detectors developed during the preceding sections to achieve innovative modernized GPS signal acquisition was reviewed. The chapter then focused on the extensions of the following detectors due to their critical appeal to the problem of modernized GPS signal acquisition.

- Generalized post-correlation differential detector based L2C code acquisition

- Multi-correlation differential detector based NH code acquisition

Both the detectors readily allowed for fine frequency estimation in addition to acquisition sensitivity improvements over a traditional post-correlation noncoherent detector. However, it was limited by the navigation data transition for CM code acquisition. Furthermore, the degradation in correlation performance due to suboptimal detection

were also analyzed. Similarly, the multi-correlation differential yielded optimal detection performance for NH20 code acquisition due to the absence of navigation data. More importantly, the vulnerability of short synchronization code in terms of residual frequency error was introduced. An exhaustive search immediately revealed the existence of better synchronization codes in comparison to the standardized NH 10 and 20-bit codes. Furthermore, the analysis also indicated the relationship between optimal synchronization codes to the structured Golay codes. The performance improvements with the proposed short synchronization codes were then demonstrated using simulation analysis. The chapter finally concluded with acquisition performance evaluation for both GPS L2C and GP L5 NH code acquisition. The major research findings will be presented in Shanmugam et al. [2007b] and will also be published in Shanmugam et al. [2007c].

7.2 Thesis Contributions

The seminal contributions of this dissertation specifically to the problem of HS GPS detection and generally in the area of detection/estimation of periodic signals are summarized below:

1. Fundamental theoretical considerations based on the generalized likelihood ratio test (GLRT), as applied to GPS signal detection, were established.

2. The design of a novel generalized post-correlation differential detection for enhanced sensitivity GPS signal acquisition. The proposed detector readily encompasses both the post-correlation noncoherent and differential detector as its special forms.

3. Two new innovations namely the pre-filtering and multi-correlation differential detection was developed utilizing the underlying PRN code characteristics. The

pre-filtering in conjunction with MCDD was shown to be asymptotically optimal but was resilient to residual frequency errors and that of data modulation.

4. A novel design of a simple yet efficient CW interference detection, estimation and suppression based on the multi-correlation differential detection was developed.

5. Innovative design of modernized GPS L2C CM and CL code detection schemes based on generalized post-correlation differential detection were developed. The L2C acquisition using the same detector offered improved detection performance, fine frequency estimation and much needed flexibility.

6. Innovative extension of basic multi-correlation differential detection to address the problem of GPS L5 NH code detection. The MCDD based NH code acquisition accomplishes optimal detection performance and fine frequency estimation that is critically required for NH code acquisition.

7. A critical analysis on the design of short synchronization codes and subsequent development of new and improved short 10-bit and 20-bit synchronization codes. The results can be further utilized to design of optimal short sequences of arbitrary length.

8. The proposed research is not only limited to GPS signal detection but can generally be applied for detection/estimation of periodic signals in various related fields. For instance, the proposed research can be readily adapted to address the detection/estimation problems in the related fields such as communication systems, radar signal processing, and system identification.

7.3   Recommendations

The research presented in this dissertation focused primarily on specific aspects of enhanced sensitivity GPS signal detection owing to the broad nature of the research topic. Naturally, it is important to recognize the precincts of the developed research and also to identify the future scope of the research presented in this dissertation. Based on the results presented in the previous chapters and the subsequent conclusions made in this chapter, the following recommendations can be made to further the proposed research.

Development of Theoretical Bounds

The analysis of residual signal effects was carried out independently for the navigation data modulation and residual carrier. In contrast, a more accurate modelling on the combined effects of navigation data modulation and residual carrier could reveal other interesting characteristics of the developed detectors. The theoretical performance carried out in this thesis mostly utilized the central limit theorem argument to invoke Gaussian approximation. Secondly, the detection performance analysis carried out in this thesis utilized the relationship between the deflection coefficient (or PSNR), the probability of false alarm and the probability of correct detection. While the relationship is accurate for Gaussian distributed decision statistics, it is only an approximation for non-Gaussian distributed decision statistics. Accordingly, the current analysis can be extended to include more accurate derivation of Gaussian approximation.

Computational Complexity Analysis

The real impact of any new detection algorithms is not only influenced by its detection performance, but also by the levels of complexity it necessitates for its implementation. Accordingly, gate-level complexity analysis of the new detection algorithms critically

influence the subsequent adoption of these detectors in future GPS receivers. Interestingly, the trade-offs and the existence of further optimization was signified in the preceding chapters. Hence, system level optimization can reveal hot spots, where the developed detectors outperform conventional detectors for GPS signal acquisition.

Development of Code/Carrier Tracking Algorithms

The analysis of differential detectors critically revealed the similarities with the phase discriminators. For instance, the generalized post-correlation detector can be readily viewed as an array of phase discriminators and thus readily adapted to achieve better frequency tracking. Similar modifications can also be applied to the multi-correlation differential to accomplish robust frequency tracking to deal with high dynamics situations. More importantly, the developed detectors can be utilized in conjunction with a frequency domain tracking implementation as well (Yang [2003]). It is interesting to note that Lin [2000] already demonstrated a low complexity code tracking loop with chip-level differential detection for spread spectrum receivers. This is of critical significance as it permits code independent frequency tracking even under high dynamics situations. The concept reported in Lin [2000] can be readily improved with the understanding of the detectors gained in the preceding chapters.

Interference Suppression

Chapter 5 of this thesis essentially demonstrated the advantage of the proposed detectors in terms of interference detection and suppression. However, further investigation and analysis is still required to wholly utilize the developed detectors for the problem of GPS signal acquisition under RFI. For instance, the use of multi-correlation differential detection in conjunction with interference cancellation for self-interference mitigation should be further investigated. Besides, theoretical analysis on the performance of the various detectors could reveal vital information for subsequent development of interfer-

ence mitigation schemes.

Adaptation to Galileo and Compass Signals

In a broader perspective, GNSS is currently witnessing major developments including the EU's Galileo and China's Compass systems. While these new GNSS systems might employ different signal structures, they still utilize spread spectrum modulation in their respective systems. Accordingly, the detectors presented in this thesis can be readily extended to the acquisition problem for these new GNSS systems. In some cases, the developed detectors cannot be directly applied and should be carefully adapted to yield optimal acquisition performance.

Applications Beyond GNSS

At a more fundamental level, the thesis addressed the problem of detection of deterministic signals with unknown parameters. The corresponding analysis readily exerts critical implications in related signal processing fields such as communication theory, radar and system identification. For example, both pre-filtering and multi-correlation differential detection structures have been independently proposed for UWB synchronization (Nekoogar et al. [2004]) and data demodulation (Pausini et al. [2006]). Interestingly, the complimentary nature utilized in the proposed PF/MCDD can yield better performance to both the problem of synchronization and data demodulation in transmitted-reference UWB systems. Similarly, the developed research can be further extended to detection of random periodic processes, which has a plethora of applications in various fields. For example, the multi-correlation differential detection can be readily adopted to address the problem of detection of periodic random vibrations in rotating machines (McCormick and Nandi [1998]). Therefore, a comprehensive review of related fields could reveal various applications, wherein the developed detectors can offer attractive solutions.

Bibliography

Abraham, C. and F. van Diggelen (2001). Indoor GPS: The No-Chip Challenge. GPS World.

Akos, D. M., P. L. Normark, J. T. Lee, K. G. Gromov, J. B. Y. Tsui, and J. Schamus (2000). Low Power Global Navigation Satellite System (GNSS) Signal Detection and Processing. Proceedings of GPS 2000, (Session D2, Salt Lake City, UT, 19–22 September), The Institute of Navigation, Fairfax, VA, pages 784–791.

Akos, D. M. and M. Pini (2006). Effect of Sampling Frequency on GNSS Receiver Performance. Navigation: Journal of The Institute of Navigation, 53(2), pages 85–95.

Amoroso, F. (1983). Adaptive A/D Converter to Suppress CW Interference in DSPN Spread Spectrum Communications. IEEE Transactions on Communications, 31(10), pages 1117–1123.

Ashjaee, J. (2006). Galileo, GLONASS, and GPS. GPS World,.

Axelrad, P. and R. G. Brown (1996). GPS navigation algorithms, volume 1 of Global Positioning System: Theory and Applications,. American Institute of Aeronautics and Astronautics, Inc., Cambridge, Massachusetts, 1st edition.

Balaei, A. T. (2006). Statistical Inference Technique in Pre-correlation Interference Detection in GPS Receivers. Proceedings of ION GNSS 2006, (Session B5a, 26–29 September), The Institute of Navigation, pages 2232–2240.

Barker, B. C., J. W. Betz, J. E. Clark, J. T. Correia, J. T. Gillis, S. Lazar, A. K. Rehborn, and J. R. Straton (2000). Overview of the GPS M Code Signal. Proceedings of ION NTM 2001 (Session D2, 26–28 January), Anaheim, CA, pages 542–549.

Betz, J. W. (2001-2002). Binary offset carrier modulations for radionavigation. Navigation: Journal of The Institute of Navigation, 48(4), pages 226–246.

Bryant, R. (2005). Assisted GPS – Using Cellular Telephone Networks for GPS Anywhere. GPS World, pages 40–46.

Burgi, C., E. Mey, A. Orzati, and A. Thiel (2006). Highly-Integrated Solution for Ultra–fast Acquisition and Precise Tracking of Weak GPS and Galileo L1 Signals. GNSS 19th International Technical Meeting of the Satellite Division, (Session C1, Fort Worth, TX, 26–29 September), The Institute of Navigation, Fairfax, VA, pages 226–235.

Carroll, J. V. (2003). Vulnerability Assessment of the U.S. Transportation Infrastructure that Relies on GPS. The Journal of Navigation, 56(2), pages 185–193.

Casbona, M. M. and M. W. Rosen (1999). Discussion of GPS Anti-Jam Technology. GPS Solutions, 2(3), pages 18–23.

Chansarkar, M. M. and L. Garin (2000). Acquisition of GPS signals at very low signal to noise ratio. Proceedings of NTM 2000 (Session E1, Anaheim, CA, 26 – 28 January), The Institute of Navigation, Fairfax, VA, pages 731–737.

Cho, D. J., C. Park, and S. J. Lee (2004). An Assisted GPS Acquisition Method using L2 Civil Signal in Weak Signal Environment. Proceedings of The 2004 International Symposium on GPS/GNSS (Session 7B, 6–8 December), Sydney, Australia, page 11.

Chung, C. (1995). Differentially Coherent Detection Technique for Direct-Sequence Code Acquisition in a Rayleigh Fading Mobile Channel. IEEE Transactions on Communications, 43(234), pages 1116–11,126.

Clinton, W. J. (2000). Improving the Civilian Global Positioning System. Office of Science and Technology Policy.

Coenen, A. and D. Van Nee (1992). Novel fast GPS/GLONASS code-acquisition technique using low update rate FFT. IEEE Electronics Letters, 28(9), pages 863–865.

Curry, G. R. (2001). Radar System Performance Modeling. Artech House, Norwood, MA.

Cutright, C., J. R. Burns, and M. Braasch (2003). Characterization of Narrow-Band Interference Mitigation Performance Versus Quantization Error in Software Radios. Proceedings of the 59th Annual Meeting/CIGTF 22nd Guidance Symposium (Session D3, 23–25 June), pages 323–332.

Davisson, L. D. and P. G. Flikkemama (1988). Fast Single–Element PN Acquisition for the TDRSS MA System. IEEE Transactions on Communications, 36(11), pages 1226–1235.

Deshpande, S. and M. E. Cannon (2004). Interference Effects on the GPS Signal Acquisition. Proceedings of ION NTM 2004 (Session E2, Anaheim, CA 26–28 January), pages 1026–1036.

DiFranco, J. V. and W. L. Rubin (1980). Radar Detection. Artech House, Norwood, MA.

Diggelen van, F. (2002). Indoor GPS theory and implementation. IEEE Position Location and Navigation Symposium, pages 240–247.

Dipietro, R. (1989). An FFT based Technique for Suppressing Narrow-Band Interference, in PN Spread Spectrum Communications Ssystems. Prcoceedings of ICASSP-89, 2, pages 1360–1363.

Elders-Boll, H. and U. Dettmar (2004). Efficient Differentially Coherent Code/Doppler Acquisition of Weak GPS Signals. Proceedings of 8th IEEE ISSTA Symposium, pages 731–735.

Enge, P. and P. Misra (1999). Scanning the issue/technology: special issue on global position system. Proceedings of IEEE, 87(1).

ESA (2007). GIOVE-A navigation signal available to users. http://www.esa.int/esaNA/SEM4EDN0LYE_galileo_0.html.

Fontana, R. D., W. Cheung, and T. Stansell (2001). The Modernized L2 Civil Signal. GPS World, pages 28–34.

Golay, M. (1961). Complementary series. IEEE Transactions on Information Theory, 7(2), pages 82–87.

Gold, R. (1967). Optimal Binary Sequences for Spread Spectrum Multiplexing. IEEE Transactions on Information Theory, 13(4), pages 618 – 621.

Gore., A. A. (1999). New Global Positioning System Modernization Initiative. Press Release, The White House, Office of Vice President.

Grelier, T., J. Dantepal, A. Delatour, A. Ghion, and L. Ries (2007). Initial Observations and Analysis of Compass MEO Satellite Signals. Inside GNSS, pages 39–43.

Haag de, M. U. and J. M. Kelly (2004). Influence of Oscillator Variations on the Observed Frequency Behavior in Software-Based Navigation Receivers. IEEE Signal Processing Letters, 11(3), pages 390 – 392.

Hartfiel, J. D. (2000). Matrix Theory and Applications With Matlab. CRC Press.

Hegarty, C., M. Tran, and A. J. Van Dierendonck (2003). Acquisition Algorithms for the GPS L5 Signal. Proceedings of ION GPS/GNSS 2003 (Session B1, 9–12 September), Portland, OR, pages 176–177.

Hopkins, P. (1977). A unified analysis of pseudonoise synchronization by envelope correlation. IEEE Transactions on Communications, 25(8), pages 770–778.

ICD-GPS-200 (1997). ICD-GPS-200 GPS : Interface Control Document. Technical report, GPS Joint Program Office, ARINC Research Corporation.

ICD-GPS-200C (2003). Interface Control Document: Navstar GPS Space Segment/Navigation User Interfaces. Technical report, US DOD, IRN-200C-005R1, http://www.navcen.uscg.gov/gps/geninfo/ICD-GPS-200Cf.

ICD-GPS-705 (2002). Navstar GPS Space Segment/ User Segment L5 Interfaces. Technical report, US DOD, IRN-200C-005R1, http://www.navcen.uscg.gov/gps/modernization/Number.pdf.

Jiang, Z., C. Ma, and G. Lachapelle (2004). Mitigation of Narrow-band Interference on Software Receivers Based on Spectrum Analysis. Proceedings of GNSS 2004 (Session B1, 21–24 September), Long Beach, CA, pages 144–155.

Kaplan, E. D. and C. J. Hegarty (2006). Understanding GPS Principles and Applications. Artech House, Boston, London, 2nd edition.

Kay, S. M. (1993a). Fundamentals of Statistical Signal Processing: Detection theory, volume II. Prentice-Hall, Englewood, NJ, USA.

Kay, S. M. (1993b). Fundamentals of Statistical Signal Processing: Estimation theory, volume I. Prentice-Hall, Inc, Englewood Cliffs, NJ.

Klukas, R., O. Julien, L. Dong, M. E. Cannon, and G. Lachapelle (2004). Effects of building materials on UHF ranging signals. GPS Solutions, 8(1), pages 1–8.

Lachapelle, G., H. Kuusniemi, D. T. H. Dao, G. MacGougan, and M. E. Cannon (2003). HSGPS Signal Analysis and Performance under Various Indoor Conditions. Proceedings of GNSS 2003 (Session C3, Portland, OR, 9-12 September), The Institute of Navigation, Fairfax, VA., pages 1171–1184.

Ledvina, B. M., S. Powell, P. M. Kintner, and M. L. Psiaki (2003). A 12–Channel Real–Time GPS L1 Software Receiver. Proceedings of NTM 2003 (Session E1, Anaheim, CA, 22 – 24 January), The Institute of Navigation, Fairfax, pages 767–782.

Lempel, A., M. Cohn, and W. L. Eastman (1977). A Class of Balanced Binary Sequences with Optimal Autocorrelation Properties. IEEE Transactions on Information Theory, 23(1), pages 38–42.

Lijun, W., Z. Huichang, Z. Gang, and Z. Shuning (2005). AM-FM interference suppression for GPS receivers based on time-frequency analysis and synthesis. Proceedings of 2005 Microwave, Antenna, Propagation and EMC Technologies for Wireless Communications, 2, pages 1378–1381.

Lim, D. W., S. W. Moon, C. Park, and S. J. Lee (2006). L1/L2CS GPS Receiver Implementation with Fast Acquisition Scheme. Proceedings of IEEE/ION PLANS 2006 (Session C5, 25–27 April) San Diego, CA, pages 840–844.

Lin, D. and J. Tsui (1998). Acquisition schemes for software GPS receiver. Proceedings of GPS 1998 (Session D1, Nashville, TN, 15 – 18 September), The Institute of Navigation, Fairfax, VA, pages 317–325.

Lin, D. M. and J. M. Tsui (2000). Comparison of Acquisition Methods for Software GPS Receiver. Proceedings of ION GPS 2000, The Institute of Navigation, pages 165 – 177.

Lin, J.-C. (2000). Low-complexity code tracking loop with chip-level differential detection for DS/SS receivers. IEEE Electronic Letters, 1(1), pages 125–133.

Macabiau, C., O. Julien, and E. Chatre (2001). Use of Multicorrelator Techniques for Interference Detection. Proceedings of NTM 2001 (Session B3, Long Beach, CA, 22 – 24 January), The Institute of Navigation, Fairfax, pages 353–363.

Macabiau, C., L. Ries, F. Bastide, and J.-L. Issler (2003). GPS L5 Receiver Implementation Issures. Proceedings of ION GPS/GNSS 2003 (Session B1, 9 –12 September), Portland, OR, pages 153–164.

MacGougan, G. (2003). High–Sensitivity GPS Perfromance Analysis in Degraded Signal Environments. Master's thesis, UCGE Report 210176, Department of Geomatics Engineering, University of Calgary, Calgary, Canada.

MacGougan, G., G. Lachapelle, R. Klukas, K. Siu, L. Garin, H. Shewfelt, and G. Cox (2002). Degraded GPS Signal Measurements with a Stand-Alone High Sensitivity Receiver. Proceedings of National Technical Meeting, The Institute of Navigation (San Diego, CA, Jan 28 – 30), pages 191–204.

Madhani, P. H., P. Axelrad, K. Krumvieda, and J. Thomas (2003). Application of successive interference cancellation to the GPS pseudolite near-far problem. IEEE Transactions on Aerospace and Electronic Systems, 39(2), pages 481–488.

Mathieu, M.-L., S. E. Christiansen, and A. Mozes (2005). Charting Future GNSS Markets: Exploratory Applications and Services. GPS World, 16(10), page 6.

McCormick, A. C. and A. K. Nandi (1998). CYCLOSTATIONARITY IN ROTATING MACHINE VIBRATIONS. Mechanical Systems and Signal Processing (Elsevier Science), 12(2), pages 225–242.

Mertens, S. (1996). Exhaustive search for low-autocorrelation binary sequences. J. Phys. A:Math Gen, 29, pages L473–L481.

Misra, P. and P. Enge (2001). Global Positioning System: Signals, Measurements, and Performance. Ganga-Jamuna Press, Lincoln, Masssachusetts, 1st edition.

Mitelman, A., P.-L. Normark, M. Reidevall, J. Thor, O. Gronqvist, and L. Magnusson (2006). The Nordnav Indoor GNSS Reference Receiver. Proceedings of GNSS 2006 (Session D5, Fort Worth, TX, 26–29 September), The Institute of Navigation, pages 2494–2502.

Moghaddam, A. R. A., R. Watson, G. Lachapelle, and J. Nielsen (2006). Exploiting the Orthogonality of L2C Code Delays for a Fast Acquisition. Proceedings of ION GNSS 2006 (Session C3, 26–29 September), Fort Worth, TX, pages 1233–1241.

Moreau, M., P. Axelrad, J. L. Garrison, D. Kelbel, and A. Long (1999). GPS Receiver Architecture Expected Performance for Autonomous GPS Navigation in Highly Eccentric Orbits. Proceedings of ION 55th Annual Meeting, Cambridge, MA, pages 653–665.

Ndili, A. and P. Enge (1998). GPS receiver autonomous interference detection. Proceedings of IEEE PLANS-98, pages 123–130.

Nekoogar, F., F. Dowla, and A. Spiridon (2004). Rapid Synchronization of Ultra-Wideband Transmitted-Reference Receivers. Proceedings of Wireless 2004 (Calgary, AB, 12–14 July), page 5.

Neuman, F. and L. Hofman (1971). New Pulse Sequences with Desirable Correlation Properties. Proceedings of National Telemetry Conference, Washington, D.C., pages 272–282.

Novatel (2005). OEM4–G2 Product Data Sheet. http://www.novatel.com/products/oem4g2.htm, Calgary, Canada.

Novatel (2006). GPS–700 Antenna Series: Product Datasheet. Technical report, Novatel, http://www.novatel.com/Documents/Papers/GPS700.pdf.

O' Driscoll, C. (2007). Performance Anaylsis of the Parallel Acquisition of Weak GPS Signals. Ph.D. thesis, Department of Electrical and Electronic Engineering, National University of Ireland, Cork, Ireland.

Papoulis, A. (1984). Probability, random variables and stochastic processes. McGraw-Hill, 1984, 2nd ed., New York.

Park, S., I. Choi, S. Lee, and Y. Kim (2002). A Novel GPS Initial Synchronization Scheme using Decomposed Differential Matched Filter. Proceedings of ION NTM 2002, (Session A3, Sandiego, CA, 28–30, January), pages 246–253.

Parkinson, B. W. (1996). Introduction and Heritage of NAVSTAR, the Global Positioning System. Global Positioning System: Theory and Applications, Volume I. American Institute of Aeronautics and Astronautics, Inc., Cambridge, Massachusetts, 1st edition.

Pausini, M., J. M. Janssen, and K. Witrisal (2006). Performance Enhancement of Differential UWB Autocorrelation Receivers Under ISI. IEEE Journal On Selected Areas In Communications, 24(4), pages 815–821.

Peterson, B., J. Hartnett, R. Fiedler, and A. Nebrich (1996). Frequency domain techniques for fast GPS acquisition and interference detection/rejection. Navigation, The Institute of Navigation, 43(3), pages 237–255.

Proakis, J. G. (2001). Digital Communications. McGraw Hill, Boston, MA, 4th edition.

Psiaki, M. L. (2001). Block acquisition of weak GPS signals in a software receiver. Proceedings of ION GPS–2001, Salt Lake City, pages 2838–2850.

Psiaki, M. L. (2004). FFT-Based Acquisition of GPS L2 Civilian CM and CL Signals. Proceedings of ION GNSS 2004 (Session A2, 21–24 September), Long Beach, CA, pages 457–473.

Psiaki, M. L. (2007). MATLAB Based GPS L1 Software Signal Simulator. Internal.

Revnivykh, S. (2006). GLONASS Status Update. 46th CGSIC Meeting, Fort Worth, TX, USA.

Ries, L., C. Macabiau, Q. Nouvel, W. Jeandel, W. Vigneau, V. Calmettes, and J.-L. Issler (2002). A Software Receiver for GPS-IIF L5 Signal. Proceedings of IOn GPS 2002 (Session, 24–27 September) Portlan, OR, pages 1540–1553.

Riley, W. J. (1999). A Rubidium Clock for GPS IIF. Joint Meeting of the 13th European Frequency and Time Forum and 1999 IEEE International Frequency Control Symposium, Besancon, France.

Sarwate, D. V. and M. B. Pursley (1980). Crosscorrelation Properties of Pseudorandom and Related Sequences. Proc. of IEEE, 68(5), pages 593 – 619.

Schmid, A. and A. Neubauer (2004). Performance of Differential Correlation for Single Shot Measurement Positioning. GNSS 17th International Technical Meeting of the Satellite Division, (Session D5, Long Beach, CA, 21–24 September), The Institute of Navigation, Fairfax, VA, pages 1998–2009.

Schmid, A. and A. Neubauer (2005). Adaptive Phase Correction Loop for Enhanced Acquisition Sensitivity. Proceedings of GNSS 2005 (Session C1, Long Beach, CA, 13-16 September), The Institute of Navigation, Fairfax, VA., pages 168–177.

Shanmugam, K., J. Nielsen, R. Watson, and G. Lachapelle (2007a). Enhanced GPS C/A Code Acquisition Using Innovative Differential Detection Techniques. IEEE Transaction on Aerospace Electronics and Systems (Preliminary Acceptance), page 10.

Shanmugam, K. S., J. Nielsen, and G. Lachapelle (2007b). Enhanced Differential Detection Scheme for Weak GPS Signal Acquisition. ION GNSS 2007 (Session C1, Fort Worth, TX, 25 – 28 September), The Institute of Navigation, Fairfax, page 14.

Shanmugam, K. S., J. Nielsen, G. Lachapelle, and R. Watson (2006a). Differential Signal Processing Schemes for Enhanced GPS Acqusition. U.s. patent filing.

Shanmugam, K. S., J. Nielsen, R. Watson, and G. Lachapelle (2006b). Pre-Correlation Noise and Interference Suppression for Use in Direct-Sequence Spread With Periodic PRN Codes. Proceedings of GNSS 2006 (Session C3, Forth Worth, TX, 26 – 29 September), The Institute of Navigation, Fairfax, pages 1297–1308.

Shanmugam, K. S., R. Watson, J. Nielsen, and G. Lachapelle (2005). Differential Signal Processing Schemes for Enhanced GPS Acquisition. Proceedings of GNSS 2005 (Session C1, Long Beach, CA, 13 – 16 September), The Institute of Navigation, Fairfax, pages 212–221.

Shanmugam, S. K. (2006). Improving GPS L1 C/A Code Correlation Properties Using a Novel Multi-correlator Differential Detection Technique. Proceedings of GNSS 2006 (Session D5, Forth Worth, TX, 26 – 29 September), The Institute of Navigation, Fairfax, pages 2453–2464.

Shanmugam, S. K. (2007). Narrowband Interference Suppression Performance of Multi-Correlation Differential Detection. Proceedings of European Navigation Conference on GNSS, (Session B5, Geneva, Switzerland, 29–31 May), page 12.

Shanmugam, S. K., C. Mongredein, J. Nielsen, and G. Lachapelle (2007c). Design of Short Synchronization Codes for Future GNSS Signals. International Journal of Navigation and Observation (in submission).

Sklar, B. (1997). Rayleigh Fading Channels in Mobile Digital Communication Ssytems Part I: Characterization. IEEE Communications Magazine, 35(7), pages 90–100.

Skone, S., G. Lachapelle, D. Yao, W. Yu, and R. Watson (2005). Investigating the Impact of Ionospheric Scintillation Using a GPS Software Receiver. Proceedings of GNSS 2005 (Session C3, Long Beach, CA, 13 – 16 September), The Institute of Navigation, Fairfax, pages 1126–1137.

Spilker, J. J. (1996). GPS Signal Structure and Theoretical Performance. Global Positioning System: Theory and Applications, Volume I. American Institute of Aeronautics and Astronautics, Inc., Cambridge, Massachusetts, 1st edition.

Spilker, J. J. and F. D. Natali (1996). Interference Effects and Mitigation Techniques, volume 1 of Global Positioning System: Theory and Applications. American Institute of Aeronautics and Astronautics, Inc., Cambridge, Massachusetts, 1st edition.

Spilker Jr, J. J. and A. J. Van Dierendonck (2001). Proposed New L5 Civil GPS Codes. Navigation: Journal of The Institue of Navigation, 48(3), pages 135–143.

Syrjarinne, J. (2001). Wireless-Assisted GPS: Keeping Time with Moblies. GPS World, pages 22–31.

Taylor, R. and J. Sennott (1984). Navigation system and method. United States Patent (4445118).

Tran, M. and C. Hegarty (2003). Performance Evaluations of the New GPS L5 and L2 Civil (L2C Signals. Proceedings of ION NTM 2003 (Session C2, 22–24 January), Anaheim, CA, pages 521–535.

Tsui, J. B. (2000). Fundamentals of Global Positioning System Receivers: A Software Approach. John Wiley & Sons, New York, 1st edition.

Tylavsky, D. J. and G. R. L. Sohie (1986). Generalization of the matrix inversion lemma. IEEE Proceedings, 74(7), pages 1050–1052.

van Dierendonck, A. J. (1996). GPS Receivers. Global Positioning System: Theory and Applications, Volume I. American Institute of Aeronautics and Astronautics, Inc., Cambridge, Massachusetts, 1st edition.

Van Dierendonck, A. J. and C. Hegarty (2000). The New L5 Civil GPS Signal. GPS World, 11(9), pages 64 – 71.

van Diggelen, F. and C. Abraham (2001). Indoor GPS : The No-Chip Challenge. GPS World,.

Van Nee, D. and A. Coenen (1991). New fast GPS code-acquisition technique using FFT. IEEE Electronics Letters, 27(2), pages 158–160.

Ward, W. P. (1995). GPS Receiver RF Interference Monitoring, Mitigation and Anaylsis Techniques. Journal of The Institute of Navigation, 41(4), pages 367–391.

Ward, W. P. and W. J. Betz (2006). Interference, Multipath, and Scintillation. Artech House, Inc., Boston, Massachusetts, 2nd edition.

Watson, R. (2005). High-Sensitivity GPS L1 Signal Aanlysis for Indoor Channel Modeling. Master's thesis, UCGE Report 20216, Department of Geomatics Engineering, University of Calgary.

Watson, R., G. Lachapelle, R. Klukas, S. Turunen, S. Pietila, and I. Halivaara (2005). Investigating GPS Signals Indoors with Extreme High-Sensitivity Detection Techniques. Journal of Navigation, The Institute of Navigation, Al, 52(4), pages 199–213.

Wirth, W. D. (1995). Energy saving by coherent sequential detection of radar signals with unknown Doppler shift. IEE Proceedings on Radar, Sonar and Navigation, 142(3), pages 145–152.

Wolfert, R., S. Chen, S. Kohli, D. Leimer, and J. Lascody (1998). Rapid direct P(Y)-code acquisition in a hostile environment. Proceedings of the International Technical Meeting of the Satellite Division, (Session D1, Nashville, TN, 15–18 September), The Institute of Navigation, Fairfax, VA, pages 353 –360.

Yang, C. (2003). Tracking of GPS Code Phase and Carrier Frequency in the Frequency Domain. Proceedings of ION GPS 2003, (Session B1, Portland, OR, 9–12 September), The Institute of Navigation, pages 628–637.

Yang, C. (2005). Joint Acquisition of CM and CL Codes for GPS L2 Civil (L2C) Signals. Proceedings of ION AM 2005 (Session C2, 27–29 June), Cambridge, MA, pages 553–562.

Yang, C., M. Miller, E. Blasch, and T. Nguyen (2007). Comparative Study of Coherent, Non-Coherent And Semi-Coherent Integration Schemes For GNSS Receivers. Proceedings of ION AM 2007 (Session E5, 23–25 April), Cambridge, MA, pages 572–588.

Yang, C., J. Vasquez, and J. Chaffee (1999). Fast Direct P(Y)-Code Acquisition Using XFAST. Proceedings of ION GPS-99 (Session D1, 14–17 September), Nashville, TN, pages 317–324.

Yu, W. (2006). Performance Evaluation of a Differential Approach Based Detector. Proceedings of ION GNSS 2006 (Session D5, 26–29 September, Fort Worth, TX), pages 2441–2452.

Zarrabizadeh, M. and E. S. Sousa (1997). A Differentially Coherent PN Code Acquisition Receiver for CDMA Systems. IEEE Transactions on Communications, 45(11), pages 1456 – 1465.

Zheng, B. and G. Lachapelle (2004). Acquisition Schemes for a GPS L5 Software Receiver. Proceedings of GNSS 2004 (Session A3, Long Beach, CA, 21–24 September), The Institute of Navigation, pages 1035–1040.

Ziedan, N. and J. Garrison (2004). Unaided acquisition of weak GPS signals using circular correlation or double-block zero padding. Proceedings of IEEE PLANS/ION 2004 (San Diego, CA, 24–26 April), pages 461–470.

Appendix A

This appendix derives the decision statistics of the *estimator correlator* detector for the received GPS signal with unkown signal parameters.

Estimator Correlator Detector

The matched filter was able to detect the received GPS signal in AWGN by detecting the change in the mean of the decision statistic. This was possible as the received GPS signal was assumed to be deterministic or the signal parameters were obtained via ML search (i.e. code/frequency search). Hence, its presence altered the mean of the received data. In stand-alone GPS receivers, the received GPS signal is more appropriately modeled as a random process due to the presence of unknown navigation data modulation. For instance, the received composite GPS signal comprises of multiple PRN code signals, which are zero-mean (asymptotically) and thus can readily be modeled as a zero-mean Gaussian random process. Similarly, the output of matched filter can also be modeled as zero-mean Gaussian random process due to the presence of navigation data. Accordingly, modeling the received GPS signal as a Gaussian process with an arbitrary covariance matrix, we obtain the NP detector as the *estimator correlator* (Kay [1993a]).

Development of the Detector

To derive the decision statistics of the estimator correlator, we consider a general detection problem,

$$
\begin{aligned}
H_0 &: x(k) = w(k) & k = 0, 1, ..., N-1. \\
H_1 &: x(k) = s(k) + w(n) & k = 0, 1, ..., N-1.
\end{aligned}
\tag{7.1}
$$

We model the input to be a random process $(s(k))$ with covariance matrix $\mathbf{C}_s$. The noise at the input of the estimator-correlator is assumed to be zero mean AWGN process with variance σ_w^2. The likelihood ratio test is given by,

$$L(\mathbf{x}) = \frac{\frac{1}{(2\pi)^{N/2} det^{1/2}(\mathbf{C}_s+\sigma_w^2\mathbf{I})} e^{\left[-\frac{1}{2}\mathbf{x}^T\left(\mathbf{C}_s+\sigma_w^2\mathbf{I}\right)^{-1}\mathbf{x}\right]}}{\frac{1}{(2\pi\sigma_w^2)^{N/2}} e^{\left[-\frac{1}{2\sigma_w^2}\mathbf{x}\mathbf{x}^T\right]}} > \gamma' \tag{7.2}$$

The Neyman-Pearson detector decides on H_1 if $L(\mathbf{x}) > \gamma'$. Taking logarithms and upon simplification yields,

$$T(\mathbf{x}) = \sigma_w^2 \mathbf{x}^T \left[\frac{1}{\sigma_w^2}\mathbf{I} - \left(\mathbf{C}_s + \sigma_w^2\mathbf{I}\right)^{-1}\right] \mathbf{x} > 2\sigma_w^2\gamma' \tag{7.3}$$

By setting $\mathbf{A} = \sigma^2\mathbf{I}$, $\mathbf{B} = \mathbf{D} = \mathbf{I}$ and $\mathbf{C} = \mathbf{C}_s$ and applying matrix inversion lemma[1], the above test statistic can be reduced to (Kay [1993a]),

$$T(\mathbf{x}) = \mathbf{x}^T \left[\frac{1}{\sigma_w^2}\left(\frac{1}{\sigma_w^2}\mathbf{I} + \mathbf{C}_s^{-1}\right)^{-1}\right] \mathbf{x} \tag{7.4}$$

By rearranging the signal covariance matrix and noise variance, the above equation can be written as,

$$T(\mathbf{x}) = \mathbf{x}^T \left[\mathbf{C}_s\left(\mathbf{C}_s + \sigma^2\mathbf{I}\right)^{-1}\right] \mathbf{x} \tag{7.5}$$

The product of the last two terms in the right hand side of (7.5) is essentially the MMSE estimate of the signal realization. That is,

$$\hat{s} = \mathbf{C}_s\left(\mathbf{C}_s + \sigma_w^2\mathbf{I}\right)^{-1}\mathbf{x} \tag{7.6}$$

Substituting (7.6) in (7.5) and expanding the inner product into summation produces

$$T(\mathbf{x}) = \sum_{k=0}^{N-1} x(k)\hat{s}(k) \tag{7.7}$$

From (7.7), it can inferred that the detector correlates the received signal with an estimate of the signal itself and is often termed as *estimator-correlator*. Figure 3.4 depicts the implementation of estimator-correlator detector for detecting random signal.
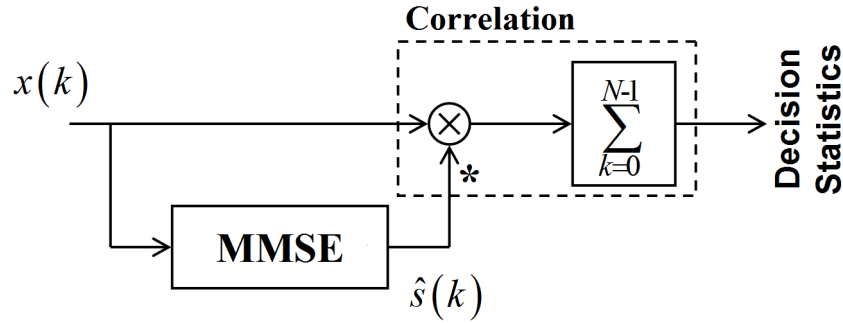
Figure 7.2: Estimator-Correlator Detector Implementation

If the input signal $x(k)$ can be modeled as a zero mean white Gaussian signal, then the corresponding decision statistic is given by,

$$T(\mathbf{x}) = \sum_{k=0}^{N-1} |x(k)|^2 \qquad (7.8)$$

Interestingly, (7.8) is very similar to the final decision statistics obtained for the energy detector as summarized in (3.60) in Section 3.4 of Chapter 3. For energy detector, we modeled the input signal as deterministic but unknown whereas in estimator correlator modeled the input signal as zero mean Gaussian random process. Hence, the detection performance will differ for both the detector structures.

For the post-correlation detectors, the output of initial coherent matched filter is correlated (over T_b) due to the presence of navigation data modulation. Hence, the covariance matrix $\mathbf{C}_s$ is no longer diagonal. Therefore, the matrix inversion in (7.6) is no longer straight forward. However, one can utilize the Taylor series method for the matrix inversion (Tylavsky and Sohie [1986]). Alternatively, for large N, we can approximate the eigen values by the power spectral density and the eigen vectors by the corresponding discrete Fourier transform vectors (Kay [1993a]).

---

[1]$(A + BCD)^{-1} = A^{-1} - A^{-1}B\left(DA^{-1}B + C^{-1}\right)^{-1} DA^{-1}$